Investigating Aqueous-Phase Adsorption for Enhancing (Electro)catalytic Hydrogenation

by

James Oluwatoyin Akinola

A dissertation submitted in partial fulfillment
of the requirements for the degree of
Doctor of Philosophy
(Chemical Engineering)
in the University of Michigan
2023

Doctoral Committee:

Assistant Professor Nirala Singh, Chair
Associate Professor Bryan Goldsmith
Professor Suljo Linic
Professor Adam Matzger

James Oluwatoyin Akinola

jakinola@umich.edu

ORCID iD: 0000-0002-8526-865X

Dedication

I dedicate this dissertation to my wife, my unshakable pillar of support throughout this Ph.D. journey. I know that you have longed to be recognized as a doctor, whether through your own academic achievements or through our association. Today, I proudly confer upon you the title of "Dr." by association. I have no doubt that you possess the qualities and abilities to pursue a Ph.D. of your own. And if you ever decide to do so, I will be here every step of the way, offering my unwavering support.

Acknowledgments

I firmly believe that a book's preface and acknowledgment sections hold immense importance, so I consider this section of my dissertation to be as important as the individual chapters. It would be a great oversight to not highlight the invaluable guidance and support given by numerous individuals who have played a role in making this Ph.D. a success. Although it is impossible to mention every one of them in this acknowledgment, I am immensely grateful for their contributions.

I want to express my deepest gratitude to my outstanding thesis committee members: Professors Nirala Singh, Bryan R. Goldsmith, Suljo Linic, and Adam Matzger. In 2018, my advisor, Professor Nirala Singh graciously welcomed me into his lab, even though I possessed no prior research experience in electrocatalysis. Under his meticulous leadership and guidance, my capacity to think critically about fundamental science questions in research grew significantly. I literally learned almost everything about giving oral presentations from him. I consider professor Singh an exemplary person who knows how to nurture the potential of others. I am thankful to him for bringing out the king in me in different seasons of my Ph.D. journey, helping me to be productive throughout every of those phases. I would also like to thank Professor Bryan Goldsmith, whom I consider my second advisor. As an experimentalist, I have had the opportunity to engage in regular bi-weekly interactions with a thoughtful theorist like Bryan. He is literally the best person to get feedback from regarding writing. Interactions with Professor Goldsmith has immensely improved my knowledge of computational catalysis and definitely made me a more complete researcher.

Whenever I have the opportunity to chat with Professor Linic, I am always amazed by his profound intelligence. In fact, I chose to do research in renewable energy after taking the Energy Seminar class with professor Linic. Thanks to his extensive experience and wisdom, I have avoided unfruitful directions in my Ph.D. culminating in the success of this dissertation. Professor Matzger graciously opened his lab to me, allowing me to conduct complex Raman experiments. I remember my first interaction with you and you said this to me and Harsh: “everything you guys need to do great research and help your advisor get tenured, I am happy to provide”. Thank you for saying and doing that, and always willing to assist us in troubleshooting Raman experiments. I know so much about Raman today thanks to the frequent discussions with professor Matzger.

When I joined the Singh lab, I truly believe the Lord ordered my step to share the same office space with Harsh Agarwal, the most brilliant graduate student I have ever encountered to this day. Over three consecutive years as office mates, our daily insightful conversations aided my seamless transition and progress as a Ph.D. student. Being able to witness the growth and contributions of multiple generations of Singh lab members has been a tremendous privilege for me. Each person has played a vital role in fostering the lab's vibrant and collaborative atmosphere and fueling my own progress as a researcher. Former members of the Singh lab, Dr. Ben Silcox, Dr. Zixuan Wang, Dr. Harsh Agarwal, Dr. Danielle Richards, and Dr. Cailin Buchanan, have all displayed exemplary Ph.D. achievements, setting a remarkably high standard for me. The current cohort of graduate students and postdoctoral researchers, including Claire, Jackie, Wendy, Jared, Christina, Dr. Libo Yao, Dr. Gyan Sharma, and Dr. Rocky Li, have diligently carried forward the tradition of excellence and community building in the lab. Their unwavering commitment to doing beautiful science continues to inspire me.

During my Ph.D. journey, I had the privilege of directly supervising the progress of two undergraduate students, Benjamin Furness and Amanullah Azim, and a master's student Takaaki Miki. This experience proved to be one of the most fulfilling and rewarding aspects of my Ph.D., as it allowed me to teach and reinforce the knowledge I have personally garnered. I want to thank these individuals for their inquisitiveness which has truly enriched our interactions and made the process of imparting knowledge even more enjoyable. It was a pleasure to work with Isaiah Barth, who was part of the same Ph.D. cohort as me. I couldn't have wished for a more understanding and productive collaborator. Let me mention here that every computational result presented in this dissertation was expertly conducted by him.

Beyond the lab, I have another home from home. My church family at the Redeemed Christian Church of God, Mountain of the Lord parish, and the Redeemed Christian Campus Fellowship at the University have been my resting place in so many ways. I am also thankful for every friend I made in the ChE department. To my family back in Nigeria, my mum especially, your daily calls kept me going through the last 5 years, I am grateful for their unrelenting support!

Table of Contents

Dedication ii

Acknowledgments iii

List of Tables xii

List of Figures xiii

Abstract xviii

Chapter 1 Introduction and Background 1

1.1 Motivation 1

1.2 Background 4

1.2.1 Bio-oils from Pyrolysis and Hydrothermal Liquefaction of Waste Biomass 4

1.2.2 Hydrogenation Reaction to Upgrade Bio-oil 5

1.2.3 Role of an Electrocatalyst for Electrocatalytic Hydrogenation (ECH) 8

1.2.4 ECH and TCH Mechanism in Aqueous Phase 9

1.2.5 Adsorption in the Gas vs. Aqueous Phase 13

1.2.6 Effect of Temperature on Gas vs. Aqueous-Phase Adsorption 17

1.2.7 Rational Design of ECH Catalysts based on Adsorption Energies 20

1.3 Scope of Work 23

1.4 References 27

Chapter 2 Experimental Methods 32

2.1 Introduction 32

2.2 Cyclic Voltammetry and Hydrogen Underpotential Deposition 32

2.2.1 Obtaining the Fraction of H_{upd} Inhibited and Organic Coverage 34

2.2.2 Reversibility of Hydrogen Underpotential Deposition in Acetate Buffer and in the Presence of Phenol 34

2.2.3 Change in Bulk Phenol Concentration by Adsorption of Phenol 37

2.2.4 Reproducibility of the Effect of Phenol Adsorption on H_{upd} 38

2.2.5 Reversibility of Organic Adsorption on Rh and Pt 39

2.3 Fitting Experimental Adsorption Isotherm Data using the Temkin Model 41

2.3.1 Converting from Aqueous Free Energies of Adsorption to Aqueous Enthalpies of Adsorption 43

2.4 Electrode Preparation for Supported Catalysts 47

2.4.1 Catalyst Ink Preparation and Deposition on Glassy Carbon 47

2.4.2 Direct Synthesis of Catalysts on Carbon Felt 48

2.5 Catalyst Characterization Techniques 50

2.5.1 X-ray Absorption Fine Structure Spectroscopy (XAFS) 50

2.5.2 X-ray Diffraction 54

2.5.3 Scanning Electron Microscopy 56

2.5.4 X-ray Photoelectron Spectroscopy 56

2.5.5 Transmission Electron Microscopy 58

2.5.6 Inductively Coupled Plasma-Mass Spectrometry 59

2.6 Surface Enhanced Raman Spectroscopy (SERS) 60

2.6.1 Synthesizing Roughened Au Electrodes for SERS 62

2.6.2 Removing Adventitious carbon on Roughened Electrodes 65

2.6.3 Depositing Pinhole-Free Thin Films of Transition Metals on Roughened Au 70

2.6.4 Measuring SERS Spectra 74

2.7 Hydrogenation Rate Measurements 75

2.7.1 Electrocatalytic Hydrogenation 75

2.7.2 Product Quantification using Gas Chromatography (GC) 76

2.8 References 77

Chapter 3 Adsorption Energies of Oxygenated Aromatics and Organics on Rhodium and Platinum in Aqueous Phase... 82

3.1 Summary 82

3.2 Introduction 83

3.3 Experimental and Computational Methods... 87

3.3.1 Cyclic Voltammetry 87

3.3.2 Dilution of Organic Concentration to Determine Reversibility 88

3.3.3 Adsorption Isotherm Fitting 89

3.3.4 Computational Methods 90

3.4 Results and Discussions 94

3.4.1 Impact of Phenol on the Underpotential Deposition of Hydrogen on Pt and Rh......... 94

3.4.2 Extracted Adsorption Energies of Phenol on Platinum and Rhodium 97

3.4.3 Difference in Gas-phase and Aqueous-phase Adsorption Energies of Phenol 101

3.4.4 Impact of other Oxygenated Aromatics and Organics on the Underpotential Deposition of Hydrogen on Rh. 103

3.4.5 Adsorption Energies of Furfural, Benzaldehyde, Benzyl Alcohol, and Cyclohexanol on Rh 105

3.4.6 Comparing Experiments with Implicit Solvent and Bond-additivity Calculations.... 108

3.4.7 Consequences of Weaker Effective Organic Adsorption on Pt and Rh on Hydrogenation Rates 111

3.5 Conclusions 112

3.6 References 113

Chapter 4 Temperature Dependence of Aqueous-Phase Phenol Adsorption on Pt and Rh 119

4.1 Summary 119

4.2 Introduction 120

4.3 Experimental Section 123

4.3.1 Cyclic Voltammetry 123

4.3.2 Adsorption Isotherm Fitting 124

4.4 Results and Discussion 125

4.4.1 Temperature Dependence of Phenol Adsorption and Hydrogen Underpotential Deposition on Pt 125

4.4.2 Enthalpy and Entropy of Adsorption of Gas-Phase Phenol compared to Aqueous-Phase Phenol 129

4.4.3 Entropy and Enthalpy of Adsorption of Phenol on Rh 131

4.4.4 Entropy of Adsorption of Phenol in the Absence and Presence of Water 134

4.4.5 Differences in Entropies and Enthalpies of Adsorption in Gas and Aqueous Phase . 139

4.4.6 Implications for Aqueous-Phase Hydrogenation Kinetics 140

4.5 Conclusions 141

4.6 References 142

Chapter 5 Effects of Solvents on Adsorption: A General Bond Additivity Model 146

5.1 Summary 146

5.2 Introduction 147

5.3 Results and Discussion 149

5.3.1 Bond-Additivity Model for Molecules of Finite Thickness 149

5.3.2 Solvation Energy 150

5.3.3 Adsorption Energy of Solvated Reactant Molecule 152

5.3.4 Reactant Molecule of Non-Rectangular Shape 155

5.3.5 Case study for Effect of Adsorbate Thickness 162

5.3.6 Solvation Energies per Unit Molecular Area, and Organic/Solvent Adhesion Energies 167

5.4 Conclusions 168

5.5 References 169

Chapter 6 Electrocatalytic Hydrogenation of Phenol on Platinum-Cobalt Alloys 173

6.1 Summary 173

6.2 Introduction 174

6.3 Experimental & Computational Methods 176

6.3.1 Chemicals and Materials 176

6.3.2 Catalyst Preparation.. 177

6.3.3 Catalyst Characterization and Surface Area Measurements 178

6.3.4 Hydrogen Evolution Reaction (HER) 181

6.3.5 Electrocatalytic Hydrogenation of Phenol... 183

6.3.6 Density Functional Theory Modeling 184

6.4 Results and Discussion... 186

6.4.1 Comparing Hydrogen Evolution Activity to Hydrogen Adsorption Energy on Pt_xCo_y/C 186

6.4.2 Synthesis and Characterization of Pt_xCo_y Alloys Supported on Conductive Carbon Felt 189

6.4.3 Electrocatalytic Hydrogenation of Phenol on Pt_xCo_y Alloys 195

6.4.4 Effect of Co Alloying on Phenol Adsorption and Hydrogenation Barriers 196

6.4.5 Explaining ECH Activity on Pt_xCo_y Alloys Using a Langmuir-Hinshelwood Model 200

6.5 Conclusions 204

6.6 References 204

Chapter 7 Conclusions and Future Projections 210

7.1 Summary and Conclusions.. 210

7.2 Extension of Current Research.. 214

7.2.1 Measuring Adsorption Energies on Non-Pt Group Metals and Alloys...................... 214

7.2.2 Probing Intrinsic and Apparent Adsorption Energies in Different Solvents............. 216

7.2.3 Synthesis and Stabilization of Pt/Pt_xCo_y Catalyst Structure 221

7.3 Outlooks 223

7.4 References 224

Appendix 227

List of Tables

Table 2.1 Desorption charges for H_{upd} (Q_{des}) on Rh wire in acetate buffer supporting electrolyte corresponding to data in Figure 2.2 at 100, 50, or 20 mV s^{-1} scan rate....................................... 35

Table 2.2 H_{upd} desorption charge (Q_{des}) at 0 and 60 µM phenol and the fraction of H_{upd} inhibited on Rh wire at 60 µM phenol for the different measurements shown in Figure 2.4...................... 39

Table 2.3 The H_{upd} desorption charge without phenol, with 60 µM phenol, and after replacing phenol solution with new supporting electrolyte on Pt wire (Figure 2.5a) and Rh wire (Figure 2.5e). 41

Table 2.4 Henry's law constant (K_H) at 298.5 K, gas-phase entropy, and enthalpy of solvation for molecules studied in this work.. 44

Table 3.1 Measured adsorption free energies and enthalpies of organic compounds on Rh and Pt wires at 298 K in aqueous phase from hydrogen site blocking experiments............................. 108

Table 4.1 Adsorption energies, coverage dependence of adsorption energies (α), adsorption equilibrium constants, enthalpies, and entropies of phenol adsorption on Pt and Rh obtained from isotherms and van't Hoff plot using the best fit... 134

Table 5.1 Solvation energy, footprint surface area, total surface area exposed to solvent in bulk solution, solvation energy per unit area, solvent/reactant adhesion energy, and predicted change in adsorption energy on Pt(111) due to the solvent for reactants in different solvents.................. 160

Table 5.2 Predicted energies of adsorption in solvents estimated from experimental gas-phase heats of adsorption using Eq. 5.9 and listed values in Table 5.1. 161

Table 6.1 Tabulated fitting results for EXAFS of the Pt foil and pretreated Pt_xCo_y/felt catalysts at the Pt L_3-edge.. 190

Table 6.2 Particle sizes from TEM and XRD using the Scherrer equation for the pretreated Pt_xCo_y on felts and on Vulcan carbon. 195

Table A.1 Tabulated linear combination fitting results of XANES for Pt_xCo_y/felt catalysts at the Pt L_3-edge using Pt foil and PtO_2 as standards. Fitting was performed at −20 eV below the edge and 30 eV post edge.. 238

List of Figures

Figure 1.1. CO_2 intensity by different sectors and the lifetime of different fossil sources. 3

Figure 1.2 Diagram illustrating the potential of utilizing electrocatalytic hydrogenation to upgrade bio-oil derived from waste biomass and plastic materials, enabling their conversion to transportation fuels and industrial chemicals. 5

Figure 1.3 Select model compounds in bio-oil and their electrocatalytic hydrogenation pathways. 7

Figure 1.4 Energy diagram showing the pathway for an uncatalyzed and a catalyzed reaction for heterogeneous catalysis. 9

Figure 1.5 Kinetics and spectroscopic evidence for a LH mechanism for phenol on Pt group metals under thermochemical and electrochemical conditions. 11

Figure 1.6 Schematic showing adsorption of an organic in a) aqueous phase and b) gas phase. 15

Figure 1.7 Entropies of unadsorbed and adsorbed hydrocarbon molecules in gas phase and the temperature dependence of adsorbate coverages in the gas phase. 19

Figure 1.8 Top and side view of idealized bimetallic surface structures with one monolayer of 3d metals on a Pt(111) substrate reproduced from ref [64]. 21

Figure 1.9 Gas-phase hydrogenation activity and the binding energies of hydrogen and cyclohexene on Pt based alloy catalysts reproduced from ref [69]. 22

Figure 2.1 Cyclic voltammetry procedure on Pt supported on Vulcan carbon deposited on a glassy carbon disk electrode in 3 M acetate buffer at 23.3°C. 33

Figure 2.2 Cyclic voltammograms showing the H_{upd} on Rh wire in acetate buffer (100 mM acetic acid, 100 mM sodium acetate, pH = 5) at 298 K and varying scan rates. 35

Figure 2.3 The H_{upd} adsorption charge (from reduction, Q_{ads}) and desorption charge (from oxidation, Q_{des}) as a function of phenol concentration on polycrystalline metal wires. 36

Figure 2.4 Cyclic voltammograms to test the reproducibility of phenol adsorption on rhodium wire from three different repetitions. 39

Figure 2.5 Cyclic voltammograms showing the reversibility of organic adsorption on rhodium and platinum after controlled dilution. 40

Figure 2.6 Outlined procedure of estimating the aqueous phase adsorption enthalpies from CV method and isotherms. 43

Figure 2.7. Cyclic voltammogram of Pt supported on Vulcan carbon (Pt/C) ink drop casted on a carbon felt showing the H_{upd} region before and after typical ECH pretreatment procedures. 49

Figure 2.8 Methodology for synthesizing Pt_xCo_y catalysts directly supported on carbon felt using sodium borohydride as reductant. 49

Figure 2.9 X-ray absorption experiment setup in transmission and flourescence mode. 50

Figure 2.10 XAFS spectra representation for a Pt foil performed at the Advanced Photon Source at the Argonne National Laboratory. 51

Figure 2.11 Diagram showing the fundamental principle of X-ray diffraction. 54

Figure 2.12 Background subtracted XPS spectra for an uncleaned roughned Au electrode showing the Au 4f and C 1s peaks. 58

Figure 2.13 ICP-MS calibration plot for Pt and Co standards prepared using water as the solvent. 60

Figure 2.14 Raman scpectroscopy showing the incident ray, Rayleigh scatering where the final state frequency v is the same as the initial frequency of the photon, Stokes Raman scattering and Anti-Stokes Raman scattering. 61

Figure 2.15 Electrochemical Raman cell set up. 63

Figure 2.16 Roughening procedure for Au film deposited on silicon wafer. 64

Figure 2.17 SERS spectra and SEM images of electrode surfaces after various cleaning procedures. 67

Figure 2.18 SERS spectra for ClO_4^- in water after the different cleaning procedures. 69

Figure 2.19 Cyclic voltammogram of unroughened Au, roughened Au, electrodeposited Pt and atomic layer deposited Pt. 72

Figure 2.20 Surface enhanced Raman spectroscopy of carbon monoxide dissolved in water on roughened Au, electrodeposited Pt and atomic layer deposited Pt. 74

Figure 2.21 Gas chromatrophy calibration for quantifying phenol and the associated products from ECH. 77

Figure 3.1 Cyclic voltammograms showing the H_{upd} region at different bulk phenol concentrations on metal surfaces. 95

Figure 3.2 Adsorption isotherms of phenol on metal surfaces. 98

Figure 3.3 DFT-computed heats of adsorption in implicit solvent (orange), gas phase (blue), and aqueous phase using a bond-additivity (B.A) model. 102

Figure 3.4 Cyclic voltammograms in the H_{upd} region with increasing bulk organic concentration on a Rh wire for different organics. 104

Figure 3.5. Adsorption isotherms of organics on Rh wire in aqueous phase. 107

Figure 3.6. Calculated heats of adsorption using the PBE-D3 functional referenced to experimental heats of adsorption for organics using different methods. 110

Figure 4.1 Cyclic voltammograms of a Pt wire in 100 mM acetate buffer supporting electrolyte showing the hydrogen underpotential deposition region at different phenol concentrations and temperatures. 126

Figure 4.2 Fraction of hydrogen underpotential deposition charge inhibited as a function of phenol concentration on Pt at varying temperatures. 128

Figure 4.3 Natural log of aqueous-phase adsorption constant of phenol on platinum from Figure 4.2 plotted as a function of inverse temperature (van't Hoff plot) on Pt. 130

Figure 4.4 Fraction of hydrogen underpotential deposition charge inhibited as a function of phenol concentration on Rh at varying temperatures. 132

Figure 4.5 The van't Hoff plots of the adsorption of phenol on Rh. 133

Figure 4.6 Structures of displaced interfacial water and corresponding phenol adsorption entropy for different situations. 138

Figure 5.1 Thermodynamic cycle to determine the energy of adsorption of a reactant molecule (R) with finite thickness onto a solid surface (M) in a condensed-phase solvent (S) from its energy of adsorption in the gas-phase. 150

Figure 5.2 Thermodynamic cycle to determine the energy of adsorption of a reactant molecule (R) with finite thickness onto a solid surface (M) in a condensed-phase solvent (S) from its energy of adsorption in the gas-phase, where the reactant has a top area that is different than its footprint area on the surface. 155

Figure 5.3 Phenol represented as a uniform molecule with footprint and total outer surface area. If phenol is infinitely thin. 163

Figure 5.4 Energy of adsorption of phenol onto Pt(111) in water at 298 K as a function of the ratio of the footprint of phenol on the Pt surface to the total surface area of phenol, calculated using Eq. 5.7 166

Figure 6.1 Linear scan voltammograms and Tafel plots for Pt/C and Pt_xCo_y/C 182

Figure 6.2 XRD spectra and lattice constant as a function of Co fraction for Pt, Pt_3Co and PtCo face-centered cubic structures. 186

Figure 6.3 Hydrogen evolution activity related to the hydrogen adsorption energy on different Pt_xCo_y structures. 188

Figure 6.4 Ex-situ XAS and XRD for Pt_xCo_y/felt catalysts. 192

Figure 6.5 TEM histogram distribution of particle diameters and representative micrograph (inset image) of the Pt_xCo_y catalysts. 194

Figure 6.6 Experimental ECH turnover frequency and current efficiency on Pt_xCo_y/felt catalysts as a function of Co fraction for different applied potentials. 196

Figure 6.7 Phenol adsorption energies from adsorption experiments on Pt_xCo_y/C catalysts. 197

Figure 6.8 Activation enthalpy for the first hydrogenation step of phenol. 200

Figure 6.9 ECH turnover frequency on Pt_xCo_y/felt, as a function of Co fraction and potential using a Langmuir-Hinshelwood model. 202

Figure 7.1 Schematic showing organic adsorption and displacement of water molecules in aqueous phase. 212

Figure 7.2 Schematic showing a catalyst surface for platinum group metals (PGMs) and alloys containing non PGMs during adsorption measurements using different methods. 215

Figure 7.3 Final step in the bond additivity model showing the assumption that intrinsic bond energy between a molecule and the metal is unaffected by the solvent environment. 217

Figure 7.4 Surface enhanced Raman spectra on Au compared to Pt for thionine and phenol dissolved in water. 219

Figure 7.5 Surface enhanced Raman spectra of thionine and phenol dissolved in different solvents on roughened Au. 221

Figure 7.6 Synthesis methods employed to prepare Pt shell on a Pt_xCo_y core nanoparticle structure. 222

Figure A.1 The H_{upd} adsorption charge (Q_{ads}) and desorption charge (Q_{des}) as a function of furfural concentration. 229

Figure A.2 Fraction of unrecovered H* (or electrons) in the desorption region $(Q_{ads} - Q_{des})/Q_{ads,no\ furfural}$ as a function of furfural concentration at 25, 50 and 100 mV s^{-1} scan rates. 230

Figure A.3 Cyclic Voltammogram and adsorption isotherms of furfural on Pt wire. 231

Figure A.4 Cyclic voltammograms of as prepared Pt_xCo_y/felt catalysts. 232

Figure A.5 Cyclic voltammograms of the pretreated catalysts synthesized on carbon felt support. 233

Figure A.6 Cyclic voltammograms of the pretreated catalysts supported on Vulcan carbon.... 234

Figure A.7 EXAFS spectra of Pt foil and Pt_{100}/felt catalysts performed at the Pt L_3-edge and their fit. 235

Figure A.8 EXAFS spectra of $Pt_{86}Co_{14}$/felt and $Pt_{80}Co_{20}$/felt catalysts performed at the Pt L_3-edge and their fit. 236

Figure A.9 EXAFS spectra of $Pt_{62}Co_{38}$/felt at the Pt L_3-edge and fit. 237

Figure A.10 XANES of Pt_{100}/felt at the Pt L_3-edge at −0.05 V vs. RHE and Pt foil. 238

Figure A.11 Representative TEM micrographs of the catalysts. 239

Abstract

Bio-oil derived from biomass and plastic wastes is a promising substitute to traditional petroleum for use as transportation fuels and chemical precursors and as such it has the potential to combat global warming. However, bio-oil must be upgraded as soon as it is produced to address its instability, primarily caused by high oxygen content and excess water. In this dissertation, we investigate electrocatalytic hydrogenation (ECH) in the aqueous phase to sustainably stabilize bio-oil molecules. ECH still exhibits poor performance for many bio-oil molecules and catalyst materials, which is in part due to a poor understanding of aqueous-phase adsorption and how it governs ECH activity and catalyst design. The chapters in this dissertation investigate aqueous adsorption for model bio-oil molecules on metals and alloy catalyst materials to link their adsorption energies in the aqueous phase to ECH activity.

We first explore the role of the aqueous environment on the adsorption energies and enthalpies of C5/C6 organics on Pt and Rh metal surfaces. We show that the aqueous adsorption enthalpies measured from experimental adsorption isotherms are 50–250 kJ mol^{-1} lower than their gas-phase values. The lower aqueous adsorption enthalpy is due to organic solvation and solvent displacement, which introduces a large enthalpic penalty for adsorption in the aqueous phase. Secondly, the molecules display similar aqueous adsorption enthalpies on Pt and Rh despite a huge difference in their gas-phase values. The lower aqueous adsorption strengths explain why ECH of these molecules can occur with appreciable rates in the aqueous phase at room temperature. We also show that Pt and Rh have similar ECH activity toward phenol and benzaldehyde because Pt and Rh adsorb these molecules with similar adsorption energies.

We next explore the entropy of the displaced interfacial water molecules upon phenol adsorption by examining the temperature dependence of phenol adsorption. We have initially assumed that the displaced interfacial water only results in an enthalpic penalty but retains its structure and does not influence the aqueous adsorption entropy. We show that the aqueous adsorption entropy is slightly positive in contrast to the negative adsorption entropy in the gas phase. This is because the water molecules upon displacement gain about half of the entropy of bulk liquid water. Consequently, temperature would have a less negative impact on coverages in aqueous phase compared to gas phase.

Considering the importance of obtaining accurate aqueous-phase adsorption energies to explain ECH activity correctly, we developed a mathematical model that accounts for solvation and solvent displacement to aid the prediction of aqueous adsorption energies for molecules of any shape and size. This model uses gas-phase adsorption energies along with values from thermochemistry tables to calculate aqueous adsorption energies that are in semi-quantitative agreement with experiments.

Finally, we synthesized Pt and Pt_xCo_y alloys to elucidate the impact of catalyst structure and composition on phenol ECH turnover frequency and current efficiency. Pt_xCo_y alloys have weaker hydrogen adsorption energies than Pt and are more active toward hydrogen evolution reaction than Pt, resulting in lower ECH current efficiencies. However certain Pt_xCo_y alloys are more active at certain potentials due to a higher ECH barrier with Co fraction. By using kinetic modeling, we capture qualitative trends in the measured ECH turnover frequency as a function of Co fraction and potential. Ultimately, this dissertation advances our knowledge of aqueous-phase adsorption and ECH activity.

Chapter 1 Introduction and Background

Portions of **sections 1.2.4** and **1.2.5** in this chapter were adapted from Barth, I.; **Akinola, J**.; Lee, J.; Gutiérrez, O. Y.; Sanyal, U.; Singh, N.; Goldsmith, B. R. J. Chem. Phys**. 2022**, 156, 104703.

1.1 Motivation

During the spring and summer of 2023, Canada experienced its most severe wildfires ever recorded, burning over 1 trillion square meters of land.[1] In fact, several places in the world and even in the US like California and Hawaii have not been spared by these ravaging wildfires. On another note, the month of July 2023 is currently touted by many as the hottest month recorded in human history, where cities in the U.S. like Phoenix, witnessed a streak of temperatures above 120 °F for several days. Sadly, the increasing consequences of global warming exacerbated by humanity's dependence on fossil sources for energy and chemical manufacturing are no longer a myth or a mystery but a reality we now experience.[2] The onus is now on policymakers and researchers like me to take responsibility for discovering new technologies and materials to salvage our global climate.

The use of fossil sources for petrochemical and transportation applications has been a cornerstone of modern industrialization and economic development. Fossil fuels, primarily coal, oil, and natural gas, have provided an abundant and relatively inexpensive source of energy that has fueled the growth of industries and enabled global transportation networks over a long history that dates to the Industrial Revolution.[3] Fossil sources are still the dominant energy and raw material providers for the transportation and petrochemical sectors.[4–6] Crude oil, derived from fossil sources, serves as the primary feedstock for the production of petrochemicals, which are the building blocks for a wide range of products such as plastics, fertilizers, pharmaceuticals, and textiles.[7,8] Furthermore, energy-dense fossil fuels like jet fuel, gasoline, and diesel continue to power the majority of airplanes and vehicles worldwide, enabling the mobility and transportation of goods and people.[9] Even though these fossil reserves are geographically distributed, many countries possess significant reserves, with organized networks ensuring a reliable supply of energy and raw materials around the world.[10]

Despite their relevance, the use of fossil sources for chemical and transportation applications has raised significant environmental concerns.[2] Burning fossil fuels for energy releases greenhouse gases, such as carbon dioxide (CO_2), into the atmosphere, offsetting the carbon cycle, and contributing to climate change and global warming. The transportation sector has long been a significant contributor to CO_2 emissions as highlighted by the US Energy Information Administration (EIA) (**Figure 1.1a**).[9] The continual burning of fossil fuels in cars, trucks, airplanes, and ships releases vast amounts of CO_2 into the atmosphere, exacerbating climate change. For example, in the United States, over 143 billion gallons of motor gasoline are consumed annually to power transportation.[9] As the demand for transportation continues to grow worldwide, it becomes imperative to address the environmental impact of this sector by transitioning towards cleaner and more sustainable alternatives.

The depletion of fossil fuel reserves is another pressing concern that further complicates the situation. **Figure 1.1b** shows the ratio between proved reserves of crude oil, coal and natural gas and the annual rate at which these fossil sources are unearthed for use.[10] It is clear that these fossil reserves are not eternal and will eventually run out. As our reliance on fossil fuels for energy and transportation persists especially with increasing global population, the finite nature of these reserves becomes increasingly apparent. The gradual depletion of these fossil sources poses not only an environmental challenge but also an economic one, as the scarcity of these resources could disrupt energy systems particularly in developing countries and impact various industries that depend on them.

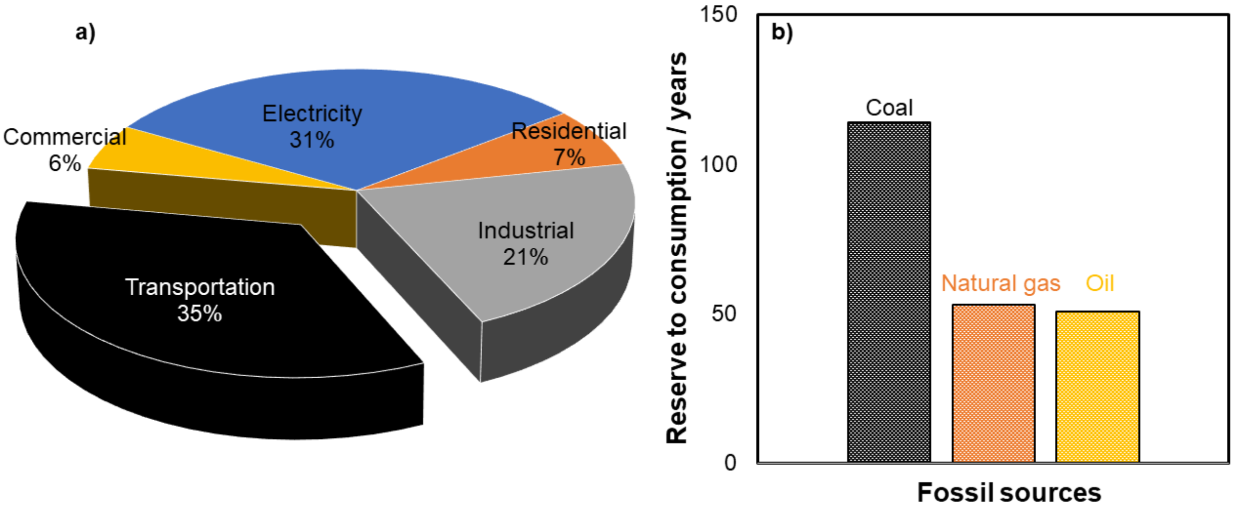

Figure 1.1. CO_2 intensity by different sectors and the lifetime of different fossil sources. a) CO_2 intensity by end-use sectors in 2021 extracted from ref [9]. **b)** Total proved fossil reserves divided by their annual rate of production from their reserves. Data was extracted from ref [10]. CO_2 intensities are calculated as CO_2 emissions per unit of energy output.

To address these interconnected challenges of global warming and depletion of fossil sources, there is a growing need to invest in renewable energy sources, increase energy efficiency, and accelerate the development and adoption of sustainable technologies.[11] For example, renewable electricity produced from solar and wind can be used to power electric vehicles for ground transportation, whereas biomass-derived bio-oils can be upgraded to replace jet fuels for the aviation sector where reliability, safety and energy density are top priorities. In this way, we can reduce our reliance on fossil fuels and mitigate their environmental impact. This dissertation focuses on developing a fundamental understanding of aqueous-phase electrocatalytic hydrogenation (ECH) through which bio-oils derived from waste biomass can be upgraded to become sustainable alternatives to fossil sources.

1.2 Background

1.2.1 Bio-oils from Pyrolysis and Hydrothermal Liquefaction of Waste Biomass

Bio-oils have gained considerable attention as a sustainable alternative to fossil sources as they can be derived from the fast pyrolysis[12] or hydrothermal liquefaction (HTL)[13] of waste biomass. Biomass wastes, such as agricultural residues, forestry residues, and energy crops, holds great potential as a feedstock for bio-oil production.[14] The conversion of waste biomass alone into liquid fuel or chemical products for industrial use holds the potential to eliminate significant amounts of petroleum consumption. Fast pyrolysis of biomass is a promising technology that converts biomass at 400–600 °C without oxygen, decomposing the biomass to produce valuable products such as bio-oil, biochar, and syngas.[15] On the other hand, HTL process involves the submersion of biomass in a water-based solvent, typically at lower operating temperatures than fast pyrolysis ranging from 250–400 °C. Here, biomass undergoes a series of complex chemical reactions in the HTL reactor, including hydrolysis, dehydration, decarboxylation, and polymerization, resulting in the formation of a bio-oil or sometimes called biocrude.[16] Bio-oil contains a wide range of organics, including oxygenated compounds, phenols, aldehydes, and hydrocarbons dissolved in large amounts of water that can be upgraded to produce transportation fuels or used as a feedstock for various chemical processes.[17]

Although bio-oils are a promising alternative for the transportation and chemical industry, their quality and stability are crucial issues that limit their use and commercialization. These oxygenated aromatics and hydrocarbons significantly influence the physical and chemical properties of bio-oil, including the viscosity, density, heating value, water content, acidity, and stability. In addition, bio-oil typically contains a substantial amount of water, which can cause phase separation, reduce its heating value and stability as well. In **Chapter 3**, we investigate the role of water on adsorption of select bio-oil molecules on relevant catalytic surfaces to gain understanding into ECH in aqueous phase.

1.2.2 Hydrogenation Reaction to Upgrade Bio-oil

To overcome the challenges associated with the quality and stability of bio-oil, several physical,[18] chemical,[19] and catalytic methods such as hydrodeoxygenation[20] and zeolite cracking[20,21] have been employed to address different deficiencies of bio-oil. Hydrodeoxygenation, a combination of hydrogenation and deoxygenation reactions, directly addresses the high oxygen content in bio-oil molecules which is the root problem of poor bio-oil quality and stability. Hydrogenation can be performed through ECH (**Figure 1.2**), or thermocatalytic hydrogenation (TCH), and is aimed at saturating bio-oil molecules with hydrogen to increase the H/C ratio, energy density, and increase the H/O ratio, thus making deoxygenation more feasible.[13]

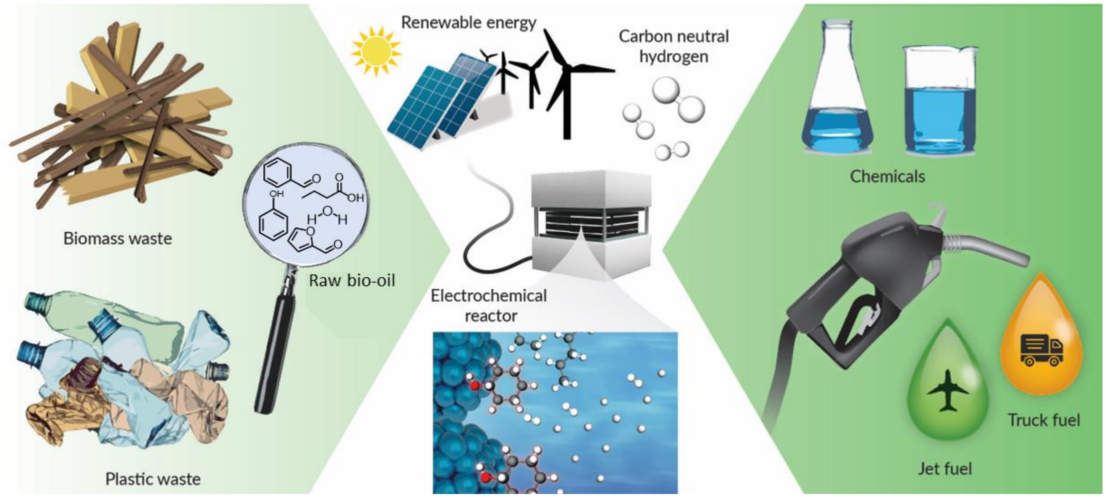

Figure 1.2 Diagram illustrating the potential of utilizing electrocatalytic hydrogenation to upgrade bio-oil derived from waste biomass and plastic materials, enabling their conversion to transportation fuels and industrial chemicals.

Electrocatalytic hydrogenation of bio-oil offers several advantages over thermocatalytic hydrogenation. Bio-oil TCH involves the use of H_2 typically from methane steam reforming, which is a non-renewable H_2 source, thereby defeating the intent of making bio-oil a renewable alternative to fossil sources. Electrocatalytic hydrogenation on the other hand, is a more sustainable route for hydrogenation (**Figure 1.2**) where the hydrogen equivalents can be obtained by the reduction of protons from water already present in bio-oil. As cheaper renewable electricity generation is anticipated to rise significantly in the coming decades,[9] leveraging this growth for biomass hydrogenation presents an appealing pathway to create sustainable, energy-dense and cost effective transportation fuels. In addition, the use of modular electrochemical reactors for ECH allows facilities to be strategically located near abundant waste biomass sources in remote areas, hence the problem of transporting an already unstable bio-oil to a central upgrading facility is avoided. ECH processes can also be operated at low pressures and temperatures[22,23] compared to TCH, eliminating the need for high temperature reaction, further promoting cost-effectiveness and sustainability. Moreover, technoeconomic analysis (TEA) reveals that hydrogenation is the most energy-intensive and expensive step in the bio-oil production process, contributing to an overall increased cost of bio-oil compared to petroleum,[24,25] necessitating a potentially lower cost process like ECH.

The overall ECH cost will be largely determined by the size of the electrochemical reactor (capital cost) and the kilowatt-hours of electricity used to produce a unit of upgraded bio-oil. TEA studies have suggested that significant market adoption could occur if ECH current densities matched those of a typical commercial proton exchange membrane electrolyzer, where the total overpotential is less than 1 V, indicating high efficiency close to thermodynamic limits.[13] However, achieving these desired ECH current densities up to 1 A cm^{-2} at overpotentials less than 0.5 V has not yet been demonstrated, largely due to gaps in understanding the aqueous phase ECH mechanism and the important variables that directly impact ECH rates. A fundamental understanding of aqueous-phase ECH mechanism would aid the design of electrochemical systems, reaction conditions and catalyst materials to improve ECH activity and current efficiency that will lead to an eventual commercialization of bio-oil.[22]

To gain fundamental understanding of ECH mechanism in this dissertation, we study model compounds representative of bio-oil instead of utilizing actual bio-oil (**Figure 1.3**), because of the simultaneous hydrogenation of multiple functional groups in bio-oil which could obscure accurate understanding of the mechanism. For example, ECH of benzaldehyde and furfural targets the carbonyl group first whereas phenol ECH targets the aromatic ring first (**Figure 1.3**). In **Chapter 2** we study the aqueous adsorption of select bio-oil model compounds (phenol, benzaldehyde, and furfural as well as cyclohexanol and benzyl alcohol which are hydrogenated products of phenol and benzaldehyde, respectively) on Pt and Rh. We choose these surfaces due to their activity for bio-oil hydrogenation.[26]

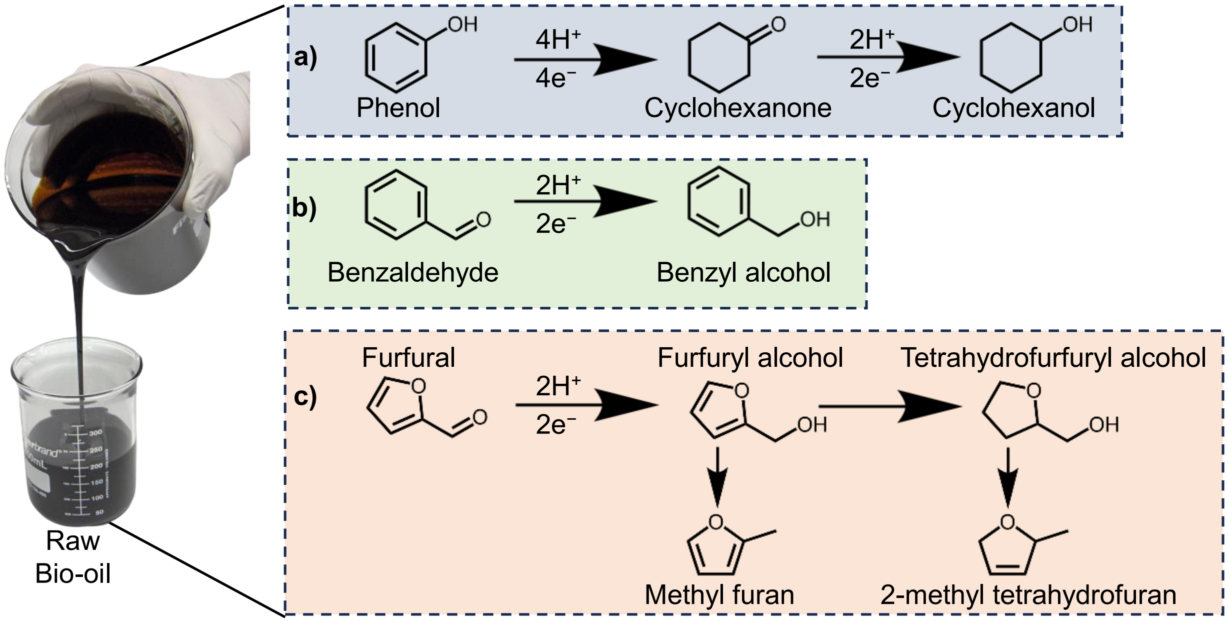

Figure 1.3 Select model compounds in bio-oil and their electrocatalytic hydrogenation pathways. a) Phenol to cyclohexanone and cyclohexanol. **b)** Benzaldehyde to benzyl alcohol. **c)** Furfural to furfuryl alcohol, methyl furan, tetrahydrofurfuryl alcohol, and 2-methyltetrahydrofuran.

1.2.3 Role of an Electrocatalyst for Electrocatalytic Hydrogenation (ECH)

A solid catalyst surface is required in ECH to provide an enabling platform to break several C-O, C-H, C-C, and C=C bonds in the oxygenated bio-oil molecules and form new bonds to produce the hydrogenated molecules with lower oxygen content. The molecules to be transformed (bio-oil organic and hydrogen) first adsorb on the active sites of the catalyst and the favorable interaction between the surface and the molecules weaken the existing bonds of the molecules thereby reducing the activation barrier to cause a reaction.[27] **Figure 1.4** shows how a catalyst can lower the barrier for a reaction, by providing alternative pathways with lower energy barriers through which adsorbed reactant molecules can react. The final product then desorbs and opens the catalyst site for another reaction to occur. As such, the catalyst is not consumed during the reaction but undergo many turnovers until it becomes deactivated. The turnover number (TON) defines the number of reactions a single catalyst site performs before it deactivates. The turnover frequency (TOF) is an important variable that describes the catalyst activity and is defined as the rate of turnover (i.e., TON/time with units of time^{-1}). An excellent catalyst would therefore be able to carry out the desired reaction at a very high TOF. As a rule-of-thumb, the 1 A cm^{-2} desired in ECH reactors[13] is the same as a TOF of 1 s^{-1} for a four-electron process on Pt(111) or other metal surfaces.

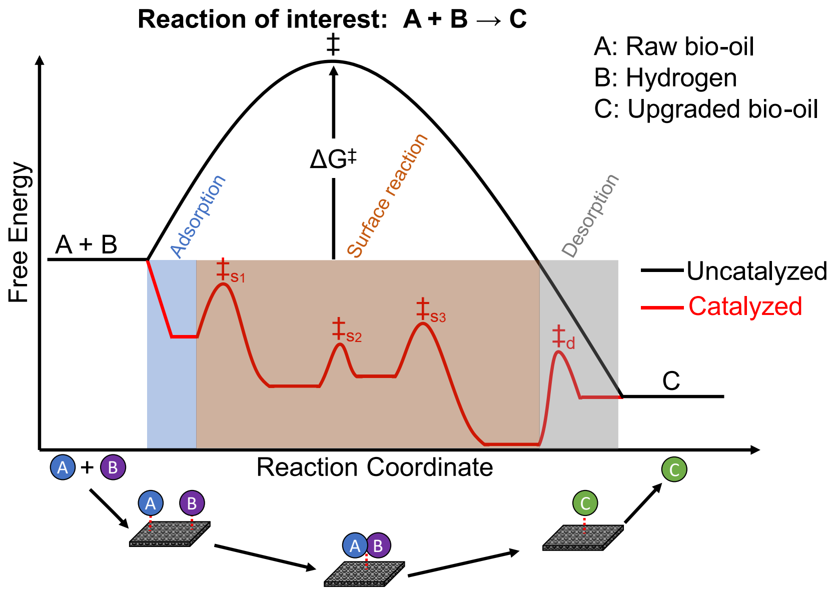

Figure 1.4 Energy diagram showing the pathway for an uncatalyzed and a catalyzed reaction for heterogeneous catalysis. The catalyst reduces activation barriers often by forming stable intermediates along the uncatalyzed reaction route, or by facilitating entirely novel pathways. The adsorption step, series of surface reaction steps and a desorption step are shown for a catalyzed reaction route.

An electrochemical reactor for ECH can be made more affordable both in terms of lowering the capital and operating costs by increasing the TOF through proper design of the catalyst material, liquid electrolyte environment, reaction conditions (e.g., concentration, temperature and applied potential). A higher TOF would translate to a reduced catalyst amount, electrode area, and membrane area required to achieve a given production rate of upgraded bio-oil thus reducing the capital cost. In addition, because the reaction rate is faster, the charge (current × time) and thus kilowatt-hour of electricity required for ECH will be lower thus reducing the operating cost. In **Chapter 6** we describe the influence of alloy catalyst materials on the ECH TOF for aqueous phenol and show how the TOF varies with catalyst composition and applied potential.

1.2.4 ECH and TCH Mechanism in Aqueous Phase

For both aqueous-phase ECH and TCH, adsorbed hydrogen (H*) reacts with the adsorbed oxygenated aromatic molecule for hydrogenation to occur, and if the adsorption and desorption steps are fast, surface hydrogenation becomes the slowest or rate-determining step (RDS). This mechanism is known as the Langmuir-Hinshelwood (LH) mechanism.[28,29] There are several ECH reactions on platinum group metals (PGMs) surfaces where the mechanism is proposed to proceed via a rate-determining surface hydrogenation step, similar to the LH mechanism in TCH. This similarity in mechanism is based on comparable apparent activation energies and product distribution with time for TCH and ECH on PGMs for a molecule like phenol.[30,31] An indirect evidence for a LH mechanism for TCH and ECH is also shown in **Figure 1.5**, where competition between adsorbed phenol and hydrogen dictates the turnover frequency.[26] In **Figure 1.5a** and **b**, when phenol concentrations are too low, there is not enough adsorbed phenol to achieve high TOF, resulting in a positive reaction order in phenol. But when phenol concentrations are too high, the surface is poisoned by phenol causing a lower TOF and a negative reaction order in phenol. There is an intermediate concentration where sufficient coverage of adsorbed phenol and hydrogen exist to give a maximum TOF, typical of a LH mechanism where the Sabatier principle of catalysis is applicable.[32]

Figure 1.5c shows X-ray absorption near edge spectra (XANES) under electrochemical conditions, where the adsorbed hydrogen on Pt shown by the Pt-H_{ad} broad feature at 11572 eV is reduced by addition of phenol, indicating competition between adsorbed hydrogen and phenol for Pt sites. ECH on certain metals may occur by direct electrochemical reduction but typically at a much higher cathodic overpotentials of –1 V vs. RHE,[33] which will result in low current efficiency due to competing hydrogen evolution reaction (HER). Thus, in **Chapters 3 and 4**, we focused on PGM metals, particularly Pt and Rh, as well as reaction conditions where previous kinetics and spectroscopy measurements indicate a Langmuir-Hinshelwood surface hydrogenation mechanism.[31,34] We also extended our catalysts to include alloying Pt with less expensive Co metal in **Chapter 6** to investigate the ECH mechanism and TOF for alloy materials under varying applied potential and metal composition. We further show in this work that this same LH mechanism actually captures our experimental TOF results on alloy surfaces.

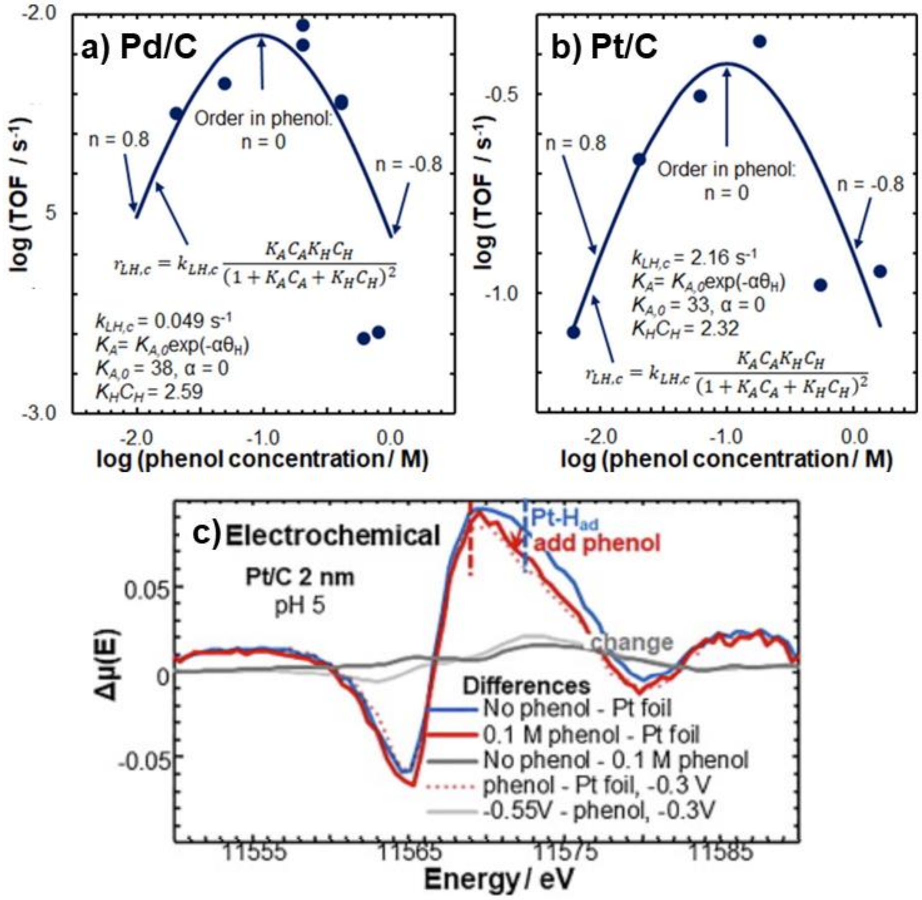

Figure 1.5 Kinetics and spectroscopic evidence for a LH mechanism for phenol on Pt group metals under thermochemical and electrochemical conditions. Effect of phenol concentration on the TOFs at 25 °C for phenol TCH on **a)** Pd/C and **b)** Pt/C reproduced from ref [26]. Fits based on a Langmuir-Hinshelwood mechanism with competitive adsorption are shown by the solid lines. The points on the fit where the order, n, in phenol is 0.8, 0, and −0.8 are indicated. Concentrations of phenol where the order in phenol equaled to 0.8, 0 and −0.8 are indicated. TCH were conducted at 1 bar H_2 in water. **c)** In-situ X-ray absorption near edge spectroscopy difference spectra for 2 nm Pt/C and Pt foil at the Pt-L_3 edge in the absence and presence of phenol reproduced from ref [35]. Electrochemical measurments were performed at −0.55 V vs. Ag/AgCl unless otherwise stated.

Since both ECH and TCH follows a LH rate model where adsorption of the organic and hydrogen is the first step, and a surface reaction RDS afterwards, the turnover frequency (TOF) will be controlled by the rate constant towards ECH (k_{ECH}) and equilibrium coverages (θ) of the adsorbed organic and hydrogen. If we represent the organic molecule as P and hydrogen as H, we can describe the LH model by **Eq. 1.1**.

$$\mathrm{TOF} = k_{ECH}\theta_P\theta_H \tag{1.1}$$

Because the surface reaction is rate-determining, θ_P and θ_H are assumed to be quasi-equilibrated and controlled by the aqueous equilibrium adsorption constants on the active site (K_P and K_H). The TOF can be written in terms of the bulk organic concentration divided by the standard concentration of 1 M (C_P) and the aqueous hydrogen concentration (C_H) in **Eq. 1.2**.

$$\mathrm{TOF} = k_{ECH}\frac{K_P C_P K_H C_H}{(1 + K_P C_P + K_H C_H)^2} \tag{1.2}$$

Here, C_H is equivalent to $[P_{H_2} / (1\text{ bar})]^{1/2}$ for TCH, where P_{H_2} is the pressure of hydrogen in equilibrium with the solution. For ECH, C_H is the concentration of H^+ divided by 1 M.[26] For TCH, K_H is the equilibrium adsorption constant of H* from ½ H_2. For ECH, K_H is also the equilibrium adsorption constant of H*, but from H^+ and e^-, thus K_H increases with more negative applied potential due to the increased thermodynamic driving force to form H*. The potential dependence of phenol ECH TOFs on Pt/C and Rh/C are qualitatively explained by **Eq. 1.2** by considering this change in K_H.[26] In summary, the TOF increases with more negative applied potential at low hydrogen coverages and decreases with more negative applied potential at high hydrogen coverages due to competitive adsorption with phenol.[26]

The aqueous equilibrium adsorption constants K_P and K_H are exponentially dependent on the aqueous adsorption energies of the organic, $\Delta G_{P,ad}$ and hydrogen, $\Delta G_{H,ad}$ (**Eqs. 1.3** and **1.4**).

$$K_P = \exp\left(\frac{-\Delta G_{P,ad}}{RT}\right) \tag{1.3}$$

$$K_H = \exp\left(\frac{-\Delta G_{H,ad}}{RT}\right) \tag{1.4}$$

For a representative bio-oil molecule, phenol in acetate buffer, the LH model has been shown to approximate the ECH and TCH rates on PGMs.[26,31,35] **Eq. 1.2** has been used to fit the TOF measured over a range of phenol concentrations for TCH of phenol on Pt/C (**Figure 1.5a** and

b),[26] where the extracted K_P value on the active site was compared with K_P values of stepped facets and Pt(111)-like sites extracted independently from adsorption isotherms on polycrystalline Pt.[26,36] Subsequently, a similar K_P value from the LH rate model and adsorption experiments was used to determine the active facet for phenol hydrogenation as the Pt(111)-like sites. Due to the significance of K_P and $\Delta G_{P,ad}$ in describing the aqueous-phase ECH mechanism and TOF for bio-oil molecules it becomes crucial to understand how the presence of water in bio-oil influence the value of K_P and $\Delta G_{P,ad}$ in the aqueous phase.

1.2.5 Adsorption in the Gas vs. Aqueous Phase

Solvent (e.g., water) can influence the hydrogenation rate of organic molecules by changing the adsorption thermodynamics and hydrogenation barriers of elementary steps. Significant influence of solvents have been reported in both homogenous catalysis,[37] and heterogenous catalysis such as acid base reactions,[38] hydrogenation[39–41] and oxidation reactions.[42,43] The rate enhancements in the presence of solvents for these heterogenous reactions are typically attributed to a reduced activation barrier facilitated by the interaction between the solvent and the reacting molecules. However, less attention has been directed towards the role of the solvent in directly contributing to the rate through changing adsorption energies of relevant reactants and intermediates. This is in part due to limited understanding of how solvent impacts adsorption energies.

Adsorption thermodynamics have been heavily studied in gas/vapor phase systems and has contributed significantly to understanding catalysis in vapor phase, but much less is known about aqueous and liquid phase adsorption. Experimental[44–46] and theoretical[47,48] studies on gas-phase adsorption and reactivity have been so well developed that very close agreement between experiments and theory oftentimes exist for these systems, making rate predictions and catalyst design much more advanced for gas-phase reactions. However, a substantial disparity in knowledge and experimental data exists for adsorption in liquid compared to gas phase, with the former exhibiting notably lesser understanding, resulting in gaps about understanding liquid-phase heterogenous catalysis.

Adsorption on solid electrodes in the gas phase is very distinct from aqueous/liquid-phase adsorption, where interactions between the adsorbing molecule, solvent and solid surface can lead to very wide differences in adsorption energies between aqueous-phase and gas-phase systems. The description for aqueous-phase adsorption here, will also apply to adsorption involving solvents other than water as will be discussed further in **Chapter 7**, where I propose probing organic adsorption in different solvents using surface enhanced Raman spectroscopy. The first key difference between gas-phase and aqueous-phase adsorption is the fact that the molecules are solvated in the aqueous phase (i.e., they form thermodynamically favorable organic−H_2O bonds) but in the gas phase these molecules do not form any bond-interaction with the environment (**Figure 1.6**). This organic-water (i.e., molecule-solvent) interaction is described by the solvation free energy (ΔG^0_{solv}) where molecules that are less solvated in a given solvent (i.e., more positive ΔG^0_{solv}) adsorb much stronger to the solid surface.[49] In **Chapter 5**, we developed a mathematical model that explains this stronger adsorption for organics in solvents with less favorable solvation energies.

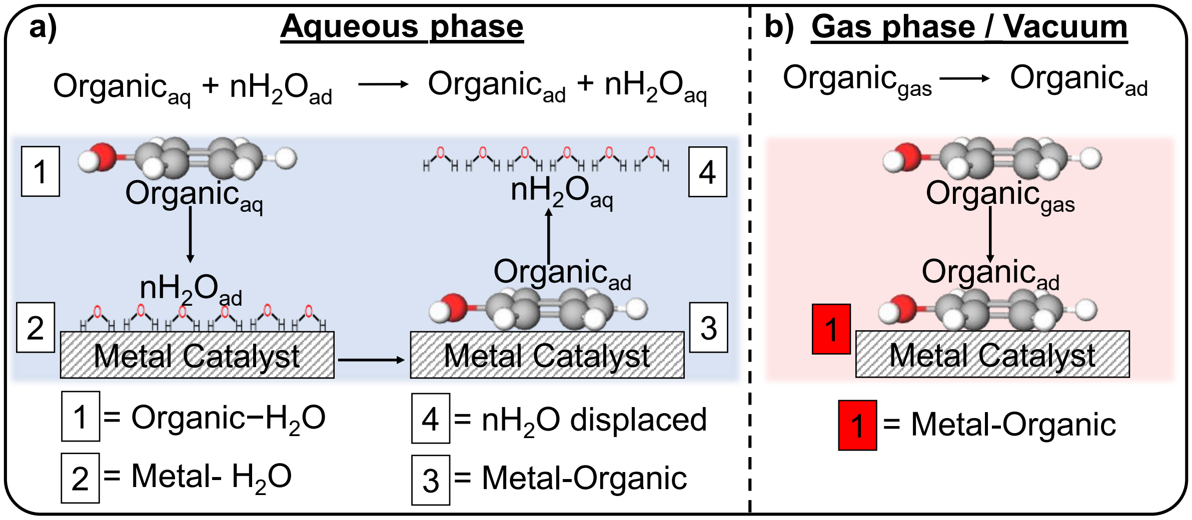

Figure 1.6 Schematic showing adsorption of an organic in a) aqueous phase and b) gas phase. In the aqueous phase 4 different interactions (Organic-H_2O, Metal-H_2O, Metal-organic, and number of H_2O displaced) needs to be accounted for to understand adsorption. Whereas in the gas phase only the metal-organic interaction describes the adsorption energy. The concept of aqueous-phase adsorption as shown in the figure was obtained from ref [50].

The second and perhaps most important difference shown in **Figure 1.6** is that the solid surface is solvated in the aqueous phase but bare in the gas phase. This means an organic molecule adsorbing in the gas phase can simply be represented by a simple bond formation with one or multiple metal atoms (metal-organic bond) depending on the foot-print of the molecule (**Figure 1.6b**).[50] A molecule like phenol would need 9 Pt atoms coordinated together to adsorb on a Pt(111) single crystal surface.[51] In the aqueous phase however, organic molecules with large footprints, such as aromatics, must first displace solvent molecules at the solvent/metal interface by breaking the metal−H_2O bonds before they can form metal−organic bonds and adsorb on the metal surface. The number of water/solvent molecules ($n$$H_2O$) that will be displaced will be dependent on the foot-print of the adsorbed molecule and the coverage of the solvent molecules. For example the coverage of water on Pt(111) is 0.72 ML,[52] that means a molecule of phenol adsorbing on 9 Pt atoms,[51] will displace roughly 6.5 (from 0.72 ×9) water molecules.

The apparent aqueous-phase adsorption energies after accounting for the organic−H_2O, metal−H_2O, and number of displaced H_2O will eventually be weaker than those in the gas phase because of solvation and the energetic penalty of solvent displacement according to **Eq. 1.6**.

$$\text{Organic}_{\text{aq}} + n\text{H}_2\text{O}_{\text{ad}} \rightarrow \text{Organic}_{\text{ad}} + n\text{H}_2\text{O}_{\text{aq}} \tag{1.5}$$

$$\Delta G_{ad,\text{organic}}^{aq} = \Delta G_{ad,\,\text{organic}} - n(\Delta G_{ad,\text{H}_2\text{O}}) \tag{1.6}$$

Where $\Delta G_{ad,\text{organic}}^{aq}$ is the apparent adsorption energy in aqueous phase, $\Delta G_{ad,\,\text{organic}}$ intrinsic metal-organic adsorption energy which can be likened to the gas-phase adsorption energy if the water environment does not influence the intrinsic metal-organic bond strength. $\Delta G_{ad,\text{H}_2\text{O}}$ is the water adsorption energy on the metal. This difference in gas and aqueous-phase adsorption energies will directly translate to differences in catalytic behavior in either phase and will certainly lead to inaccurate predictions of aqueous-phase catalytic behavior when using gas-phase adsorption energy data. For example, let us consider the case of phenol on Pt(111) whose adsorption energy is so strong (-220 kJ mol^{-1})[44] that room-temperature hydrogenation would seem impossible because the surface will be poisoned by phenol with very little surface hydrogen. Yet phenol hydrogenation on Pt occurs in the aqueous-phase at room temperature.[23,31,35,53,54] In the gas-phase, Pt(111) and Rh(111) are predicted by density functional theory (DFT) modeling to have ~50 kJ mol^{-1} difference in their adsorption energy of phenol,[47] but these metals show similar aqueous-phase hydrogenation turnover frequencies (TOFs) and apparent activation barriers,[30,31] seemingly in contradiction to the Sabatier principle. As discussed earlier, the active sites for phenol ECH and TCH have been identified as the (111) facets on Pt,[26,36] and even on Rh.[55] It becomes imperative to ascertain whether a contradiction like this stem from intrinsic variations in the mechanisms and pathways of catalytic reactions between the gas and aqueous phase, or if they can be elucidated by differences in apparent adsorption energies measured in these distinct environments. Considering the importance of obtaining accurate adsorption energies in order to correctly describe aqueous-phase catalysis, we measured aqueous adsorption energies for many relevant bio-oil molecules in **Chapter 3**. And in **Chapter 5**, we developed a mathematical model to aid the prediction of accurate aqueous adsorption energies that matches experiment. This will enable low cost and accurate prediction of new catalyst materials for relevant liquid-phase catalysis like ECH.

1.2.6 Effect of Temperature on Gas vs. Aqueous-Phase Adsorption

Temperature can influence the reaction rate of catalytic reactions by controlling both the reaction rate constant and the adsorption equilibrium constant. For a LH-type reaction such as ECH, the rate constant (k_{ECH}) and the organic and hydrogen adsorption constants (K_P and K_H) are the only intrinsic variables that describe the turnover frequency according to **Eq. 1.2**. The rate constant, k of a reaction has been well described by the transition state theory and collision theory to be function of the collision frequency per volume and Arrhenius in 1889 showed its temperature dependence (**Eq. 1.7**).[56]

$$k = A \exp\left(\frac{-E_a}{RT}\right) \tag{1.7}$$

Where k is the rate constant, A is the pre-exponential factor or frequency factor, E_a is the activation energy, R is the gas constant, and T is the absolute temperature in Kelvin. Consequently, increasing the temperature can provide more thermal energy to molecules, allowing them to go through the reaction energy barrier more easily and thus increase the reaction rate. In fact, several chemical reactions in the industry e.g., Haber-Bosch[57] process and Fischer-Tropsch synthesis,[58] are mostly operated at elevated temperatures to take advantage of the exponential increase in the rate constant with temperature.

Beyond the rate constant, temperature can also contribute to the reaction rate by changing the coverages of adsorbed reactants and intermediates through their adsorption equilibrium constant. According to Gibb's free energy change equation (**Eq. 1.8**), the adsorption free energy will depend on the temperature through the adsorption entropy.

$$\Delta G_{ad} = \Delta H_{ad} - T\Delta S_{ad} \tag{1.8}$$

Here ΔG_{ad} is the adsorption free energy, ΔH_{ad} is the enthalpy of adsorption, T is temperature in Kelvin and ΔS_{ad} is the adsorption entropy. In gas phase, the loss of translational and rotational degrees of freedom as well as the hindered vibration upon adsorption of a molecule often leads to an overall entropy loss (i.e., $\Delta S_{ad} < 0$). **Figure 1.7a** shows the entropy of several hydrocarbon molecules upon adsorption in gas phase compared to their gas-phase entropy before adsorption.[46] For every hydrocarbon molecule shown, the adsorbed molecule has a much lower entropy compared to their unadsorbed gas-phase molecules (i.e., $\Delta S_{ad} < 0$). This negative ΔS_{ad} in the gas phase means that according to **Eq. 1.8**, higher temperatures will result in more positive ΔG_{ad} and thus smaller equilibrium adsorption constants, and decreased adsorbate coverages (**Figure 1.7b**). The low coverages at higher temperatures are often mitigated by operating at higher pressures of reactants.

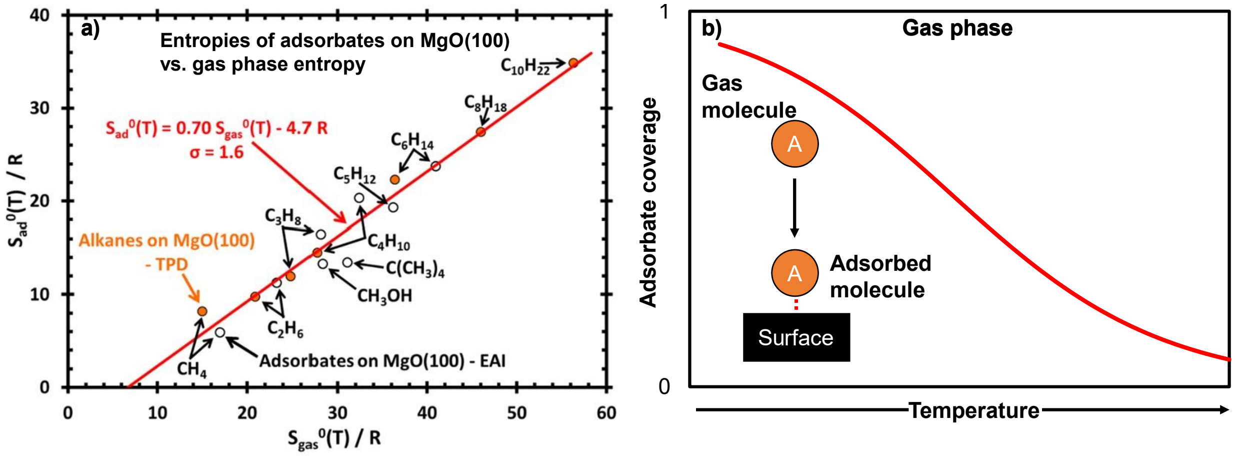

Figure 1.7 Entropies of unadsorbed and adsorbed hydrocarbon molecules in gas phase and the temperature dependence of adsorbate coverages in the gas phase. a) Plot of the standard entropies of molecular adsorbates on MgO(100) smoke determined by equilibrium adsorption isotherms (EAI), from ref [59], plotted versus the standard entropy of the gas-phase molecule at the same temperature. The standard entropies of these same and other adsorbates are determined using desorption prefactors from temperature programmed desorption data. The agreement with EAI results proves the accuracy of this method. The best linear fit to these data is also shown, along with the standard deviation (σ) of the adsorbate entropies from this line. Figure was reproduced from ref [46]. **b)** Schematic showing how negative adsorption entropy directly impacts the temperature dependence of the adsorbate coverages in gas phase.

Adsorption entropy in aqueous environments includes more than just the loss of entropy from the adsorbed molecules but also includes the entropy gain that may result from the displacement of the adsorbed interfacial water to the bulk according to **Eq. 1.9**.

$$\Delta S_{ad,organic}^{aq} = (S_{ad,organic}^{aq} - S_{organic}^{aq}) + n(S_{H_2O(sol)} - S_{ad,H_2O}) \tag{1.9}$$

Where $\Delta S_{ad,organic}^{aq}$ is the net entropy of adsorption in water, $S_{ad,organic}^{aq}$ is the entropy of adsorbed molecule, $S_{organic}^{aq}$ is the entropy of aqueous organic molecule, S_{ad,H_2O} is the entropy of adsorbed water and $S_{H_2O(sol)}$ is the entropy of the displaced water. Depending on the entropy of the displaced interfacial water and the number of water molecules displaced, the entropy of water displacement, $n(S_{H_2O(sol)} - S_{ad,H_2O})$ can be positive resulting in a positive net adsorption entropy, which is in stark contrast to the adsorption entropy in gas phase. This means the temperature dependence on reaction rates in gas-phase reactions will be acutely different compared to aqueous phase. Tremendous efforts are ongoing to learn how to predict reaction rates from theoretically calculated rate constants and adsorption equilibrium constants for several important liquid-phase reactions.[60] The entropy and enthalpy of the adsorbed molecules are very essential for these calculations, and much effort has been devoted to measuring and calculating enthalpies for adsorbates. However, fewer studies have been reported for adsorption entropies particularly in the liquid phase despite their importance to heterogenous catalysis in liquid phase. In **Chapter 4** we investigate the structure of the displaced interfacial water layer and measure the net adsorption entropy in aqueous phase for phenol molecule on Pt and show there exists disparity between aqueous and gas-phase adsorption entropy that is often ignored.

1.2.7 Rational Design of ECH Catalysts based on Adsorption Energies

Several monometallic catalysts materials have been studied for the ECH of bio-oil model compounds with each displaying very different ECH turnover frequency and selectivity.[61–63] Among these are Pt group metals (Pt, Rh, Ru, Pd) where extensive work has been done establish the contributions of varying particle size,[53,55] temperature[23,31] and applied potential[53] to the ECH turnover frequency. While these monometallics have offered great insights into ECH mechanism through experimental kinetic analysis, adsorption studies and spectroscopic investigations, they have not yet demonstrated turnover frequencies reaching up to 1 s^{-1} as desired from technoeconomic analysis. For example, from kinetics and adsorption studies on monometallic Pt/C and Rh/C, we now know that the active site for phenol ECH on Pt and Rh nanoparticles is the (111) facets that adsorb phenol much weaker than their step sites, yet the maximum TOF recorded on these metals even after increasing the fraction of these active sites was 0.2 s^{-1}.[55] In the design of less expensive and active catalyst materials we can use the fundamental knowledge on adsorption and kinetics from monometallics to design bimetallic materials with different structures (**Figure 1.8**) to reach higher turnover frequencies.

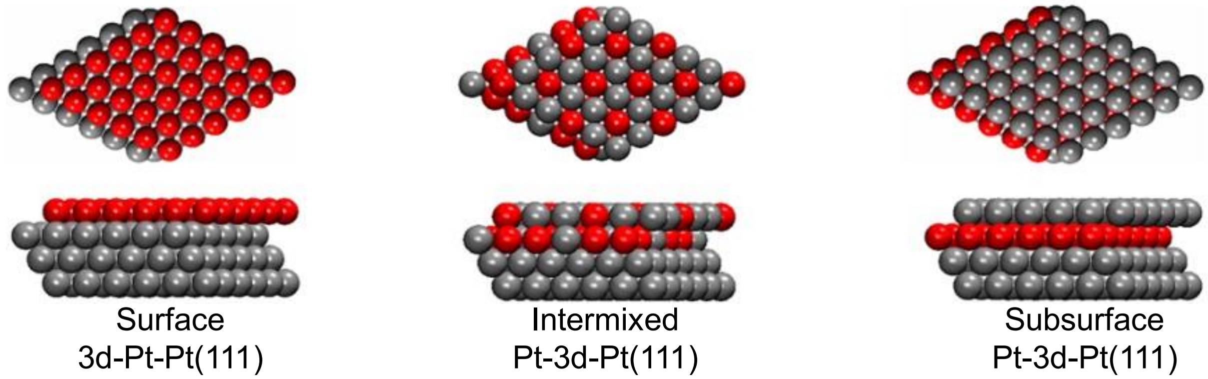

Figure 1.8 Top and side view of idealized bimetallic surface structures with one monolayer of 3d metals on a Pt(111) substrate reproduced from ref [64].

Bimetallics can improve the rates by synergistically combining metals with different adsorption energies to achieve optimal adsorption energies of reactants and intermediates in the rate determining step. If a Brønsted-Evans-Polanyi (BEP)[65,66] relationship which correlates the activation energy of a reaction to the reaction enthalpy (**Eq 1.10**) exist for ECH, we can tune adsorption energies and enthalpies of the reactants using bimetallics[64,67] to alter the reaction enthalpies and thus the rate constant via the activation energy.

$$E_a \approx \alpha - \beta \Delta H_{rxn} \tag{1.10}$$

Where E_a is the activation energy in kJ mol^{-1}, α is a constant likened to the activation energy for a reaction enthalpy (ΔH_{rxn}) of zero, β is the slope related to the transition state position which can be early ($0 < \beta < 0.5$), midway ($\beta = 0.5$), or late ($0.5 < \beta < 1$) along the reaction pathway. The sign of β for a BEP relevant reaction will determine what direction to tune the adsorption energies to affect ΔH_{rxn} and reduce E_a.

Gas-phase hydrogenation reactions with a surface reaction rate limiting step have been often understood using BEP relations.[64,68] For example, lower activation energies for surface hydrogenation have been observed when the organic and H bind to the catalyst weakly (**Figure 1.9**).[69,70] When BEP relations hold, an ideal adsorption energy to maximize the rate usually exists (**Figure 1.9b**). For example, Pt-Ni-Pt alloy has the optimal cyclohexene adsorption energy and thus the highest hydrogenation activity. Whereas Fe-Pt-Pt alloy adsorbs cyclohexene too strongly such that cyclohexene poisons the surface and inhibits hydrogenation.

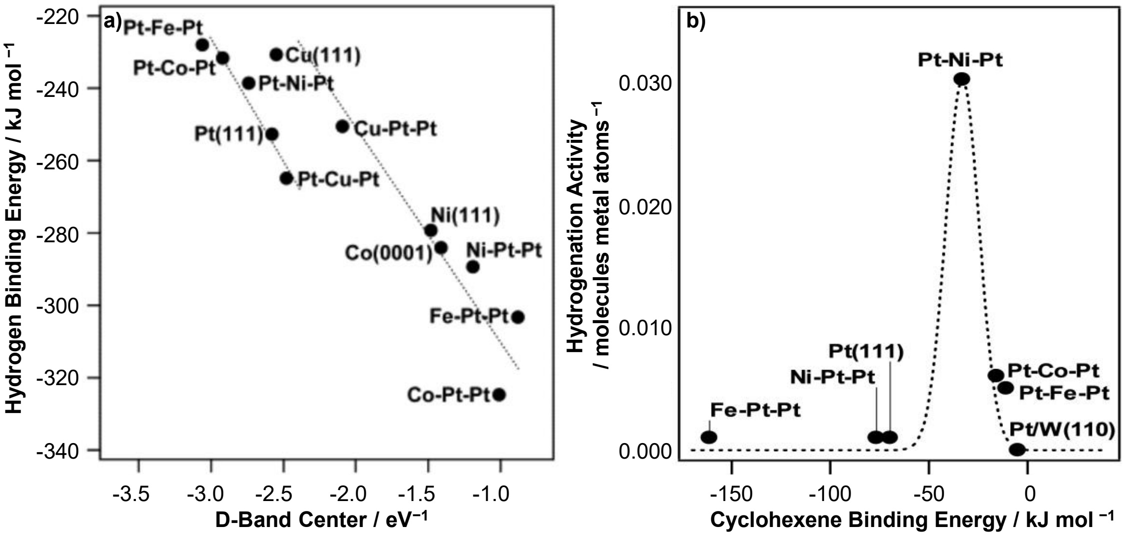

Figure 1.9 Gas-phase hydrogenation activity and the binding energies of hydrogen and cyclohexene on Pt based alloy catalysts reproduced from ref [69]. a) Correlation between hydrogen binding energy and d-band center of bimetallic surfaces. **b)** Experimental hydrogenation activity correlated to the binding energy of cyclohexene determined from density funcional theory.

BEP relations allow one to estimate reaction rates solely based on knowledge of adsorption energies, which are much easier to calculate compared to kinetic parameters such as activation energies and rate constants. When considering a surface reaction with different species like ECH, the adsorption energy for both reactants (the oxygenated aromatic and hydrogen) is important. Whether a given metal will adsorb both the oxygenated aromatic and hydrogen with “ideal” energies is dependent on whether those adsorption energies follow linear free-energy “adsorbate scaling relations”.[71–73] If the hydrogen and aromatic adsorption energies follow adsorbate scaling relations, then the two adsorption energies are coupled and thus scale together, which gives rise to intrinsic limitations in the obtainable adsorption energies. Both adsorbate and BEP relations exist for gas-phase hydrogenation and dehydrogenation on metals for simple molecules (e.g., CH_4) on bulk surfaces and nanoparticles.[73] We hypothesize that similar adsorbate scaling relations and BEP relations would exist for ECH of oxygenated aromatics in water. In **Chapter 6** of this dissertation, we synthesize alloys containing Pt and Co to modify hydrogen and organic adsorption energies in the aqueous phase and identify whether BEP relationship holds for ECH as they would serve as valuable guidelines in predicting new active catalysts for ECH.

1.3 Scope of Work

Electrocatalytic hydrogenation presents a pathway to upgrade bio-oil sustainably, thereby enabling bio-oil to be stored or transported to facilities where they can be converted into value-added products such as chemicals and transportation fuels. To develop a cost-effective ECH process, it is crucial to understand the aqueous-phase ECH mechanism and improve the kinetics by developing suitable catalysts and reaction conditions and environments. In the aqueous phase, there is a gap in understanding adsorption and predicting adsorption energies which is very crucial for understanding and improving ECH. Consequently, five major objectives were targeted in this dissertation:

1. Understand the differences in adsorption energies in the aqueous phase compared to gas phase for model bio-oil compounds and how they impact hydrogenation rates.
2. Understand the contributions of temperature to aqueous phase adsorption.
3. Develop a mathematical model to predict accurate adsorption energies on relevant catalytic surfaces in aqueous phase to enable prediction of new catalyst materials.
4. Synthesize bimetallic catalysts alloys catalysts with varying organic and hydrogen adsorption energies to link intrinsic ECH rates to adsorption energies.
5. Understand the effect of catalyst alloy structure, composition and applied potential on the desired ECH reaction and parasitic hydrogen evolution reaction.

To achieve these objectives, this dissertation is divided into seven chapters outlined below:

Chapter 1: Introduction and Background

This chapter begins by highlighting the prevailing challenges of global warming which stems from over reliance on fossil sources. Here, I recommended transitioning to bio-oil sourced from waste biomass as a viable and renewable carbon alternative. The mechanism of electrocatalytic hydrogenation as a method to upgrade bio-oil using renewable electricity is discussed with focus on aqueous-phase adsorption as a significant gap in knowledge that must be addressed to improve ECH process. Additionally, this chapter provides background discussion prompting the need for the various projects undertaken in **Chapters 3** to **Chapter 6**.

Chapter 2: Experimental Methods

This chapter elaborates on the methodologies utilized in this dissertation, organized into four main areas: (i) method for extracting aqueous organic adsorption energies, (ii) synthesis and characterization of electrode materials, (iii) surface-enhanced Raman spectroscopy (SERS) electrode preparation and measurements, and (iv) quantifying ECH activity. Cyclic voltammetry and hydrogen underpotential deposition technique on Pt group metals to probe organic adsorption and test the reversibility of organic and hydrogen adsorption are presented here. Details about adsorption isotherm construction and fitting to an adsorption model, including the procedure for converting between adsorption energies from isotherm fits to adsorption enthalpies are also discussed. This chapter also covers the preparation of Vulcan carbon supported catalysts inks on glassy carbon electrodes for hydrogen evolution reaction, and discusses the direct synthesis of Pt_xCo_y alloy catalysts on conductive carbon felt for ECH. Extensive state-of-the-art characterization techniques for the alloy catalyst and SERS active substrate are discussed in this chapter. Detailed preparation and cleaning procedures for roughened Au electrodes to remove adventitious carbon, as well as thin film deposition of transition metals on Au substrates are described here. Finally, the procedure to perform ECH experiments and quantify catalyst performance are discussed. These techniques will be helpful in reproducing the results discussed in this dissertation or for conducting new experiments using these techniques.

Chapter 3: Adsorption Energies of Oxygenated Aromatics and Organics on Rhodium and Platinum in Aqueous Phase

This chapter compared aqueous-phase adsorption energies experimentally measured for five bio-oil model compounds; phenol, benzaldehyde, furfural, cyclohexanol and benzyl alcohol with DFT computed gas-phase values. Here the measured organic adsorption energies on Pt and Rh wires were ~50–250 kJ mol^{-1} lower than their computed gas-phase values, highlighting the vast difference between aqueous-phase and gas-phase adsorption energies as I explained earlier in **section 1.2.5** of this chapter. Differences like these stems from the solvation and solvent displacement penalties that if not properly understood and accounted for, aqueous-phase catalytic reactions like ECH will be inaccurately understood from adsorption thermodynamics in contrast to what is obtainable for many gas-phase reactions. The lower measured aqueous adsorption energies for phenol and benzaldehyde on Pt and Rh were used to explain why ECH of these molecules occur seamlessly at room temperature, whereas the gas-phase values were incorrectly suggesting that higher temperatures would be required for ECH of these molecules.

Chapter 4: Temperature Dependence of Aqueous-Phase Phenol Adsorption on Pt and Rh

This chapter explores the contribution of solvent displacement to the adsorption entropy for phenol in water. Here we identified that the interfacial water layer upon displacement by adsorbed phenol does not retain an ordered structure, thus contributing to a slightly positive adsorption entropy. This makes the temperature dependence of aqueous phenol adsorption to be very different than in the gas phase where the adsorption entropy is always negative as discussed in **section 1.2.6** of **Chapter 1**. The findings here indicate that temperature will have a less negative impact on the coverages of adsorbed phenol in aqueous phase compared to a larger decrease in coverage that is expected in the gas phase due to a negative adsorption entropy.

Chapter 5: Effects of Solvents on Adsorption: A General Bond Additivity Model

This chapter provides a mathematical model to predict liquid-phase adsorption energies for organics of any shape and size using the gas-phase adsorption energy, the solvent's adhesion energy to the solid surface and the gas-phase adsorbate's solvation energy. This model accounts for the interactions that are required to extensively capture adsorption in the liquid phase as discussed in **section 1.2.5** of **Chapter 1**. The results here extend beyond aqueous-phase catalysis, highlighting how using different solvents including non-aqueous ones with distinct adhesion energy on a catalyst surface can be used to control organic adsorption to enhance or inhibit reaction rates in liquid phase.

Chapter 6: Electrocatalytic Hydrogenation of Phenol on Platinum-Cobalt Alloys

This chapter highlights the performance of bimetallic Pt_xCo_y alloys for phenol ECH and HER. These alloys display higher HER activity than Pt and the HER activity correlates with a weakening of the hydrogen adsorption energy. But this weakened hydrogen adsorption energy did not translate to an increase in ECH activity for all the Pt_xCo_y alloys, although, certain Pt_xCo_y alloys are more active for ECH at low overpotentials (−0.1 V vs RHE) but at higher overpotentials HER dominate leading to lower current efficiency. We use a microkinetic model based on a Langmuir-Hinshelwood model to describe the measured aqueous-phase ECH turnover frequency for these alloys at different applied potentials. We show in this work that phenol ECH on these alloys follow a BEP relationship as discussed in **section 1.2.7** of **Chapter 1**. The BEP relationship we identified in this work suggests that a catalyst with a Pt monolayer on a Pt_xCo_y core, would have lower reaction energies and activation barriers and thus enhance ECH activity more than the Pt_xCo_y catalysts we synthesized in this work.

Chapter 7: Conclusions and Outlooks

This chapter summarizes key findings in this dissertation and discusses how they in part improve on what we previously know about adsorption and electrocatalytic hydrogenation in aqueous phase. Results from the different chapters opened new scientific questions for which I provide thoughts and hypotheses on how new Ph.D. students can further explore these questions. In particular, I discuss how SERS can be used to probe the intrinsic organic-metal bond strength in solvents with different adhesion energies on metal surfaces. I also discuss procedures to synthesize and stabilize the Pt monolayer on a Pt_xCo_y core structures suggested from results in **Chapter 6**. Beyond ECH, I discuss other areas that also require significant research investment to make the overall production of upgraded bio-oil feasible in the near future.

1.4 References

(1) Popovich, N. *How Canada's Record Wildfires Got so Bad, so Fast.* https://www.nytimes.com/interactive/2023/07/18/climate/canada-record-wildfires.html%0ACanadian Interagency Forest Fire Center (accessed **2023-10-08**).
(2) McGlade, C.; Ekins, P. The Geographical Distribution of Fossil Fuels Unused When Limiting Global Warming to 2 °C. *Nature* **2015**, *517* , 187–190.
(3) Hubbert, M. K. Energy from Fossil Fuels. *Science.* **1949**, *109*, 103–109.
(4) Weissermel, K.; Arpe, H. *Industrial Organic Chemistry*; John Wiley & Sons, Inc, **2008**.
(5) Bozell, J. J. Connecting Biomass and Petroleum Processing with a Chemical Bridge. *Science.* **2010**, *329*, 522–523.
(6) Wittcoff, H. A.; Green, M. Organic Chemistry Principles and Industrial Practice *Org. Process Res. Dev.* **2004**, *8*, 293–294.
(7) Speight, J. *Handbook of Industrial Hydrocarbon Processes.*; Gulf Professional Publishing, **2019**.
(8) Daly, H. Fossil Fuels. *Appl. Energy* **1994**, *47* (2–3), 101–121.

(9) U.S. Energy Information Administration. *Annual Energy Outlook 2019 with Projections to 2050*, Office of Energy Analysis, U.S. Department of Energy: Washington, DC 20585, **2019**.
(10) Dale, S. *BP Statistical Review of World Energy*; London, United Kingdom, **2019**.
(11) Gupta, J. A History of International Climate Change Policy. *Wiley Interdiscip. Rev. Clim. Chang.* **2010**, *1*, 636–653.
(12) Czernik, S.; Bridgwater, A. V. Overview of Applications of Biomass Fast Pyrolysis Oil. *Energy & Fuels* **2004**, *18*, 590–598.
(13) Weber, R. S.; Holladay, J. E. Modularized Production of Value-Added Products and Fuels from Distributed Waste Carbon-Rich Feedstocks. *Engineering* **2018**, *4*, 330–335.
(14) Jacobson, K.; Maheria, K. C.; Kumar Dalai, A. Bio-Oil Valorization: A Review. *Renew. Sustain. Energy Rev.* **2013**, *23*, 91–106.
(15) French, R.; Czernik, S. Catalytic Pyrolysis of Biomass for Biofuels Production. *Fuel Process. Technol.* **2010**, *91*, 25–32.
(16) Toor, S. S.; Rosendahl, L.; Rudolf, A. Hydrothermal Liquefaction of Biomass: A Review of Subcritical Water Technologies. *Energy* **2011**, *36*, 2328–2342.
(17) Machado, H.; Cristino, A. F.; Orišková, S.; Galhano dos Santos, R. Bio-Oil: The Next-Generation Source of Chemicals. *Reactions* **2022**, *3*, 118–137.
(18) Baldwin, R. M.; Feik, C. J. Bio-Oil Stabilization and Upgrading by Hot Gas Filtration. *Energy & Fuels* **2013**, *27*, 3224–3238.
(19) Xu, J.; Jiang, J.; Dai, W.; Zhang, T.; Xu, Y. Bio-Oil Upgrading by Means of Ozone Oxidation and Esterification to Remove Water and to Improve Fuel Characteristics. *Energy and Fuels* **2011**, *25*, 1798–1801.
(20) Mortensen, P. M.; Grunwaldt, J. D.; Jensen, P. A.; Knudsen, K. G.; Jensen, A. D. A Review of Catalytic Upgrading of Bio-Oil to Engine Fuels. *Appl. Catal. A Gen.* **2011**, *407*, 1–19.
(21) Ibarra, Á.; Hita, I.; Azkoiti, M. J.; Arandes, J. M.; Bilbao, J. Catalytic Cracking of Raw Bio-Oil under FCC Unit Conditions over Different Zeolite-Based Catalysts. *J. Ind. Eng. Chem.* **2019**, *78*, 372–382.
(22) Li, Z.; Kelkar, S.; Raycraft, L.; Garedew, M.; Jackson, J. E.; Miller, D. J. A Mild Approach for Bio-Oil Stabilization and Upgrading : Electrocatalytic Hydrogenation Using Ruthenium Supported on Activated Carbon Cloth. **2014**, *16*, 844–852.
(23) Song, Y.; Gutiérrez, O. Y.; Herranz, J.; Lercher, J. A. Aqueous Phase Electrocatalysis and Thermal Catalysis for the Hydrogenation of Phenol at Mild Conditions. *Appl. Catal. B Environ.* **2016**, *182*, 236–246.
(24) Zhu, Y.; Biddy, M. J.; Jones, S. B.; Elliott, D. C.; Schmidt, A. J. Techno-Economic Analysis of Liquid Fuel Production from Woody Biomass via Hydrothermal Liquefaction (HTL) and Upgrading. *Appl. Energy* **2014**, *129*, 384–394.
(25) Meyer, P. A.; Snowden-Swan, L. J.; Rappé, K. G.; Jones, S. B.; Westover, T. L.; Cafferty, K. G. Field-to-Fuel Performance Testing of Lignocellulosic Feedstocks for Fast Pyrolysis and Upgrading: Techno-Economic Analysis and Greenhouse Gas Life Cycle Analysis. *Energy & Fuels* **2016**, *30*, 9427–9439.
(26) Singh, N.; Sanyal, U.; Ruehl, G.; Stoerzinger, K. A.; Gutiérrez, O. Y.; Camaioni, D. M.; Fulton, J. L.; Lercher, J. A.; Campbell, C. T. Aqueous Phase Catalytic and Electrocatalytic Hydrogenation of Phenol and Benzaldehyde over Platinum Group Metals. *J. Catal.* **2020**, *382*, 372–384.
(27) Peters, B. Catalysis. In *Reaction Rate Theory and Rare Events Simulations*; Elsevier, **2017**;

Vol. 51, pp 79–128.
(28) Hinshelwood, C. N. *The Kinetics of Chemical Change*; Claredon, Oxford, **1940**.
(29) Hinshelwood, C. N. *Ann. Rep. Prog. Chem* **1927**, *24*, 314–317.
(30) Song, Y.; Chia, S. H.; Sanyal, U.; Gutiérrez, O. Y.; Lercher, J. A. Integrated Catalytic and Electrocatalytic Conversion of Substituted Phenols and Diaryl Ethers. *J. Catal.* **2016**, *344*, 263–272.
(31) Singh, N.; Song, Y.; Gutiérrez, O. Y.; Camaioni, D. M.; Campbell, C. T.; Lercher, J. A. Electrocatalytic Hydrogenation of Phenol over Platinum and Rhodium: Unexpected Temperature Effects Resolved. *ACS Catal.* **2016**, *6*, 7466–7470.
(32) Che, M. Nobel Prize in Chemistry 1912 to Sabatier: Organic Chemistry or Catalysis. *Catal. Today* **2013**, *218–219* , 162–171.
(33) Chadderdon, X. H.; Chadderdon, D. J.; Matthiesen, J. E.; Qiu, Y.; Carraher, J. M.; Tessonnier, J. P.; Li, W. Mechanisms of Furfural Reduction on Metal Electrodes: Distinguishing Pathways for Selective Hydrogenation of Bioderived Oxygenates. *J. Am. Chem. Soc.* **2017**, *139*, 14120–14128..
(34) Singh, N.; Nguyen, M. T.; Cantu, D. C.; Mehdi, B. L.; Browning, N. D.; Fulton, J. L.; Zheng, J.; Balasubramanian, M.; Gutiérrez, O. Y.; Glezakou, V. A.; Rousseau, R.; Govind, N.; Camaioni, D. M.; Campbell, C. T.; Lercher, J. A. Carbon-Supported Pt during Aqueous Phenol Hydrogenation with and without Applied Electrical Potential: X-ray Absorption and Theoretical Studies of Structure and Adsorbates. *J. Catal.* **2018**, *368*, 8–19.
(35) Singh, N.; Lee, M.; Akhade, S. A.; Cheng, G.; Camaioni, D. M.; Gutiérrez, O. Y.; Glezakou, V.; Rousseau, R.; Lercher, J. A.; Campbell, C. T. Impact of pH on Aqueous-Phase Phenol Hydrogenation Catalyzed by Carbon-Supported Pt and Rh. *ACS Catal.* **2019**, *9*, 1120–1128.
(36) Singh, N.; Sanyal, U.; Fulton, J. L.; Gutiérrez, O. Y.; Lercher, J. A.; Campbell, C. T. Quantifying Adsorption of Organic Molecules on Platinum in Aqueous Phase by Hydrogen Site Blocking and in Situ X-ray Absorption Spectroscopy. *ACS Catal.* **2019**, *9*, 6869–6881.
(37) Dyson, P. J.; Jessop, P. G. Solvent Effects in Catalysis: Rational Improvements of Catalysts via Manipulation of Solvent Interactions. *Catal. Sci. Technol.* **2016**, *6*, 3302–3316.
(38) Cram, D. J.; Rickborn, B.; Kingsbury, C. A.; Haberfield, P. Electrophilic Substitution at Saturated Carbon. XIII. Solvent Control of Rate of Acid-Base Reactions That Involve the Carbon-Hydrogen Bond 1,2. *J. Am. Chem. Soc.* **1961**, *83*, 3678–3687.
(39) Akpa, B. S.; D'Agostino, C.; Gladden, L. F.; Hindle, K.; Manyar, H.; McGregor, J.; Li, R.; Neurock, M.; Sinha, N.; Stitt, E. H.; Weber, D.; Zeitler, J. A.; Rooney, D. W. Solvent Effects in the Hydrogenation of 2-Butanone. *J. Catal.* **2012**, *289*, 30–41.
(40) Hidalgo-Carrillo, J.; Aramendía, M. A.; Marinas, A.; Marinas, J. M.; Urbano, F. J. Support and Solvent Effects on the Liquid-Phase Chemoselective Hydrogenation of Crotonaldehyde over Pt Catalysts. *Appl. Catal. A Gen.* **2010**, *385*, 190–200.
(41) Wan, H.; Vitter, A.; Chaudhari, R. V.; Subramaniam, B. Kinetic Investigations of Unusual Solvent Effects during Ru/C Catalyzed Hydrogenation of Model Oxygenates. *J. Catal.* **2014**, *309*, 174–184.
(42) Zope, B. N.; Hibbitts, D. D.; Neurock, M.; Davis, R. J. Reactivity of the Gold/Water Interface During Selective Oxidation Catalysis. *Science.* **2010**, *330*, 74–78.
(43) Hibbitts, D. D.; Neurock, M. Influence of Oxygen and pH on the Selective Oxidation of Ethanol on Pd Catalysts. *J. Catal.* **2013**, *299*, 261–271.
(44) Carey, S. J.; Zhao, W.; Mao, Z.; Campbell, C. T. Energetics of Adsorbed Phenol on Ni(111) and Pt(111) by Calorimetry. *J. Phys. Chem. C* **2019**, *123*, 7627–7632.

(45) Campbell, C. T.; Ertl, G.; Kuipers, H.; Segner, J. A Molecular Beam Study of the Catalytic Oxidation of CO on a Pt(111) Surface. *J. Chem. Phys.* **1980**, *73*, 5862–5873.

(46) Campbell, C. T.; Sellers, J. R. V. The Entropies of Adsorbed Molecules. *J. Am. Chem. Soc.* **2012**, *134*, 18109–18115.

(47) Honkela, M. L.; Björk, J.; Persson, M. Computational Study of the Adsorption and Dissociation of Phenol on Pt and Rh Surfaces. *Phys. Chem. Chem. Phys.* **2012**, *14*, 5849–5854.

(48) Gautier, S.; Steinmann, S. N.; Michel, C.; Fleurat-Lessard, P.; Sautet, P. Molecular Adsorption at Pt(111). How Accurate Are DFT Functionals? *Phys. Chem. Chem. Phys.* **2015**, *17*, 28921–28930.

(49) Blomgren, E.; Bockris, J. O.; Jesch, C. The Adsorption of Butyl, Phenyl and Naphthyl Compounds at the Interface Mercury—Aqueous Acid Solution. *J. Phys. Chem.* **1961**, *65*, 2000–2010.

(50) Gileadi, E. *Electrosorption*; Springer Science & Business Media, **2012**.

(51) Lu, F.; Salaita, G. N.; Laguren-Davidson, L.; Stern, D. A.; Wellner, E.; Frank, D. G.; Batina, N.; Zapien, D. C.; Walton, N.; Hubbard, A. T. Characterization of Hydroquinone and Related Compounds Adsorbed at Pt(111) from Aqueous Solutions: Electron Energy-Loss Spectroscopy, Auger Spectroscopy, LEED, and Cyclic Voltammetry. *Langmuir* **1988**, *4*, 637–646.

(52) Lew, W.; Crowe, M. C.; Karp, E.; Campbell, C. T. Energy of Molecularly Adsorbed Water on Clean Pt(111) and Pt(111) with Coadsorbed Oxygen by Calorimetry. *J. Phys. Chem. C* **2011**, *115*, 9164–9170.

(53) Sanyal, U.; Song, Y.; Singh, N.; Fulton, J. L.; Herranz, J.; Jentys, A.; Gutiérrez, O. Y.; Lercher, J. A. Structure Sensitivity in Hydrogenation Reactions on Pt/C in Aqueous-phase. *ChemCatChem* **2019**, *11*, 575–582.

(54) Sasaki, K.; Kunai, A.; Harada, J.; Nakabori, S. Electrolytic Hydrogenation of Phenols in Aqueous Acid Solutions. *Electrochim. Acta* **1983**, *28*, 671–674.

(55) Barth, I.; Akinola, J.; Lee, J.; Gutiérrez, O. Y.; Sanyal, U.; Singh, N.; Goldsmith, B. R. Explaining the Structure Sensitivity of Pt and Rh for Aqueous-Phase Hydrogenation of Phenol. *J. Chem. Phys.* **2022**, *156* (10), 104703. https://doi.org/10.1063/5.0085298.

(56) Arrhenius, S. *J. Phys. Chem.* **1889**, *2*.

(57) Liu, H. Ammonia Synthesis Catalyst 100 Years: Practice, Enlightenment and Challenge. *Chinese J. Catal.* **2014**, *35*, 1619–1640.

(58) Fischer, H. T. Bren. *Brennstoff-Chem* **1927**, *7*, 97.

(59) Campbell, C. T.; Sellers, J. R. V. Enthalpies and Entropies of Adsorption on Well-Defined Oxide Surfaces: Experimental Measurements. *Chem. Rev.* **2013**, *113*, 4106–4135.

(60) Liu, J. X.; Richards, D.; Singh, N.; Goldsmith, B. R. Activity and Selectivity Trends in Electrocatalytic Nitrate Reduction on Transition Metals. *ACS Catal.* **2019**, *9*, 7052–7064.

(61) Jung, S.; Karaiskakis, A. N.; Biddinger, E. J. Enhanced Activity for Electrochemical Hydrogenation and Hydrogenolysis of Furfural to Biofuel Using Electrodeposited Cu Catalysts. *Catal. Today* **2019**, *323*, 26–34.

(62) Sanyal, U.; Koh, K.; Meyer, L. C.; Karkamkar, A.; Gutiérrez, O. Y. Simultaneous Electrocatalytic Hydrogenation of Aldehydes and Phenol over Carbon-Supported Metals. *J. Appl. Electrochem.* **2021**, *51*, 27–36.

(63) Nirala, S.; Udishnu, S.; Griffin, R.; Stoerzinger, K. A.; Oliver, Y. G.; Donald, M. C.; John, L. F.; Johannes, A. L.; Charles, T. C. Aqueous Phase Catalytic and Electrocatalytic

Hydrogenation of Phenol and Benzaldehyde over Platinum Group Metals. *J. Catal.* **2020**, *382*, 372–384.

(64) Yu, W.; Porosoff, M. D.; Chen, J. G. Review of Pt-based Bimetallic Catalysis: From Model Surfaces to Supported Catalysts. Chem. Rev. **2012**, 112, 5780–5817.

(65) Evans, M. G.; Polanyi, M. Inertia and Driving Force of Chemical Reactions. *Trans. Faraday Soc.* **1938**, *34*, 11.

(66) Jencks, W. P. A Primer for the Bema Hapothle. An Empirical Approach to the Characterization of Changing Transition-State Structures. *Chem. Rev.* **1985**, *85*, 511–527.

(67) Studt, F.; Abild-Pederson, F.; Bligaard, T.; Sørensen, R. Z.; Christensen, C. H.; Nørskov, J. K. Identification of Non-Precious Metal Alloy Catalysts for Selective Hydrogenation of Acetylene. *Science.* **2008**, *320*, 1320–1322.

(68) Wang, S.; Petzold, V.; Tripkovic, V.; Kleis, J.; Howalt, J. G.; Skúlason, E.; Fernández, E. M.; Hvolbæk, B.; Jones, G.; Toftelund, A.; Falsig, H.; Björketun, M.; Studt, F.; Abild-Pedersen, F.; Rossmeisl, J.; Nørskov, J. K.; Bligaard, T. Universal Transition State Scaling Relations for (de)Hydrogenation over Transition Metals. *Phys. Chem. Chem. Phys.* **2011**, *13*, 20760–20765.

(69) Lu, S.; Menning, C. A.; Zhu, Y.; Chen, J. G. Correlating Benzene Hydrogenation Activity with Binding Energies of Hydrogen and Benzene on Co-Based Bimetallic Catalysts. *ChemPhysChem* **2009**, *10*, 1763–1765.

(70) Neurock, M.; Mei, D. Effects of Alloying Pd and Au on the Hydrogenation of Ethylene: An Ab Initio-Based Dynamic Monte Carlo Study. *Top. Catal.* **2002**, *20*, 5–23.

(71) Hammer, B.; Nørskov, J. K. Theoretical Surface Science and Catalysis—Calculations and Concepts BT - Impact of Surface Science on Catalysis. *Impact Surf. Sci. Catal.* **2000**, *45*, 71–129.

(72) Su, H. Y.; Sun, K.; Wang, W. Q.; Zeng, Z.; Calle-Vallejo, F.; Li, W. X. Establishing and Understanding Adsorption-Energy Scaling Relations with Negative Slopes. *J. Phys. Chem. Lett.* **2016**, *7*, 5302–5306.

(73) Calle-Vallejo, F.; Martínez, J. I.; García-Lastra, J. M.; Rossmeisl, J.; Koper, M. T. M. Physical and Chemical Nature of the Scaling Relations between Adsorption Energies of Atoms on Metal Surfaces. *Phys. Rev. Lett.* **2012**, *108*, 1–5.

Chapter 2 Experimental Methods

Portions of this chapter were adapted from **Akinola, J**.; Barth, I.; Goldsmith, B. R.; Singh, N. Adsorption Energies of Oxygenated Aromatics and Organics on Rhodium and Platinum in Aqueous Phase. *ACS Catal*. **2020**, 10, 4929–4941. Copyright American Chemical Society. Portions of section 2.6.2 were adapted from a manuscript currently in preparation by Harsh Agarwal, Jacob Fields, **James Akinola**, Martin Moskovits, Syed Mubeen, and Nirala Singh.

2.1 Introduction

This chapter provides a detailed description of the different techniques used in this dissertation to study the adsorption and hydrogenation of organic molecules in the aqueous phase. It includes the techniques to measure and extract adsorption energies (sections 2.2 and 2.3), catalyst synthesis and characterization (sections 2.4 and 2.5), and extracting kinetic data (section 2.7). It also discusses procedures for preparing roughened Au electrodes and removing adventitious carbon from the electrodes for surface-enhanced Raman spectroscopy measurements (section 2.6).

2.2 Cyclic Voltammetry and Hydrogen Underpotential Deposition

Cyclic voltammetry (CV) is one of the most useful electrochemical techniques for studying redox-active species in an electrochemical system.[1] Here, we use the CV technique primarily to probe hydrogen adsorption and indirectly measure organic adsorption on an electrode surface. A CV involves the cyclic variation of the applied potential where the potential is scanned linearly between two extremes at a constant scan rate.[2] **Figure 2.1** shows a typical cyclic voltammetry experiment used in this dissertation for Pt supported on Vulcan carbon catalyst (Pt/C) where the potential is changed with time between 0 and 1.4 V vs. RHE at a scan rate of 100 mV s^{-1}. The current response is recorded in **Figure 2.1b**, allowing for the analysis of various electrochemical processes such as hydrogen adsorption ($H^+ + e^- + * \rightleftharpoons H^*$). Where * is a site on the catalyst surface where protons can form hydrogen adatoms. At potentials more positive than 0 V vs. RHE (i.e., 0.05–0.4 V) where hydrogen adsorption and desorption occurs in **Figure 2.1b** is the underpotential deposition of hydrogen (H_{upd}) which we use for (i) counting metal sites to obtain the electrochemical active surface area (ECSA) and (ii) probing organic adsorption through site-blocking of the underpotentially adsorbed hydrogen by adsorbed organic.

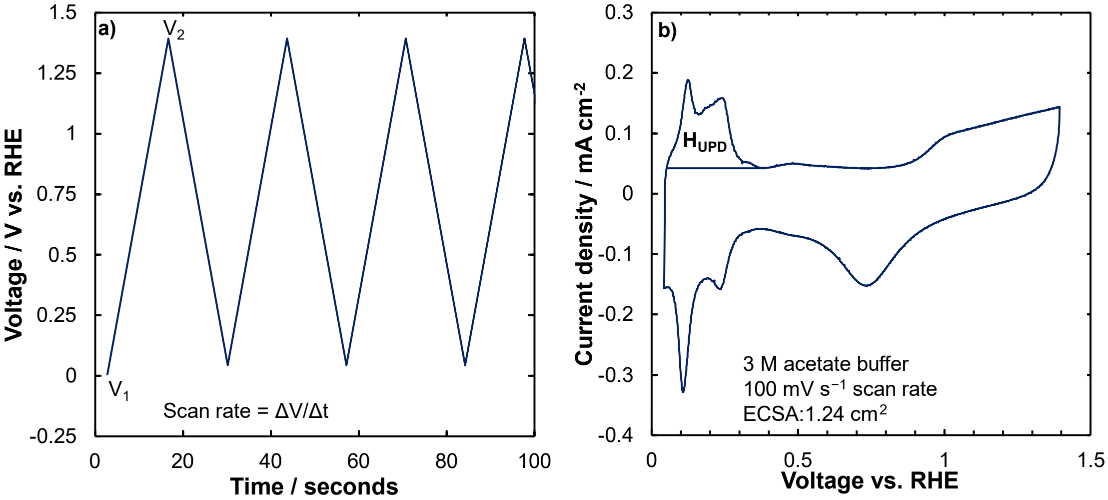

Figure 2.1 Cyclic voltammetry procedure on Pt supported on Vulcan carbon deposited on a glassy carbon disk electrode in 3 M acetate buffer at 23.3°C. a) Voltage vs. time plot showing cycling between $V_1 = 0.05$ V and $V_2 = 1.40$ V vs. RHE at a scan rate of 100 mV s^{-1}. **b)** Current density vs. voltage plot showing the H_{upd} region on Pt.

The hydrogen underpotential deposition for platinum group metals (PGMs) is a fundamental concept in electrochemistry that describes the adsorption of hydrogen atoms onto the surface of PGM electrodes at potentials before their bulk hydrogen evolution potential. PGMs, such as Pt, Pd, Rh, Ru exhibit this unique property due to their ability to adsorb hydrogen atoms at sub-monolayer coverages before the standard redox potential for hydrogen evolution (0 V vs. RHE).[3,4] This phenomenon is a result of the strong interaction between the metal surface and the hydrogen atoms, resulting in the formation of a stable hydrogen adlayer. H_{upd} provides insights into the formation of adsorbed hydrogen for site counting without and with organic present.

2.2.1 Obtaining the Fraction of H_{upd} Inhibited and Organic Coverage

The inhibition of a fraction of H_{upd} sites by the presence of aqueous organics is used to indirectly obtain the organic coverage. In the absence of organic in the supporting acetate buffer electrolyte, the catalyst surface is originally covered with adsorbed hydrogen (H*), whereas with an organic present in solution there is competition with H* for adsorption sites, which manifests as a noticeable drop in measured H_{upd} charge (Q_{des}) because fewer electrons are required to adsorb hydrogen on the fewer available sites. The fraction of H_{upd} inhibited when organic adsorbs is denoted by **Eq. 2.1**:

$$Fraction\ of\ H_{upd}\ inhibited = \frac{Q_{des}\ without\ organic - Q_{des}\ with\ organic}{Q_{des}\ without\ organic} \tag{2.1}$$

Assuming this drop is only due to organic (e.g., phenol) adsorption, the fraction of H_{upd} inhibited normalized to the fraction of H_{upd} inhibited at saturation is the coverage of organic $\theta_{organic}$ (**Eq. 2.2**). Thus $\theta_{organic}$ = 1 is at complete saturation with organic and $\theta_{organic}$ = 0 is when no organic is in solution.

$$\theta_{organic} = \frac{Q_{des}\ without\ organic - Q_{des}\ with\ organic}{Q_{des}\ without\ organic - Q_{des}\ with\ organic\ at\ saturation} \tag{2.2}$$

2.2.2 Reversibility of Hydrogen Underpotential Deposition in Acetate Buffer and in the Presence of Phenol

For the H_{upd} technique to yield valid organic adsorption energies and equilibrium constants, both hydrogen and organics must adsorb reversibly. We would expect the total charge (current integrated over time) to be independent of the scan rate for an equilibrated process. In **Figure 2.2** we show the current densities in the H_{upd} region on Rh metal in acetate buffer at different scan rates from which we extract the H_{upd} charge.

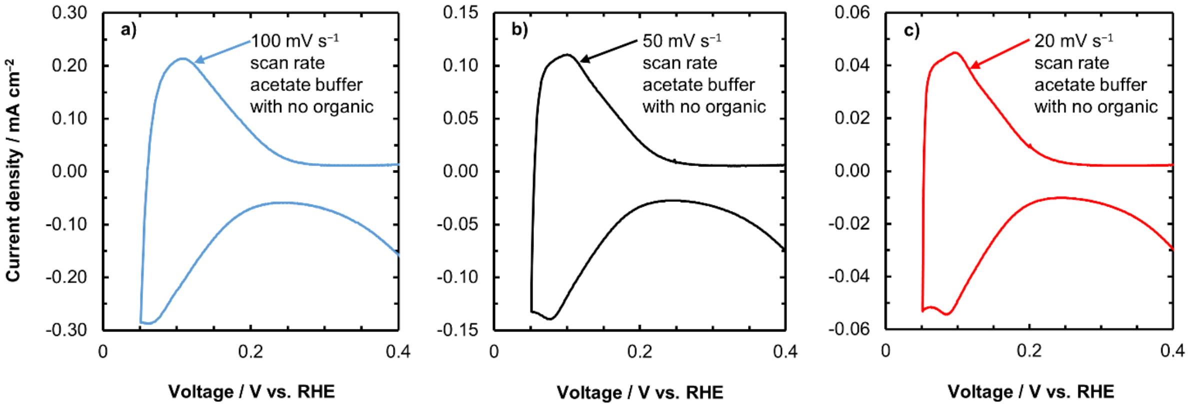

Figure 2.2 Cyclic voltammograms showing the H_{upd} on Rh wire in acetate buffer (100 mM acetic acid, 100 mM sodium acetate, pH = 5) at 298 K and varying scan rates. a) 100 mV s^{-1} **b)** 50 mV s^{-1} **c)** 20 mV s^{-1}.

The change in the H_{upd} desorption charge with scan rate (**Table 2.1**) is approximately 7%. Partially this may be related to errors in determining the charge (e.g., where to select the background double layer charging current), and partially may be real differences in the amount of H_{upd} that is adsorbed and desorbed at slower scan rates. For our studies because we did not see any significant differences in the adsorption isotherms derived at the different scan rates, we selected the faster scan rates (100 mV s^{-1}) to minimize the total time required for the full set of CV experiments.

Table 2.1 Desorption charges for H_{upd} (Q_{des}) on Rh wire in acetate buffer supporting electrolyte corresponding to data in Figure 2.2 at 100, 50, or 20 mV s^{-1} scan rate.

Scan rate	**100 mV s^{-1}**	**50 mV s^{-1}**	**20 mV s^{-1}**
Q_{des} (μC)	10.2	10.7	10.9

The data in **Figure 2.3** shows that H adsorption and H* desorption on Pt and Rh are reversible with and without phenol. The difference in the charge from H adsorption (Q_{ads}) and H* desorption (Q_{des}) is nearly constant even with increasing concentration of phenol for both Pt and Rh wires. For Rh, the higher adsorption charge compared with the desorption charge is caused by the convolution of the Rh_2O_3 reduction peak with the H^+ reduction peak, causing the ‘adsorption’ charge (in actuality the reduction charge) to be larger than the desorption charge. Thus, we use Q_{des} to represent the H_{upd} charge unless stated otherwise (i.e., the fraction of H_{upd} charge inhibited refers to the effect of the organic on the desorption charge because of site blocking). The constant ratio of Q_{ads} and Q_{des} at all phenol concentrations indicates that H* does not react with adsorbed phenol within our CV potential window and scan rate, as otherwise the Q_{des} would decrease relative to Q_{ads} at higher phenol concentrations.

The Q_{ads} was obtained by integrating the area under the H adsorption region after converting the H_{upd} potential window to a time using the voltage scan rate and subtracting the baseline (double layer) charge from the CVs. The baseline current for Rh was chosen at 500 mM phenol because at this high concentration, the H^+ and the Rh_2O_3 reduction peaks were completely inhibited by phenol adsorption. The Q_{des} was obtained by integrating the area under the H* desorption peak in the positive oxidation scan and subtracting the double layer charge.

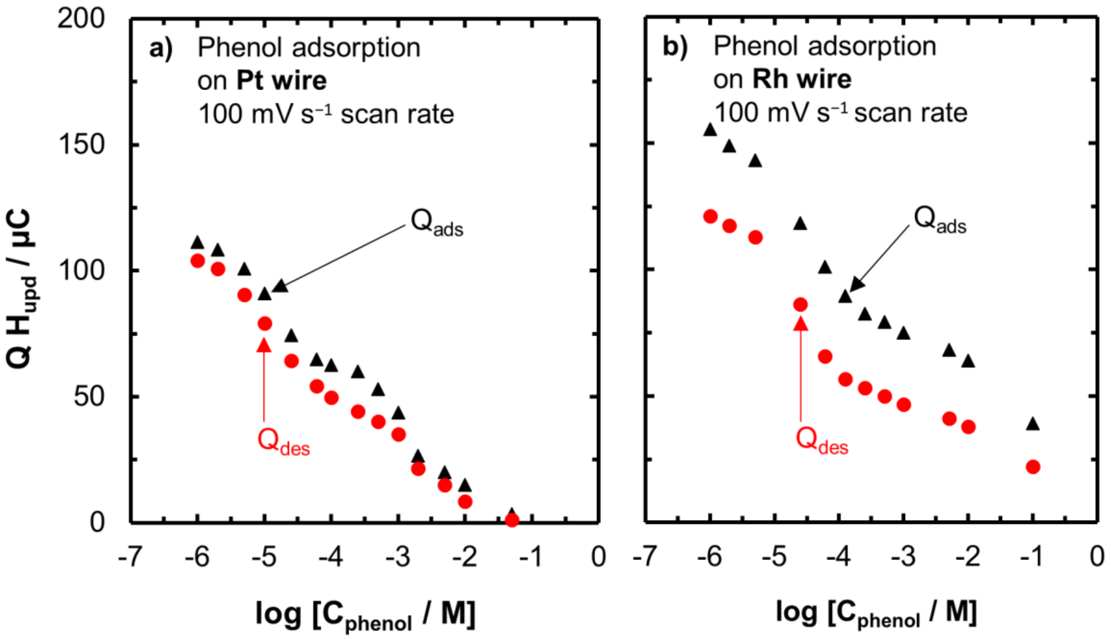

Figure 2.3 The H_{upd} adsorption charge (from reduction, Q_{ads}) and desorption charge (from oxidation, Q_{des}) as a function of phenol concentration on polycrystalline metal wires. a) Pt wire **b)** Rh wire. The larger adsorption charge for Rh than desorption charge is because of the Rh_2O_3 reduction peak overlapping with the H_{upd} reduction peak, causing an overprediction of the Q_{ads} charge. The reversibility of the H_{upd} charge is constant with phenol concentration for both metals.

2.2.3 Change in Bulk Phenol Concentration by Adsorption of Phenol

It is important to know if there is an appreciable change in the bulk phenol concentration after phenol adsorbs on the metal surface since an accurate isotherm is dependent on knowing the actual bulk organic concentration. Here we show there is not an appreciable change in the bulk phenol concentration upon phenol adsorption on Rh wire. We base this analysis on the maximum Rh surface area (0.661 cm^2) exposed in our experiments and the lowest bulk phenol concentration used. The total volume of the electrolyte (130 mL) was kept the same in all measurements.

We assume the same number of Rh and Pt atoms per cm^2 = 1.31×10^{15} atoms from refs [5,6]. Thus, the number of Rh (or Pt) atoms covered by phenol at maximum coverage is:

$$Rh\ atoms = 1.31 \times 10^{15}\ atoms\ cm^{-2} \times max.phenol\ coverage \times ECSA$$

where ECSA is the electrochemical active surface area and we assume the maximum phenol coverage is 1 monolayer. Using the maximum ECSA (0.661 cm^2) of the exposed Rh gives:

$$Rh\ atoms = 1.31 \times 10^{15}\ atoms\ cm^{-2} \times 1 \times 0.661\ cm^2 = 8.66 \times 10^{14}\ atoms$$

Assuming that one phenol molecule adsorbing flat covers five Rh atoms, the number of moles of phenol to completely block the Rh wire (i.e., at adsorption saturation) is:

$$8.66 \times 10^{14}\ Rh\ atoms \times \frac{1\ phenol\ molecule}{5\ Rh\ atoms} \times \frac{1\ mol\ phenol}{6.02 \times 10^{23}\ phenol\ molecules}$$

$$= 2.874 \times 10^{-10}\ moles\ phenol$$

The volume of acetate buffer + phenol in solution in our cell is 130 mL. Therefore, the moles of phenol in 1 µM solution (the lowest phenol concentration we studied) is 1.3×10^{-7} moles. Even if a saturation adsorption coverage of phenol from the bulk concentration is reached, the amount of phenol remaining in bulk solution would be:

$$1.3 \times 10^{-7}\ moles\ phenol - 2.874 \times 10^{-10}\ moles\ phenol = 1.297 \times 10^{-7}\ moles\ phenol$$

The new concentration of solution after phenol adsorption would then be:

$$\frac{1.297 \times 10^{-7}\ moles\ phenol}{0.13\ L} = 9.977 \times 10^{-7}\ mol\ L^{-1} = 0.9977\ \mu M$$

Therefore, the bulk phenol concentration remains approximately constant even at the lowest bulk phenol concentration of 1 µM (0.2% loss in concentration at 1 µM). However, at these low bulk concentrations much less than a full monolayer of phenol is adsorbed based on the small decrease in H_{upd} charge, so in actuality the decrease in bulk phenol concentration would be even smaller. This analysis holds for all organics on Pt as well because a similar area of Pt or Rh was immersed in the supporting electrolyte.

2.2.4 Reproducibility of the Effect of Phenol Adsorption on H_{upd}

To determine the reproducibility of the H_{upd} method for quantifying phenol adsorption on Rh, we conducted several repetitions at the same bulk concentration of phenol. In **Figure 2.4a**, 60 µM phenol was added after stepwise increments from five intermediate concentrations. However, in **Figure 2.4b** and **Figure 2.4c**, prepared in separate runs, 60 µM was added after a single increment in phenol concentration. For all three runs, a similar relative drop in H_{upd} charge was observed, showing that the fraction of H_{upd} inhibited was reproducible and independent of the surface areas exposed and the path taken to attain the desired concentration. That is, CV measurements performed at lower concentration ranges did not impact later measurements at higher concentrations. The fraction of H_{upd} inhibited at 60 µM phenol for the three runs in **Figure 2.4**, also listed in **Table 2.2** are in the range of 0.43 ± 0.01 even with different amounts of time in reaching the desired phenol concentration. This result indicates that no time effect is present in our estimations of the phenol coverage.

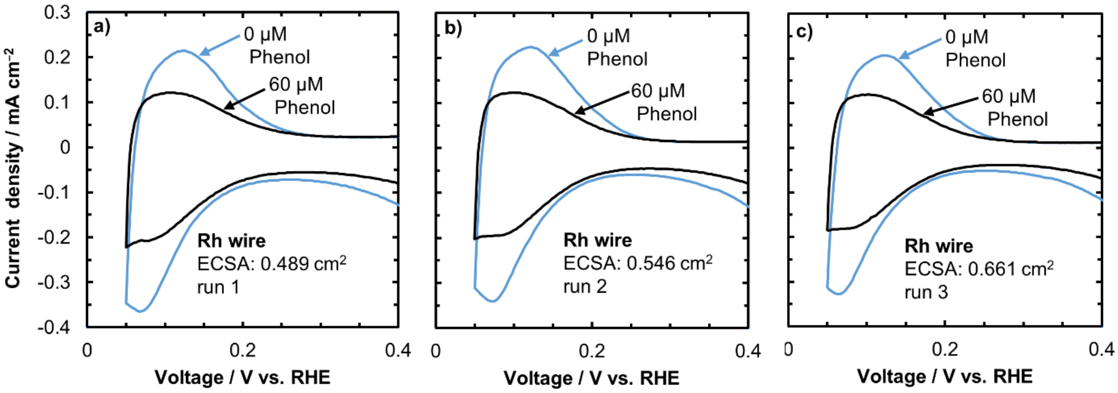

Figure 2.4 Cyclic voltammograms to test the reproducibility of phenol adsorption on rhodium wire from three different repetitions. a), the final 60 μM concentration was reached by adding five intermediate concentrations (1, 2, 5 10, 25 μM) and taking CVs at each of those intermediate concentrations. In **b)** and **c)** the 60 μM concentration was directly reached in one addition, without CV measurements at intermediate concentrations. The supporting electrolyte was 100 mM acetate buffer at 298 K and the scan rate was 100 mV s^{-1}. The ECSA shown is of the run with no phenol, which is used to normalize the current. A value of 221 μC cm^{-2} was used to calculate the ECSA.[7,8]

Table 2.2 H_{upd} desorption charge (Q_{des}) at 0 and 60 μM phenol and the fraction of H_{upd} inhibited on Rh wire at 60 μM phenol for the different measurements shown in Figure 2.4.

	Repetition 1		**Repetition 2**		**Repetition 3**	
Phenol concentration (μM)	Q_{des} (μC)	Fraction of H_{upd} inhibited	Q_{des} (μC)	Fraction of H_{upd} inhibited	Q_{des} (μC)	Fraction of H_{upd} inhibited
0	108	--	120	--	147	--
60	60.4	0.439	66.8	0.444	84.7	0.427

2.2.5 Reversibility of Organic Adsorption on Rh and Pt

Adsorption of organics must be reversible in the H_{upd} potential window in order to extract accurate adsorption energies. The H_{upd} desorption charge after phenol replacement with new supporting electrolyte is close to the H_{upd} charge without phenol, with about 99% of the H_{upd} charge recovered on Rh and 97% of the H_{upd} charge recovered on Pt. In **Figure 2.5**, the initial CV of the supporting electrolyte containing no organic is shown by a blue line, while CVs with 1 mM, 100 μM, or 60 μM organic in supporting electrolyte are indicated by a black line. The CV of the diluted organic(i.e., from 1 mM to 100 µM, 100 µM to 10 µM or 60 µM to 0 µM) is shown by a red dashed line. The phenol concentration in **Figure 2.5a** and **2.5e** was increased to 60 µM and the new cyclic voltammogram shows a drop in the H_{upd} charge compared to when no phenol is in the supporting electrolyte.

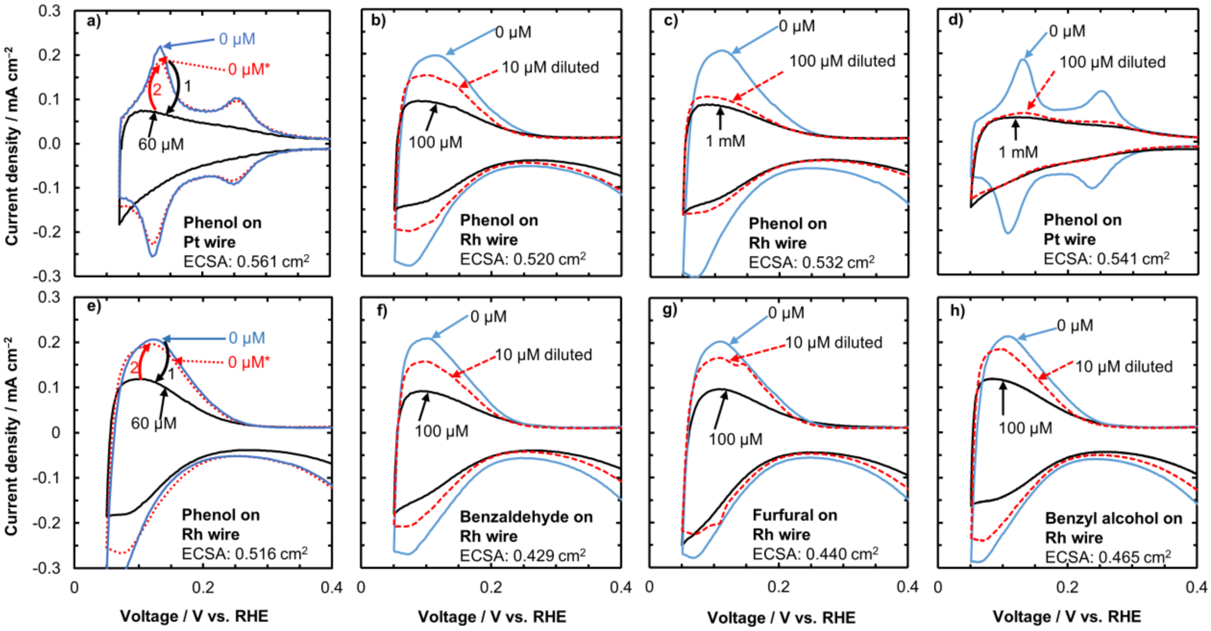

Figure 2.5 Cyclic voltammograms showing the reversibility of organic adsorption on rhodium and platinum after controlled dilution. a) Dilution from 60 µM phenol to 0 µM on Pt. **b)** Dilution from 100 µM phenol to 10 µM on Rh. **c)** Dilution from 1 mM phenol to 100 µM on Rh. **d)** Dilution from 1 mM phenol to 100 µM on Pt. **e)** Dilution from 60 µM phenol to 0 µM on Rh. **f)** Dilution from 100 µM benzaldehyde to 10 µM on Rh. **g)** Dilution from 100 µM furfural to 10 µM on Rh. **h)** Dilution from 100 µM benzyl alcohol to 10 µM on Rh. Supporting electrolyte is acetate buffer (pH 5), and the CV is obtained at 100 mV s^{-1} scan rate and 298 K. In a and e, step 1 (black arrow) represents phenol addition while step 2 (red arrow) represents dilution. 0 µM* the CV of the new solution is slightly different from 0 µM because of a small amount of phenol remaining in the cell after dilution.

When the 60 µM phenol solution is replaced with acetate buffer containing no phenol (without removing or recleaning the Pt or Rh wire), the H_{upd} charge is 97% and 99% recovered on Pt and Rh, respectively as adsorbed phenol desorbs reversibly from the metal (**Table 2.3**). The reason the H_{upd} charge in **Figure 2.5a** and **2.5e** is incompletely recovered is because of small traces of phenol remaining in the electrochemical cell. For all cases and organics, the CV of the diluted organic showed a higher H_{upd} charge compared to the initial concentration before dilution, and matched the CVs taken at the concentrations directly without diluting. This observation shows that organic adsorption/desorption is reversible in this potential window.

Table 2.3 The H_{upd} desorption charge without phenol, with 60 µM phenol, and after replacing phenol solution with new supporting electrolyte on Pt wire (Figure 2.5a) and Rh wire (Figure 2.5e).

	Pt wire		**Rh wire**	
Phenol concentration (µM)	Q_{des} (µC)	Fraction of H_{upd} inhibited	Q_{des} (µC)	Fraction of H_{upd} inhibited
0	16.6	0	148	0
60	7.1	0.571	85.5	0.426
0*	16.1	0.0303	146	0.0143

Also listed is the fraction of H_{upd} inhibited, calculated from the exact desorption charge before rounding to three significant figures. * means the concentration is in actuality > 0 due to trace remaining phenol in the cell after replacing 60 µM phenol with new supporting electrolyte, as well as from any phenol desorbed from the electrode surface.

2.3 Fitting Experimental Adsorption Isotherm Data using the Temkin Model

Here we describe the fitting of experimental adsorption isotherms for phenol, albeit this process is applicable to all the organics studied in this work. The adsorption of bulk phenol in solution ($Ph_{(aq)}$) onto a free catalyst site available for phenol adsorption ($*$) to form an adsorbed phenol ($Ph*$) is shown by **Eq. 2.3**:

$$Ph_{(aq)} + * \rightleftharpoons Ph* \tag{2.3}$$

The equilibrium adsorption constant ($K_{eq,ads,\theta}^{aq}$) of **Eq. 2.3** is shown in **Eq. 2.4**:

$$K_{eq,ads,\theta}^{aq} = \frac{\theta_{Ph}}{C_{Ph}\theta_*} \tag{2.4}$$

where C_{Ph} is the bulk concentration of phenol, θ_{Ph} is the coverage of phenol (we use *Ph* here for phenol, but could also represent other organics), and θ_* is the fraction of free sites. The bulk concentration of phenol is not changed upon adsorption in our experiments as discussed earlier. In this H_{upd} method we assume that hydrogen can adsorb on the free sites, but not on the sites that phenol is adsorbed onto, therefore we can indirectly determine the phenol coverage using **Eq. 2.5**:

$$\theta_{Ph} + \theta_{*} = 1 \tag{2.5}$$

Combining **Eqs. 2.4** and **2.5** gives an adsorption isotherm (**Eq. 2.6**), where the equilibrium adsorption constant is $K_{eq,ads,\theta}^{aq}$, with the subscript θ referring to the phenol coverage, included to indicate that the equilibrium adsorption constant may be dependent on phenol coverage because of adsorbate-adsorbate interactions.[9,10]

$$\frac{\theta_{Ph}}{\theta_{sat}} = \frac{K_{eq,ads,\theta}^{aq}\, C_{Ph}}{\left(1 + K_{eq,ads,\theta}^{aq} C_{Ph}\right)} \tag{2.6}$$

Where θ_{sat} is the saturation coverage. If we assume that the equilibrium adsorption constant follows a Temkin model, such that the free energy of adsorption changes linearly with coverage, then:

$$K_{eq,ads,\theta}^{aq} = \exp\left(\frac{-(\Delta G_{ads,aq,\theta=0}^{0} + \alpha\theta_{Ph})}{RT}\right) \tag{2.7}$$

where α is a parameter with units of kJ mol^{-1} that represents the strength of adsorbate-adsorbate interactions, and $\Delta G_{ads,aq,\theta=0}^{0}$ is the adsorption free energy in kJ mol^{-1} at a phenol coverage of zero. **Eqs. 2.6** and **2.7** can be combined to give:

$$\frac{\theta_{Ph}}{\theta_{sat}} = \frac{\exp\left(\frac{-(\Delta G_{ads,aq,\theta=0}^{0} + \alpha\theta_{Ph})}{RT}\right) C_{Ph}}{\left(1 + \exp\left(\frac{-\Delta G_{ads,aq,\theta=0}^{0} + \alpha\theta_{Ph})}{RT}\right) C_{Ph}\right)} \tag{2.8}$$

Using the constructed adsorption isotherms of the coverage of phenol measured indirectly by the decrease in H_{upd} charge as a function of the bulk phenol concentration, we can fit the data to **Eq. 2.8** by varying the parameters of $\Delta G_{ads,aq,\theta=0}^{0}$, α and θ_{sat}. For a two-site adsorption model, the saturation coverage for site 1 was chosen as the coverage where the isotherm first plateaus, whereas adsorption on site 2 begins at the organic concentration immediately above that which saturates site 1. The coverage measurements from the H_{upd} technique are not at the potential of zero charge (PZC), or at a slightly cathodic potential where maximum coverage is typically achieved.[11] Nevertheless, coverages obtained here for phenol on Pt using the H_{upd} method match closely to reported coverages obtained by radiotracer method at potentials close to the PZC,[12] corroborating the accuracy of H_{upd} method.

2.3.1 Converting from Aqueous Free Energies of Adsorption to Aqueous Enthalpies of Adsorption

The process for converting aqueous-phase adsorption free energies obtained from adsorption isotherms to aqueous-phase enthalpies of adsorption is outlined in **Figure 2.6** and elsewhere.[13] The process consists of three steps, i) converting the organic aqueous equilibrium adsorption constant ($K_{eq,ads,\theta}^{aq}$) to the free energy of adsorption of the gas-phase organic in aqueous phase ($\Delta G_{ads,aq,gas,\theta}^{0}$) using Henry's law constant, K_H , ii) converting to the enthalpy of adsorption of the gas-phase organic ($\Delta H_{ads,aq,gas,\theta}^{0}$) using an estimate of the adsorption entropy,[14] and iii) converting to the enthalpy of adsorption of the aqueous-phase organic ($\Delta H_{ads,aq,\theta}^{0}$) by subtracting the organic enthalpy of solvation ($\Delta H_{solvation}^{0}$). The value of $\Delta H_{ads,aq,gas,\theta}^{0}$ determined through this method can be directly compared to values calculated from density functional theory (DFT). The value of $\Delta H_{ads,aq,\theta}^{0}$ can be directly compared to values from solution calorimetry.

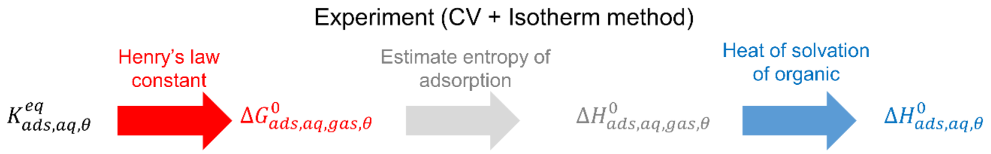

Figure 2.6 Outlined procedure of estimating the aqueous phase adsorption enthalpies from CV method and isotherms.

The values used for the three steps outlined in **Figure 2.6** are shown in **Table 2.4**. The Henry's law constant, K_H, at 298.15 K for each individual organic in water is used to convert the aqueous adsorption constant to the equilibrium constant and thus free energy of adsorption of a gas-phase organic relative to the adsorbed organic in the aqueous phase according to **Eq. 2.9**.

$$K_{eq,ads,aq,\theta}^{gas} = K_{eq,ads,\theta}^{aq}/K_H = e^{\frac{-\Delta G_{ads,aq,gas,\theta}^{0}}{RT}} = e^{\frac{-\Delta H_{ads,aq,gas,\theta}^{0}}{RT}} e^{\frac{\Delta S_{ads,aq,gas}^{0}}{R}} \tag{2.9}$$

The enthalpy of adsorption of the gas-phase organic relative to the adsorbed organic in aqueous phase is estimated by assuming an entropy of adsorption from the correlation in ref [14]. This correlation uses gas-phase entropies to predict adsorption entropies. For molecules where the gas-phase entropies were not tabulated we used entropies calculated by ideal gas statistical mechanics.

Table 2.4 Henry's law constant (K_H) at 298.5 K, gas-phase entropy, and enthalpy of solvation (ΔH_{Solv}) for molecules studied in this work.

Molecule	**Henry's law constant (bar M^{-1})**	**Gas phase entropy (J mol^{-1} K^{-1})**	**ΔH_{Solv} (kJ mol^{-1})**
Phenol	5.0×10^{-4} from ref [15]	314.8 from ref [16] 313.5 *	−50.0 from ref [17]
Benzaldehyde	2.6×10^{-2} from ref [15]	334.1 *	−42.2 from ref [18]
Furfural	3.86×10^{-3} from ref [19]	318.4 *	−58.0 from refs [15,20]
Benzyl alcohol	1.1×10^{-4} from ref [15]	347.9 *	−66.9 from ref [21]
Cyclohexanol	5.9×10^{-3} from ref [15]	353.83 from ref [16] 339.7 *	−70.7 from ref [22]

* Values calculated in this work by ideal gas statistical mechanics.

The heat of solvation ($-\Delta H_{Solv}$) of a given organic was obtained either directly from references or by applying the van't Hoff equation (**Eq. 2.10**) and using the reported temperature dependence of the Henry's law constant. ΔH_{Solv} was subtracted from the gas-phase adsorption enthalpy to obtain the adsorption enthalpy of the solvated organic.

$$\frac{d\ln K_H}{d\left(\frac{1}{T}\right)} = \frac{-\Delta H_{Solv}}{R} \tag{2.10}$$

To clarify, here is an example of how the aqueous-phase adsorption enthalpies were estimated. For example, from fitting the adsorption isotherm for Rh in **Figure 3.2** of **Chapter 3**, the aqueous phase equilibrium constant for phenol on site 1 was $K_{eq,ads,\theta}^{aq} = 37{,}600$ (unitless), where the assumed standard state coverage is $\theta^0 = 0.5$. To obtain the adsorption equilibrium constant in aqueous phase relative to gas phase phenol, $K_{eq,ads,aq,\theta}^{gas}$, we used the Henry's law constant K_H:

$$K_{eq,ads,aq,\theta}^{gas} = \frac{K_{eq,ads,\theta}^{aq}}{K_H} = \frac{37{,}600}{5 \times 10^{-4}} = 7.52 \times 10^7$$

To be consistent with our previous work in ref [13] we next shift the standard state coverage to $\theta^0 = 0.054$ before making an approximation of the entropy of adsorption to determine enthalpies. We use a standard state coverage of $\theta^0 = 0.054$ for phenol on Pt(111), which is calculated as outlined in ref [23] using the atomic surface density of Pt(111) and the saturation coverage of phenol on Pt(111).[24] This value of θ^0 is thus specifically for Pt(111) with phenol based on previous experimental measurements, but we use it for all systems here (including Rh) despite the slight differences in the saturation coverage and number of metal atoms per cm^2.

$$K_{eq,ads,aq,\theta=0.054}^{gas} = \frac{K_{eq,ads,\theta}^{aq}}{\frac{\theta^0}{1-\theta^0} K_H} = \frac{37{,}600}{\frac{0.054}{1-0.054} 5 \times 10^{-4}} = 1.32 \times 10^9$$

The entropy correlation from ref [14] (**Eq. 2.11**) is used to estimate the aqueous-phase adsorption entropy using gas-phase organic entropy. We assume that the adsorbed organic entropy is the same in the aqueous phase as it would be in the gas phase assuming there is no entropy change in displacement of the water adlayer. In **chapter 4** we further probe the assumption that the adsorption entropy is unchanged when the interfacial water adlayer is displaced.

$$\Delta S^0_{ad,aq,gas} = S^0_{ad} - S^0_{gas} = \left(0.70S^0_{gas} - 3.3R\right) - S^0_{gas} = -\left[0.30S^0_{gas} + 3.3R\right] \qquad (2.11)$$

Where R is the gas constant = 8.314 J mol^{-1} K^{-1}, S^0_{gas} is the standard gas-phase entropy of the organic (phenol in this case), S^0_{ad} is the standard adsorbate entropy, and $\Delta S^0_{ad,aq,gas}$ is the entropy of the adsorbed solvated organic relative to gas phase.

For phenol, S^0_{gas} = 314.8 J mol^{-1} K^{-1} = (38 R) from ref [16]. Therefore, we can calculate the entropy of adsorption of gas-phase phenol onto Rh in the aqueous phase by:

$$\Delta S^0_{ad,aq,gas} = -[0.30 \times 38R + 3.3R] = -14.7R$$

Using the estimated entropy of adsorption, we convert the equilibrium constant of adsorption for gas-phase phenol unto a solvated Rh wire into an enthalpy of adsorption. Note that the entropy of adsorption is calculated using $\theta^0 = 0.054$, and would be shifted by 2.5 R if instead we reported at $\theta^0 = 0.5$ as discussed in refs [13,23]. The resulting enthalpies obtained using $\theta^0 = 0.054$ are those reported in **Table 3.1** of **Chapter 3**.

$$\Delta H^0_{ads,aq,gas,\theta=0.054} = T\Delta S^0_{ads,aq,gas} - RT\ln K^{gas}_{eq,ads,aq,\theta=0.054}$$

$$= T(-14.7R) - RT\ln K^{gas}_{eq,ads,aq,\theta=0.054}$$

$$= RT[-14.7 - \ln K^{gas}_{eq,ads,aq,\theta=0.054}]$$

$$= 8.314\frac{J}{mol\ K} \times 298.15\ K \times [-14.7 - \ln\,[1.32 \times 10^9]]$$

$$\Delta H^0_{ads,aq,gas,\theta=0.054} = -88.6\ kJ\ mol^{-1}$$

To estimate the aqueous phase adsorption enthalpy of phenol, we subtract the enthalpy of solvation ΔH_{Solv} listed in **Table 2.4**, which for phenol is −50 kJ mol^{-1}.

$$\Delta H^{0}_{ads,aq,\theta=0.054} = \Delta H^{0}_{ads,aq,gas,\theta=0.054} - \Delta H_{Solv}$$

$$\Delta H^{0}_{ads,aq,\theta=0.054} = -88.6\ kJ\ mol^{-1}\ - (-50)\ kJ\ mol^{-1}\ = -38.6\ kJ\ mol^{-1}$$

2.4 Electrode Preparation for Supported Catalysts

Pt_xCo_y alloys are studied in **Chapter 6** for electrocatalytic hydrogenation (ECH) and hydrogen evolution reaction (HER) requiring these alloy catalyst materials to serve as the working electrode. For the HER studies, the Pt_xCo_y alloys were supported on Vulcan carbon and deposited unto a glassy carbon. Whereas for the ECH studies, the alloys were directly synthesized Onto a porous carbon felt support for stability. Adsorption studies in **Chapters 3** and **4** were performed directly on a Pt or Rh wire as the working electrode.

2.4.1 Catalyst Ink Preparation and Deposition on Glassy Carbon

The rotating disk electrode (RDE) is the conventional setup for measuring rates for a reaction with very fast kinetics like the HER in acids. For RDE studies, a 5 mm diameter glassy carbon disk was first thoroughly cleaned by scrubbing the disk surface on a micro polishing cloth containing a few drops of alumina suspension for 5 minutes. After polishing, the glassy carbon disk was rinsed in Millipore water and placed in a sealed beaker with Millipore water before ultrasonication for a minimum of 30 minutes. The catalyst ink to be deposited was prepared by adding 3 mg of the catalyst supported on Vulcan carbon into a mixture of Millipore water and isopropanol (1:1 volume ratio, 5 mL total). For catalysts supported on carbon felt rather than powder supports like Vulcan carbon, the felts were first grounded to powder before making them to inks.

Nafion 117 solution is the typical binder used for our ink preparation for which 17.5 µL is added to the catalyst mixture. Nafion 521, which is slightly less miscible with water but has similar or perhaps a better binding capability than Nafion 117 can also be used. Nafion 521 should be used in a smaller volume, such as 10 µL for the same 5 mL catalyst mixture to prevent poor catalyst dispersion due to immiscibility. After mixing the catalyst with water, isopropanol, and Nafion solution, the container was sealed and ultrasonicated for a minimum of 30 minutes or longer if needed. After cleaning and drying the glassy carbon disk, it was assembled in a Teflon disk holder with its shiny surface exposed before dropping 8 µL of the freshly ultrasonicated catalyst mixture onto the surface. After 30 mins, a second drop cast was performed and allowed to dry for another 30 minutes minimum. The electrode now containing 9.6 µg of the deposited catalysts is ready for RDE experiments.

2.4.2 Direct Synthesis of Catalysts on Carbon Felt

For ECH studies in **Chapter 6,** where a negative potential is applied during electrode pretreatment and hydrogen is also evolved on the electrode surface during reaction, it was difficult to retain the Vulcan carbon catalysts on the felt using the ink drop casting method (**Figure 2.7**). To improve adhesion between the metal nanoparticles on the felt support, we chemically reduced the metal ions from their precursor salts to form nanoparticles directly on the carbon felt supports. To begin, the carbon felts were subjected to thermal pretreatment in air at 400°C for 16 hours to increase their surface area. Pt_xCo_y alloys synthesized on conductive carbon felts was carried out via chemical reduction with sodium borohydride. Different compositions, namely Pt/felt, Pt_3Co/felt, PtCo/felt, and $PtCo_3$/felt, were targeted by adjusting the amounts of Pt and Co precursors used. Here, a specific amount of $Co(OH)_2$ was dissolved in a 20 mL mixture of methanol and Millipore water in a 1:1 volume ratio. The pH was then adjusted to 2 by adding 37%

HCl dropwise with a pipette. A 20 mL aqueous solution of chloroplatinic acid ($H_2PtCl_6{\cdot}6H_2O$) was prepared separately before combining the two solutions with 4 pieces of carbon felt in a beaker followed by two hours of ultrasonication. A total of 4 beakers were prepared.

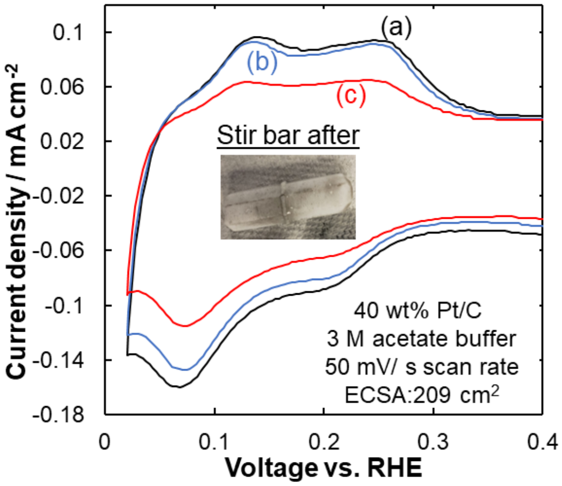

Figure 2.7. Cyclic voltammogram of Pt supported on Vulcan carbon (Pt/C) ink drop casted on a carbon felt showing the H_{upd} region before and after typical ECH pretreatment procedures. (a) Immediately after voltammtric cleaning cycle i.e., initial CV. **(b)** After applying −40 mA polarization for 30 mins. **(c)** After applying −0.1 V vs. RHE without phenol for 1 hr. The inset image shows the stir bar stained by Pt/C that leaches from the felt.

In a separate vial, sodium borohydride ($NaBH_4$) was dissolved in 5 mL of water to achieve a $NaBH_4$ to metal molar ratio of 12:1. Dropwise additions of borohydride solution were made to the precursor solution containing carbon felt while being sonicated in a water bath for three more hours. The carbon felt was afterwards removed from the solution and rinsed three times with Millipore water before drying overnight at 80°C in a vacuum oven. Before using the felt for ECH measurements, it was thoroughly rinsed with Millipore water again to remove any unreacted precursor. **Figure 2.8** outlines the alloy synthesis methodology.

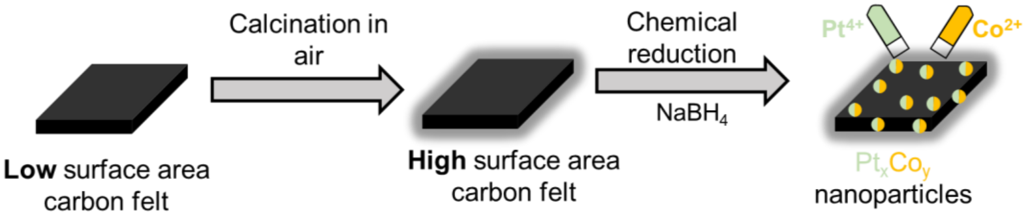

Figure 2.8 Methodology for synthesizing Pt_xCo_y catalysts directly supported on carbon felt using sodium borohydride as reductant.

2.5 Catalyst Characterization Techniques

After synthesizing the alloy catalyst nanoparticles, it is important to understand their nanostructure, particle size distribution, bulk and surface metal composition and coordination environment. All these aspects play a significant role in comprehending the catalyst material thoroughly before ascribing any kinetics results to properties of the synthesized material.

2.5.1 X-ray Absorption Fine Structure Spectroscopy (XAFS)

2.5.1.1 XAFS Fundamentals

In X-ray absorption experiments, X-rays that are intense and tunable to the core-energy of the relevant atom are supplied to eject a photo-electron from the atom.[25] When X-rays are passed through a sample (**Figure 2.9**), the probability that the X-rays will be absorbed given by the absorption coefficient, μ is described by Beer's law (**Eq. 2.12**):

$$I_T = I_0 e^{-\mu t} \tag{2.12}$$

Where I_0 is the incident X-ray intensity, I_T is the intensity of the X-ray transmitted through the sample and t is the sample thickness.

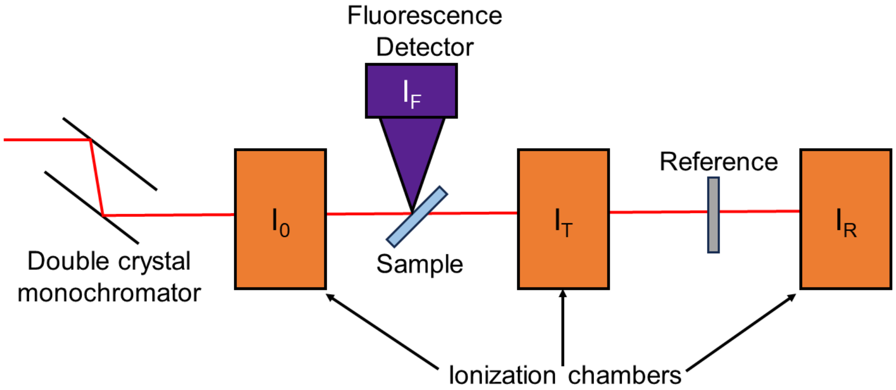

Figure 2.9 X-ray absorption experiment setup in transmission and flourescence mode. The incident X-ray, I_0 which is usually a mochromatic light passes through the sample where the transmission detector is located parallel to the sample but the florescence detector is at a 45° angle to the detector. Diagram was modified from ref [25].

When the X-rays promote a core-level electron to the continuum, a sharp rise in the absorption is observed also known as the absorption edge (**Figure 2.10a**). The empty core-hole leaves the atom in an excited state for a few femtoseconds after which a decay occurs either through fluorescence where a higher energy electron fills the core hole or through the Auger effect where a higher energy electron fills the core hole and then another photoelectron is ejected to the continuum. Beyond the absorption edge, the absorption coefficient depends on the energy of the beam such that μ(E) can be measured either in transmission (**Eq. 2.13**) or fluorescence mode (**Eq. 2.14**) as shown in **Figure 2.9**.

$$\mu(E) = ln\left(\frac{I_0}{I_T}\right) \tag{2.13}$$

$$\mu(E) = \frac{I_F}{I_0} \tag{2.14}$$

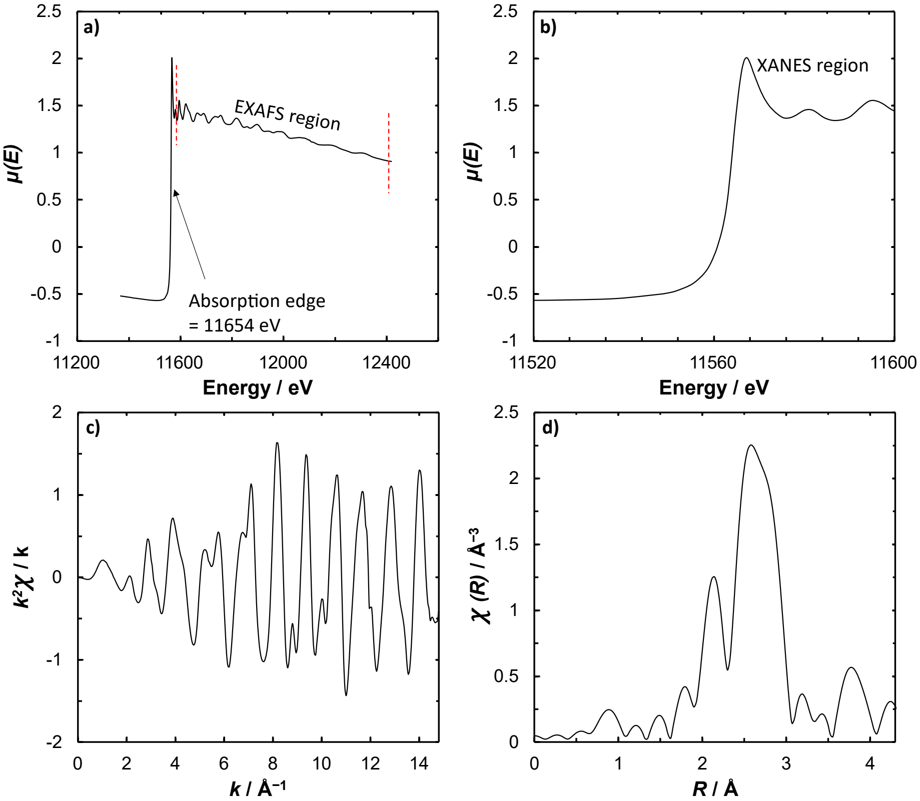

Figure 2.10 XAFS spectra representation for a Pt foil performed at the Advanced Photon Source at the Argonne National Laboratory. a) XAFS μ(E) showing the absorption edge energy and the EXAFS region. **b)** Zoomed image of μ(E) showing the XANES region. **c)** k-weighted XAFS $k^2\chi(k)$. **d)** The maginude of the EXAFS in real space.

Figure 2.10 shows an example of the XAFS spectra for a Pt foil performed at the Pt L_3 edge (11564 eV). The oscillations 30 eV above the edge are known as extended X-ray absorption fine structure (EXAFS), while the oscillations that occur between 30 eV before and 30 eV after the edge are known as the X-ray absorption near edge structure (XANES). We use both the XANES and EXAFS region in this dissertation to obtain the oxidation state and coordination environment of our synthesized metals and metal alloy catalyst materials. The oscillation in the EXAFS region is defined by the EXAFS function $\chi(E)$:

$$\chi(E) = \frac{\mu(E) - \mu_0(E)}{\Delta\mu_0(E)} \tag{2.15}$$

Where $\mu(E)$ is the absorption coefficient, $\mu_0(E)$ is the background function and $\Delta\mu_0(E)$ is the observed jump in absorption. Often time $\chi(E)$ is represented in terms of the wave number as $\chi(k)$ or $k^n\chi(k)$ instead of the energy (**Figure 2.10c**). Where n is the order to which k is raised. The scattering between nearest neighbor atoms as seen by the oscillations in the plot of $k^2\chi(k)$ can be modelled with the EXAFS equation:

$$\chi(k) = \sum_j \frac{N_j f_j(k) e^{-2k^2\sigma_j^2}}{kR_j^2} \sin\left[2kR_j + \delta_j k\right] \tag{2.16}$$

Where N is the number of nearest neighbor atoms and R is the distance between them. The properties of the scattering atoms are denoted by $f(k)$ and $\delta(k)$. This complex EXAFS equation can be Fourier transformed to give an imaginary and real parts. For example, the magnitude of the real part for a Pt foil is shown in **Figure 2.10d** from which the bond distances between nearest neighbor atoms can be determined.

2.5.1.2 XAFS Experiments and Fitting

We analyzed the Pt_xCo_y samples used for ECH and HER in **Chapter 6** both in ex-situ and in-situ using both transmission and fluorescence modes. Experiments were performed at the Advanced Photon Source at the Argonne National Laboratory. Ex-situ samples were prepared by mixing grounded catalyst with boron nitride, a pelletizer, and using a pellet press at 12,000 psi to press pellets of 1 cm diameter. In transmission mode, the amounts of catalyst and boron nitride needed to obtain edge steps greater than 0.25 and absorption lengths less than 2.5 were calculated using Hephaestus software.[26] The pellets were probed in transmission mode at the Pt L_3 edge (11564 eV), but fluorescence mode was used for the Co edge (7709 eV) as no catalyst and boron nitride ratio could give sufficient edge steps for experiments in transmission mode. A few samples with a low metal loading were also probed in florescence mode. Four separate scans were taken for each pellet before merging to give an average XAFS spectra.

For the in-situ experiments, our lab have designed an a two compartment electrochemical XAFS cell[27] to operate in fluorescence mode. The working and counter electrode compartment was separated by a Nafion 117 membrane. The felt containing the synthesized catalysts was cut into a disk shape and loaded to fit the working electrode side before being contacted with a protruding graphite rod (1.57 mm outer diameter, Graphtek LLC). Carbon felt without a metal catalyst was used as the counter electrode. Acetate buffer supporting electrolyte (3 M, pH 5.2) was first degassed, then passed at a flow rate of 0.5 mL/min to the counter and working electrode compartment using a syringe pump. A leak-free Ag/AgCl electrode was used as the reference electrode. A cathodic potential (−0.05 and −0.1 V vs. RHE) was applied before introducing X-rays to the sample. Four separate scans were taken at each potential before merging to give an average XAFS spectra.

XAFS data was processed using Athena.[26,28] Reference channels spectra such as a Pt or Co foils were calibrated first before alignment and merging. A Fourier cut-off of $R_{bkg} = 1$ was used to normalize the merged spectra after inspecting the pre-edge and post-edge regions and subtracting the background. The data was afterwards Fourier transformed in the k range of 3−14 $Å^{-1}$. A linear combination of the metallic Pt foil and PtO_2 standard spectra was used to obtain the percentage of oxidized Pt in the catalysts based on the XANES region.

Artemis software[26,28] was used to fit the Athena processed data to a Pt-Pt, Pt-Co scattering paths for the first and second coordination shell. The scattering paths were generated from FEFF calculations using Pt and Pt_3Co symmetrized CIF files. A Pt foil was used to obtain the amplitude factor S_0^2 from which the Pt-Pt and Pt-Co coordination numbers and bond lengths were obtained.

2.5.2 X-ray Diffraction

X-ray diffraction is a bulk characterization technique that uses X-rays to study the crystallographic structure of materials.[29] It basically takes advantage of two properties of light: (1) light travels in a straight line and (ii) light interferes with itself and with other objects in order of its wavelength. So, when light strikes the crystal of a sample it diffracts in all directions leading to either a constructive or destructive interference (**Figure 2.11**).

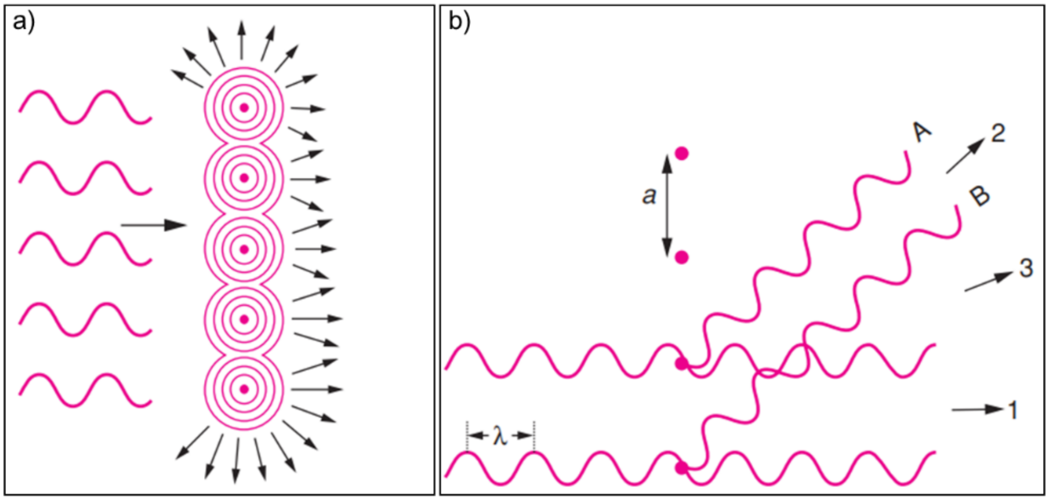

Figure 2.11 Diagram showing the fundamental principle of X-ray diffraction. a) Light strkes an optical grating and scattters in all directions. **b)** Constructive interference in directions 1 and 2 and destructive interference in direction 3. Diagram reproduced from ref [29].

The constructive interference can be described by the Bragg's law which states that constructive interference can only occur when the path between the scattered lights is in multiples of the X-ray wavelength λ. Mathematically Bragg's law is given by **Eq. 2.17**:

$$2d\sin\theta = n\lambda \tag{2.17}$$

Where n is the diffraction order which must be an integer, d is the distance between lattice planes and θ is angle of incidence. In **chapter 6** we performed powder X-ray diffraction on the synthesized alloys on carbon felts after grinding 50 mg of the samples to powder, but for the Pt_xCo_y supported on Vulcan carbon, the powder was directly used. A Rigaku Miniflex X-ray diffractometer with Cu Kα radiation and a Ni filter that has an X-ray wavelength of 1.5406 Å (8034.6 eV) was used. The voltage and current was set to 40 kV and 15 mA, respectively before scanning was carried out at 3°/min with a 0.02° step in the range of $10° < 2\theta < 90°$. The XRD data was compared to Pt and Pt_xCo_y JCPDS standards to identify their crystal structure. Bragg's law was used to obtain the lattice parameter of the samples using the (111) plane at 2θ degrees between 39−42°. Other diffraction peaks should give similar values of the lattice parameter, but we used the (111) peak because it is the most prominent peak. In order to compare the XRD crystallite size with other techniques like transmission electron microscopy, we calculated the XRD crystallite size using the Scherrer equation.[30]:

$$D_{hkl} = \frac{k\lambda}{B\cos\theta} \tag{2.18}$$

Here D_{hkl} is the average crystallite thickness perpendicular to the hkl plane, k is the shape factor (0.88), λ is the wavelength of the X-ray source (i.e., 1.5406 Å for Cu Kα source), B is the full width at half maximum of the diffraction peak. The value of B can be obtained by fitting the diffraction peaks as Gaussian peaks using a graphing software like OriginPro.

2.5.3 Scanning Electron Microscopy

Scanning electron microscopy (SEM) is both an imaging and analytical tool that offers certain advantages over a regular optical microscope because of the higher image resolution. When electron beam hits the sample, both elastic and inelastic scattering occurs.[31] The secondary, backscattered or Auger electrons that come from the sample after this event carry different information about the topography and composition of the sample. These scattered electrons are then collected by detectors and processed to form a magnified image of the sample's surface with the associated chemical analysis of the material. In highlighting the efficacy of our electrode cleaning procedure for surface enhanced Raman spectroscopy, SEM experiments were performed on the Au electrodes at the Michigan Center for Materials Characterization using a TSF Nova 200 Nanolab with an accelerating voltage of 5 kV and a current of 0.4 nA. After the cleaning procedure on the roughened Au electrodes, the samples were immediately immersed in Millipore water to minimize exposure to air. The samples were quickly transferred to the SEM stubs already placed in the instrument vacuum chamber before closing the chamber. All samples were analyzed at a magnification of 50000, a brightness of 40, and a contrast of 70 with only slight differences.

2.5.4 X-ray Photoelectron Spectroscopy

X-ray photoelectron spectroscopy (XPS) is a technique that is based on photoemission, where a core electron in a material is ejected by monoenergetic soft X-rays.[32] Although the X-rays can penetrate deep into the material in the order of 1−10 μm, only photoelectrons ejected near the surface (2−10 nm) can penetrate out of the sample to the detector thus making it a surface sensitive technique. Because an atom's binding energy for its core electron is fixed for a given element, the kinetic energy (i.e., X-ray energy − binding energy) of the ejected electrons can be used to identify the elements present in the sample, and the intensity of these electrons can be used to quantify the relative abundance of the elements.

XPS was used to quantify the presence of adventitious carbon present on roughened Au electrodes after varying chemical and coulometric cleaning procedures were performed. The same samples used for SEM were used for XPS. After SEM, the samples were immediately placed back into Millipore water and then transferred into the sample transfer chamber of the Kratos Axis Ultra X-ray photoelectron spectrometer. The pressure in the analysis chamber was set to 1×10^{-9} Torr. Monochromatic X-rays were generated from an Al source (10 mA and 12 kV, pass energy of 12 eV and step size of 1 eV). A number of locations on each sample were identified where the carbon intensity was highest to measure the effectiveness of the cleaning process. Survey scans were performed for binding energy (BE) range of 0 to 1200 eV to identify the location of the C and Au peaks. Data for C peaks was obtained over 30 sweeps at BE energies of 70−97 eV, while Au peak was obtained over 10 sweeps at BE energies of 275−300 eV (**Figure 2.12**). Counts for C were small compared to Au, so more sweeps were made for C. The CasaXPS software[33] was employed to analyze the XPS spectra, where the intensity of the background subtracted C peaks was used to evaluate the effectiveness of removal of adventitious C after the cleaning procedure.

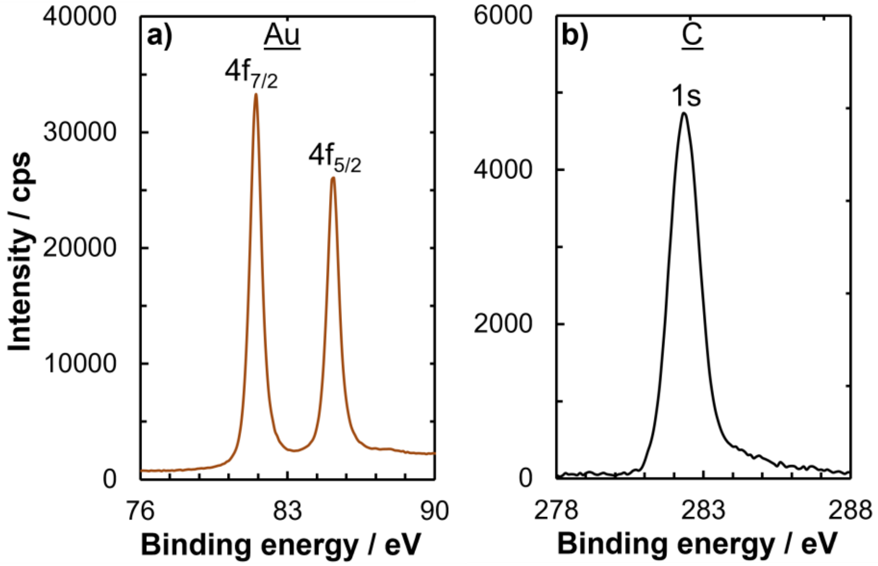

Figure 2.12 Background subtracted XPS spectra for an uncleaned roughned Au electrode showing the Au 4f and C 1s peaks.

2.5.5 Transmission Electron Microscopy

Transmission electron microscopy (TEM) is an imaging technique that uses focused accelerating electrons to pass through a very thin sample. Because the electrons used in this technique are at very high energies and low wavelengths, the image resolution can go as high as sub-Angstrom scales.[34] When the electrons go through the sample and interact with the atoms and electrons, some electrons are scattered and the electrons that pass through the samples are collected downwards on a detector that resolves the signal on a photographic film to give a high-resolution image. Scanning transmission electron microscopy (STEM) is a broader field of TEM that allows for nanoscale elemental and chemical analysis during imaging. We conducted STEM and TEM imaging and experiments in **Chapter 6** using a Thermo Fisher Scientific Talos F200X G2 electron microscope equipped with a Super-X EDX detector and operating at an accelerating voltage of 200 keV. To prepare the sample, a small piece of the catalyst on carbon felt was washed, dried, and ground. Subsequently, 1 mg of the ground catalyst was dissolved in 1 mL of isopropanol and a drop of the resulting suspension was placed on a clean Cu grid. This single drop had sufficient nanoparticles to be counted, however when poor catalyst dispersion occurs, the isopropanol volume was increased accordingly. The Cu grid was left to dry overnight before imaging. ImageJ software was used to count the number and size distribution of the metal nanoparticles.

2.5.6 Inductively Coupled Plasma-Mass Spectrometry

Inductively coupled plasma-mass spectrometry (ICP-MS)[35] is a destructive analytical technique for determining the bulk elemental composition of a material. Here a high temperature plasma usually from argon gas is used to dissociate an already digested sample into atoms and ions. The ions are then separated from the plasma and sent to the mass spectrometer which further separates the ions based on their mass to charge ratio (m/z). The intensity of the ions for a given m/z ratio is proportional to the concentration of the analyte.

In **Chapter 6** we determined the Pt and Co loadings Pt_xCo_y catalysts using a PerkinElmer NexION 2000 ICP-MS. 1 mg of the catalyst was digested in 2 mL aqua regia solution (3:1 molar $HCl:HNO_3$) for at least 48 hours. This solution was further diluted with Millipore water by a factor of 10000 to about 10–20 ppb. 20 ppb bismuth and 20 ppb scandium were co-fed as internal standard in the instrument to normalize Pt and Co intensities, respectively. The concentrations of Pt and Co in the sample were determined by comparing their intensities to calibration standards of Pt and Co of known concentrations (**Figure 2.13**).

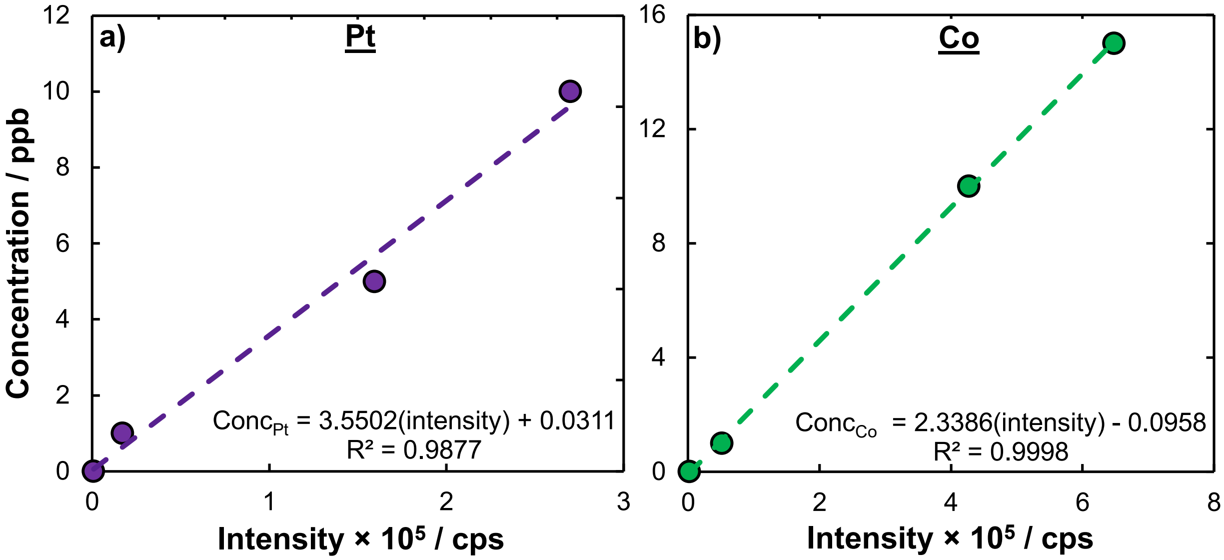

Figure 2.13 ICP-MS calibration plot for Pt and Co standards prepared using water as the solvent.

2.6 Surface Enhanced Raman Spectroscopy (SERS)

In **Chapter 7** we discuss in detail how to investigate the intrinsic organic adsorption strength in different solvents by measuring the vibrational modes of molecules using surface enhanced Raman spectroscopy. Raman spectroscopy is based on the phenomenon of Raman scattering,[36,37] which occurs when incident photons interact with a sample such that a small fraction of the scattered photons undergo energy shifts due to interactions with molecular vibrations. Rayleigh scattering also occurs simultaneously, where the incident photon retains its original energy state (**Figure 2.14**). The energy shift in Raman scattering corresponds to the difference in energy between the ground state and excited state of the molecule (Stokes/anti-Stokes shift). By analyzing the energy shift and intensity of the Raman scattered light, valuable information about molecular structure, chemical composition, adsorption strength and orientation can be obtained.

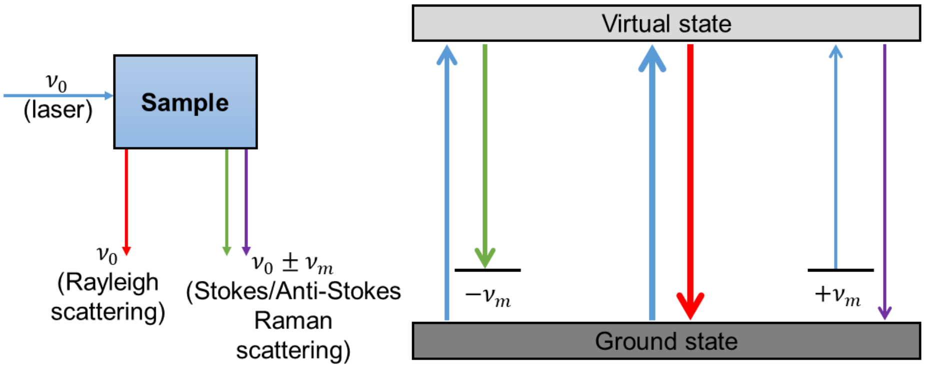

Figure 2.14 Raman scpectroscopy showing the incident ray, Rayleigh scatering where the final state frequency ν is the same as the initial frequency of the photon, Stokes Raman scattering ($\nu < \nu_0$) and Anti-Stokes Raman scattering ($\nu > \nu_0$).

Surface-enhanced Raman spectroscopy (SERS) is a form of Raman spectroscopy used to obtain enhanced vibrational molecular information with single-molecule detection sensitivity.[38–40] The enhanced sensitivity stems from the fact that a nanostructured material (such as silver, gold, or copper) has superior localized surface plasmon resonances. When these materials are illuminated with light of an appropriate wavelength, the optical fields re-radiated by the nanostructure and the incident field can superimpose, redistributing the radiant energy. This process creates regions of concentrated electromagnetic energy (hot spots) where the field amplitude can be enhanced by factors of tens or even hundreds.[38–41] This unique spectroscopic phenomenon has been exploited over several decades for a wide variety of applications in the field of medicine, art, biology, material science, and chemistry.[42–44]

Recently, using SERS to probe photo or electrochemical-induced chemical transformations in real-time has been gaining considerable attention,[45,46] even though experimental clues to that possibility have existed for decades or more.[38,47] A series of recent results indicate that SERS can be used to examine adsorbate molecules of reactants, intermediates, and products for various reactions under applied electrochemical potential,[48] while following the reaction dynamics at electrocatalyst surfaces.[45,49]

2.6.1 Synthesizing Roughened Au Electrodes for SERS

Au films (400 nm) were used as the substrates for SERS experiments performed in this chapter and in **Chapter 7**. The Au films were prepared on silicon wafer with a 10 nm seed layer of Ti in between as adherent for the Au onto the wafer. The lab 18-2 sputtering tool at the Lurie Nanofabrication Lab at the University of Michigan was used for this deposition. The sputtering instrument works by setting a material with very high purity as the target for a gas plasma.[50] The highly energetic atoms of the plasma then collide with the target material. For this deposition a Ti target was first used before a Au target material. This bombardment results in the ejection of atoms from the target material, which then travel to the surface of the Si substrate to form a uniform thin film. In this operation, 10 nm of Ti was first deposited before depositing 400 nm of Au without removing the substrate from the instrument vacuum.

The Au film was then subjected to electrochemical roughening as outlined by Weaver and co-workers[51] to create nanostructures that enhance the signal for SERS. A custom-built electrochemical Raman cell (**Figure 2.15**) was used to perform the roughening procedure. This same cell was used for SERS experiments to evaluate various cleaning procedures discussed later in this chapter and for organic adsorption experiments discussed in **Chapter 7**. This cell geometry produced greater roughening than a typical H cell because by looping the Pt wire counter electrode around the Au working electrode, we were able to obtain a more uniform current density.

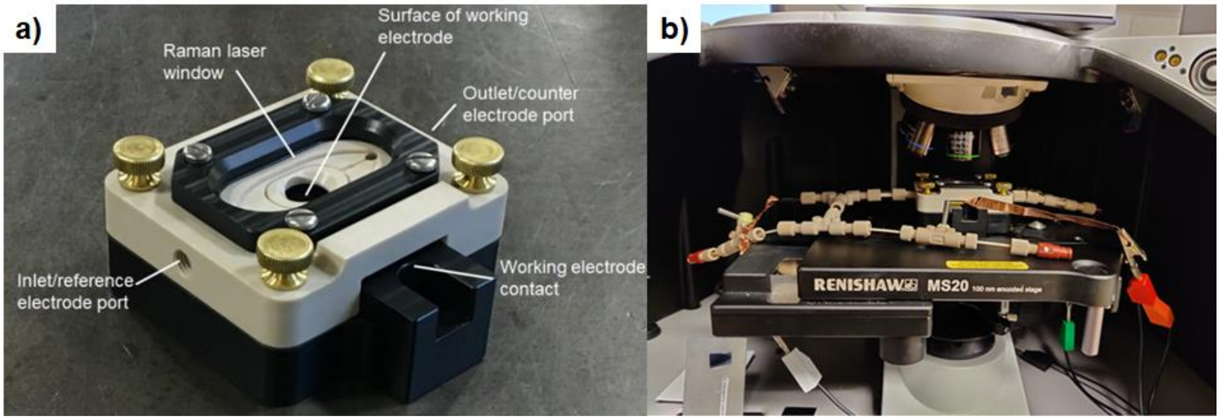

Figure 2.15 Electrochemical Raman cell set up. a) Electrochemical Raman cell showing the working, counter and reference electrode. **b)** Assembly of the cell in a Reinshaw Raman instrument showing the tubing for the flow of electrolyte and the electrode connection from a potentiostat under typical operation.

The Au surface is roughened based on repeated oxidation and reduction cycles that corrode the Au surface and redeposit the Au ions as Au metal.[51] A 0.1 M KCl was used as the supporting electrolyte where the dissolution of Au forms mainly $AuCl_4^-$ at a standard redox potential of 1.0 V vs. SHE.[52]

$$AuCl_4^- + 3\,e^- \rightleftharpoons Au + 4\,Cl^- \tag{2.19}$$

The Au film on the silicon wafer was first cut to a rectangular piece measuring 2.5×1.5 cm. A 5 cm copper electroplating tape (3M) for connection to the potentiostat was attached to the tip of the Au electrode. In order to prevent contact between the copper tape and the electrolyte in the cell, two pieces of clean room vinyl tape from Fisher Scientific (4 cm long, 1 inch wide) were applied to the top and back sides of the electrode. The top tape was first perforated to make a 6 mm diameter hole where the electrolyte would contact the Au film before attaching the back side tape (see **Figure 2.16a**). The exposed Au area was thoroughly cleaned with isopropanol, ethanol, and Millipore water to remove any impurities before performing the roughening. The prepared Au on silicon wafer was then assembled as the working electrode in the electrochemical Raman cell. A Pt wire and a leak free Ag/AgCl were used as the counter and reference electrode respectively. The supporting electrolyte (0.1 M KCl) was filled into the working electrode chamber using a syringe connected to a syringe pump at a low flowrate of 0.5 mL/min to prevent the formation of gas pockets in the chamber. A combination of linear sweep voltammetry (LSV) and chronoamperometry (CA) technique in series was then applied for 50 cycles. In this procedure, LSV was applied for a potential range of −0.255 to 1.245 V vs. Ag/AgCl at a scan rate of 1 V/s (**Figure 2.16b**). A constant potential of 1.245 V was then maintained by applying a CA method for 1.3 seconds. Next another LSV was applied but this time the starting potential was 1.245 V, the end potential was −0.255 V vs. Ag/AgCl and the scan rate was set to 0.5 V/s. Following that, the potential was held constant at −0.255 vs. Ag/AgCl for 30 seconds using the CA technique. These four techniques were repeated in this same order for 50 cycles to prepare a roughened Au sample (see inset image of **Figure 2.16c**). **Figure 2.16c** show the cyclic voltammogram during the LSV procedures where the peaks at 0.80V vs. Ag/AgCl (i.e., 1.0 V vs. SHE) during LSV 2 corresponds to Au metal deposition from $AuCl_4^-$.

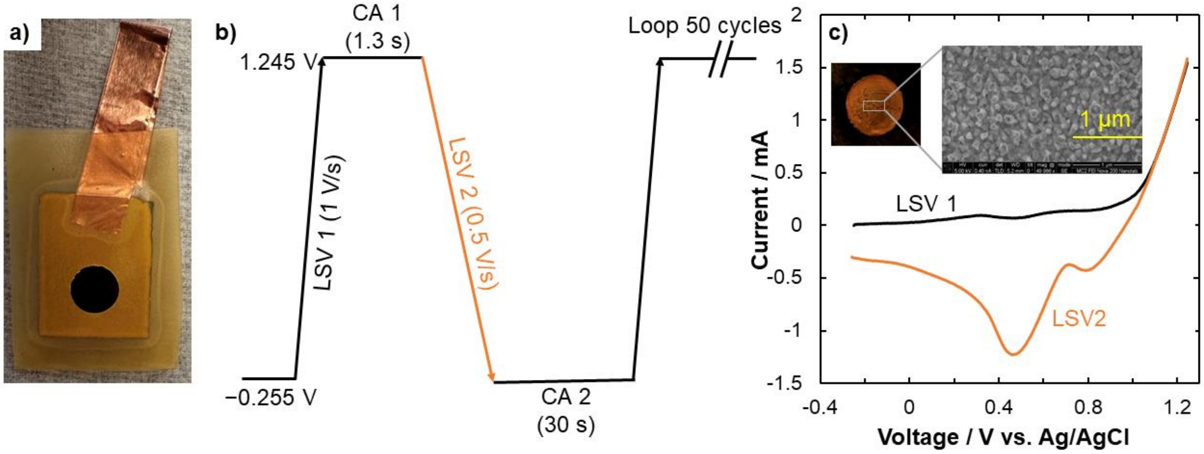

Figure 2.16 Roughening procedure for Au film deposited on silicon wafer. a) Unroughened Au film on silicon wafer with a copper tape and vinyl adhesive tape assembled together showing the exposed Au surface to be roughened. **b)** Schematic of the 4 techniques employed to roughen the Au surface showing the potentials and scan rates used. **c)** Cyclic voltammogram showing the shape of the LSV techniques when the roughening procedure is going on correctly. The inset image in **c)** is the cut out circular portion of the exposed Au showing a roughened structure with a different color than the unroughened part. The associated SEM image (inset) was taken at 50,000 × magnification.

2.6.2 Removing Adventitious carbon on Roughened Electrodes

Despite the importance of SERS enhancements to probe molecular adsorption on surfaces, the degree of surface contamination and its role on electrocatalysis is less investigated. For instance, SERS in the presence of adventitious carbon and other contaminants from ambient air could significantly affect SERS reproducibility and sensitivity.[39,41,53–55] Furthermore, the presence or absence of these contaminants and adventitious carbon at the surfaces could further convolute the already complex SERS spectra and thus misinform correct mechanistic interpretation. A clear understanding of how the presence of adventitious carbon affects SERS spectra will allow us to design reliable, robust SERS substrates for operando investigation and electrocatalysis.

Here, we identify cleaning strategies to remove adventitious carbon from the surface of roughened Au electrodes without any adverse effect on the SERS or electrocatalytic activity of the substrate. We show that over 99% of the adventitious carbon on Au can be removed by piranha or oxygen plasma cleaning. To establish the applicability of our cleaning methods we show that all the modes associated with molecular vibration of a simple supporting electrolyte like perchloric acid (ClO_4^-) molecule are visible on electrodes cleaned using piranha and plasma procedures. The results of the relatively simple cleaning procedure shown here highlight a new approach of creating and maintaining surfaces with high SERS activity for detecting adsorbed molecules.

2.6.2.1 Plasma and Piranha Cleaning to Remove Adventitious Carbon from Roughened Au Electrodes

The presence of carbon on nanostructures for SERS impedes their ability to detect molecular vibrations of adsorbates and intermediates. Carbon has two broad bands between 1000–1800 cm^{-1}, (i) disordered (D) band around 1345 cm^{-1} and (ii) graphitic (G) band around 1585 cm^{-1}.[56–58] The presence of these broad D and G bands makes detecting vibrations for molecules in this range difficult during SERS. Removing these adventitious carbon can help us utilize SERS more effectively to understand adsorption of organic molecules relevant to bio-oil catalysis such as toluene and phenol that has over 10 unique vibrational modes in the range of this adventitious carbon.[59]

Over 99% of the adventitious carbon on the surface of roughened Au can be removed by oxygen plasma or piranha cleaning treatments. The presence of adventitious carbon is identified by the occurrence of broad D and G bands in the Raman spectra of uncleaned roughened Au electrodes in water as shown in **Figure 2.17a**. Apart from the broad D and G bands, several small bands are also observed at lower wavenumbers between 600−1000 cm^{-1} on the uncleaned Au electrodes in **Figure 2.17a** due to the amorphous nature of the carbon and presence of other carbonaceous species like alcohols and ketones.[58,60–63] We performed a series of chemical and electrochemical cleaning procedures to remove these carbonaceous species and observe that cleaning the roughened Au electrodes with oxygen plasma or piranha significantly reduces the SERS intensity of D and G bands as shown in **Figure 2.17a**. Over 99% of the adventitious carbon was removed from the surface relative to uncleaned Au surface with these cleaning procedures (**Figure 2.17b**). On the contrary, electrochemical oxidative cleaning of the roughened Au electrodes shows smaller decrease in intensity of D and G bands as shown in **Figure 2.17a** and removes just about 50% of the carbon content relative to the uncleaned substrate.

The ordered nature of the carbon on the roughened Au surface remains almost unchanged with the cleaning treatments. The unchanging distribution of disordered and graphitic carbon is visible by a similar decline in the intensity of D and G bands with increasing treatment time as shown in **Figure 2.17b**. The similar decline in D and G bands indicates that the structure of the remaining adventitious carbon on roughened Au electrodes remains unchanged with cleaning.

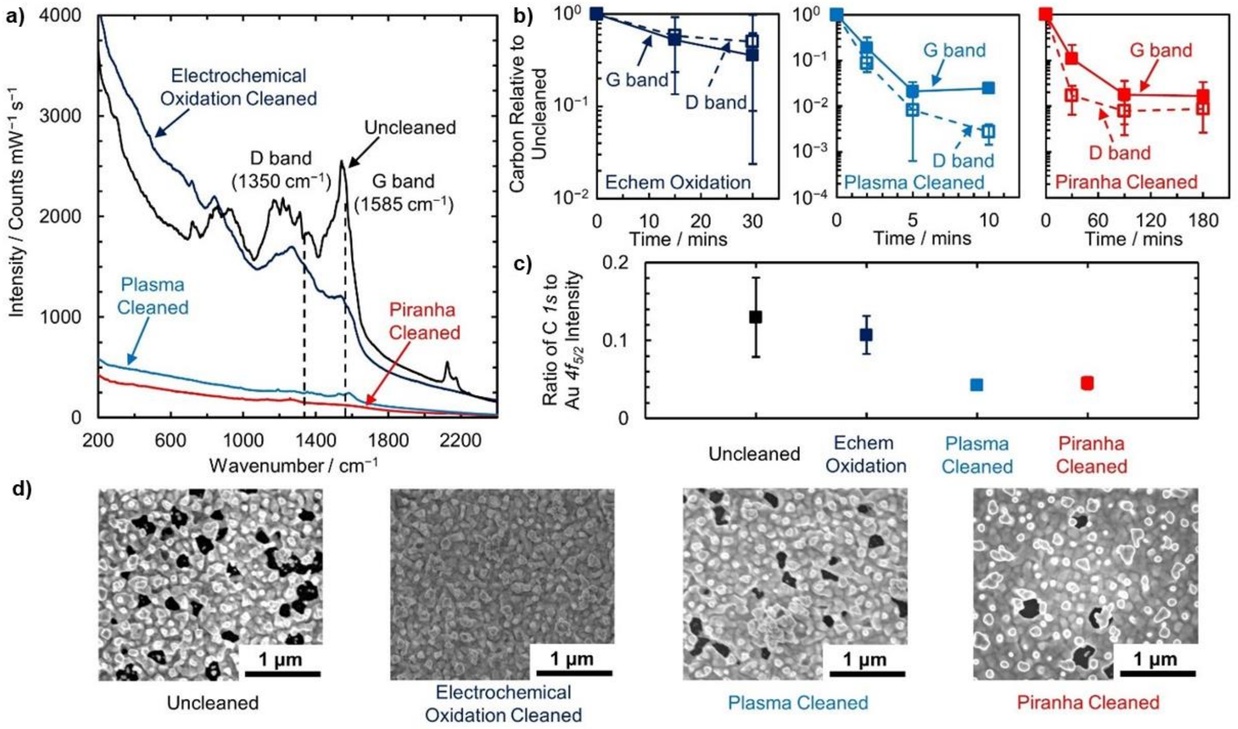

Figure 2.17 SERS spectra and SEM images of electrode surfaces after various cleaning procedures. a) Raman spectra of electrochemically roughened Au electrodes in water for different electrode treatments: (i) Uncleaned and exposed to air (black), (ii) Electrochemical oxidation cleaned i.e; cleaned by applying electrochemical oxidizing potential of 1.8 V for 30 minutes in 0.1 M $KClO_4$ followed by replacing with fresh 0.1 M $KClO_4$ and reducing at −0.8 V for 20 minutes vs. RHE (dark blue), (iii) Piranha cleaned i.e; cleaned with Piranha solution for 90 minutes (red), (iv) Plasma cleaned i.e; cleaned with O_2 plasma for 5 minutes and reduced back to Au (blue). Peaks at 1350 and 1585 cm^{-1} represent D and G bands of carbon respectively. **b)** Carbon content relative to uncleaned Au electrode plotted on a log scale (for D and G band peaks) as a function of cleaning time. **c)** Carbon content relative to gold from XPS. **d)** SEM of uncleaned electrodes and elecrodes prepared after the different cleaning methods. The black portions in the SEM micrographs correspond to pinholes exposing the Si underlayer substrate. All Raman spectra are collected using 785 nm laser at 23.75 mW power, with 16 accumulations, 10 seconds exposure time and high gain using 20x objective lens.

The plasma cleaning removed carbon at a faster rate than piranha cleaning under the conditions used here. For example, the same amount of carbon is removed after 5 min of plasma treatment as is removed after 90 min of piranha cleaning (**Figure 2.17b**). We observe that further decrease in carbon content on plasma and piranha cleaned electrodes is negligible after 5 and 90 mins respectively, as shown in **Figure 2.17b**, hence we use these treatment times in this study. Following plasma and piranha cleaning, the Au surface has a reduced overall carbon content, and any residual carbon is distributed more uniformly than on the uncleaned surface. The lower C to Au XPS signal for the plasma and piranha cleaned electrodes compared to the uncleaned and electrochemical oxidatively cleaned Au surfaces highlights the effectiveness of plasma and piranha cleaning for removing adventitious carbon (**Figure 2.17c)**. XPS samples a wider area of the Au surface in the order of microns compared to Raman that is in the nanometer range. Therefore, the large XPS error bars in **Figure 2.17c** indicate that the carbon distribution in the uncleaned electrodes is not uniform compared to plasma and piranha cleaned electrodes.

Scanning electron microscopy images of the uncleaned and cleaned roughened Au electrodes in **Figure 2.17d** show that the structure of the roughened Au electrodes remains unchanged after the cleaning. Although there are no visible changes in the microstructure of Au electrodes after cleaning, there is a decline in the number and aspect ratio of the nanostructures on the surface of plasma and piranha electrodes. This decline can slightly reduce the electrochemically active surface area and modify facet distribution leading to changes in activity for a structure sensitive reaction like phenol ECH.[64] The results in **Figure 2.17** provide conclusive evidence that carbon content on roughened Au electrodes is significantly reduced after oxygen plasma and piranha cleaning. The plasma and piranha cleaning lead to a 100-fold removal of adventitious carbon and uniform distribution of the remaining adventitious carbon. In the next section, we investigate whether the plasma and piranha cleaning techniques will improve SERS signals for a simple supporting electrolyte molecule such as perchlorate (ClO_4^-).

2.6.2.2 Impact of Cleaning on SERS Signal of Adsorbates

Stretch modes (ν) and deformation modes (δ) of the ClO_4^- molecule are clearly distinguishable on the oxygen plasma and piranha cleaned Au electrodes. The ClO_4^- molecule has four Raman active modes, characteristic symmetric stretch mode ($\nu_{\mathrm{s,ClO_4^-}}$) at 933 cm^{-1}, asymmetric stretch mode at 1113 cm^{-1} ($\nu_{\mathrm{as_1,ClO_4^-}}$) with a small shoulder at 1272 cm^{-1} ($\nu_{\mathrm{as_2,ClO_4^-}}$), symmetric deformation mode ($\delta_{\mathrm{s,ClO_4^-}}$) at 630 cm^{-1}, and asymmetric deformation mode ($\delta_{\mathrm{as,ClO_4^-}}$) at 460 cm^{-1}.[65–69] All the four Raman active modes of ClO_4^- are clearly visible on the plasma and piranha cleaned electrodes in **Figure 2.18a**. However, due to the overlapping signals from adventitious carbon on uncleaned Au electrode, the $\nu_{\mathrm{as}_1,\mathrm{ClO}_4^-}$ mode along with $\nu_{\mathrm{as}_2,\mathrm{ClO}_4^-}$ is not clearly identifiable as shown in **Figure 2.18a**. **Figure 2.18b** shows a zoomed version of the SERS spectra around 1000−1200 cm^{-1} revealing that the $\nu_{\mathrm{as}_1,\mathrm{ClO}_4^-}$ is clearly identifiable on plasma and piranha cleaned electrodes. Although the ClO_4^- deformation modes (i.e., $\delta_{\mathrm{s},\mathrm{ClO}_4^-}$ and $\delta_{\mathrm{as},\mathrm{ClO}_4^-}$), seem visible on the uncleaned Au electrodes in **Figure 2.18a**, the signals from adventitious carbon makes it difficult to clearly attribute those peaks to ClO_4^-.

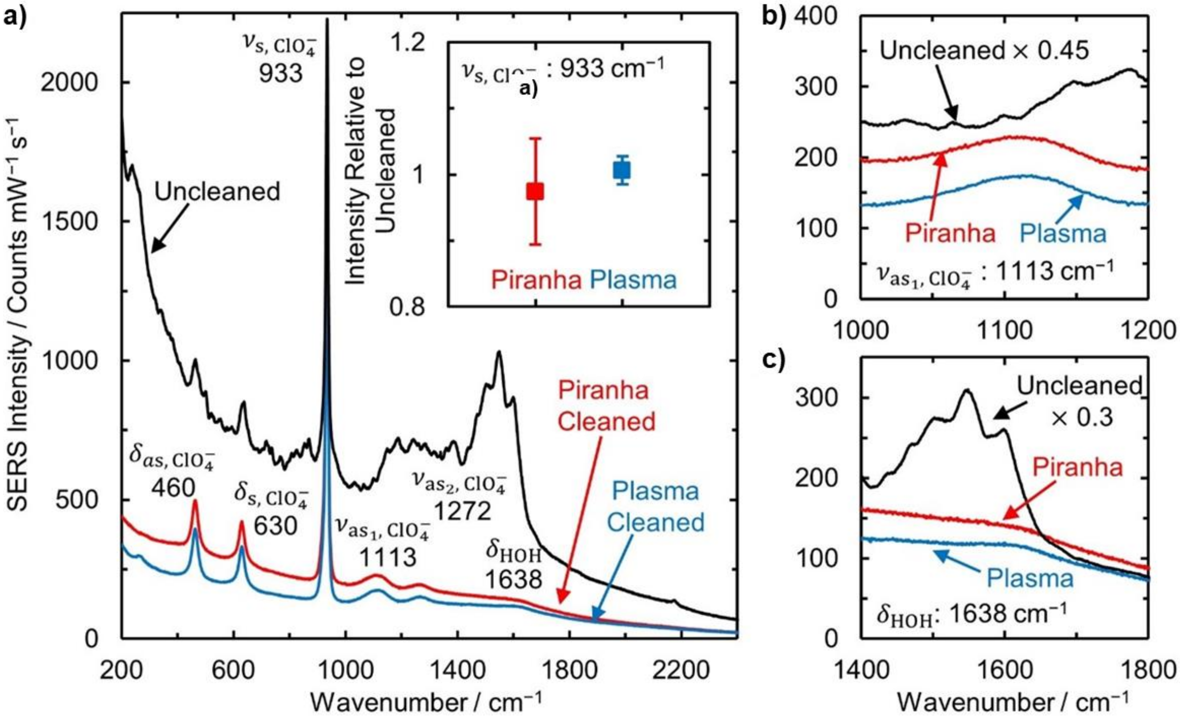

Figure 2.18 SERS spectra for ClO_4^- in water after the different cleaning procedures. a) Suface enhanced Raman spectra of $HClO_4$ (4 M) showing the locations of the different vibrational modes of ClO_4^- and H_2O molecules. Inset shows the background corrected intensity of the symmetric stretch mode of ClO_4^- ($\boldsymbol{\nu_{\mathrm{s},\mathrm{ClO}_4^-}}$) at 933 cm^{-1} on piranha and plasma cleaned electrode relative to the uncleaned roughened Au electrode. Error bars are evaluated by taking the average of intensities relative to uncleaned at five different locations on the cleaned sample. **b)** Asymmetric stretch mode of ClO_4^- ($\boldsymbol{\nu_{\mathrm{as}_1,\mathrm{ClO}_4^-}}$) at 1113 cm^{-1}. **c)** Deformation mode of water ($\boldsymbol{\delta_{\mathrm{HOH}}}$) at 1638 cm^{-1} visible on the plasma and piranha cleaned electrodes but not on the uncleaned Au electrodes. The $HClO_4$ spectra on the uncleaned electrode is multiplied by an approriate factor (e.g., 0.45 for b) and 0.3 for c)) for making intensities comparable to plasma and piranha cleaned electrodes. All Raman spectras are collected using 785 nm laser at 23.75 mW power, with 16 accumulations, 10 seconds exposure time and high gain using a 20x objective lens.

The oxygen plasma and piranha cleaning does not reduce the SERS enhancement factors of the roughened Au electrodes. **Figure 2.18a** inset image shows the constant SERS intensity of the characteristic symmetric $\nu_{\mathrm{s,ClO_4^-}}$ stretch mode on the piranha and plasma cleaned electrodes relative to uncleaned Au electrodes. The constant SERS intensity after treatment is consistent with the unchanging microstructure of the Au electrode as seen from the SEM micrographs in **Figure 2.17d**. Plasma and piranha cleaned electrodes are also able to detect the water deformation mode. The water deformation mode (δ_{HOH}) occurs around 1638 $\mathrm{cm^{-1}}$.[48,67,68,70] **Figure 2.18a** clearly shows that the δ_{HOH} is visible on plasma and piranha cleaned electrodes and not on uncleaned electrodes. The expanded view of the region surrounding δ_{HOH} in **Figure 2.18c** also shows the presence of small additional peaks on the uncleaned electrode due to the presence of adventitious carbon from the surroundings.

2.6.3 Depositing Pinhole-Free Thin Films of Transition Metals on Roughened Au

After synthesizing the roughened Au electrodes and performing the rigorous cleaning procedure to remove adventitious carbon as discussed above, SERS experiments will be more informative on surfaces such as Pt group metals (Pt, Rh, Ni, Pd, Ru) that are catalytically active for hydrogenation. Pt group metals are inherently unable to perform SERS, but we use either electrodeposition or atomic layer deposition to make thin films of these catalytically relevant metals on the cleaned SERS active Au surface.

2.6.3.1 Electrodeposition

Metal electrodeposition is a cathodic process where metal ions typically from a salt solution are reduced to a metallic state. A more negative potential than the standard reduction potential for the metal to be deposited is a thermodynamic requirement for this procedure.[2] If the surface for deposition provides a more favorable thermodynamics for deposition at potentials more positive than the standard reduction potential this is otherwise called underpotential deposition as we have seen for adsorbed hydrogen in the H_{upd} region. We performed electrodeposition of Pt following a procedure outlined by Weaver and coworkers[71] where $PtCl_6^-$ were reduced from hydrogen hexachloroplatinate (IV) to Pt metal.

$$PtCl_6^- + 4\ e^- \rightleftharpoons Pt_{(M)} + 6Cl^- \quad (1.435\ V) \tag{2.20}$$

Here the cleaned roughened Au was rinsed with Millipore water and assembled in the electrochemical Raman cell. A concentration of 1×10^{-4} M of H_2PtCl_6 was introduced into the cell using a syringe pump flowing at 0.5 mL/min. The counter electrode was a Pt wire loop (0.25 mm diameter) and a Ag/AgCl electrode was used as the reference. A constant potential of 0.186 V vs. Ag/AgCl was applied for two minutes to deposit a few monolayers of Pt. The Cyclic voltammogram in **Figure 2.19** show features such as the typical Pt H_{upd}, and Pt oxidation and reduction peaks indicating Pt metal was clearly deposited. We tried a constant current deposition as described in ref [72] even at a different constant current density but was unable to deposit Pt, Pd, Rh or Ru from their chloride salts. The constant current would have been advantageous to carefully control the quantity of charge supplied to deposit an accurate film thickness.

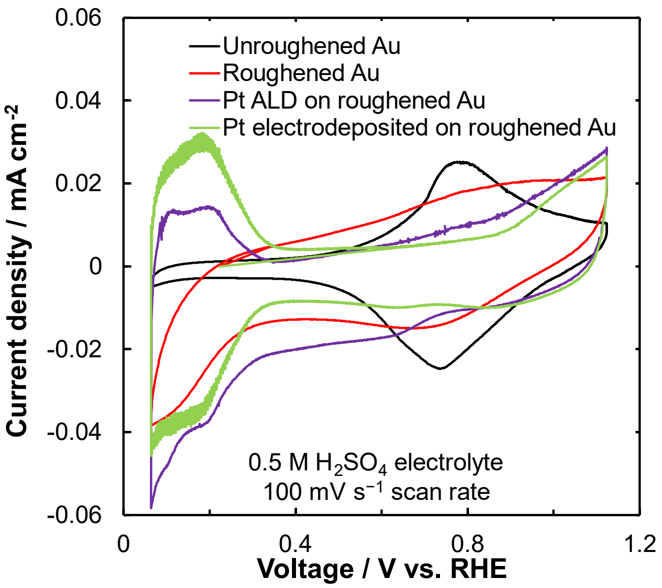

Figure 2.19 Cyclic voltammogram of unroughened Au, roughened Au, electrodeposited Pt and atomic layer deposited Pt. CVs were performed in 0.5 M H_2SO_4 supporting electrolyte and 23.3°C at a scan rate of 100 mV s^{-1}.

2.6.3.2 Atomic Layer and Physical Vapor Deposition

While electrodeposition has been successful in depositing thin Pt films, we have not been able to deposit other metals of interest, such as Ni, Rh, Ru, and Pd using this technique. Atomic layer deposition (ALD)[73] and physical vapor depositions (PVD)[74] are other routes to deposit these metals on the roughened Au. The ALD technique is another class of chemical vapor deposition that creates conformal films with precise thickness. We used the Veeco Fiji ALD tool at the Lurie Nanofabrication lab to deposit about 5 monolayers of Pt on roughened Au surfaces and show in **Figure 2.19** that the ALD Pt show CV features similar to electrodeposited Pt. Despite the advantages of ALD, this Veeco Fiji ALD has seven recipes for metal oxides and only one recipe to deposit Pt as the only metal, which presents a challenge.

Physical vapor deposition is not as conformal as ALD, especially for thin films (5–10 monolayers), but they can deposit Ni and Pd films for which an ALD recipe is unavailable. We used the Lab 18-2 tool as well as the PVD 75 magnetron proline to deposit thin films of Ni by modifying the number of deposition cycles. The characterization data for the tool was used to determine the number of cycles required to obtain a given thickness after the metal nucleation.

2.6.3.3 Verifying the Formation of Pinhole-Free Surfaces

While we have evidence from cyclic voltammetry that we can deposit thin films of transition metals on the roughened and cleaned Au surfaces, these films might be too thin where some of the Au surfaces may become exposed (pinholes) which can obfuscate SERS spectra. For example, if the goal of probing the Pt-organic intrinsic bond strength is plagued with too many Au pinholes, then the spectra will be influenced by the Au-organic bond strength which may lead to wrong interpretation of the Pt-organic bond strength. To probe the surface pinholes, we used the unique vibrational information of carbon monoxide intramolecular C−O stretch (ν_{CO}) and metal−CO stretch (ν_{M-CO}) frequencies. CO adsorption has a unique feature, ν_{CO} at ∼2115 cm^{-1} only on Au,[72,75] which can be used to distinguish surfaces containing exposed Au.

For this check, Pt thin film deposited on roughened Au were assembled in the Raman cell, CO was sparged at a flow rate of 50 mL/min for 30 minutes to a sealed beaker containing 10 mL of Millipore water in a fumehood. The CO-sparged water was quickly transferred to the assembled cell and sealed properly. Raman measurements were immediately performed in static mode at high gain with an exposure time of 20 seconds in the wavenumber range of 1700−2300 cm^{-1}.

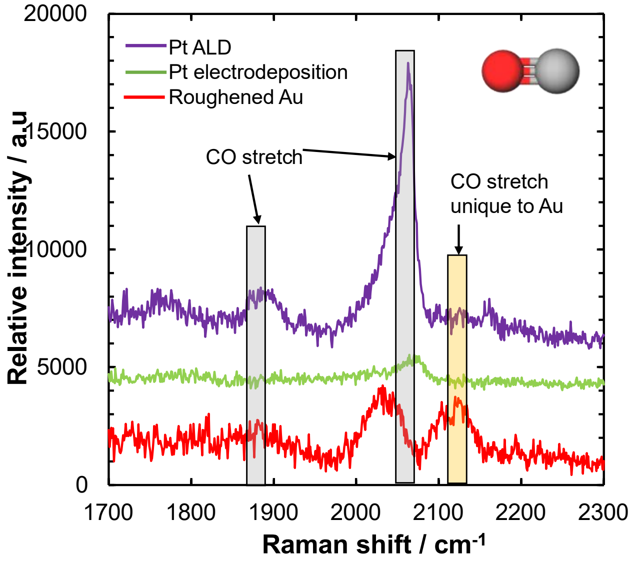

Figure 2.20 Surface enhanced Raman spectroscopy of carbon monoxide dissolved in water on roughened Au, electrodeposited Pt and atomic layer deposited Pt.

2.6.4 Measuring SERS Spectra

Raman measurements for evaluating the efficacy of our cleaning procedure discussed in this chapter or for performing adsorption studies in different solvents in **Chapter 7** were conducted in our custom-built electrochemical Raman cell (**Figure 2:15**) using a Renishaw inVia Raman microscope. The roughened Au or deposited metal on Au electrode was used as the working electrode, Pt wire (0.25 mm diameter) was used as the counter electrode and a 1 mm leakless Ag/AgCl was used as the reference electrode. The Raman cell has an active volume of ~1.5 mL and uses a quartz window where the supporting electrolyte can be filled to be in contact with the working electrode. All the measurements associated with carbon and perchlorate were conducted using 785 nm laser. Extended mode measurements are conducted between 200–2400 cm^{-1} at 23.75 mW laser power using a 20x objective lens. 16 accumulations were taken for each spectrum with 10 seconds exposure time and high gain. Mapping measurements were conducted on at least three 400 μm × 200 μm regions with grid spacing of 5 μm (total of 3321 points for each region) at 47.5 mW laser power, with 1 accumulation, 0.5 seconds exposure time and high gain using a 20x objective lens. The measurements associated with phenol adsorption measurements in different solvents were conducted using a 633 nm laser. Measurements were conducted in both static and extended mode between 200−2400 cm^{-1} at 8.75 mW laser power, with 16 accumulations for each spectrum, 10 seconds exposure time and high gain when possible using 20x objective lens. All spectra were collected and processed (smoothed and baseline corrected) using the WiRE 5.3 software package (Renishaw). Initial spectra calibrations were performed using a silicon standard in static mode.

2.7 Hydrogenation Rate Measurements

2.7.1 Electrocatalytic Hydrogenation

In **Chapter 6**, ECH was performed on synthesized Pt_xCo_y/felt catalysts using a two-compartment batch electrolysis cell where the cathodic and anodic compartments were separated with a Nafion 117 membrane. The Pt_xCo_y/felt catalysts were attached to a 3 mm diameter graphite rod (Sigma Aldrich, 99.99%) and used as the working electrode in the 140 mL cathodic compartment. Acetate buffer (3M, pH 5.2) sparged with N_2 was used as the supporting electrolyte in both cathodic and anodic compartments. A Ag/AgCl double junction electrode was used as the reference electrode and the counter electrode was a 3 mm diameter graphite rod (Sigma Aldrich, 99.99%). To perform ECH, the desired potential was first applied for 1 hr to the working electrode to polarize the catalyst surface and saturate the solution with in-situ generated H_2. Phenol sparged with N_2 was added to the cathodic compartment to achieve 20 mM phenol concentration before performing ECH at a fixed potential of either −0.1, −0.15 and −0.2 V vs. RHE using a Bio-Logic VSP-300. The series resistance was automatically compensated at 85% using impedance spectroscopy at a frequency of 200 kHz and the remaining 15% was manually corrected to give ±10 mV of the reported iR-free applied potentials. No change in the pH of acetate buffer plus phenol solution before and after performing ECH for 2 hr was observed, indicating sufficient buffering capacity.

2.7.2 Product Quantification using Gas Chromatography (GC)

A 1 mL aliquot was taken from the cathodic compartment every 30 mins to monitor ECH reaction progress. ECH products (i.e., cyclohexanone and cyclohexanol) and the phenol reactant were extracted from the aqueous supporting electrolyte into an organic phase using through three sequential liquid-liquid extractions with ethyl acetate as the solvent. For every extraction step, about 5 mg of sodium chloride was added to the aliquot before mixing with 1 mL of pure ethyl acetate to aid separation of the organic and aqueous phase. Three extractions were sufficient to transfer all organics from the aqueous-phase aliquot to the organic phase because no phenol or product was detected upon additional extraction and the extraction points shown as blue points in **Figure 2.21** matches the expected concentration in the calibration plot. Any water present in the organic phase was removed using anhydrous Na_2SO_4 (Sigma Aldrich 99%). Dimethoxybenzene (DMB) was used as an external standard, where 10 µL DMB was mixed with 1 mL of the dried organic phase before injecting 1 µL of the mixture to an Agilent Varian 450 gas chromatograph equipped with a flame ionization detector. The concentration of reacted phenol and associated products were obtained by using both the measured area of the GC peaks associated with the molecule of unknown concentration and the calibration equation in **Figure 2.21**. ECH was performed at less than 10% conversion and carbon balances were greater than 90%. The turnover frequency for each Pt_xCo_y/felt catalyst was calculated from the rate of cyclohexanol and cyclohexanone formed per surface Pt atom estimated from the hydrogen underpotential deposition.

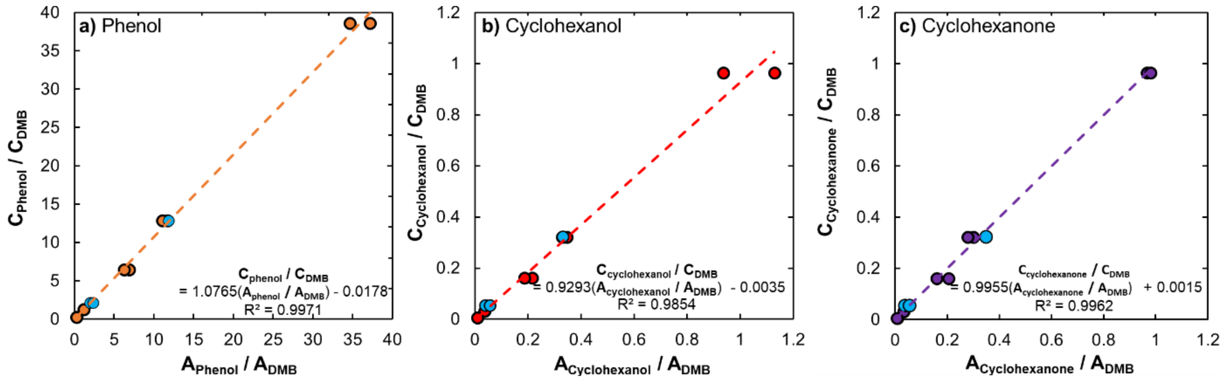

Figure 2.21 Gas chromatrophy calibration for quantifying phenol and the associated products from ECH. a) phenol **b)** cyclohexanol **c)** cyclohexanone. The blue data points are the liquid-liquid extraction data, showing that all the reactants and products were mostly transferred from the aqueous to the organic phase.

2.8 References

(1) Kissinger, P. T.; Heineman, W. R. Cyclic Voltammetry. *J. Chem. Educ.* **1983**, *60*, 702–706.

(2) Bard, A. J.; Faulkner, L. R. *Electrochemical Methods: Fundamentals and Applications (Vol 2)*; Wiley: New York, **2001**.

(3) Łukaszewski, M.; Soszko, M.; Czerwiński, A. Electrochemical Methods of Real Surface Area Determination of Noble Metal Electrodes – an Overview. *Int. J. Electrochem. Sci* **2016**, 4442–4469.

(4) Jerkiewicz, G. Electrochemical Hydrogen Adsorption and Absorption. Part 1: Under-Potential Deposition of Hydrogen. *Electrocatalysis* **2010**, *1*, 179–199.

(5) Biegler, T.; Rand, D. A. J.; Woods, R. Limiting Oxygen Coverage on Platinized Platinum; Relevance to Determination of Real Platinum Area by Hydrogen Adsorption. *J. Electroanal. Chem. Interfacial Electrochem.* **1971**, *29*, 269–277.

(6) Bett, J.; Kinoshita, K.; Routsis, K.; Stonehart, P. A Comparison of Gas-Phase and Electrochemical Measurements for Chemisorbed Carbon Monoxide and Hydrogen on Platinum Crystallites. *J. Catal.* **1973**, *29*, 160–168.

(7) Woods, R.; Bard, A. J. *Electroanalytical Chemistry: A Series of Advances*; Marcel Dekker and Basel: New York, **1976**; Vol. 9.

(8) Rand, D. A. J.; Woods, R. The Nature of Adsorbed Oxygen on Rhodium, Palladium and Gold Electrodes. *J. Electroanal. Chem. Interfacial Electrochem.* **1971**, *31*, 29–38.

(9) Garrone, E.; Bolis, V.; Fubini, B.; Morterra, C. Thermodynamic and Spectroscopic Characterization of Heterogeneity among Adsorption Sites: CO on Anatase at Ambient Temperature. *Langmuir* **1989**, *5*, 892–899.

(10) Vassiliev, Y. B.; Bagotzky, V. S.; Khazova, O. A.; Cherny, V. V.; Meretsky, A. M. Mechanism of Adsorption, Electroreduction and Hydrogenation of Compounds with Ethylenic Bonds on Platinum and Rhodium: Part I. Kinetics of Adsorption and Electroreduction. *J. Electroanal. Chem. Interfacial Electrochem.* **1979**, *98*, 253–272.

(11) Bockris, J. O.; Green, M.; Swinkels, D. A. J. Adsorption of Naphthalene on Solid Metal Electrodes. *J. Electrochem. Soc.* **1964**, *111*, 743–748.

(12) Bockris, J. O.; Jeng, K. T. In-Situ Studies of Adsorption of Organic Compounds on Platinum Electrodes. *J. Electroanal. Chem.* **1992**, *330*, 541–581.

(13) Singh, N.; Sanyal, U.; Fulton, J. L.; Gutiérrez, O. Y.; Lercher, J. A.; Campbell, C. T. Quantifying Adsorption of Organic Molecules on Platinum in Aqueous Phase by Hydrogen

Site Blocking and in Situ X-ray Absorption Spectroscopy. *ACS Catal.* **2019**, *9*, 6869–6881.

(14) Campbell, C. T.; Sellers, J. R. V. The Entropies of Adsorbed Molecules. *J. Am. Chem. Soc.* **2012**, *134*, 18109–18115.

(15) Sander, R. *Henry's Law Constant in NIST Chemistry WebBook, NIST Standard Reference Database Number 69*; P.J.Linstrom, W.G.Mallard, Eds.; National Institute of Standards and Technology: Gaithersburg MD, 20899, **2018**.

(16) Kudchadker, S. A.; Kudchadker, A. P.; Wilhoit, R. C.; Zwolinski, B. J. Ideal Gas Thermodynamic Properties of Phenol and Cresols. *J. Phys. Chem. Ref. Data* **1978**, *7*, 417–423.

(17) Guedes, R. C.; Coutinho, K.; Costa Cabral, B. J.; Canuto, S. Differential Hydration of Phenol and Phenoxy Radical and the Energetics of the Phenol O−H Bond in Solution. *J. Phys. Chem. B* **2003**, *107*, 4304–4310.

(18) Kühne, R.; Ebert, R.-U.; Schüürmann, G. Prediction of the Temperature Dependency of Henry's Law Constant from Chemical Structure. *Environ. Sci. Technol.* **2005**, *39*, 6705–6711.

(19) Howard, P. H.; Meylan, W. The Physical Properties Database (PHYSPROP). Syracuse Research Corp: Syracuse, NY **2006**.

(20) Grote, F.; Ermilova, I.; Lyubartsev, A. P. Molecular Dynamics Simulations of Furfural and 5-Hydroxymethylfurfural at Ambient and Hydrothermal Conditions. *J. Phys. Chem. B* **2018**, *122*, 8416–8428.

(21) Abraham, M. H.; Whiting, G. S.; Fuchs, R.; Chambers, E. J. Thermodynamics of Solute Transfer from Water to Hexadecane. *J. Chem. Soc. Perkin Trans. 2* **1990**, *2*, 291–300.

(22) Costa, F. S.; Ermelinda Eusébio, M.; Redinha, J. S.; Leitão, M. L. P. Enthalpies of Solvation of Hydroxyl Cyclohexane Derivatives in Different Solvents. *J. Chem. Thermodyn.* **1999**, *31*, 895–903.

(23) Campbell, C. T.; Sprowl, L. H.; Árnadóttir, L. Equilibrium Constants and Rate Constants for Adsorbates: Two-Dimensional (2D) Ideal Gas, 2D Ideal Lattice Gas, and Ideal Hindered Translator Models. *J. Phys. Chem. C* **2016**, *120*, 10283–10297.

(24) Carey, S. J.; Zhao, W.; Mao, Z.; Campbell, C. T. Energetics of Adsorbed Phenol on Ni(111) and Pt(111) by Calorimetry. *J. Phys. Chem. C* **2019**, *123*, 7627–7632.

(25) Newville, M. 2. Fundamentals of XAFS. In *Spectroscopic Methods in Mineralogy and Material Sciences*; DE GRUYTER, **2014**; pp 33–74.

(26) Ravel, B.; Newville, M. ATHENA , ARTEMIS , HEPHAESTUS : Data Analysis for X-ray Absorption Spectroscopy Using IFEFFIT. *J. Synchrotron Radiat.* **2005**, *12*, 537–541.

(27) Singh, N.; Nguyen, M. T.; Cantu, D. C.; Mehdi, B. L.; Browning, N. D.; Fulton, J. L.; Zheng, J.; Balasubramanian, M.; Gutiérrez, O. Y.; Glezakou, V. A.; Rousseau, R.; Govind, N.; Camaioni, D. M.; Campbell, C. T.; Lercher, J. A. Carbon-Supported Pt during Aqueous Phenol Hydrogenation with and without Applied Electrical Potential: X-ray Absorption and Theoretical Studies of Structure and Adsorbates. *J. Catal.* **2018**, *368*, 8–19.

(28) Newville, M. IFEFFIT : Interactive XAFS Analysis and FEFF Fitting. *J. Synchrotron Radiat.* **2001**, *8*, 322–324.

(29) Dollase, W. A. Solid State Chemistry and Its Applications by A. R. West. *Acta Crystallogr. Sect. B Struct. Sci.* **1985**, *41*, 454–455.

(30) Patterson, A. L. The Scherrer Formula for X-ray Particle Size Determination. *Phys. Rev.* **1939**, *56*, 978–982.

(31) Reimer, L. Scanning Electron Microscopy: Physics of Image Formation and Microanalysis,

Second Edition. *Meas. Sci. Technol.* **2000**, *11*, 1826–1826.

(32) Moulder, J. F.; Stickle, W. F.; Sobol, P. E.; Bomben, K. D. *Handbook of X-ray Photoelectron Spectroscopy*; Chastain, J., King, R. C., Eds.; Physical Electronics Division, Perkin-Elmer Corporation: Minnesota, **1992**; Vol. 40.

(33) Fairley, N. CasaXPS. Casa software LTD **2011**.

(34) Woods, A. E.; Stirling, J. W. Transmission Electron Microscopy. In *Bancroft's Theory and Practice of Histological Techniques*; Elsevier, **2019**; pp 434–475.

(35) Thomas, R. *Practical Guide to ICP-MS*; CRC Press, **2008**.

(36) Long, D. A. *Raman Spectroscopy*; New York, **1977**.

(37) Fleischmann, M.; Hendra, P. J.; McQuillan, A. J. Raman Spectra of Pyridine Adsorbed at a Silver Electrode. *Chem. Phys. Lett.* **1974**, *26*, 163–166.

(38) Li, M.-D.; Cui, Y.; Gao, M.-X.; Luo, J.; Ren, B.; Tian, Z.-Q. Clean Substrates Prepared by Chemical Adsorption of Iodide Followed by Electrochemical Oxidation for Surface-Enhanced Raman Spectroscopic Study of Cell Membrane. *Anal. Chem.* **2008**, *80*, 5118–5125.

(39) De, R.; Shin, Y. S.; Lee, C. L.; Oh, M. K. Long-Standing Stability of Silver Nanorod Array Substrates Functionalized Using a Series of Thiols for a SERS-Based Sensing Application. *Appl. Spectrosc.* **2016**, *70*, 1137–1149.

(40) Gonçalves, M. R.; Enderle, F.; Marti, O. Surface-Enhanced Raman Spectroscopy of Dye and Thiol Molecules Adsorbed on Triangular Silver Nanostructures: A Study of Near-Field Enhancement, Localization of Hot-Spots, and Passivation of Adsorbed Carbonaceous Species. *J. Nanotechnol.* **2012**, 1–15.

(41) Moran, C. H.; Xia, X.; Xia, Y. Improving Correlated SERS Measurements with Scanning Electron Microscopy: An Assessment of the Problem Arising from the Deposition of Amorphous Carbon. *Phys. Chem. Chem. Phys.* **2013**, *15*, 5400–5406.

(42) Cailletaud, J.; De Bleye, C.; Dumont, E.; Sacré, P. Y.; Netchacovitch, L.; Gut, Y.; Boiret, M.; Ginot, Y. M.; Hubert, P.; Ziemons, E. Critical Review of Surface-Enhanced Raman Spectroscopy Applications in the Pharmaceutical Field. *J. Pharm. Biomed. Anal.* **2018**, *147*, 458–472.

(43) Pozzi, F.; Leona, M. Surface-Enhanced Raman Spectroscopy in Art and Archaeology. *J. Raman Spectrosc.* **2016**, *47*, 67–77.

(44) Muehlethaler, C.; Leona, M.; Lombardi, J. R. Review of Surface Enhanced Raman Scattering Applications in Forensic Science. *Analytical Chemistry*. American Chemical Society January **2016**, pp 152–169.

(45) Dix, S. T.; Linic, S. In-Operando Surface-Sensitive Probing of Electrochemical Reactions on Nanoparticle Electrocatalysts : Spectroscopic Characterization of Reaction Intermediates and Elementary Steps of Oxygen Reduction Reaction on Pt. *J. Catal.* **2021**, *396*, 32–39.

(46) Han, X. Bin; Kannari, K.; Ye, S. In Situ Surface-Enhanced Raman Spectroscopy in Li–O2 Battery Research. *Curr. Opin. Electrochem.* **2019**, *17*, 174–183.

(47) Shi, C.; Zhang, W.; Birke, R. L.; Lombardi, J. R. Detection of Short-Lived Intermediates in Electrochemical Reactions Using Time-Resolved Surface-Enhanced Raman Spectroscopy. *J. Phys. Chem* **1990**, *94*, 4766–4769.

(48) Wang, Y.-H.; Zheng, S.; Yang, W.-M.; Zhou, R.-Y.; He, Q.-F.; Radjenovic, P.; Dong, J.-C.; Li, S.; Zheng, J.; Yang, Z.-L.; Attard, G.; Pan, F.; Tian, Z.-Q.; Li, J.-F. In Situ Raman Spectroscopy Reveals the Structure and Dissociation of Interfacial Water. *Nature* **2021**, *600*, 81–86.

(49) Meng, Y.; Zhang, X.; Hung, W.-H.; He, J.; Tsai, Y.-S.; Kuang, Y.; Kenney, M. J.; Shyue, J.-J.; Liu, Y.; Stone, K. H.; Zheng, X.; Suib, S. L.; Lin, M.-C.; Liang, Y.; Dai, H. Highly Active Oxygen Evolution Integrated with Efficient CO2 to CO Electroreduction. *Proc. Natl. Acad. Sci.* **2019**, *116*, 23915–23922.

(50) Sigmund, P. Theory of Sputtering. I. Sputtering Yield of Amorphous and Polycrystalline Targets. *Phys. Rev.* **1969**, *184*, 383–416.

(51) Gao, P.; Patterson, M. L.; Tadayyoni, M. A.; Weaver, M. J. Gold as a Ubiquitous Substrate for Intense Surface-Enhanced Raman Scattering. *Langmuir* **1985**, *1*, 173–176.

(52) Vanysek, P. Electrochemical Series. In *CRC handbook of chemistry and physics*; **2000**; pp 8–33.

(53) Matikainen, A.; Nuutinen, T.; Itkonen, T.; Heinilehto, S.; Puustinen, J.; Hiltunen, J.; Lappalainen, J.; Karioja, P.; Vahimaa, P. Atmospheric Oxidation and Carbon Contamination of Silver and Its Effect on Surface-Enhanced Raman Spectroscopy (SERS). *Sci. Rep.* **2016**, *6*, 37192.

(54) Šubr, M.; Petr, M.; Peksa, V.; Kylián, O.; Hanuš, J.; Procházka, M. Ag Nanorod Arrays for SERS: Aspects of Spectral Reproducibility, Surface Contamination, and Spectral Sensitivity. *J. Nanomater.* **2015**, 1–7.

(55) Negri, P.; Marotta, N. E.; Bottomley, L. A.; Dluhy, R. A. Removal of Surface Contamination and Self-Assembled Monolayers (SAMs) from Silver (Ag) Nanorod Substrates by Plasma Cleaning with Argon. *Appl. Spectrosc.* **2011**, *65*, 66–74.

(56) Wang, Y.; Alsmeyer, D. C.; Mccreery, R. L. Raman Spectroscopy of Carbon Materials: Structural Basis of Observed Spectra. *Chem. Mater* **1990**, *2*, 557–563.

(57) Li, Y.; Jarosova, R.; Weese-Myers, M. E.; Ross, A. E. Graphene-Fiber Microelectrodes for Ultrasensitive Neurochemical Detection. *Anal. Chem* **2022**, *94*, 4803–4812.

(58) Veres, M.; Füle, M.; Tóth, S.; Koós, M.; Pócsik, I. Surface Enhanced Raman Scattering (SERS) Investigation of Amorphous Carbon. *Diam. Relat. Mater.* **2004**, *13*, 1412–1415.

(59) Zou, S.; Williams, C. T.; Chen, E. K.-Y.; Weaver, M. J. Surface-Enhanced Raman Scattering as a Ubiquitous Vibrational Probe of Transition-Metal Interfaces: Benzene and Related Chemisorbates on Palladium and Rhodium in Aqueous Solution. *J. Phys. Chem. B* **1998**, *102*, 9039–9049.

(60) Ray III, K. G.; McCreery, R. L. Characterization of the Surface Carbonyl and Hydroxyl Coverage on Glassy Carbon Electrodes Using Raman Spectroscopy. *J. Electroanal. Chem.* **1999**, *469*, 150–158.

(61) Li, X.; Liu, M.; Lee, J.-P.; Ding, D.; Bottomley, L. A.; Park, S.; Liu, M. An Operando Surface Enhanced Raman Spectroscopy (SERS) Study of Carbon Deposition on SOFC Anodes. *Phys. Chem. Chem. Phys* **2015**, *17*, 21112–21119.

(62) Norrod, K. L.; Rowlen, K. L. Removal of Carbonaceous Contamination from SERS-Active Silver by Self-Assembly of Decanethiol. *Anal. Chem.* **1989**, *70*, 4218–4221.

(63) Bokobza, L.; Bruneel, J.-L.; Couzi, M. Raman Spectra of Carbon-Based Materials (from Graphite to Carbon Black) and of Some Silicone Composites. *C* **2015**, *1*, 77–94.

(64) Barth, I.; Akinola, J.; Lee, J.; Gutiérrez, O. Y.; Sanyal, U.; Singh, N.; Goldsmith, B. R. Explaining the Structure Sensitivity of Pt and Rh for Aqueous-Phase Hydrogenation of Phenol. *J. Chem. Phys.* **2022**, *156*, 104703.

(65) Zapata, F.; García-Ruiz, C. The Discrimination of 72 Nitrate, Chlorate and Perchlorate Salts Using IR and Raman Spectroscopy. *Spectrochim. Acta Part A Mol. Biomol. Spectrosc.* **2018**, *189*, 535–542.

(66) Nikolakakos, G.; Whiteway, J. A. Laboratory Investigation of Perchlorate Deliquescence at the Surface of Mars with a Raman Scattering Lidar. *Geophys. Res. Lett.* **2015**, *42*, 7899–7906.

(67) Rudolph, W. W.; Irmer, G. Hydration and Ion Pair Formation in Aqueous Y^{3+}–Salt Solutions. *Dalt. Trans.* **2015**, *44*, 18505.

(68) Rudolph, W. W.; Irmer, G. Hydration of the Calcium(II) Ion in an Aqueous Solution of Common Anions (ClO4 −, Cl−, Br−, and NO3 −). *Dalt. Trans.* **2013**, *42*, 3919–3935.

(69) Dunuwille, M.; Yoo, C.-S. Phase Diagram of Ammonium Perchlorate: Raman Spectroscopic Constrains at High Pressures and Temperatures. *J. Chem. Phys* **2016**, *144*, 244701.

(70) Rudolph, W. W.; Irmer, G. Hydration and Speciation Studies of Mn^{2+} in Aqueous Solution with Simple Monovalent Anions (ClO4 −, NO3 −, Cl−, Br−). *Dalt. Trans.* **2013**, *42*, 14460–14472.

(71) Leung, L. wing H.; Weaver, M. J. Extending Surface-Enhanced Raman Spectroscopy to Transition-Metal Surfaces: Carbon Monoxide Adsorption and Electrooxidation on Platinum- and Palladium-Coated Gold Electrodes. *J. Am. Chem. Soc.* **1987**, *109*, 5113–5119.

(72) Zou, S.; Weaver, M. J. Surface-Enhanced Raman Scattering on Uniform Transition-Metal Films: Toward a Versatile Adsorbate Vibrational Strategy for Solid-Nonvacuum Interfaces? *Anal. Chem.* **1998**, *70*, 2387–2395.

(73) George, S. M. Atomic Layer Deposition: An Overview. *Chem. Rev.* **2010**, *110*, 111–131.

(74) Mahan, J. E. *Physical Vapor Deposition of Thin Films*; Wiley: New York, **2000**.

(75) Cao, P.; Sun, Y.; Yao, J.; Ren, B.; Gu, R.; Tian, Z. Adsorption and Electro-Oxidation of Carbon Monoxide at the Platinum-Acetonitrile Interface as Probed by Surface-Enhanced Raman Spectroscopy. *Langmuir* **2002**, *18*, 2737–2742.

Chapter 3 Adsorption Energies of Oxygenated Aromatics and Organics on Rhodium and Platinum in Aqueous Phase

This chapter is adapted from **Akinola, J**.; Barth, I.; Goldsmith, B. R.; Singh, N. Adsorption Energies of Oxygenated Aromatics and Organics on Rhodium and Platinum in Aqueous Phase. *ACS Catal*. **2020**, 10, 4929–4941. Copyright American Chemical Society. The computational portion of this chapter was performed by Isaiah Barth.

3.1 Summary

This chapter provides a resource for benchmarking methods for predicting aqueous-phase adsorption energies of C5/C6 organics on metal surfaces. In this chapter, we report the aqueous-phase adsorption enthalpies and free energies of phenol, benzaldehyde, furfural, benzyl alcohol, and cyclohexanol on polycrystalline Pt and Rh determined via experimental isotherms and density functional theory modeling. The experimental aqueous heats of adsorption for all organics are ~50–250 kJ mol^{-1} lower than calculated gas-phase heats of adsorption, with a larger decrease for Rh compared with Pt. Unlike in the gas phase, phenol and other aromatic organics adsorb with similar strength on Pt and Rh in the aqueous phase. The similar aqueous adsorption strength of phenol and benzaldehyde on Pt and Rh explains their comparable aqueous-phase hydrogenation activities, which are rate limited by a Langmuir-Hinshelwood surface reaction. A widely used implicit solvation model largely overpredicts the heats of adsorption for all organics compared with experimental measurements. However, accounting for the enthalpic penalty of displacing multiple water molecules upon organic adsorption using a bond-additivity model gives much closer agreement between experimental measurements and predicted heats of adsorption. This bond-additivity model explains that the similar adsorption strength of organics on Pt and Rh in the

aqueous phase is due to the stronger adhesion of water to Rh than Pt, which offsets the stronger gas-phase organic adsorption energy on Rh.

3.2 Introduction

Over 143 billion gallons of motor gasoline are consumed annually within the USA to power transportation, emitting huge amounts of greenhouse gases like CO_2.[1] The need to supply energy for transportation in a sustainable manner has spurred efforts to replace fossil fuels with renewable and CO_2-neutral transportation fuels. One promising strategy is to produce transportation fuels from lignin biomass waste.[2–5] Converting the oxygenated aromatic compounds in water that come from fast pyrolysis of lignin (i.e., bio-oil) to transportation fuels or chemical precursors requires aqueous-phase catalytic or electrocatalytic hydrogenation and hydrodeoxygenation,[6] typically rate-limited on metals by surface reactions. To improve the kinetics of these and other aqueous-phase catalytic reactions, an understanding of the effect of water (or solvent) on organic adsorption is critical, because adsorption energies can determine coverages and alter activation barriers.

Although adsorption energies on metals are generally well understood in the gas phase and have been used effectively to predict and understand gas-phase catalytic behavior, much less is known about adsorption in the aqueous phase. Generally, the lack of understanding of aqueous-phase adsorption can lead to inaccurate predictions of aqueous-phase catalytic behavior. This issue often occurs when gas-phase adsorption energies are used to explain aqueous-phase catalytic activity trends. For example, the experimental gas-phase adsorption of phenol (a model bio-oil species) on Pt(111) is so strong (-220 kJ mol^{-1})[7] that room-temperature hydrogenation would seem unlikely to occur because of site poisoning by phenol, yet phenol hydrogenation on Pt occurs in the aqueous phase at room temperature.[8–12] Also, Pt(111) and Rh(111) are predicted by density functional theory (DFT) modeling to have a ~50 kJ mol^{-1} difference in their adsorption energy of phenol in the gas phase,[13] but have similar aqueous-phase hydrogenation turnover frequencies (TOFs) and apparent activation barriers,[8,14] seemingly in contradiction to the Sabatier principle. It is important to determine whether this contradiction is due to intrinsic differences in the mechanism and pathways of gas-phase vs. aqueous-phase catalytic reactions or can be explained by the differences in effective adsorption energies in gas and aqueous phase.

In this work, we report adsorption enthalpies and free energies on Pt and Rh for select US Department of Energy platform chemicals that serve as bio-oil model compounds. Specifically phenol, benzaldehyde, and furfural,[15] as well as two hydrogenated products—benzyl alcohol and cyclohexanol—in aqueous phase on active hydrogenation electrocatalysts, Rh and Pt, are studied using cyclic voltammetry (CV) and DFT modeling. We show the first direct comparison of DFT-computed adsorption energies with experimentally extracted values for these molecules and surfaces in the aqueous phase. We also show that the initial apparent discrepancies in catalytic behavior of phenol and benzaldehyde hydrogenation in the aqueous-phase can be explained by the stark differences in gas-phase and aqueous-phase adsorption energies.

Adsorption of reactants in the condensed phase is more complex than in gas phase because it requires displacement of adsorbed solvent before reactants can adsorb. To accurately describe surface reactions at liquid-solid interfaces, the energy of water/solvent displacement on the adsorption energetics of adsorbates must be adequately captured. The current first-principles modeling paradigm (i.e., using DFT) for predicting adsorption energies and coverages to use in microkinetic models typically neglect the energetic cost of displacing adsorbed solvent from the catalyst surface. Because adsorption energies play such a significant role in catalytic activity, these errors could qualitatively change predicted trends in catalyst performance.

Recent work shows that the aqueous-phase heat of adsorption of phenol on a Pt(111)-like surface is much smaller than in the gas phase,[16] which was attributed to the enthalpy associated with the displacement of multiple water molecules from the Pt surface upon adsorption of phenol and described by a bond-additivity model.[17] This more moderate adsorption energy of phenol is consistent with the aqueous-phase electrocatalytic and thermocatalytic hydrogenation activity observed at room temperature. Nonetheless, the aqueous-phase heats of adsorption and the role of water displacement on metals are unknown for most other oxygenated aromatic and organic species of relevance to bio-oil catalysis. This lack of knowledge prevents understanding of how adsorption strength of reactants correlates with catalytic activity in the aqueous-phase and also precludes important benchmarking of computational predictions.

In this work, we: (1) apply a state-of-the-art bond-additivity model to five molecules on Pt(111) terraces, Pt(110) steps, Rh(111) terraces, and Rh(110) steps; (2) confirm the adsorption of these molecules is reversible, which is a requirement for extracting adsorption energies using adsorption isotherms; and (3) perform a DFT analysis for all studied molecules to compare adsorption energies quantitatively with our experimental measurements. We show that these DFT-computed adsorption energies can be directly compared with experimentally extracted values for these molecules and surfaces in the aqueous phase. Each of these three aspects improves upon previous investigations and taken together provide a more advanced study of molecule adsorption in the aqueous phase than prior work.[16–18]

We use CV to measure the charge from reversible hydrogen underpotential deposition (H_{upd}) and desorption ($H^+ + e^- + * \,(\mathrm{Metal}) \rightleftarrows H^*$)[19–21] on polycrystalline Rh and Pt without organics present and with increasing organic concentration. The decrease in H_{upd} charge due to adsorbed organics[11,22–24] is used to estimate the organic coverage as a function of organic concentration and construct adsorption isotherms.[16] Aqueous-phase adsorption equilibrium constants are extracted using a Temkin adsorption model to fit the adsorption isotherms. Enthalpies are determined from the Gibbs free energies of adsorption as previously described.[16] Adsorption enthalpies and free energies of these organics on Pt and Rh surfaces are also predicted using DFT modeling and a bond-additivity model to compare with experimental values.

Ultimately, our work finds that the heats of adsorption of organics in the aqueous phase are reduced by 50–250 kJ mol^{-1} compared with their gas-phase values because of the enthalpic penalty of displacing several water molecules upon adsorption. This weaker adsorption explains why surface reactions of organics that bind too strongly to react in the gas phase can occur at room temperature in water. Additionally, we show that unlike in gas phase, Rh and Pt have similar adsorption energies in aqueous phase for phenol, benzaldehyde, and their reaction intermediates. This similar adsorption energy in aqueous phase could be responsible for the comparable aqueous catalytic hydrogenation activity of these model bio-oil compounds observed on Pt and Rh. We also show that using DFT modeling with only implicit solvation overestimates adsorption energies and does not capture observed experimental trends, which prevents accurate predictions of coverages. Using a bond-additivity model combined with gas-phase DFT calculations enables more accurate predictions of aqueous adsorption energies of C5/C6 organics. These results highlight the necessity of properly accounting for the effect of solvent displacement at the metal interface when modeling adsorption of organic molecules of relevance to condensed-phase catalytic reactions such as bio-oil hydrogenation, particularly those with large adsorption footprints such as aromatics.

3.3 Experimental and Computational Methods

3.3.1 Cyclic Voltammetry

The working electrode for the CV measurements was either a polycrystalline Pt wire (0.5 mm diameter, 99.997% Alfa Aesar) or Rh wire (0.5 mm diameter, 99.8% Alfa Aesar) and the counter electrode was a graphite rod. A two-compartment electrochemical cell with a working and reference electrode compartment and a counter electrode compartment separated by a N117® Nafion membrane was used. The working electrodes were first exposed to a flame for cleaning any adventitious organic, followed by rinsing with Milli-Q water. Before each use, the cell was cleaned with Milli-Q water and oven dried at 80 °C three times. This cleaning procedure removes trace impurities of organics that would otherwise result in inconsistent measurements from run to run. An Ag/AgCl reference electrode was calibrated to 0 V vs. reversible hydrogen electrode (RHE) in the supporting electrolyte and all potentials are reported vs. RHE based on this calibration. Acetate buffer (pH 5) containing 100 mM acetic acid (Sigma Aldrich, 99.995%) and 100 mM sodium acetate (Sigma Aldrich 99.999%) was used as the supporting electrolyte. Acetic acid is used in this work to mimic a bio-oil environment containing carboxylic acids[25] and has negligible adsorption on Pt and Rh in the H_{upd} region.[26] The working electrode compartment was filled with 130 mL of acetate buffer and sparged with N_2 (99.999%) to remove dissolved oxygen. The working electrode was further cleaned under voltammetric conditions in the potential window of −0.2 V to 1.8 V vs. RHE for 60 cycles at a scan rate of 100 mV s^{-1}. After voltammetric cleaning, CV was carried out at a 100 mV s^{-1} scan rate in the potential window of 0.05 V to 1.1 V for Rh wire and 0.05 V to 1.3 V for Pt wire. Within these potential windows the cyclic voltammograms were repeatable and reversible.

Organics dissolved in acetate buffer solution were introduced to the cell to increase the concentration of organics from 1 μM up to 500 mM. The organics used for adsorption studies were phenol (Sigma Aldrich, >99%), benzaldehyde (Sigma Aldrich >99%), furfural (Sigma Aldrich 99%), benzyl alcohol (Sigma Aldrich 99.8%), and cyclohexanol (Sigma Aldrich 99%). At the lowest organic concentration (1 μM), the bulk organic concentration would decrease by at most 0.2% upon adsorption of a complete monolayer of the organic onto the metal electrode, thus we assumed the bulk concentration was unchanged by adsorption (see **Chapter 2**). The electrolyte was stirred and re-sparged with N_2 to remove oxygen prior to CV measurements for each organic concentration. The working electrode was continuously cycled in the same potential window between each CV measurement (0.05 V to 1.1 V for Rh and 0.05 V to 1.3 V for Pt).

The CV measurements were repeated under the conditions specified at each organic concentration until steady state was reached. The charge from chemisorbed hydrogen in the H_{upd} region (0.05 V–0.35 V) was obtained by integrating the area under the desorption peaks in the CV, dividing by the scan rate, and then subtracting the baseline capacitive charge calculated from the double layer charging region of the CV. With phenol present, the H_{upd} charge from H* adsorption and desorption match closely on Pt (see **Chapter 2**). On Rh, the H adsorption region had a contribution from the Rh_2O_3 reduction peak,[19] causing the apparent adsorption charge to be larger than the desorption charge, hence the H_{upd} desorption peak was used instead to estimate the amount of chemisorbed hydrogen on both Rh and Pt.

3.3.2 Dilution of Organic Concentration to Determine Reversibility

To test whether organic adsorption was reversible, after taking a cyclic voltammogram at a given organic concentration the organic concentration was diluted by removing a given volume of the existing solution and replacing with the same volume of acetate buffer supporting electrolyte while the working electrode containing the adsorbed organic was kept in place under a continuous blanket of N_2. After dilution, the working electrode was cycled at the normal potential window used for H_{upd} measurements until the adsorbed organic reached equilibrium with the diluted cell solution concentration (indicated by a stable CV). This stable CV at the diluted concentration was compared to measurements done at the same concentration, but without previously going to higher organic concentrations (see **Chapter 2**).

3.3.3 Adsorption Isotherm Fitting

Each isotherm was fit by a one site or two site model using the same procedure from ref [16]. Briefly, the equilibrium constant of adsorption $K_{eq,ads,\theta}^{aq}$ for each site was obtained by fitting the fraction of H_{upd} inhibited at different organic concentrations to a Temkin isotherm Error! Reference source not found.), where the saturation coverage for site 1 was the coverage (θ) where the first plateau is seen, and the saturation coverage of site 2 was the second plateau. $\Delta G_{ads,aq,\theta=0}^{0}$ is the adsorption free energy of the aqueous organic at zero coverage, R is the ideal gas constant, and T is the temperature. Several models can be used to fit the adsorption isotherm, such as the Langmuir-Hinshelwood (LH) model where metal surface sites can either be unoccupied, have adsorbed hydrogen, or have adsorbed organic. Instead of a LH model, we used a modified Langmuir model where the organic adsorption energy varies linearly with the coverage because of adsorbate-adsorbate interactions (also known as the Temkin model).[27,28] The Temkin model assumes that the coverage of organic does not depend on adsorbed H in the reversible H_{upd} region but depends only on the bulk organic concentration and the organic equilibrium adsorption constant. This model is used because of its simplicity compared to the LH model. Recently, a LH model was used to fit kinetics for Pt/C for aqueous-phase phenol hydrogenation over a range of phenol concentrations, resulting in an equilibrium constant for phenol of 33 (standard-state concentration of 1 M phenol, as used here).[29] This value is similar to the adsorption equilibrium constant of 38 measured for phenol/Pt(111) using the Temkin model,[16] supporting the accuracy of the Temkin model used for this work. Additional discussion about the isotherm derivation and fitting is provided in **Chapter 2**.

$$K_{eq,ads,\theta}^{aq} = \exp\left(\frac{-\Delta G_{ads,aq,\theta=0}^{0} + \alpha\theta}{RT}\right) \tag{3.1}$$

Ideally the measurements would be done as a function of surface charge on both Pt and Rh to determine the influence of the surface charge of the metal electrode on the water layer and organic adsorption[30,31] or at a potential where maximum organic adsorption is reached, often slightly cathodic to the potential of zero charge.[32] However, the H_{upd} technique inherently cannot be done at a single potential but requires cycling over a range of potentials. Hence, our reported values may be underpredictions of the organic adsorption strength relative to the adsorption on an uncharged surface. Despite this, there is still general agreement between the adsorption energies extracted through this method and solution calorimetry, as well as gas-phase calorimetry once the effects of the water layer on the metal surface have been accounted for.[17]

3.3.4 Computational Methods

Density functional theory (DFT) calculations were done using the Vienna Ab Initio Simulation Package (VASP).[33,34] All DFT calculations were non-spin polarized because spin polarization was found to have 0.14% and 0.43% average change in the organic and water adsorption energies, respectively, on Pt and Rh in gas phase. The Perdew-Burke-Ernzerhof functional with the semi-empirical D3 dispersion correction (PBE-D3) was used because of its good trade-off between computational cost and accuracy, although PBE-D3 has been shown to overestimate adsorption strengths of aromatics.[35–38] Projector-Augmented Wave pseudopotentials[39] were used with a kinetic energy cutoff at 400 eV. The convergence criteria for electronic and ionic forces were set to 10^{-5} eV and 0.01 eV $Å^{-1}$. Atomic structures were geometry optimized using either the conjugate-gradient algorithm or the quasi-Newton algorithm. Lattice parameters of bulk Pt and Rh were determined by relaxing a four-atom face-centered cubic cell of each metal. A 15×15×15 Monkhorst-Pack *k*-point grid was used for bulk relaxations. The calculated lattice parameters were 3.925 Å and 3.792 Å for Pt and Rh and are within 1.2% and 0.1%, respectively, of the experimentally determined values.[40,41]

The adsorption enthalpies of phenol, benzaldehyde, furfural, benzyl alcohol, and cyclohexanol were predicted on (111) terraces and the (110)-like and (100)-like steps of the (553) and (533) surfaces, respectively. Throughout this text we refer to the steps of the (553) and (533) surfaces simply as (110) and (100). The surface slab models of Pt and Rh were modeled using 4×4 supercells that were four layers thick. For all considered surfaces, the top two layers could relax during geometry optimization, whereas the bottom two layers were fixed in their bulk coordinates. Metal slabs were separated by a 20 Å vacuum in the direction perpendicular to the surface. A 3×3×1 Monkhorst-Pack *k*-point grid was used for adsorption energy calculations of organics on 4×4 slabs corresponding to a 1/16 monolayer (ML) coverage. A 5×5×1 Monkhorst-Pack *k*-point grid was used for adsorption energy calculations of organics on 3×3 slabs corresponding to a 1/9 ML coverage. Spurious dipole interactions between periodic images were corrected in VASP (IDIPOL = 3, LDIPOL = True).

A variety of implicit and explicit modeling approaches have been used to treat the water-adsorbate-metal interface to enable prediction of thermodynamic and kinetic parameters for aqueous-phase reactions.[42,43] Explicit treatment of water through classical,[44] ab initio,[45] and hybrid[46] molecular dynamics calculations has been employed to describe water-adsorbate-metal interactions at the interface, although these approaches are computationally demanding because they require sampling over long time scales. Alternatively, simple ice-like layers have been used to explicitly model water, although this approach is too crude to accurately describe the water-adsorbate-metal interactions at standard electrochemical conditions.[44] In place of explicit solvent modeling, adsorption energies may be calculated using computationally inexpensive implicit solvent models.[47,48]

Two approaches—an implicit solvent model using the VASPsol model[49,50] and a bond-additivity model recently published by Singh and Campbell[17]—were used in this study to model solvation effects. VASPsol, which was developed to treat solvated molecules and nanocrystal surfaces, models the interactions between solvent and solute by using DFT to describe the solute explicitly and the linear Poisson-Boltzmann equation to describe the solvent as a continuum dielectric. In this work the water solvent was implicitly treated using the default VASPsol parameters for gas-phase, implicit solvent, and thermodynamic calculations). The bond-additivity model, which accounts for the formation of water-organic bonds as well as the breaking of water-water and water-metal bonds, was originally developed to estimate the aqueous-phase adsorption energy of phenol on Pt(111) based on the experimental gas-phase adsorption energy.[17]

Here, the bond-additivity model (**Eq. 3.2**)[17] was used to estimate the aqueous-phase adsorption enthalpies of all organic molecules considered at 298.15 K and 1 atm.

$$\begin{aligned} -\Delta H^0_{ads,aq,gas,R/M} &= -\Delta H^0_{ads,gas,R/M} + n\left(\Delta H^0_{ads,gas,water/M} + \Delta H^0_{vap}\right) - 2\gamma_{water(liq)}\sigma_R \\ &\quad + (water\text{-}R) \end{aligned} \tag{3.2}$$

Where $\Delta H^0_{ads,aq,gas,R/M}$ is the adsorption enthalpy of gas-phase organic R onto metal M in the aqueous phase, $\Delta H^0_{ads,gas,R/M}$ is the adsorption enthalpy of gas-phase organic R onto metal M in the gas phase, n is the number of water molecules displaced from metal M upon organic adsorption, $\Delta H^0_{ads,gas,water/M}$ is the adsorption enthalpy of a water molecule onto metal M in the gas phase, ΔH^0_{vap} is the vaporization enthalpy of water, $\gamma_{water(liq)}$ is the surface energy of liquid water, σ_R is the area of an adsorbed organic molecule, and *water*-R is $-1/2\Delta H_{Solv,R} + \gamma_{water(liq)}\sigma_R$, where $\Delta H_{Solv,R}$ is the solvation enthalpy of the organic in water. For simplicity, in the subsequent text we omit R or R/M when it is clear which metal and organic are being referred to (e.g., we refer to $\Delta H^0_{ads,aq,gas,R/M}$ as $\Delta H^0_{ads,aq,gas}$). A similar equation using experimental adhesion energies (rather than our calculated values) of aqueous and non-aqueous solvents is presented in ref [51], but as the adhesion energy of water on Rh is not experimentally available, we use **Eq. 3.2** in this work. Conceptually these equations are the same bond-additivity model.

The number of water molecules displaced upon organic adsorption, *n*, was calculated for each molecule on each surface by studying the heat of adsorption as a function of organic coverage using the bond-additivity model. Treating each modeled coverage as saturation, *n* was calculated over a range of organic coverages. In subsequent applications of the bond-additivity model, we choose the *n* that corresponds to the coverage at which the heat of adsorption reaches a maximum. Using this method, we find that phenol adsorbs on Pt(111) at 1/9 ML coverage (9 Pt atoms per phenol molecule) and displaces 6.5 water molecules assuming a water coverage of 0.72 ML.[52] This phenol coverage on Pt(111) matches the coverage in aqueous phase determined from quantitative Auger electron spectroscopy measurements,[53] and the value of 6.5 water molecules is the same as used in our previous bond-additivity model for phenol on Pt(111) using experimental values.[17] Therefore, we believe our computational approach is reasonable for estimating the number of water molecules displaced from the Pt(111) terrace upon adsorption of phenol, and we apply it to the other organics on Pt(111) and Rh(111) terraces. Because it is difficult to vary organic coverage on stepped surfaces, we calculate *n* on (110) and (100) terraces and assume that *n* is the same on the respective steps. Although, the value of *n* on stepped surfaces may be evaluated more rigorously using ab initio molecular dynamics, this computationally demanding approach was not employed in this current work. Since *n* is not calculated explicitly on (110) and (100) steps, predicted heats of adsorption on the stepped surfaces are not as accurate as the heats of adsorption on the (111) terrace.

3.4 Results and Discussions

3.4.1 Impact of Phenol on the Underpotential Deposition of Hydrogen on Pt and Rh

The data in **Figure 3.1** shows that H_{upd} on a Pt wire and a Rh wire is inhibited by phenol adsorption, which implies competitive adsorption between H* and phenol* on the surfaces of both metals in the aqueous phase. The cyclic voltammograms with phenol for the Pt wire (**Figure 3.1a**) match those measured previously, where the difference in H_{upd} charge on Pt with and without phenol was used to quantify the coverage of adsorbed phenol.[11,16] On Rh, the H_{upd} charge, proportional to the H* desorption peak area in the potential range 0.05–0.35 V, also decreases with increasing phenol concentration. Similar to Pt, we attribute the decreasing H_{upd} charge to blocking of Rh sites by adsorbed phenol, resulting in fewer sites available for hydrogen to adsorb. Hydrogen underpotential deposition on Rh in acetate buffer without phenol is kinetically fast and reversible within the potential window used in this work, shown by the symmetry of the reduction and oxidation peaks associated with H_{upd} and the H_{upd} charge independence on scan rate. The H_{upd} on Rh and Pt is also reversible when phenol is present, indicating that H* does not react with adsorbed phenol during these scans.

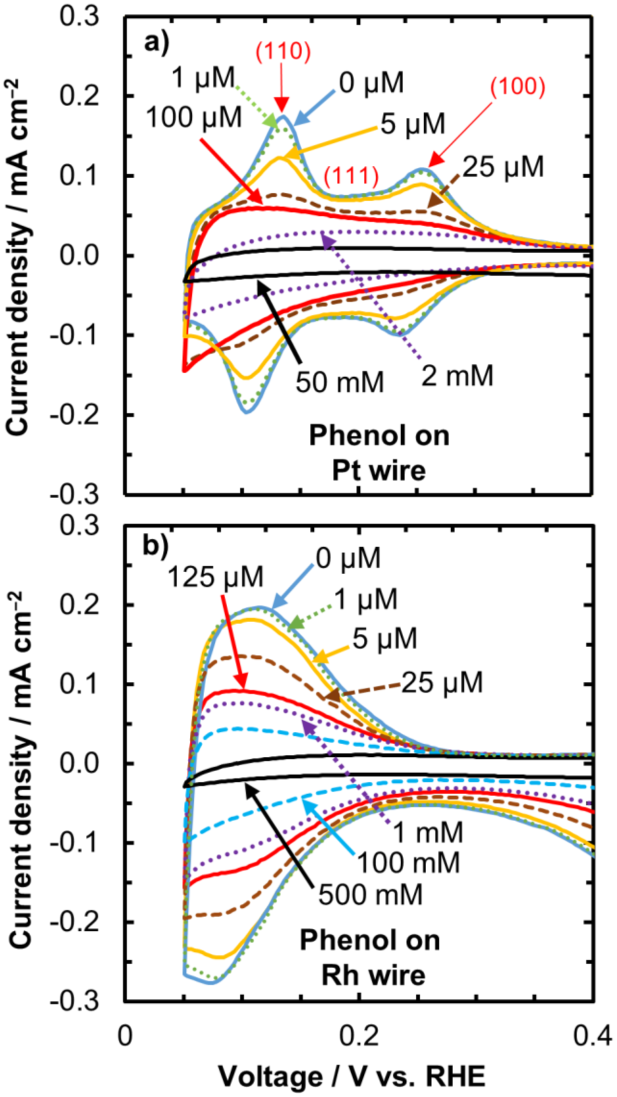

Figure 3.1 Cyclic voltammograms showing the H_{upd} region at different bulk phenol concentrations on metal surfaces. a) platinum wire **b)** rhodium wire. The H_{upd} current peaks attributed to Pt(110) steps and Pt(100) steps and the broad region corresponding to Pt(111) terraces are labeled. The H_{upd} peaks corresponding to different Rh facets overlap with one another. The cyclic voltammograms were taken in 100 mM acetate buffer supporting electrolyte (pH 5) at 298 K and using 100 mV s^{-1} scan rate. Phenol competes with H* adatoms for metal sites, hence the drop in area under the H_{upd} adsorption and desorption peaks as phenol concentration increases.

The polycrystalline Pt and Rh wires have different H_{upd} peak shapes, based on how H* interacts with the different surface facets. The peak voltages for Pt in **Figure 3.1a** are consistent with prior polycrystalline Pt studies,[11,16] and individual H_{upd} peaks have been identified on Pt single crystals in 0.1 M H_2SO_4 and $HClO_4$.[24,54] These studies indicate the peak located at ~0.10–0.15 V is from Pt(110) steps, the peak at ~0.23–0.3 V is from Pt(100) steps, and the broad feature that underlies the two peaks from ~0.05–0.35 V is from Pt(111) terraces. Contributions from H_{upd} on (111) steps, (110) terraces, and (100) terraces on Pt are at CV peak locations that overlap with those of (111) terraces, (110) steps, and (100) steps.[55–59] Unlike on Pt, the H_{upd} peaks all overlap for the facets of polycrystalline Rh[19] (i.e., Rh(110),[60] Rh(100),[61] and Rh(111)[61–63]). Consequently, a single adsorption/desorption peak is observed for H_{upd} on Rh wire in 0.1 M acetate buffer, **Figure 3.1b**. This overlap of H_{upd} peaks from the different facets of Rh, attributed to the similar hydrogen adsorption free energies on the different facets, makes deconvolution of organic adsorption on the different facets from H_{upd} alone difficult.

Adsorbed phenol blocks H_{upd} across the Pt facets to different extents, with the Pt(110) peak decreasing more than the Pt(100) peak for the same phenol concentrations, whereas the broad Pt(111) feature drops the least at concentrations between 1 µM and 100 µM (**Figure 3.1a**). Therefore, the Pt(110) and Pt(100) steps adsorb phenol stronger than the Pt(111) terrace, in agreement with a prior report.[16] In **Figure 3.1b**, any differences in phenol adsorption on the different facets of Rh wire are not immediately evident since the H_{upd} peaks of Rh(110), Rh(100), and Rh(111) cannot be distinguished. Nonetheless, we will show below based on the shape of the adsorption isotherm that there are also two distinct types of adsorption sites on Rh.

First, the inhibition of H_{upd} charge as a function of phenol concentration can be used to extract adsorption energies using an adsorption isotherm, so long as the H_{upd} process remains reversible in the presence of phenol and phenol adsorption is an equilibrated, reversible process. In **Chapter 2** we showed that the H_{upd} oxidation and reduction charges match both in the absence of phenol and with phenol present, proving reversible H^+ reduction and H^* oxidation. This observation matches the report that phenol is reduced on Pt and Rh only at lower potentials (< 0 V vs. RHE) than applied in this work.[9] To test whether the adsorption of organics on Pt and Rh is reversible we measure the H_{upd} charge at a certain bulk organic concentration, then dilute the bulk concentration to see if the H_{upd} charge recovers to that associated with the new (lower) bulk organic concentration. We observed that the H_{upd} charge and thus the coverage of phenol and other organics is recovered, i.e., there is no hysteresis in the adsorption isotherms, which implies that adsorption of phenol and other organics is an equilibrated, reversible process.

3.4.2 Extracted Adsorption Energies of Phenol on Platinum and Rhodium

Having fulfilled both criteria for reversibility as discussed above, the adsorption isotherms of phenol on Pt and Rh shown in **Figure 3.2** were constructed by plotting the fraction of H_{upd} inhibited by phenol from the cyclic voltammograms (**Figure 3.1**) against the bulk concentration of phenol. The fraction of H_{upd} inhibited, which we assume was caused by the reversible adsorption of phenol on the metal surface, was obtained from the difference in the H_{upd} charge with and without phenol in solution. The fraction of H_{upd} inhibited by phenol on Pt at different concentrations determined using the CV technique matches a report using a radiotracer method.[64] The dilution points are shown in **Figure 3.2** as open triangles to indicate the reversibility of phenol adsorption and the lack of hysteresis using this technique. For example, diluting from 100 µM (filled triangle) to 10 µM (open triangle) is shown in the isotherm in **Figure 3.2a** for phenol on Pt wire, where the diluted point matches the measurement at 10 µM without dilution. The variation between the data points after dilution compared to without dilution at the same bulk phenol concentration is within the small run-to-run variation from multiple measurements.

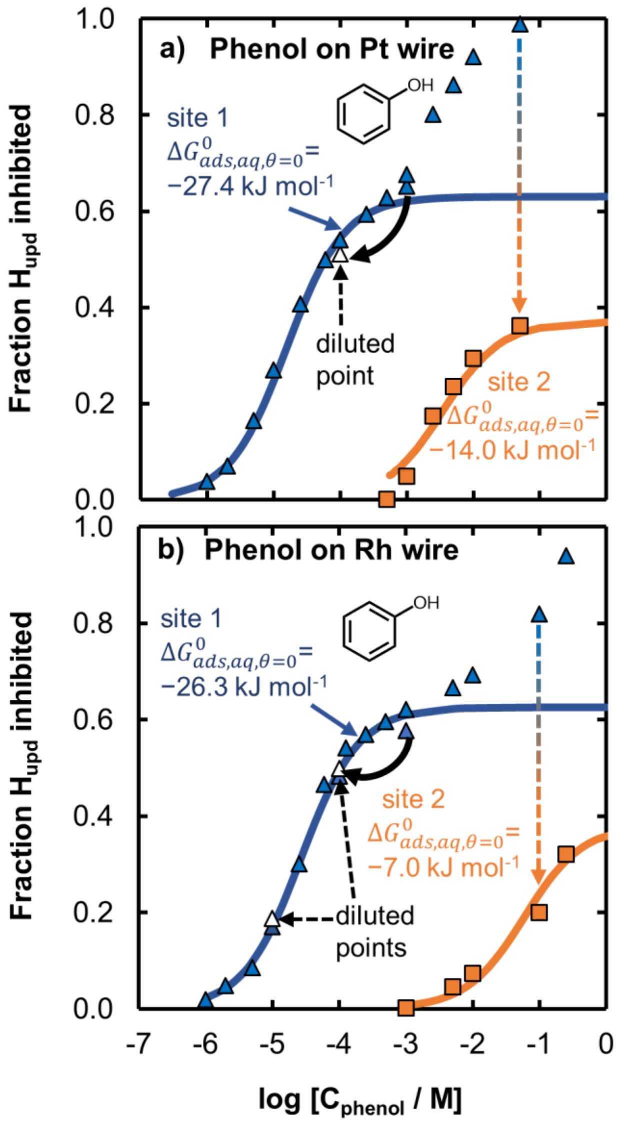

Figure 3.2 Adsorption isotherms of phenol on metal surfaces. a) Pt wire **b)** Rh wire. Isotherms were constructed by plotting the fraction of H_{upd} inhibited by phenol vs. the bulk phenol concentration. Each data point (blue triangle) is obtained from the drop in H_{upd} charge with phenol in **Figure 3.1**. Fits are from a two-site Temkin adsorption model with $\alpha = 0$ kJ mol^{-1} giving the best fit. The orange squares (site 2) correspond to the fraction of H_{upd} inhibited that is greater than the saturation amount of site 1. Thus, site 2 data points are adjusted by subtracting the saturation fraction of site 1 at the higher phenol concentration. Diluted points are shown by open triangles (solid black arrow indicates dilution by a factor of 10). The agreement of the diluted points with points directly taken by adding phenol without first reaching a higher concentration shows that phenol adsorption under these conditions is reversible.

The isotherm shapes in **Figure 3.2** indicate the presence of two distinct adsorption sites on both Pt and Rh, based on the initial increase in coverage with concentration, followed by a plateau with increasing concentration (saturation of the first site), then by a second region of increasing coverage corresponding to adsorption on the second set of sites. Thus, we divide the phenol adsorption isotherm into two sites for both Pt and Rh, where site 1 corresponds to the stronger binding site and site 2 corresponds to the weaker binding sites. The H_{upd} peaks for Pt(110) and Pt(100) in **Figure 3.2a** decrease at lower phenol concentrations, whereas the Pt(111) H_{upd} peak only decreases at higher concentrations. Thus, site 1 in **Figure 3.2a** is attributed to a combination of stepped facets of Pt(110) and Pt(100), and site 2 is attributed to Pt(111) terraces.[16] The adsorption free energy extracted in this way on site 2 matches those from a kinetic model for phenol hydrogenation, as discussed in the Methods section. The fraction of site 2 corresponding to the Pt(111) terrace-like sites (0.37 from the isotherm for Pt in **Figure 3.2** and 0.4 from Ref [16]) is similar to predictions from electrochemical Wulff construction of the fraction of (111) sites (~0.4 in the 0 V to 0.4 V vs. RHE range for Pt),[65] supporting this assignment. Our DFT calculations using the bond-additivity model for Pt also predict stronger phenol adsorption on the (110) steps compared with the (111) terraces, consistent with our assignment. The model, however, predicts weaker phenol adsorption on the (100) steps than (111) terrace despite stronger adsorption in the gas phase. This discrepancy from the experimental results may be a result of an inaccurate (too strong) water adsorption energy on the (100) step or an inaccurate number of water molecules displaced upon organic adsorption as discussed in the methods.

Although from the CV of Rh (**Figure 3.1b**) we cannot distinguish between facets, from **Figure 3.2b** it is apparent that there are two adsorption sites, where site 1 reaches saturation coverage at 1 mM phenol, followed by continued adsorption on site 2 at higher concentration. We attribute site 1 to a combination of (110) and (100) steps facets and site 2 to (111) terraces, the same as the assignment on Pt. Our assignment is supported by the similar fraction of site 1 on Pt and Rh (0.63 and 0.62 respectively). The bond-additivity calculations for Rh predict that phenol adsorbs on (110) steps the strongest, followed by (111) terraces, then (100) steps the weakest, the same order as predicted for Pt. It is possible that site 1 of Rh is only the (110) step and not the (100) step, although the weak adsorption predicted on the (100) steps may be a result of an erroneous treatment of water on the (100) steps in the model as described above for Pt.

The values of experimental adsorption free energies ($\Delta G^0_{ads,aq,\theta}$) from isotherm fitting using the procedure outlined in **Chapter 2** are compiled in **Table 3.1**, along with the free energy of gas-phase organic adsorption in aqueous phase ($\Delta G^0_{ads,aq,gas,\theta}$), calculated from $\Delta G^0_{ads,aq,\theta}$. The adsorption values are also converted to enthalpies of gas-phase organic adsorption in aqueous phase ($\Delta H^0_{ads,aq,gas,\theta}$) and aqueous organic adsorption enthalpies ($\Delta H^0_{ads,aq,\theta}$) following the method discussed in **Chapter 2**. Briefly, the standard entropy of each gas-phase organic molecule is used to estimate the entropy of adsorption using a known correlation for many gas-phase molecules,[66] allowing us to convert from $\Delta G^0_{ads,aq,gas,\theta}$ to $\Delta H^0_{ads,aq,gas,\theta}$. Although this accounts for the loss in entropy from the gas-phase organic adsorption, we assume that the displaced water layer has the same entropy, i.e., that the water layer on top of the adsorbed organic has the same structural order as the water layer on top of the metal surface. This assumption of invariant entropy from water is supported by the close agreement between aqueous-phase calorimetry of benzaldehyde on both Pt/C and Rh/C compared to the enthalpies extracted here using this method. The assumption that the water layer maintains the same entropy could be tested by measuring $\Delta G^0_{ads,aq,\theta}$ as a function of temperature and constructing a van't Hoff plot, so that this approximation is not required. If there was an increase in entropy from the water being displaced (i.e., water on the adsorbed organic has higher entropy than water adsorbed on metal), the enthalpies of adsorption would be more positive than reported here, but the effect is estimated to not be more than 11 kJ mol^{-1}.[17]

3.4.3 Difference in Gas-phase and Aqueous-phase Adsorption Energies of Phenol

Here we compare our experimentally measured aqueous-phase heats of adsorption ($-\Delta H^0_{ads,aq,gas,\theta}$) of phenol on both Pt(111)[16,17] and Rh(111) with DFT-computed values in the gas phase and aqueous phase. The data in **Figure 3.3** shows computed gas-phase heats of adsorption ($-\Delta H^0_{ads,gas,\theta}$) and aqueous-phase heats of adsorption ($-\Delta H^0_{ads,aq,gas,\theta}$) calculated using implicit solvation, the bond-additivity approach, and experimental isotherm fitting. Our gas-phase DFT calculations for phenol heat of adsorption on Pt(111) agrees with low-coverage values measured by ultrahigh vacuum calorimetry.[7] Phenol is calculated to adsorb ~50 kJ mol^{-1} stronger on Rh(111) compared with Pt(111) in the gas phase, but the experimental measurements show that Rh(111) and Pt(111) both adsorb phenol with similar and weaker strength in the aqueous phase.

Heats of adsorption computed using implicit solvation predict that phenol should adsorb stronger than in the gas phase on Pt and Rh and overpredict adsorption strengths by at least 100 kJ mol^{-1} compared with experiment. Here, calculations using only implicit solvation predict that phenol binds 29 kJ mol^{-1} stronger on Pt(111) in the aqueous phase compared with the gas phase, which is consistent with the 25 kJ mol^{-1} increase in phenol binding strength previously reported using an implicit solvation model.[47] Past work that treated water explicitly reported the aqueous-phase adsorption enthalpy of a gas-phase phenol molecule to be 37 kJ mol^{-1} more exothermic than in the gas phase.[45] Implicit and explicit solvent calculations that model water surrounding the organic but not displaced from the surface yield far more exothermic adsorption enthalpies than our equilibrated adsorption measurements and even calorimetry values. Also, DFT calculated adsorption energies that account for displacement of adsorbed water from a metal surface[18] have not been compared directly with experimental values. The consequence of these significantly stronger adsorption energies would be a many orders of magnitude error in adsorption equilibrium constants, which are used for catalysis in trying to predict or understand surface coverages (e.g., through a LH reaction or other microkinetic model).

The bond-additivity model (**Eq. 3.2**) corrects the DFT-predicted gas-phase adsorption enthalpies for solvation and water displacement at the metal interface upon organic adsorption, bringing the predictions into much closer agreement with experiment for phenol adsorption on Pt(111) and Rh(111). The bond-additivity model here does not account for the differences in the potential of zero charge (PZC) between Pt(111) and Rh(111), which could affect the metal surface charge and thus the water adsorption layer. The PZC of the (111) facets of Pt and Rh in 0.1 M H_2SO_4 are much different (0.3 V on Pt(111)[67,68] and 0.1 V on Rh(111) vs. RHE).[69] Accounting for this effect would further improve the accuracy of this model.

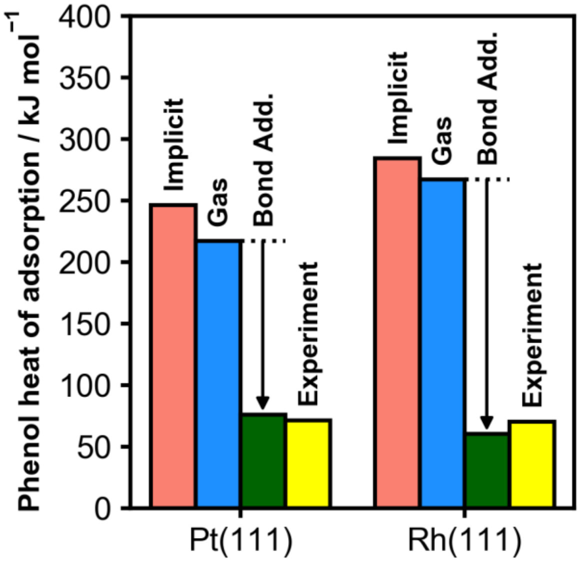

Figure 3.3 DFT-computed heats of adsorption in implicit solvent (orange), gas phase (blue), and aqueous phase using a bond-additivity (B.A) model. The BA model corrects the gas-phase calculation for solvation and water displacement at the metal interface (green). Experimentally derived heats of adsorption for gas-phase phenol on the metal in the aqueous phase for site 2, attributed to Pt(111) and Rh(111) terraces, are shown in yellow. Abbreviations: Bond Additivity = Bond Add.

As previously discussed for Pt,[17] the difference in gas-phase and aqueous-phase adsorption is mainly attributed to the fact that in aqueous phase, organics must displace water adsorbed to the metal surface. This has been described qualitatively by Gileadi[70] and Bockris,[64] but used quantitatively in recent work since we now know the number of water molecules displaced by phenol and the enthalpy associated with those adsorbed waters. For example, a phenol molecule adsorbing on Pt(111) surface in aqueous phase displaces approximately 6.5 water molecules, based on the footprint of adsorbed phenol on Pt[53] and saturation coverage of water on Pt.[52] Since Pt(111) has been recently shown to be the active facet for phenol hydrogenation,[10] it is important to understand how the presence of solvent/water impact the effective adsorption strength of phenol on this facet.

The similarity between phenol adsorption on Rh and Pt in the aqueous phase is primarily caused by the stronger water adsorption on Rh than on Pt as calculated here and in ref [71]. Our DFT calculated water/Rh(111) adsorption energy (-52 kJ mol^{-1}) is stronger than water/Pt(111) (-39 kJ mol^{-1}) in the gas phase, consistent with temperature programmed desorption experiments where water desorption on Rh(111) is observed at higher temperatures than on Pt(111).[72] We assume the phenol "footprint" is similar on Rh and Pt[53] and that n from **Eq. 3.2** is the same for the two metals. This assumption is supported by the similar adsorption geometries and metal surface area covered by phenol on Rh and Pt (0.60 nm^2 for Pt and 0.56 nm^2 for Rh) from our calculations. Thus, the stronger water adsorption on Rh offsets the stronger gas-phase phenol adsorption energy, resulting in comparable aqueous-phase adsorption energies.

3.4.4 Impact of other Oxygenated Aromatics and Organics on the Underpotential Deposition of Hydrogen on Rh.

Besides phenol, other oxygenated aromatics and organics (i.e., benzaldehyde, furfural, benzyl alcohol, cyclohexanol) tested here also compete with hydrogen for adsorption sites on Rh, as seen in **Figure 3.4**. Consequently we can broadly apply the CV technique to extract adsorption energies of organics in the aqueous phase provided that in the H_{upd} potential window the adsorbed organic and H* adsorb and desorb reversibly. The drop in the H_{upd} peaks with individual organic concentration varies in the order of furfural > benzaldehyde > phenol > benzyl alcohol >> cyclohexanol. Cyclohexanol in particular has much lower impact on the H_{upd} than the other organics, even at 200 mM.

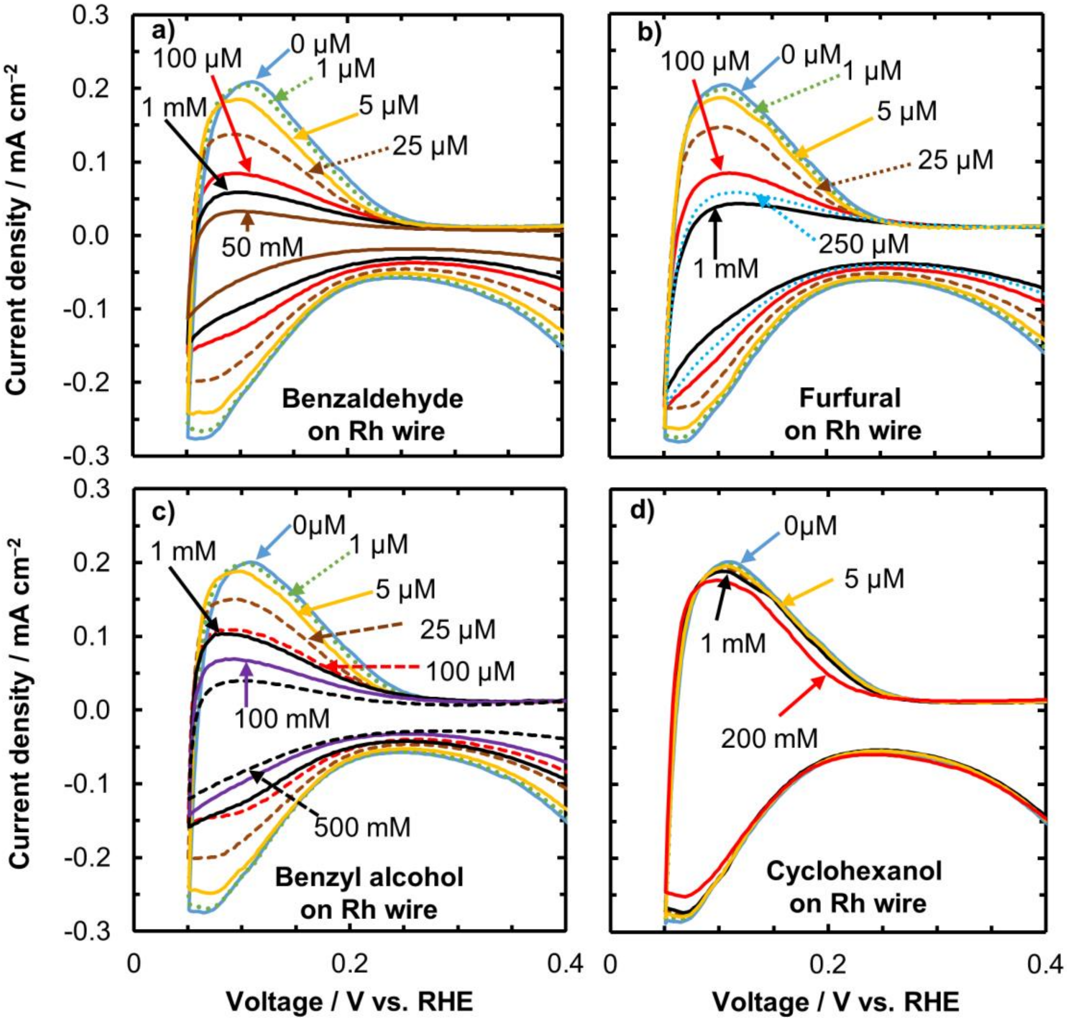

Figure 3.4 Cyclic voltammograms in the H_{upd} region with increasing bulk organic concentration on a Rh wire for different organics. a) benzaldehyde, **b)** furfural, **c)** benzyl alcohol, and **d)** cyclohexanol. Experiments were carried out in 100 mM acetate buffer supporting electrolyte (pH 5) at 298 K and using a 100 mV s^{-1} scan rate. The adsorbed organic competes with H* for sites hence the drop in H_{upd} charge indicated by the reduced current density with increasing organic concentration.

Similar to the reversibility of H_{upd} discussed above for phenol, the H_{upd} charges in the cathodic and anodic direction in the presence of benzaldehyde, benzyl alcohol, and cyclohexanol are the same, implying reversible H_{upd}, however, furfural H_{upd} (**Figure 3.4b**) became less reversible with increasing furfural concentration on Pt and Rh (see **Appendix**). With increasing furfural concentration, a larger portion of the adsorbed hydrogen is not desorbed in the H_{upd} region (i.e., the difference in H_{upd} adsorption and desorption charge increases). This irreversible reduction current is also seen at higher furfural concentrations.[73] This behavior does not seem to be due to a catalytic reaction, because the difference in H_{upd} adsorption and desorption charge was independent of scan rate. Thus, one possibility for the irreversible H_{upd} reduction in the presence of furfural may be that H* partially hydrogenates the adsorbed furfural species, but complete furfural hydrogenation and desorption does not occur in this potential region. Recent studies have shown that furfural may also decarbonylate at potentials just positive of the H_{upd} region, forming strongly adsorbed CO, adsorbed furyl fragments, and adsorbed H.[73,74] In this case, the irreversible reduction current we observe here may be related to the reduction or reaction of adsorbed furyl to furan, but without furan desorption that would allow catalytic turnover.

3.4.5 Adsorption Energies of Furfural, Benzaldehyde, Benzyl Alcohol, and Cyclohexanol on Rh

Using the data in **Figure 3.4**, the fraction of H_{upd} inhibited by the organics is shown in **Figure 3.5**, with specified points testing the reversibility of the adsorption process indicated by open symbols. The adsorption free energies of these organics were extracted the same way as was done for phenol. The two-site behavior seen for phenol on Rh is not observed for furfural and cyclohexanol. We deduce that furfural does not adsorb differently on the individual Rh facets as opposed to phenol, benzyl alcohol and benzaldehyde, which adsorb on distinct Rh sites (attributed to stronger adsorption on steps and weaker adsorption on terraces). This may also be a result of furfural decarbonylating upon adsorption, as discussed earlier. Thus, the extracted adsorption energies of furfural without a two-site adsorption behavior are an average over the different sites.

For cyclohexanol, the adsorption is not strong enough to reach sufficiently high coverages where adsorption on a second site may be seen. Further coverage increases were limited by the solubility of cyclohexanol. The fraction of H_{upd} inhibited at 1 mM cyclohexanol concentration, shown in **Figure 3.5d** is less than 5% whereas for other organics (**Figure 3.5**), greater than 50% organic coverage was achieved at 1 mM. Our DFT calculations also indicate that cyclohexanol adsorption is weaker on Pt and Rh than aromatic adsorption. As the main difference between the phenol and cyclohexanol is the aromatic ring, the weaker adsorption of cyclohexanol (**Figure 3.5d**) is consistent with the idea that the adsorption of aromatics on a transition metal arises from the interaction between the aromatic π electron system and the metal *d*-band.[75] The measured adsorption energies of the model compounds converted between free energies and enthalpies are included in **Table 3.1**. **Table 3.1** also includes the adsorption energies from calculations using DFT and adjusting using the bond-additivity model.

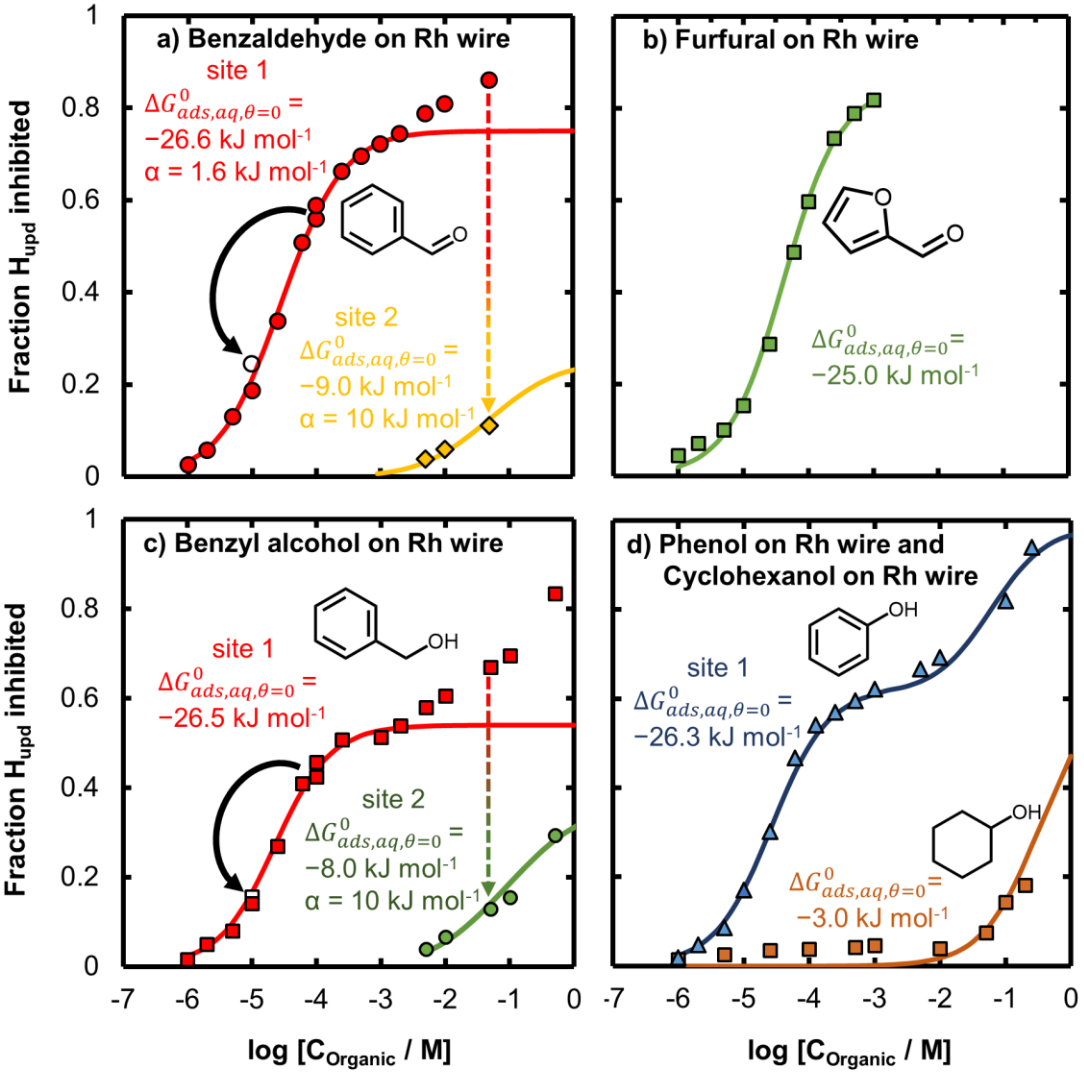

Figure 3.5. Adsorption isotherms of organics on Rh wire in aqueous phase. a) benzaldehyde, **b)** furfural, **c)** benzyl alcohol, and **d)** phenol and cyclohexanol. The data points were obtained from the fraction of H_{upd} inhibited on Rh by the different organics from **Figure 3.4** at various organic concentrations. The values for phenol in d) are from **Figure 3.2b** and are compared directly to the non-aromatic cyclohexanol values taken in a separate experiment to show the effect of the aromatic ring. A Temkin isotherm model was used to fit the data and extract the adsorption free energies. Benzaldehyde, phenol, and benzyl alcohol isotherms are divided into two sites for fitting. Furfural do not show a two-site adsorption behavior as seen for phenol. Dilution is shown by solid arrows to test the reversibility of organic adsorption. New measurements after dilution are denoted by open symbols.

Table 3.1 Measured adsorption free energies and enthalpies of organic compounds on Rh and Pt wires at 298 K in aqueous phase from hydrogen site blocking experiments. DFT calculated values adjusted using the bond-additivity model are also included.

Molecule	$\Delta G_{ads,aq,\theta=0}$ **kJ mol^{-1}** [a]	α **kJ mol^{-1}**	**Sat. frac.**	$-\Delta H^0_{ads,aq,\theta}$ **kJ mol^{-1}** [a]	$-\Delta H^0_{ads,aq,gas,\theta}$ **kJ mol^{-1}** [a]	$-\Delta H^0_{ads,aq,gas,\theta}$ **kJ mol^{-1} DFT + Bond Add.** [b]
Pt from ref [16] and measured here for furfural						
Phenol (site 1)	−29	4	0.53	41	91	130
Phenol (site 2)	−9	0	0.40	21	71	76
Benzaldehyde	−30.5	4.5	0.80	43 [c]	83	121/94
Furfural	−26.1	0	0.89	26	84	95/92
Benzyl alcohol	−33	5	0.86	32	99	159/128
Cyclohexanol [d]	−17	0	0.66	−2	69	24/ −3
Rh						
Phenol (site 1)	−26.3	0	0.62	39	89	86
Phenol (site 2)	−7	0	0.38	20	70	60
Benzaldehyde (site 1)	−26.6	1.6	0.75	39 [c]	81	124
Benzaldehyde (site 2)	−9	10	0.25	20 [c]	62	112
Furfural	−25	0	0.82	25	83	88/66
Benzyl alcohol (site 1)	−26.5	0	0.54	28	95	114
Benzyl alcohol (site 2)	−8	10	0.36	9	76	104
Cyclohexanol [d]	−3	0	0.63	−7	63	−34/−65

a. The adsorption free energies are extracted from **Figure 3.2** and **Figure 3.5**. Heats of adsorption at standard coverage $\theta^0 = 0.054$ are also listed based on conversions using the methodology described in **Chapter 2**. $-\Delta H^0_{ads,aq,\theta}$ refers to the heat of adsorption of solvated phenol and $-\Delta H^0_{ads,aq,gas,\theta}$ refers to the aqueous-phase heat of adsorption of gas-phase phenol. *b*. $-\Delta H^0_{ads,aq,gas,\theta}$ is reported here using the bond-additivity model. "Step" site values (site 1) correspond to (110) step calculations and the "terrace" sites (site 2) corresponding to (111) terraces. For molecules where two distinct adsorption sites were not found experimentally, (110) calculated values are listed first, followed by (111). *c*. Heats of adsorption measured by solution calorimetry from ref [76] on Pt/C and Rh/C were 44 kJ mol^{-1} and 39 kJ mol^{-1}, respectively. *d*. Cyclohexanol coverages did not reach saturation, so these values are estimated by using the same saturation coverage of phenol on site 1 for Rh (0.63 ML).

3.4.6 Comparing Experiments with Implicit Solvent and Bond-additivity Calculations

The aqueous-phase heats of adsorption from experiments increase in the order of benzaldehyde > phenol > benzyl alcohol > furfural >> cyclohexanol, which has the same trend as Pt in aqueous phase.[16] Furfural adsorption on Pt was not previously measured in ref [16] but is reported in the **Appendix**. The heat of adsorption for benzaldehyde on site 1 of Rh (39 kJ mol^{-1}) obtained here from the isotherm fitting is the same as the value determined from solution calorimetry of benzaldehyde on Rh/C (39 kJ mol^{-1}),[76] supporting the accuracy of this technique for estimating adsorption energies on metal surfaces. The exact order of the heats of adsorption for the aromatics differs between experiment and our computationally predicted energies (**Table 3.1**), yet this is unsurprising given the small variation in heats of adsorption on a given site, which is well within the expected accuracy of DFT-based predictions, and the assumptions/estimates of the number of waters displaced and its impact on the predicted adsorption energies. Nevertheless, the much stronger adsorption of the aromatic molecules compared with the more weakly adsorbing cyclohexanol is captured by our computational results.

The differences between experimental and predicted heats of adsorption for all five organics studied here are shown in **Figure 3.6**. Heats of adsorption were also predicted using the optB88-vdw functional,[77,78] which has been used to predict accurate gas-phase adsorption energies of phenol on Pt(111),[79] though we find no qualitative differences between using the optB88-vdw functional and PBE-D3. The heat of adsorption of each molecule on the (110) step and the (111) terrace is calculated in the gas phase and in the aqueous phase using either DFT with implicit solvent or the bond-additivity model. Here we use the (110) step to compare to the experimental site 1 and the (111) terrace to compare to site 2. The triangles for phenol in **Figure 3.6** correspond to the difference between the values shown in **Figure 3.3**. Generally, the energy of solvating organics and the penalty of displacing adsorbed water, which is explicitly accounted for in the bond-additivity model, results in a drastic reduction in the apparent adsorption energy of the organics in the aqueous phase compared with the gas phase.

For all organics, a large difference between gas-phase and experimental heats of adsorption is observed, indicating that gas-phase DFT predicts adsorption to be much stronger than what is observed experimentally in the aqueous phase. Similarly, DFT with implicit solvent predicts adsorption of the organics to be much stronger than what is experimentally measured. The heats of adsorption predicted using the bond-additivity model, however, are much closer to experimental values for all organics, with cyclohexanol as an exception. Since cyclohexanol adsorbs so weakly, we are unable to get a saturation coverage, hence the isotherm fit is poor and the extracted aqueous values may not be accurate. Furthermore, because cyclohexanol already binds weakly in the gas phase compared with the aromatics, it may have insufficient driving force to displace as many water molecules as the aromatics.

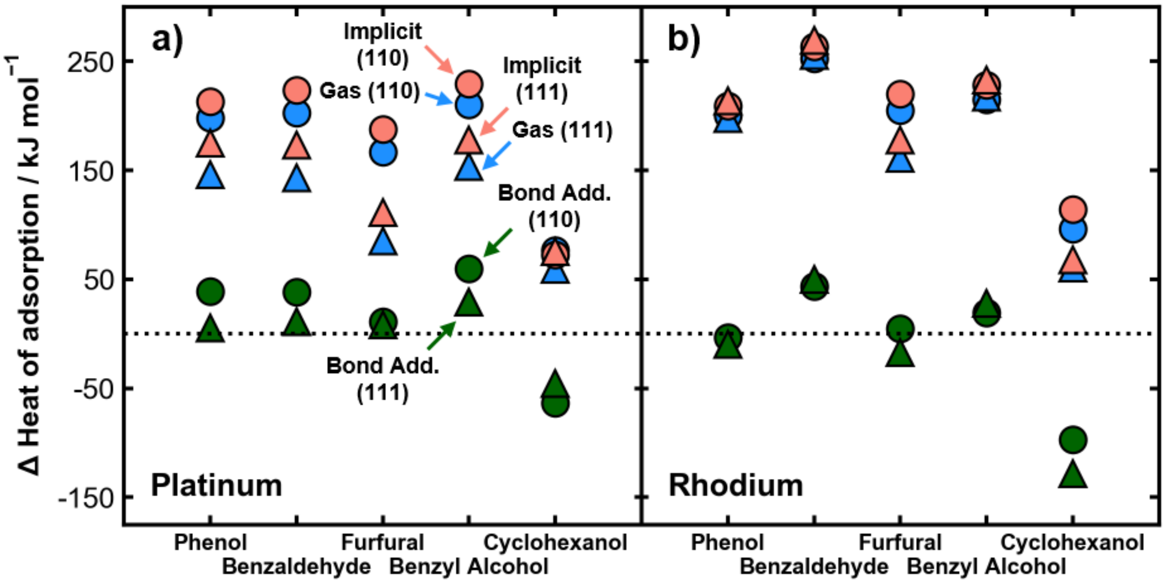

Figure 3.6. Calculated heats of adsorption using the PBE-D3 functional referenced to experimental heats of adsorption for organics using different methods. Calculations on (110) steps are compared to site 1 and (111) facets are compared to site 2. **a)** Pt(110) step and Pt(111) terrace differences between theory and experiment; **b)** Rh(110) step and Rh(111) terrace differences. Heats of adsorption are calculated in the gas phase and in the aqueous phase using an implicit solvent model or a bond-additivity model (Bond Add.). Calculated enthalpies on the (111) terrace and (110) step were referenced to the same experimental enthalpy when two distinct adsorption sites were not extracted from the isotherms. Values greater than zero indicate that adsorption is predicted by DFT to be stronger than experiment, whereas values less than zero indicate that adsorption is predicted by DFT to be weaker. Experimental values and Bond Add. values are shown in **Table 3.1.**

The number of water molecules displaced by each organic molecule (used for bond additivity) from each surface was chosen based on an estimated saturation coverage of each organic and an approximate coverage of water. Unsurprisingly, the closest agreement between bond-additivity calculations and the experimental values are for (111) terraces, where UHV work has given a more accurate understanding of the footprint of the adsorbed organic and hence number of displaced waters. Ultimately, the data in **Table 3.1** and **Figure 3.6** show that the adsorption enthalpies of the organics in aqueous phase are greatly reduced by the presence of water compared with gas-phase adsorption enthalpies, and that closer agreement with experimental measurements in aqueous phase is obtained with the bond-additivity model.

3.4.7 Consequences of Weaker Effective Organic Adsorption on Pt and Rh on Hydrogenation Rates

The comparable free energies of adsorption of phenol and benzaldehyde on Rh and Pt wires in aqueous phase may explain why there is considerable similarity in the Rh/C and Pt/C activity for both aqueous-phase thermal and electrocatalytic hydrogenation of those molecules. Aqueous-phase hydrogenation of phenol and benzaldehyde on Pt/C and Rh/C can be described using a Langmuir-Hinshelwood mechanism with a surface reaction rate-determining step,[9,76] so the adsorption energies of the organic and of hydrogen should play a key role in the observed kinetics. In particular, the adsorption energies of the reactants and intermediates will dictate the surface coverages when adsorption/desorption is fast compared to the surface reaction, thus these adsorption energies will control the reaction orders. The adsorption energies will also impact the TOF, both through the surface coverages and the activation energies. Phenol has similar TOFs and reaction orders for hydrogenation of the aromatic ring on Pt/C and Rh/C.[8,14] Benzaldehyde also shows comparable hydrogenation TOFs and reaction orders for the aldehyde group on Pt/C and Rh/C.[76] Pt and Rh have similar effective activation energies for phenol[8,9] and benzaldehyde,[76] with Rh having a slightly lower (~4 to 6 kJ mol^{-1}) effective activation energy for both reactions.

The similar hydrogen adsorption energies of Pt and Rh,[80] combined with the above evidence for aqueous-phase hydrogenation implies that there are not major differences in the organic adsorption energy on Pt and Rh. This observation is inconsistent with the different organic adsorption strengths in gas phase (e.g., phenol adsorbs 50 kJ mol^{-1} more strongly on Rh(111) than Pt(111)). However, the similar aqueous adsorption strengths for Pt and Rh in this work agree qualitatively with the observed catalytic activity for phenol and benzaldehyde hydrogenation. In addition, the much lower adsorption energy for phenol and benzaldehyde in the aqueous phase explains why these reactions can proceed at room temperature, whereas in gas phase the adsorption energy would be too strong for appreciable reaction, and desorption may be rate limiting, as opposed to the surface reaction being rate-limiting in aqueous phase. The adsorption equilibrium constant for phenol on Pt(111) using the bond-additivity model[17] in fact matches closely to the adsorption equilibrium constant for phenol hydrogenation on Pt/C,[29] whereas the adsorption constant from gas-phase or implicit solvent calculations is more than 30 orders of magnitude too large. The large difference in gas-phase and aqueous-phase adsorption energies highlights the importance of understanding adsorption in aqueous phase for catalysis, which we show can be approximated using gas-phase calculations coupled with the bond-additivity model. Although this method would enable more accurate estimates of coverage and adsorption/desorption, it would not account for solvent effects in preferentially stabilizing the transition state or identifying new reaction mechanisms that require interaction with the solvent.

3.5 Conclusions

Generally, we find that organics bind weaker in the aqueous phase compared to gas phase on Pt and Rh. This observation is well explained by a bond-additivity model that accounts for the large enthalpic penalty for displacement of multiple water molecules by the organics from the water/metal interface. Using this model, we predicted adsorption energies in aqueous phase from gas-phase calculations which match qualitatively with experiments. As a result of this water displacement enthalpy, phenol and other organics adsorb with similar strength on Pt and Rh in aqueous phase despite the considerable difference in their gas-phase adsorption enthalpies.

Although for surface reactions, this weaker adsorption in aqueous phase may apply to the energies of adsorbed products, intermediates and transition states equally relative to the adsorbed reactant species and thus may not greatly change catalytic barriers, the weakening of adsorption energies has important consequences in understanding adsorption/desorption, coverages, and TOFs. These results help explain how aromatics such as furfural, benzaldehyde, and phenol, which bind so strongly to metals in the gas phase (200–250 kJ mol^{-1}) can be hydrogenated even at room temperature in the presence of water. Additionally, these findings show how computational techniques can be used to predict and rationalize how solvents tune adsorption on metal surfaces. Understanding how solvents impact adsorption can enable the control of condensed-phase catalytic rates through selection of the solvent environment.

3.6 References

(1) EIA, U.S. Energy Information Administration. *Annual Energy Outlook 2018 with Projections to 2050*; US Energy Information Administration, Office of Energy Analysis, U.S. Department of Energy: Washington, DC 20585, **2019**.

(2) Czernik, S.; Bridgwater, A. V. Overview of Applications of Biomass Fast Pyrolysis Oil. *Energy & Fuels* **2004**, *18*, 590–598.

(3) Zhang, Q.; Chang, J.; Wang, T.; Xu, Y. Review of Biomass Pyrolysis Oil Properties and Upgrading Research. *Energy Convers. Manag.* **2007**, *48*, 87–92.

(4) Scott, D. S.; Piskorz, J.; Radlein, D. Liquid Products from the Continuous Flash Pyrolysis of Biomass. *Ind. Eng. Chem. Process Des. Dev.* **1985**, *24*, 581–588.

(5) Carneiro, J.; Nikolla, E. Electrochemical Conversion of Biomass-Based Oxygenated Compounds. *Annu. Rev. Chem. Biomol. Eng.* **2019**, *10*, 85–104.

(6) Furimsky, E. Catalytic Hydrodeoxygenation. *Appl. Catal. A Gen.* **2000**, *199*, 147–190.

(7) Carey, S. J.; Zhao, W.; Mao, Z.; Campbell, C. T. Energetics of Adsorbed Phenol on Ni(111) and Pt(111) by Calorimetry. *J. Phys. Chem. C* **2019**, *123*, 7627–7632.

(8) Singh, N.; Song, Y.; Gutiérrez, O. Y.; Camaioni, D. M.; Campbell, C. T.; Lercher, J. A. Electrocatalytic Hydrogenation of Phenol over Platinum and Rhodium: Unexpected Temperature Effects Resolved. *ACS Catal.* **2016**, *6*, 7466–7470.

(9) Song, Y.; Gutiérrez, O. Y.; Herranz, J.; Lercher, J. A. Aqueous Phase Electrocatalysis and Thermal Catalysis for the Hydrogenation of Phenol at Mild Conditions. *Appl. Catal. B Environ.* **2016**, *182*, 236–246.

(10) Sanyal, U.; Song, Y.; Singh, N.; Fulton, J. L.; Herranz, J.; Jentys, A.; Gutiérrez, O. Y.; Lercher, J. A. Structure Sensitivity in Hydrogenation Reactions on Pt/C in Aqueous-phase. *ChemCatChem* **2019**, *11*, 575–582.

(11) Sasaki, K.; Kunai, A.; Harada, J.; Nakabori, S. Electrolytic Hydrogenation of Phenols in Aqueous Acid Solutions. *Electrochim. Acta* **1983**, *28*, 671–674.

(12) Singh, N.; Lee, M. S.; Akhade, S. A.; Cheng, G.; Camaioni, D. M.; Gutiérrez, O. Y.; Glezakou, V. A.; Rousseau, R.; Lercher, J. A.; Campbell, C. T. Impact of pH on Aqueous-Phase Phenol Hydrogenation Catalyzed by Carbon-Supported Pt and Rh. *ACS Catal.* **2019**, *9*, 1120–1128.

(13) Honkela, M. L.; Björk, J.; Persson, M. Computational Study of the Adsorption and Dissociation of Phenol on Pt and Rh Surfaces. *Phys. Chem. Chem. Phys.* **2012**, *14*, 5849–5854.

(14) Song, Y.; Chia, S. H.; Sanyal, U.; Gutiérrez, O. Y.; Lercher, J. A. Integrated Catalytic and Electrocatalytic Conversion of Substituted Phenols and Diaryl Ethers. *J. Catal.* **2016**, *344*, 263–272.

(15) Werpy, T.; Petersen, G. *Top Value Added Chemicals from Biomass: Volume I -- Results of Screening for Potential Candidates from Sugars and Synthesis Gas*; Golden, CO (United States), **2004**, 6–16.

(16) Singh, N.; Sanyal, U.; Fulton, J. L.; Gutiérrez, O. Y.; Lercher, J. A.; Campbell, C. T. Quantifying Adsorption of Organic Molecules on Platinum in Aqueous Phase by Hydrogen Site Blocking and in Situ X-ray Absorption Spectroscopy. *ACS Catal.* **2019**, *9*, 6869–6881.

(17) Singh, N.; Campbell, C. T. A Simple Bond-Additivity Model Explains Large Decreases in Heats of Adsorption in Solvents Versus Gas Phase: A Case Study with Phenol on Pt(111) in Water. *ACS Catal.* **2019**, *9*, 8116–8127.

(18) Kristoffersen, H. H.; Shea, J. E.; Metiu, H. Catechol and HCl Adsorption on TiO_2(110) in Vacuum and at the Water-TiO_2 Interface. *J. Phys. Chem. Lett.* **2015**, *6*, 2277–2281.

(19) Łosiewicz, B.; Jurczakowski, R.; Lasia, A. Kinetics of Hydrogen Underpotential Deposition at Polycrystalline Rhodium in Acidic Solutions. *Electrochim. Acta* **2011**, *56*, 5746–5753.

(20) Zolfaghari, A.; Villiard, F.; Chayer, M.; Jerkiewicz, G. Hydrogen Adsorption on Pt and Rh Electrodes and Blocking of Adsorption Sites by Chemisorbed Sulfur. *J. Alloys Compd.* **1997**, *253–254*, 481–487.

(21) Jerkiewicz, G.; Zolfaghari, A. Comparison of Hydrogen Electroadsorption from the Electrolyte with Hydrogen Adsorption from the Gas Phase. *J. Electrochem. Soc.* **1996**, *143*, 1240–1248.

(22) DeBlois, M.; Lessard, J.; Jerkiewicz, G. Influence of Benzene on the H_{upd} and Anion Adsorption on Pt(110), Pt(100) and Pt(111) Electrodes in Aqueous H_2SO_4. *Electrochim. Acta* **2005**, *50*, 3517–3523.

(23) Obradović, M. D.; Lessard, J.; Jerkiewicz, G. Cyclic-Voltammetry Behavior of Pt(111) in Aqueous $HClO_4$ + C_6H_6: Influence of C_6H_6 Concentration, Scan Rate and Temperature. *J. Electroanal. Chem.* **2010**, *649*, 248–256.

(24) Gasparotto, L. H. S.; Gomes, J. F.; Tremiliosi-Filho, G. Cyclic-Voltammetry Characteristics of Poly(Vinyl Pyrrolidone) (PVP) on Single-Crystal Pt Surfaces in Aqueous H_2SO_4. *J. Electroanal. Chem.* **2011**, *663*, 48–51.

(25) Lam, C. H.; Das, S.; Erickson, N. C.; Hyzer, C. D.; Garedew, M.; Anderson, J. E.; Wallington, T. J.; Tamor, M. A.; Jackson, J. E.; Saffron, C. M. Towards Sustainable Hydrocarbon Fuels with Biomass Fast Pyrolysis Oil and Electrocatalytic Upgrading. *Sustain. Energy Fuels* **2017**, *1*, 258–266.

(26) Wieckowski, A.; Sobrowski, J.; Zelenay, P.; Franaszczuk, K. Adsorption of Acetic Acid on Platinum, Gold and Rhodium Electrodes. *Electrochim. Acta* **1981**, *26*, 1111–1119.

(27) Garrone, E.; Bolis, V.; Fubini, B.; Morterra, C. Thermodynamic and Spectroscopic Characterization of Heterogeneity among Adsorption Sites: CO on Anatase at Ambient Temperature. *Langmuir* **1989**, *5*, 892–899.

(28) Vassiliev, Y. B.; Bagotzky, V. S.; Khazova, O. A.; Cherny, V. V.; Meretsky, A. M. Mechanism of Adsorption, Electroreduction and Hydrogenation of Compounds with Ethylenic Bonds on Platinum and Rhodium: Part I. Kinetics of Adsorption and Electroreduction. *J. Electroanal. Chem. Interfacial Electrochem.* **1979**, *98*, 253–272.

(29) Singh, N.; Sanyal, U.; Ruehl, G.; Gutiérrez, O. Y.; Camaioni, D. M.; Fulton, J. L.; Lercher, J. A.; Campbell, C. T. Aqueous Phase Catalytic and Electrocatalytic Hydrogenation of Phenol and Benzaldehyde over Platinum Group Metals. *J. Catal.* **2020**, *382*, 372–384.

(30) Bard, A. J.; Faulkner, L. R. *Electrochemical Methods: Fundamentals and Applications (Vol 2)*; Wiley: New York, **2001**, 554-556.

(31) Gileadi, E. (Editor). *Electrosorption*; Springer Science & Business Media, **2012**, 93.

(32) Bockris, J. O'M; Green, M.; Swinkels, D. A. J. Adsorption of Naphthalene on Solid Metal Electrodes. *J. Electrochem. Soc.* **1964**, *111*, 743–748.

(33) Kresse, G.; Furthmüller, J. Efficiency of Ab-Initio Total Energy Calculations for Metals and Semiconductors Using a Plane-Wave Basis Set. *Comput. Mater. Sci.* **1996**, *6*, 15–50.

(34) Kresse, G.; Furthmüller, J. Efficient Iterative Schemes for Ab Initio Total-Energy Calculations Using a Plane-Wave Basis Set. *Phys. Rev. B* **1996**, *54*, 11169–11186.

(35) Goerigk, L.; Grimme, S. A Thorough Benchmark of Density Functional Methods for General Main Group Thermochemistry, Kinetics, and Noncovalent Interactions. *Phys. Chem. Chem. Phys.* **2011**, *13*, 6670–6688.

(36) Gautier, S.; Steinmann, S. N.; Michel, C.; Fleurat-Lessard, P.; Sautet, P. Molecular Adsorption at Pt(111). How Accurate Are DFT Functionals? *Phys. Chem. Chem. Phys.* **2015**, *17*, 28921–28930.

(37) Grimme, S.; Antony, J.; Ehrlich, S.; Krieg, H. A Consistent and Accurate Ab Initio Parametrization of Density Functional Dispersion Correction (DFT-D) for the 94 Elements H-Pu. *J. Chem. Phys.* **2010**, *132*, 154104.

(38) Perdew, J. P.; Burke, K.; Ernzerhof, M. Generalized Gradient Approximation Made Simple. *Phys. Rev. Lett.* **1996**, *77*, 3865–3868.

(39) Blöchl, P. E. Projector Augmented-Wave Method. *Phys. Rev. B* **1994**, *50*, 17953–17979.

(40) Haas, P.; Tran, F.; Blaha, P. Calculation of the Lattice Constant of Solids with Semilocal Functionals. *Phys. Rev. B* **2009**, *79*, 085104.

(41) Kittel, C. *Introduction to Solid State Physics*, 8th ed.; Wiley: New Jersey, 2004, 20.

(42) Saleheen, M.; Heyden, A. Liquid-Phase Modeling in Heterogeneous Catalysis. *ACS Catal.* **2018**, *8*, 2188–2194.

(43) Sievers, C.; Noda, Y.; Qi, L.; Albuquerque, E. M.; Rioux, R. M.; Scott, S. L. Phenomena Affecting Catalytic Reactions at Solid–Liquid Interfaces. *ACS Catal.* **2016**, *6*, 8286–8307.

(44) Bodenschatz, C. J.; Sarupria, S.; Getman, R. B. Molecular-Level Details about Liquid H_2O Interactions with CO and Sugar Alcohol Adsorbates on Pt(111) Calculated Using Density Functional Theory and Molecular Dynamics. *J. Phys. Chem. C* **2015**, *119*, 13642–13651.

(45) Yoon, Y.; Rousseau, R.; Weber, R. S.; Mei, D.; Lercher, J. A. First-Principles Study of Phenol Hydrogenation on Pt and Ni Catalysts in Aqueous Phase. *J. Am. Chem. Soc.* **2014**, *136*, 10287–10298.

(46) Faheem, M.; Heyden, A. Hybrid Quantum Mechanics/Molecular Mechanics Solvation Scheme for Computing Free Energies of Reactions at Metal–Water Interfaces. *J. Chem. Theory Comput.* **2014**, *10*, 3354–3368.

(47) Iyemperumal, S. K.; Deskins, N. A. Evaluating Solvent Effects at the Aqueous/Pt(111) Interface. *ChemPhysChem* **2017**, *18*, 2171–2190.

(48) Saleheen, M.; Verma, A. M.; Mamun, O.; Lu, J.; Heyden, A. Investigation of Solvent Effects on the Hydrodeoxygenation of Guaiacol over Ru Catalysts. *Catal. Sci. Technol.* **2019**, *9*, 6253–6273.

(49) Mathew, K.; Sundararaman, R.; Letchworth-Weaver, K.; Arias, T. A.; Hennig, R. G. Implicit Solvation Model for Density-Functional Study of Nanocrystal Surfaces and Reaction Pathways. *J. Chem. Phys.* **2014**, *140*, 084106.

(50) Mathew, K.; Kolluru, V. S. C.; Mula, S.; Steinmann, S. N.; Hennig, R. G. Implicit Self-Consistent Electrolyte Model in Plane-Wave Density-Functional Theory. *J. Chem. Phys* **2019**, *151*, 234101.

(51) Rumptz, J. R.; Campbell, C. T. Adhesion Energies of Solvent Films to Pt(111) and Ni(111) Surfaces by Adsorption Calorimetry. *ACS Catal.* **2019**, *9*, 11819–11825.

(52) Lew, W.; Crowe, M. C.; Karp, E.; Campbell, C. T. Energy of Molecularly Adsorbed Water on Clean Pt(111) and Pt(111) with Coadsorbed Oxygen by Calorimetry. *J. Phys. Chem. C* **2011**, *115*, 9164–9170.

(53) Lu, F.; Salaita, G. N.; Laguren-Davidson, L.; Stern, D. A.; Wellner, E.; Frank, D. G.; Batina, N.; Zapien, D. C.; Walton, N.; Hubbard, A. T. Characterization of Hydroquinone and Related Compounds Adsorbed at Pt(111) from Aqueous Solutions: Electron Energy-Loss Spectroscopy, Auger Spectroscopy, LEED, and Cyclic Voltammetry. *Langmuir* **1988**, *4*, 637–646.

(54) Farias, M. J. S.; Camara, G. A.; Feliu, J. M. Understanding the CO Preoxidation and the Intrinsic Catalytic Activity of Step Sites in Stepped Pt Surfaces in Acidic Medium. *J. Phys. Chem. C* **2015**, *119*, 20272–20282.

(55) Souza-Garcia, J.; Climent, V.; Feliu, J. M. Voltammetric Characterization of Stepped Platinum Single Crystal Surfaces Vicinal to the (110) Pole. *Electrochem. Commun.* **2009**, *11*, 1515–1518.

(56) Domke, K.; Herrero, E.; Rodes, A.; Feliu, J. M. Determination of the Potentials of Zero Total Charge of Pt(100) Stepped Surfaces in the $[01\bar{1}]$ Zone. Effect of the Step Density and Anion Adsorption. *J. Electroanal. Chem.* **2003**, *552*, 115–128.

(57) Arán-Ais, R. M.; Figueiredo, M. C.; Vidal-Iglesias, F. J.; Climent, V.; Herrero, E.; Feliu, J. M. On the Behavior of the Pt(100) and Vicinal Surfaces in Alkaline Media. *Electrochim. Acta* **2011**, *58*, 184–192.

(58) Souza-Garcia, J.; Angelucci, C. A.; Climent, V.; Feliu, J. M. Electrochemical Features of Pt(S)[n(110)×(100)] Surfaces in Acidic Media. *Electrochem. Commun.* **2013**, *34*, 291–294.

(59) Molodkina, E. B.; Danilov, A. I.; Feliu, J. M. Cu UPD at Pt(100) and Stepped Faces Pt(610), Pt(410) of Platinum Single Crystal Electrodes. *Russ. J. Electrochem.* **2016**, *52*, 890–900.

(60) Sasahara, A.; Tamura, H.; Tanaka, K. Catalytic Activity of Pt-Deposited Rh(110) Bimetallic Surface for NO + H_2 Reaction. *J. Phys. Chem. B* **1997**, *101*, 1186–1189.

(61) Wasberg, M.; Hourani, M.; Wieckowski, A. Comparison of Voltammetry of Vacuum-Prepared Rh (100) and Rh (111) Electrodes. *J. Electroanal. Chem. Interfacial Electrochem.* **1990**, *278*, 425–432.

(62) Clavilier, J.; Wasberg, M.; Petit, M.; Klein, L. H. Detailed Analysis of the Voltammetry of Rh(111) in Perchloric Acid Solution. *J. Electroanal. Chem.* **1994**, *374*, 123–131.

(63) Hourani, M.; Wieckowski, A. Single Crystal Electrochemistry of Rhodium: Anion Effects and Order/Disorder Transitions of Clean and Silver Coated Rh (111) Surfaces. *J. Electroanal. Chem. Interfacial Electrochem.* **1988**, *244*, 147–161.

(64) Bockris, J. O.; Jeng, K. T. In-Situ Studies of Adsorption of Organic Compounds on Platinum Electrodes. *J. Electroanal. Chem.* **1992**, *330*, 541–581.

(65) McCrum, I. T.; Hickner, M. A.; Janik, M. J. First-Principles Calculation of Pt Surface Energies in an Electrochemical Environment: Thermodynamic Driving Forces for Surface Faceting and Nanoparticle Reconstruction. *Langmuir* **2017**, *33*, 7043–7052.

(66) Campbell, C. T.; Sellers, J. R. V. The Entropies of Adsorbed Molecules. *J. Am. Chem. Soc.* **2012**, *134*, 18109–18115.

(67) Weaver, M. J. Potentials of Zero Charge for Platinum(111)−Aqueous Interfaces: A Combined Assessment from In-Situ and Ultrahigh-Vacuum Measurements. *Langmuir* **1998**, *14*, 3932–3936.

(68) Gómez, R.; Feliu, J. M.; Aldaz, A.; Weaver, M. J. Validity of Double-Layer Charge-Corrected Voltammetry for Assaying Carbon Monoxide Coverages on Ordered Transition Metals: Comparisons with Adlayer Structures in Electrochemical and Ultrahigh Vacuum Environments. *Surf. Sci.* **1998**, *410*, 48–61.

(69) Xu, Q.; Linke, U.; Bujak, R.; Wandlowski, T. Preparation and Electrochemical Characterization of Low-Index Rhodium Single Crystal Electrodes in Sulfuric Acid. *Electrochim. Acta* **2009**, *54*, 5509–5521.

(70) Gileadi, E. Electrosorption of Uncharged Molecules on Solid Electrodes. *J. Electroanal. Chem (1959).* **1966**, *11*, 137–151.

(71) Meng, S.; Wang, E. G.; Gao, S. Water Adsorption on Metal Surfaces: A General Picture from Density Functional Theory Studies. *Phys. Rev. B* **2004**, *69*, 195404.

(72) Wagner, F. T.; Moylan, T. E. A Comparison between Water Adsorbed on Rh(111) and Pt(111), with and without Predosed Oxygen. *Surf. Sci.* **1987**, *191*, 121–146.

(73) Román, A. M.; Hasse, J. C.; Medlin, J. W.; Holewinski, A. Elucidating Acidic Electro-Oxidation Pathways of Furfural on Platinum. *ACS Catal.* **2019**, *9*, 10305–10316.

(74) Gong, L.; Agrawal, N.; Roman, A.; Holewinski, A.; Janik, M. J. Density Functional Theory Study of Furfural Electrochemical Oxidation on the Pt (111) Surface. *J. Catal.* **2019**, *373*, 322–335.

(75) Jing, Z.; Whitten, J. L. The Adsorption of Benzene on Ni(111). *Surf. Sci.* **1991**, *250*, 147–158.

(76) Song, Y.; Sanyal, U.; Pangotra, D.; Holladay, J. D.; Camaioni, D. M.; Gutiérrez, O. Y.; Lercher, J. A. Hydrogenation of Benzaldehyde via Electrocatalysis and Thermal Catalysis on Carbon-Supported Metals. *J. Catal.* **2018**, *359*, 68–75.

(77) Klimeš, J.; Bowler, D. R.; Michaelides, A. Chemical Accuracy for the van Der Waals Density Functional. *J. Phys. Condens. Matter* **2010**, *22*, 022201.

(78) Klimeš, J.; Bowler, D. R.; Michaelides, A. Van Der Waals Density Functionals Applied to Solids. *Phys. Rev. B - Condens. Matter Mater. Phys.* **2011**, *83*, 195131.

(79) Jia, X.; An, W. Adsorption of Monocyclic Aromatics on Transition Metal Surfaces: Insight into Variation of Binding Strength from First-Principles. *J. Phys. Chem. C* **2018**, *122*, 21897–21909.

(80) Gorodetskii, V. V.; Nieuwenhuys, B. E.; Sachtler, W. M. H.; Boreskov, G. K. Adsorption of Hydrogen on Rhodium; Comparison with Hydrogen Adsorption on Platinum and Iridium. *Surf. Sci.* **1981**, *108*, 225–234.

Chapter 4 Temperature Dependence of Aqueous-Phase Phenol Adsorption on Pt and Rh

This chapter is adapted from **Akinola, J.;** Singh, N. Temperature Dependence of Aqueous-Phase Phenol Adsorption on Pt and Rh. *J. Appl. Electrochem.* **2021**, *51*, 37–50. Copyright Journal of Applied Electrochemistry.

4.1 Summary

Condensed/aqueous phase surface reactions such as electrocatalytic hydrogenation of bio-oil often involve reactant adsorption and displacement of adsorbed solvent molecules. The enthalpy and entropy of these adsorption processes will influence the kinetics of surface reactions in the condensed/aqueous phase. The value of the adsorption entropy will have a significant effect on how the reactant coverages vary as a function of temperature. Here, adsorption isotherms from 10 to 40 °C and van't Hoff plots were constructed to directly extract the adsorption entropy and enthalpy of phenol, a bio-oil model compound, on Pt and Rh in aqueous media. We show that the effective adsorption entropy of phenol on Pt and Rh in aqueous phase is positive, in contrast to the negative entropy expected in gas phase. The positive entropy values in the aqueous phase are consistent with adsorbed water gaining a fraction of the entropy of bulk liquid water upon displacement by adsorbed phenol. Consequently, the phenol surface coverage is less dependent on temperature in the aqueous phase compared to the gas phase. The results here give insight to the way in which temperature impacts reaction rates for aqueous-phase phenol hydrogenation reaction.

4.2 Introduction

Electrochemical conversion of biomass has been proposed as a method to convert waste to value-added streams, with numerous examples of model compounds being converted through electrocatalytic hydrogenation.[1–11] Technoeconomic analyses show that achieving high turnover frequencies at low overvoltages is necessary for an economically feasible process.[12] Reaching these high turnover frequencies at low overvoltages requires developing new electrocatalysts and understanding how to control reaction conditions, such as temperature, to obtain the desired rates. For gas-phase catalytic reactions, the temperature dependence of reaction rates can be understood through the intrinsic activation barrier as well as the adsorption thermodynamics of the reacting species and possible poisoning species.[13] This understanding of gas-phase catalytic reactions allows greater control and reactor design of these systems, as new sets of experiments are not needed for every new temperature or reactant concentration. Instead, the rates can be predicted using models that describe the coverages and rate constants as a function of reaction conditions. Similar concepts have been used in electrochemical conversion of waste biomass or model compounds to understand and prevent catalyst poisoning by dehydrogenation at elevated temperatures.[14] and to understand how adsorption geometry and energy of reacting species affects reaction rates.[15–17] However, a predictive understanding of how reactant coverages vary with temperature for condensed-phase surface reactions (e.g., bio-oil hydrogenation) does not exist mainly because of the complexity of competitive adsorption and solvent displacement in condensed phase. Developing a model for the thermodynamics of organic compounds' adsorption on metal catalysts in the condensed phase will aid design of surface reactions like bio-oil hydrogenation. To address this, here we probe the adsorption of a model compound, phenol in aqueous acetate buffer, on Pt and Rh as a function of temperature to determine the enthalpy and entropy of adsorption. Although bio-oil contains a variety of organic compounds other than phenols such as furans and aldehydes dissolved in aqueous acidic media,[18–20] we use phenol as a simple model compound to study the effect of water on the entropy of adsorption. A real bio-oil stream has a great deal more complexity, however, the fundamental findings for phenol can help to understand adsorption in the aqueous-phase that can be used to interpret and predict reactivity data as a function of temperature.

Unlike in the gas phase where sufficient studies of adsorption have been done to allow accurate predictive models of adsorption entropies to be developed,[21] there are fewer aqueous-phase studies. Our recent report has compared electrosorption (i.e., adsorption on electrode surfaces) of organic compounds to the gas phase adsorption of the same compounds.[22] The results showed that by incorporating different solvent effects, such as the enthalpic penalty of displacing adsorbed water from the metal surface,[23] general semi-quantitative agreement of enthalpies of adsorption in the aqueous and gas phases can be reached. This model is similar to the models used by Bockris[24] and Gileadi[25] that describe electrosorption as a replacement reaction. To obtain these enthalpies from adsorption free energies, the entropy of adsorption of gas-phase phenol (or other organics) was assumed to be the same whether the solvent layer was present. Thus, the entropy of adsorption of phenol was approximated to be negative, regardless of whether or not the solvent layer was present. This assumption was supported by the fact that the enthalpies determined using this assumption for aqueous-phase benzaldehyde adsorption on polycrystalline Pt[22] and Rh[26] were within 3 kJ mol^{-1} of the heat of adsorption measured directly by aqueous-phase calorimetry for benzaldehyde adsorption on Pt/C and Rh/C.[2]

Although this entropy approximation gave agreement in the measured heats of adsorption, a direct measurement of the entropy would be more valuable and would give information on whether the entropy of adsorption in aqueous phase is actually negative or positive. For example, the aqueous-phase adsorption entropy of statherin onto powdered hydroxyapatite surfaces at 298 K is positive,[27] implying the loss of organized water at the interface upon adsorption of statherin causes an increase in overall entropy. The adsorption of various organics on polycrystalline Pt has also been studied as a function of temperature and the positive entropy of adsorption was attributed to competing effects between water desorption and organic adsorption.[24,28] That is, the entropy of adsorption in aqueous phase is more positive than in gas phase due to the gain of entropy upon water displacement during organic adsorption. The sign of the adsorption entropy (whether negative or positive) will have large consequences on the temperature dependence of adsorption and will give insight into the interfacial water structure. Thus, it is important to understand the adsorption entropy when considering electrocatalytic hydrogenation reactions that follow surface reaction limited mechanisms, such as phenol hydrogenation on Pt and Rh.[29] Therefore, the goal of the work presented here is to identify the influence of temperature on phenol adsorption on Rh and Pt in order to probe the contributions of entropy and enthalpy on adsorption, particularly the role of the displaced water at the interface. By understanding these effects, one can predict how factors such as temperature and water displacement influence the adsorbate coverages and thus the kinetics of electrochemical reactions.

Hydrogen underpotential deposition (H_{upd}) on Pt and Rh was used to probe the amount of surface sites blocked by adsorbed phenol to determine phenol coverage. Repeating these measurements at various concentrations of phenol allows the construction of an adsorption isotherm that can be fitted to obtain equilibrium adsorption constants. By measuring the adsorption isotherms as a function of temperature, we extract the enthalpy and entropy of adsorption and compare this to estimates of the entropy using approximations of the entropy of gas phase, aqueous phase, and adsorbed species. Our major finding is that the coverage of adsorbed phenol on Pt and Rh at a particular bulk phenol concentration is relatively unchanged over the range of temperatures studied, indicating an entropy of adsorption near zero. This observation is consistent with a model where the water molecules displaced by phenol adsorption gain a fraction of the entropy of liquid water, resulting in a more positive adsorption entropy for aqueous phenol adsorption than the negative value in gas phase. The relatively constant coverage of phenol on the surface of Pt and Rh in water implies that the major changes in reaction rates for aqueous-phase hydrogenation with temperature are from a change in the rate constant, rather than changes in the coverage of the reacting species. This understanding can give a greater control over the rate in condensed phase reactions as a function of temperature.

4.3 Experimental Section

4.3.1 Cyclic Voltammetry

We quantify the adsorption of phenol using H_{upd} as detailed in earlier work, where the H_{upd} charge was measured at varying organic concentrations to count the number of surface metal sites that do not have adsorbed phenol.[22,26,30] The phenol coverage from H_{upd} matches a radiotracer measurement at similar bulk phenol concentrations.[24] The working electrode was either a polycrystalline Pt wire (0.5 mm diameter, 99.997% Alfa Aesar) or Rh wire (0.5 mm diameter, 99.8% Alfa Aesar). The working electrodes were cleaned by exposing to a flame to remove any adventitious organics, and afterwards rinsed with Milli-Q water (18.2 MΩ resistivity). A jacketed two-compartment electrochemical cell with a working and reference electrode compartment and a counter electrode compartment separated by a N117® Nafion membrane was used for all measurements. The temperature was controlled by a refrigerated/heated bath circulator (Fisher Scientific) and verified with a thermometer inserted directly to the cell solution. Introducing phenol into the cell varied the temperature of the solution by ±1 °C, but the cyclic voltammogram was taken when the temperature was equilibrated to the desired temperature in the cell. The maximum temperature studied in this work was 41 °C to prevent phenol from evaporating and also avoid the formation of dehydrogenated phenol that occurs at higher temperatures.[14] Before each use, the cell was cleaned with Milli-Q water and oven dried three times. An Ag/AgCl reference electrode was used for the studies, and all potentials are reported vs. reversible hydrogen electrode (RHE) after calibration at the desired temperature. A graphite rod counter electrode was used for all measurements. Acetate buffer (pH 5) containing 100 mM acetic acid (Sigma Aldrich, 99.995%) and 100 mM sodium acetate (Sigma Aldrich 99.999%) was used as supporting electrolyte. Acetate has negligible adsorption on Pt and Rh in the H_{upd} region (0.05 to 0.4 V vs. RHE) and so is not expected to compete with hydrogen or phenol adsorption.[31] However, in our analysis we neglect any effects acetic acid in the solution phase may have on adsorption processes. The organic used for adsorption studies was phenol (Sigma Aldrich, >99%). An SP-150 Bio-Logic potentiostat was used for the CV experiments. All measurements were conducted after sparging with N_2 to remove dissolved oxygen, and with N_2 blanketing during the measurements.

4.3.2 Adsorption Isotherm Fitting

The adsorption isotherms constructed by measuring the inhibition of H_{upd} charge at varying phenol concentrations were fitted using a Temkin model as detailed in earlier work.[22] The Temkin model accounts for situations where adsorption energies decrease linearly with coverage due to adsorbate-adsorbate interactions.[32,33] For given values of the free energy at zero coverage ($\Delta G_{ad,aq,\theta=0}$) and its coverage dependence (α), a theoretical phenol coverage vs. concentration plot can be generated. The $\Delta G_{ad,aq,\theta=0}$ and α values were iterated until the phenol coverage vs. concentration matched the experimental values in the adsorption isotherm. Other adsorption models such as the Flory-Huggins isotherm may also be able capture the information here but we chose the Temkin isotherm as the simplest adsorption model that fits the data and to enable comparison to previous work by Bockris that uses the same model.[24] The free energies and equilibrium constants determined by this method as a function of temperature (van't Hoff plot) were analyzed to extract adsorption enthalpies and entropies. Because the adsorption free energies are extracted by examining adsorption within the potential range of 0.05 to 0.4 V vs. RHE, the surface charge of the electrode will vary, depending on the potential of zero charge of the electrode. Generally, the effect of surface charge is to increase the water adsorption layer strength,[25] which weakens the effective adsorption energy of the organic. Nevertheless, the adsorption energies extracted through this method and gas-phase calorimetry agree once the effects of the water layer have been included.[23]

4.4 Results and Discussion

4.4.1 Temperature Dependence of Phenol Adsorption and Hydrogen Underpotential Deposition on Pt

The hydrogen underpotential region on Pt is shown in **Figure 4.1** at different temperatures, where in all cases the addition of phenol into the solution decreases the H_{upd} current density. The decreasing H_{upd} current density indicates fewer available surface Pt atoms for H to adsorb. This inhibition of open Pt sites is due to the competitive adsorption of phenol with hydrogen on Pt sites.[22,26] In situ X-ray absorption spectroscopy has also provided direct evidence of phenol competing with hydrogen for Pt surface sites.[34] Phenol adsorption/desorption is an equilibrated process as seen by the reversible desorption upon dilution of the bulk phenol concentration.[26]

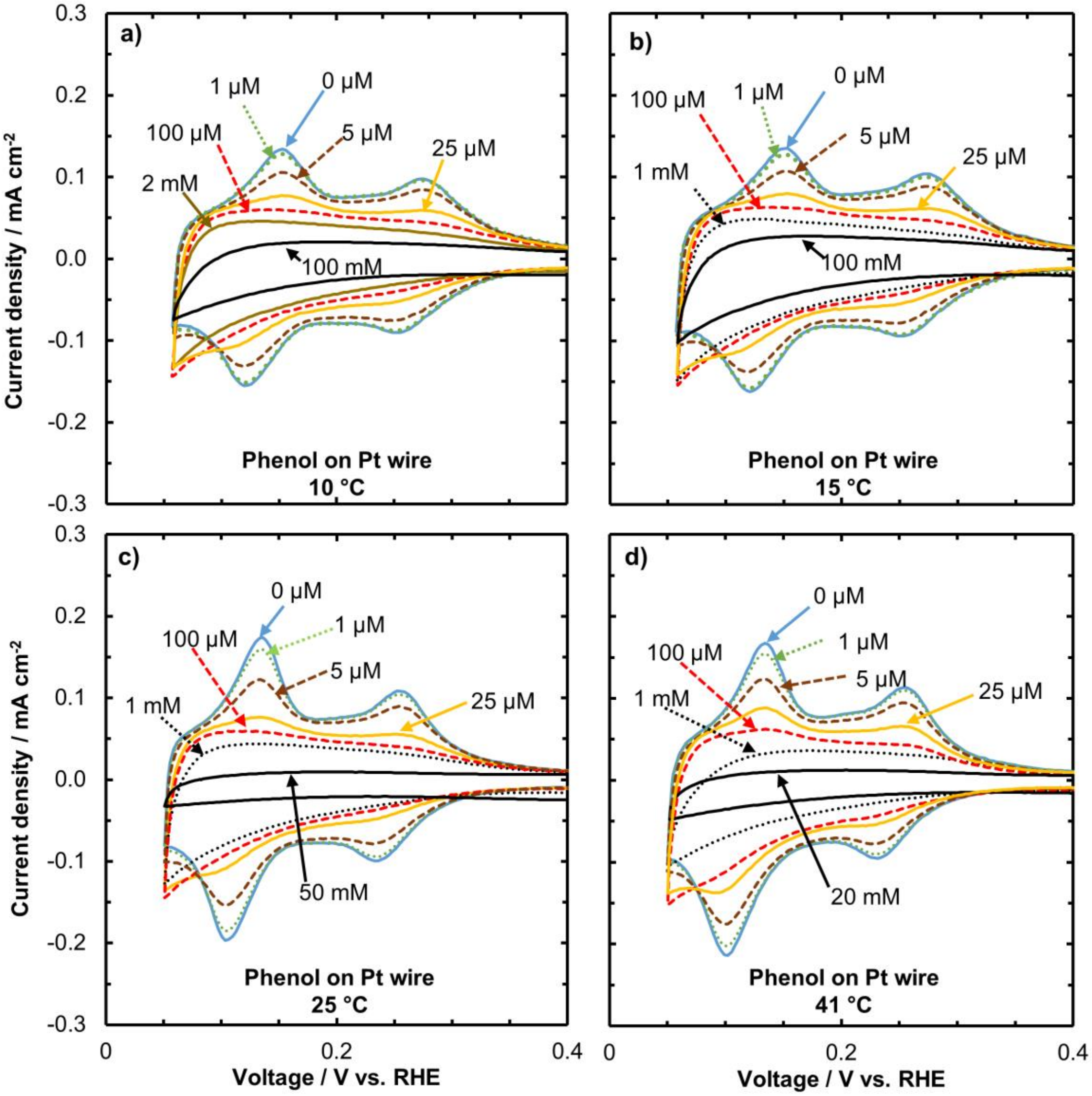

Figure 4.1 Cyclic voltammograms of a Pt wire in 100 mM acetate buffer supporting electrolyte showing the hydrogen underpotential deposition region at different phenol concentrations and temperatures. a) 10 °C, **b)** 15 °C, **c)** 25 °C, reproduced from ref [26], and **d)** 41 °C. The scan rate is 100 mV s^{-1} and the current density is relative to the electrochemically active surface area (ECSA) of Pt. The ECSA was estimated by integrating the H_{upd} current in the absence of phenol with respect to time to get a H_{upd} charge, then dividing that H_{upd} charge by the charge density of polycrystalline Pt (210 µC cm^{-2}).[35,36] A Ag/AgCl double junction electrode calibrated to RHE at the specified temperature is the reference electrode and a carbon rod is the counter electrode.

The H_{upd} adsorption/desorption peak voltages of the different Pt facets shift slightly negative (< 20 mV) with increasing temperature, consistent with temperature studies on Pt single crystal,[37] and polycrystalline samples.[38] This change in the voltage of hydrogen adsorption/desorption implies that the change in adsorption free energy of H on Pt is less than 2 kJ mol^{-1} within the temperature range studied here.[37,38] Although there might be a lower coverage of adsorbed hydrogen on Pt (in the absence of phenol) at higher temperatures,[37,38] the electrochemically active surface area (ECSA) was estimated with a constant charge density of 210 μC cm^{-2}.[35,36] The charge density of 210 μC cm^{-2} is based on measurements for polycrystalline Pt at 298 K, and is known to change with temperature, reducing slightly for Pt(111) facets but increasing for Pt(110) and (100) facets.[37] The CV currents were normalized to the approximated ECSA calculated by integrating the charge in the H_{upd} region in the absence of phenol in **Figure 4.1** at a given temperature.

Figure 4.2 shows the fraction of H_{upd} blocked on Pt as a function of phenol concentration for the different temperatures studied in **Figure 4.1**. The fraction of H_{upd} inhibited is estimated from the difference in H_{upd} charge with and without adsorbed phenol from **Figure 4.1** at a given temperature, divided by the H_{upd} charge without adsorbed phenol at that same temperature. Because we evaluate the relative change in H_{upd} charge with phenol at any given temperature by normalizing to the H_{upd} charge in the absence of phenol at that same temperature, we avoid inaccuracies associated with the constant charge density assumption discussed above. Thus, we are extracting information associated with the phenol coverage at that temperature, assuming that phenol and hydrogen are still competing for sites. A phenol adsorption isotherm is constructed for each of the temperatures studied and fitted to a two-site Temkin model to extract adsorption free energies ($\Delta G_{ad,aq}$) and equilibrium constants ($K_{ad,aq}^{eq}$) for each of the four temperatures. The values shown in **Figure 4.2** are for the adsorption free energies and equilibrium constants at zero phenol coverage ($\theta = 0$), where $\Delta G_{ad,aq} = \Delta G_{ad,aq,\theta=0} + \alpha\theta$. The values of α, which correspond to how adsorption is weakened with increasing phenol coverage, are included in **Table 4.1**, and range from 0 to 2 kJ mol^{-1}.

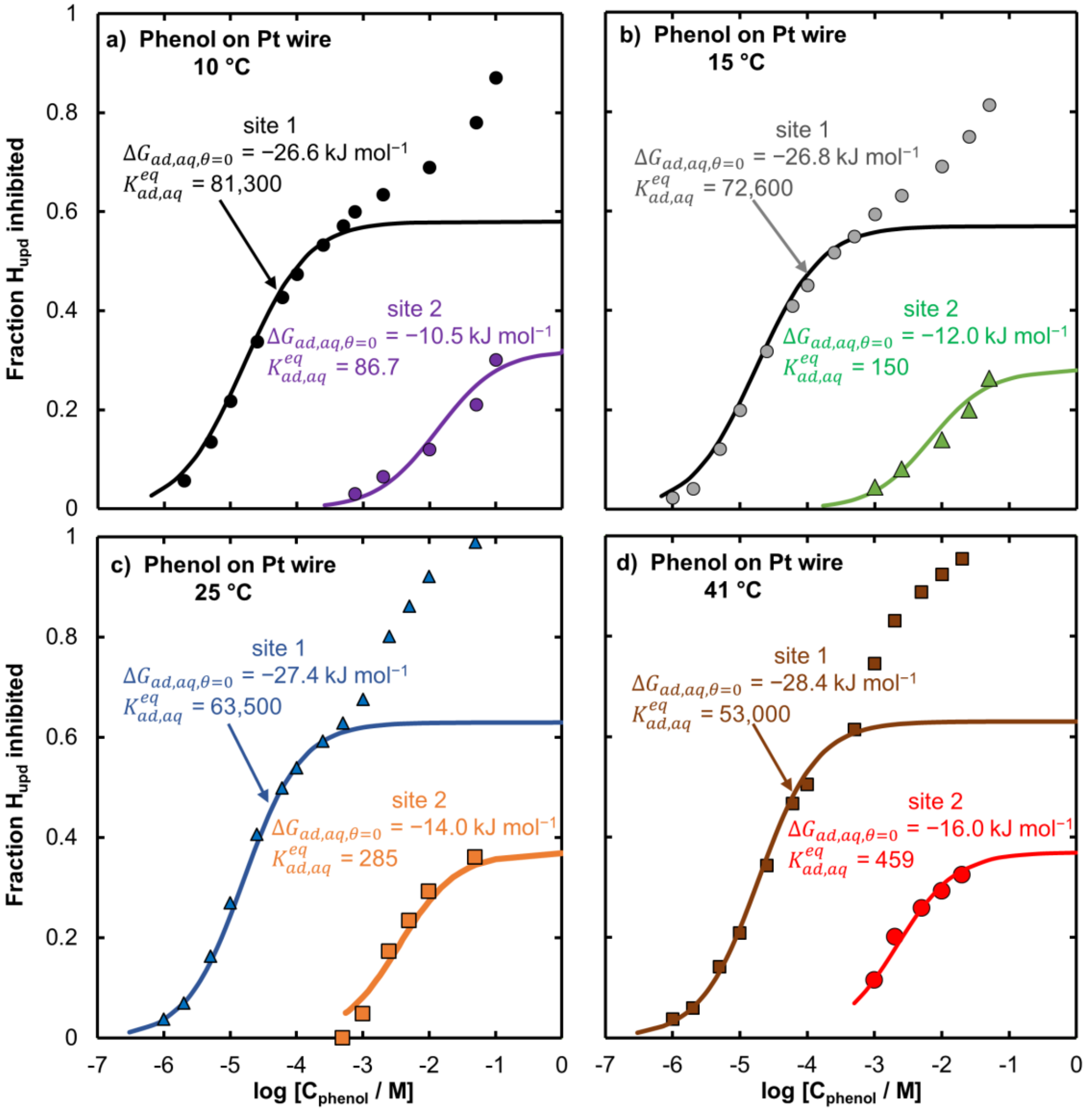

Figure 4.2 Fraction of hydrogen underpotential deposition charge inhibited as a function of phenol concentration on Pt at varying temperatures. a) 10 °C **b)** 15 °C **c)** 25 °C reproduced from ref [2] **d)** 41 °C. The fraction of H_{upd} inhibited is obtained from the difference in H_{upd} charge with and without phenol in Figure 4.1. The data here is fitted to a two-site Temkin model where site 1 is the stronger binding site and site 2 is the weaker binding site. Adsorption free energies ($\Delta G_{ad,aq,\theta=0}$) and equilibrium adsorption constants ($K_{ad,aq}^{eq}$) at zero coverage are given at the different solution temperatures. See Table 4.1 for complete set of values including coverage dependence on energies.

Based on previous work identifying at which phenol concentrations the H_{upd} peaks for different facets decrease, the stronger binding sites (site 1) are attributed to Pt steps, while the weaker binding sites (site 2) are terraces.[22,26] Both sites have a minor temperature dependence on $K_{ad,aq}^{eq}$. The $K_{ad,aq}^{eq}$ for the stronger binding site 1 decreases slightly with temperature, indicating phenol adsorption is slightly exothermic in aqueous phase, whereas the $K_{ad,aq}^{eq}$ for the weaker binding site 2 increases with temperature, indicating the adsorption enthalpy is endothermic. For both sites, $\Delta G_{ad,aq}$ decreases slightly with temperature.

The minor dependence of the free energies and adsorption equilibrium constant of phenol on Pt with temperature contrasts with the significant temperature variation expected for gas-phase adsorption. In gas-phase adsorption, because of the large entropy loss from a loss of translational degrees of freedom upon adsorption, a temperature increase will cause the adsorption free energy to be more positive according to **Eq. 4.1**.

$$\Delta G_{ad,gas} = \Delta H_{ad,gas} - T\Delta S_{ad,gas} \tag{4.1}$$

Here $\Delta G_{ad,gas}$ is the gas-phase adsorption free energy, $\Delta H_{ad,gas}$ is the enthalpy of adsorption in gas phase, T is temperature and $\Delta S_{ad,gas}$ is the gas-phase adsorption entropy, which is often a large negative value. Thus, in the gas phase, higher temperatures generally result in smaller equilibrium adsorption constants, and decreased coverages of the reactant species. Because in this aqueous environment the equilibrium adsorption constant and phenol coverage is relatively unchanged with temperature, an increase in temperature can be used to increase the rate constant without appreciable decrease in the surface coverage of phenol. In the next section we explore the role of entropy and enthalpy on this relatively constant phenol coverage on Pt in the aqueous phase.

4.4.2 Enthalpy and Entropy of Adsorption of Gas-Phase Phenol compared to Aqueous-Phase Phenol

Figure 4.3 shows the natural log of the aqueous adsorption equilibrium constant of phenol at zero coverage ($K_{ad,aq}^{eq}$) from **Figure 4.2** as a function of inverse temperature for the stronger binding Pt step sites (**Figure 4.3a**) and the weaker binding Pt terrace sites (**Figure 4.3b**). The fitted lines of these van't Hoff plots give the value of $\Delta S_{ad,aq}/R$ and $\Delta H_{ad,aq}/R$ for phenol$_{(aq)}$ on Pt as the intercept and slope, respectively, where R is the gas constant, 8.314 J mol^{-1} K^{-1}. Note that here $\Delta S_{ad,aq}$ refers to the adsorption of phenol$_{(aq)}$, not phenol$_{(g)}$.

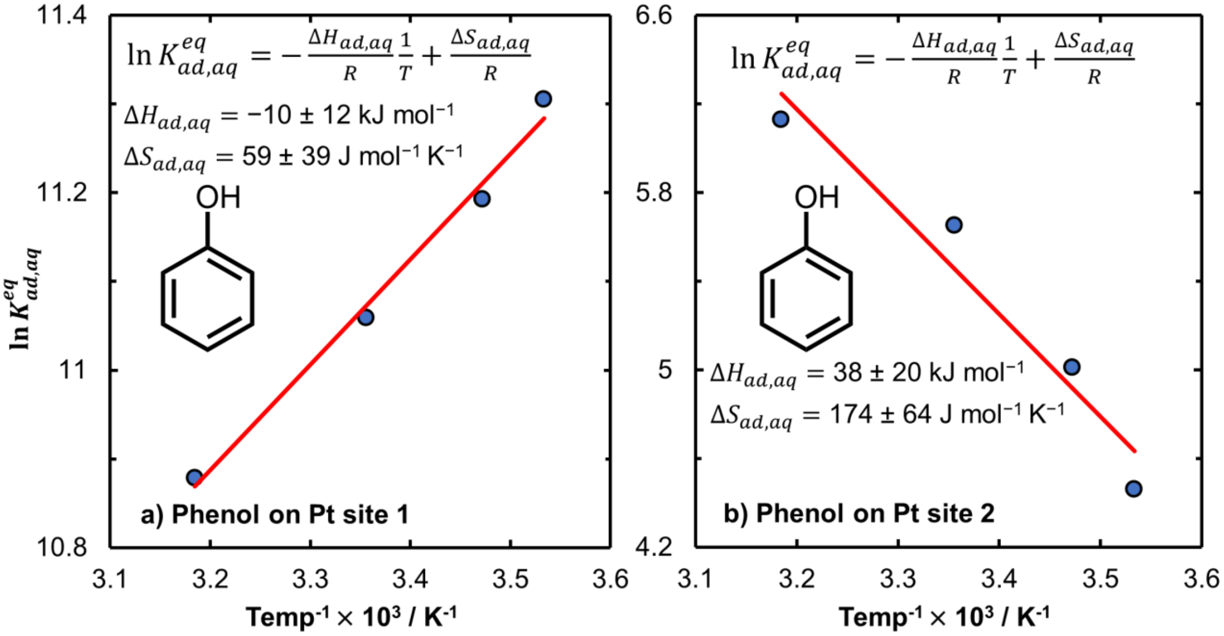

Figure 4.3 Natural log of aqueous-phase adsorption constant of phenol on platinum from Figure 4.2 plotted as a function of inverse temperature (van't Hoff plot) on Pt. a) Stronger binding site 1 of Pt. **b)** Weaker binding site 2 of Pt. The enthalpy of adsorption and entropy of adsorption are included based on fitting the data.

Although there are inaccuracies in van't Hoff plots for extracting enthalpies due to the assumption that the enthalpy is temperature independent (in reality enthalpies change with temperature through the heat capacity), this error is a less significant issue for heats of adsorption, as the temperature dependence would only arise if the heat capacity of the free and adsorbed species are different. For gases, the heat of adsorption is generally almost independent of temperature,[39] so here we assume that the enthalpy of adsorption of phenol is constant with temperature. The measured enthalpy of adsorption of aqueous phenol on Pt ($\Delta H_{ad,aq}$) from Bockris and Jeng is +15.9 kJ mol^{-1} and the entropy of adsorption ($\Delta S_{ad,aq}$) is 188 J mol^{-1} K^{-1},[24] however the supporting electrolyte used in that work was HCl, and Cl^{-} adsorption on Pt was discussed as a potential error in the measured values.[24] In our work here in acetate buffer electrolyte, the enthalpy and entropy are −10 kJ mol^{-1} and 59 J mol^{-1} K^{-1}, respectively, on the stronger binding sites of Pt (attributed to steps, or Pt(110) and Pt(100))[22,26] and 38 kJ mol^{-1} and 174 J mol^{-1} K^{-1} on the weaker binding sites. Acetate has been previously shown to have negligible adsorption on Pt in the H_{upd} potential region where this work was conducted.[31] Although the free energies of adsorption ($\Delta G_{ad,aq}$) here match those we have recently reported, these adsorption enthalpy values are weaker than in that work,[22,26] which we will explain later that is due to the entropy approximation of the water layer upon adsorption of phenol, which gave a more negative entropy of phenol adsorption than measured here. In the next section we show that this observation is not limited to Pt, but also occurs on Rh.

4.4.3 Entropy and Enthalpy of Adsorption of Phenol on Rh

The fractions of underpotentially deposited hydrogen inhibited by phenol adsorption on Rh at different temperatures are shown in **Figure 4.4**. As for Pt, a two-site Temkin adsorption model was used to fit the adsorption isotherm and extract adsorption energies for Rh, where again site 1 is attributed to the stronger binding Rh(110) and Rh(100) steps and site 2 is attributed to Rh(111).[26] The phenol coverage on Rh at a given concentration is also relatively unchanging with temperature, like Pt, indicating that the aqueous phenol adsorption entropy is also slightly positive on Rh.

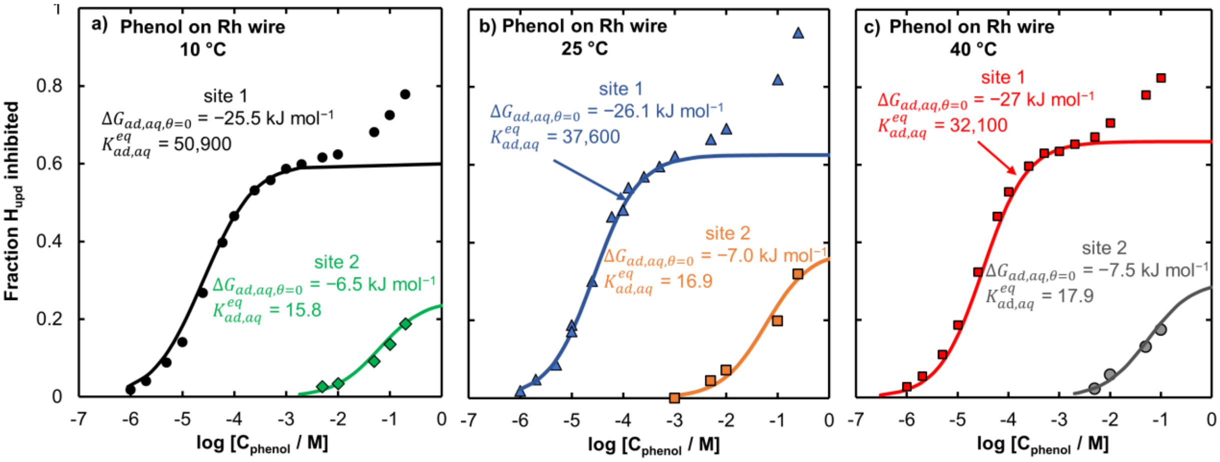

Figure 4.4 Fraction of hydrogen underpotential deposition charge inhibited as a function of phenol concentration on Rh at varying temperatures. a) 10 °C **b)** 25 °C reproduced from ref [26] **c)** 40 °C. The data is fitted to a two site Temkin adsorption model where site 1 is the stronger binding site and site 2 is the weaker binding site. Adsorption free energies and equilibrium adsorption constants are given at the different solution temperatures. See Table 4.1 for complete set of values including coverage dependence on energies.

The van't Hoff plots for the adsorption on Rh constructed from the adsorption equilibrium constants for Rh are shown in **Figure 4.5a** for site 1 and **Figure 4.5b** for site 2. The adsorption enthalpy ($\Delta H_{ad,aq}$) for site 1 is −11 ± 13 kJ mol^{-1} and for site 2 is +3.0 ± 12 kJ mol^{-1}. Like Pt, these are slightly more positive than the values estimated previously using the entropy approximation,[26] rather than direct measurement. The adsorption entropy value ($\Delta S_{ad,aq}$), for site 1 is 50 ± 43 J mol^{-1} K^{-1} and 33 ± 50 J mol^{-1} K^{-1} for site 2. The stronger binding site on Pt, shown in **Figure 4.3a**, had a similar adsorption entropy (59 ± 39 J mol^{-1} K^{-1}) as for Rh site 1 and 2. The entropy of adsorption of the weaker binding Pt site (site 2, attributed to Pt terraces) had a larger positive entropy, but it is unclear if this is an actual difference from the Rh sites/Pt site 2 vs. Pt site 1, or is related to potential errors in using the van't Hoff plot, where small experimental uncertainty can have a large effect on $\Delta S_{ad,aq}$.

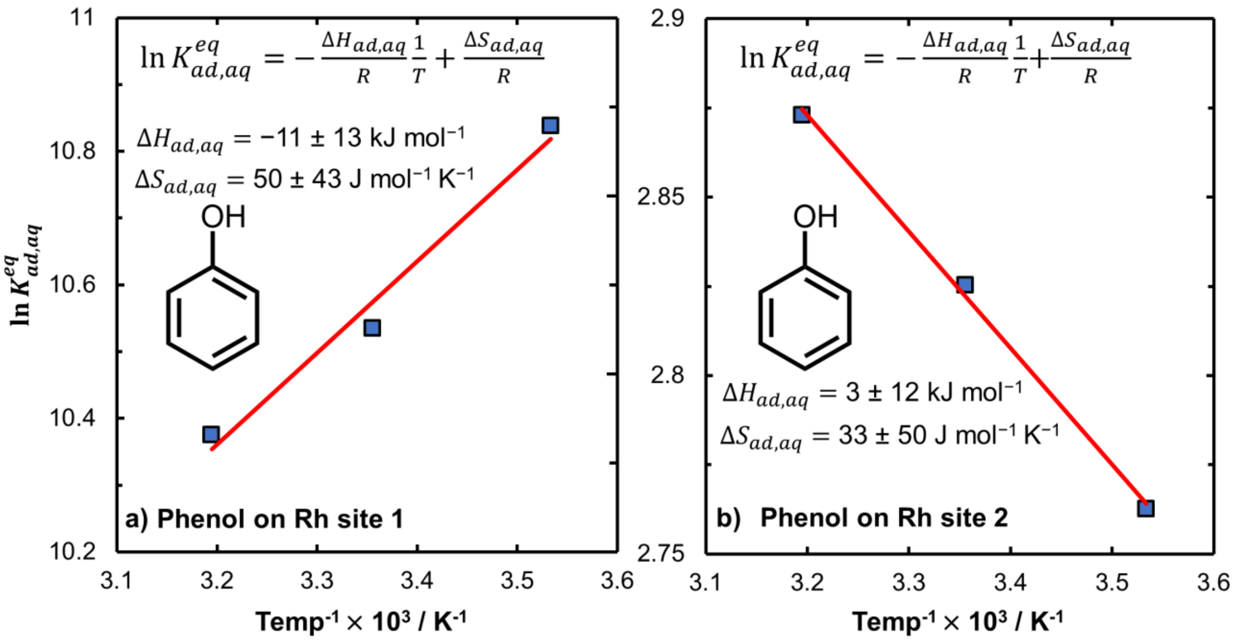

Figure 4.5 The van't Hoff plots of the adsorption of phenol on Rh. a) Stronger binding site 1 of Rh. **b)** Weaker binding site 2 of Rh. Natural log of aqueous-phase adsorption constant of phenol on rhodium from Figure 4.4 plotted as a function of inverse temperature. The slope is negative of the enthalpy of adsorption divided by *R* and the intercept is the entropy of adsorption divided by *R*.

The positive entropy of adsorption for all cases is consistent with the fact that the displaced water layer upon phenol adsorption increases the overall adsorption entropy, as posited by Bockris[24] and Gileadi.[25] In the following sections this measured entropy is compared to the gas-phase entropy of adsorption using known correlations for adsorbing species. The positive phenol adsorption entropies on Pt and Rh imply that the structure of the water layer after being displaced is more disordered than the adsorbed water layer. The adsorption free energies, equilibrium constants, enthalpies and entropies of phenol on Pt and Rh are given in **Table 4.1**, including the uncertainties in the extracted adsorption enthalpies and entropies.

Table 4.1 Adsorption energies, coverage dependence of adsorption energies (α), adsorption equilibrium constants, enthalpies, and entropies of phenol adsorption on Pt and Rh obtained from isotherms and van't Hoff plot using the best fit. All adsorption energies, constants, enthalpies and entropies are at $\theta = 0$. The large uncertainties in the heat and entropy of adsorption are because they are derived from the slope and intercept of a trendline that is sensitive to uncertainties in free energies

Adsorption site	Temperature / K	$\Delta G_{ad,aq,\theta=0}$ / kJ mol^{-1}	α / kJ mol^{-1}	$K^{eq}_{ad,aq}$	$\Delta H_{ad,aq}$ / kJ mol^{-1}	$\Delta S_{ad,aq}$ / kJ mol^{-1} K^{-1}
Pt site 1	283	−26.6	2	81,300	−10 ± 12	59 ± 39
	288	−26.8	2	72,600		
	298	−27.4	0	63,500		
	314	−28.4	0	53,000		
Pt site 2	283	−10.5	2	86.7	38 ± 19	174 ± 64
	288	−12.0	0	150		
	298	−14.0	0	285		
	314	−16.0	0	459		
Rh site 1	283	−25.5	2	50,900	−11 ± 13	50 ± 43
	298	−26.1	0	37,600		
	314	−27.0	0	32,100		
Rh site 2	283	−6.5	0	15.8	3 ± 12	33 ± 50
	298	−7.0	0	16.9		
	314	−7.5	0	17.9		

4.4.4 Entropy of Adsorption of Phenol in the Absence and Presence of Water

To convert between the aqueous-phase phenol adsorption entropy measured here and the gas-phase phenol adsorption entropy, first the entropy of solvation of phenol in water must be determined. At 298 K, the standard Gibbs free energy of solvation of phenol, $\Delta G^{\circ}_{solvation,phenol}$, and enthalpy of solvation of phenol, $\Delta H^{\circ}_{solvation,phenol}$, are −19 kJ mol^{-1} and −50 kJ mol^{-1}, respectively.[40] Thus, the standard entropy of solvation of phenol at 298 K is given by **Eq. 4.2**:

$$\Delta S^{\circ}_{solvation,phenol} = -\frac{\Delta G^{\circ}_{solvation,phenol} - \Delta H^{\circ}_{solvation,phenol}}{T} \tag{4.2}$$

$$\Delta S^{\circ}_{solvation,phenol} = -\frac{(-19\ kJ\ mol^{-1}) - (-50\ kJ\ mol^{-1})}{298\ K} = -104\ J\ mol^{-1}\ K^{-1}$$

$$= -12.5R$$

Using the entropy of solvation, the entropy of adsorption of aqueous-phase phenol onto a metal surface at 298 K ($\Delta S^{\circ}_{ad,aq,phenol(aq)}$, referred to here as $\Delta S_{ad,aq}$) can be compared to the entropy of adsorption of gas-phase phenol onto a metal surface in the aqueous-phase ($\Delta S^{\circ}_{ad,aq,phenol(g)}$):

$$\Delta S^{\circ}_{ad,aq,phenol(aq)} = \Delta S^{\circ}_{ad,aq,phenol(g)} - \Delta S^{\circ}_{solvation,phenol} = \Delta S^{\circ}_{ad,aq,phenol(g)} + 12.5R \quad (4.3)$$

We will use **Eq. 4.3** to convert between estimates of the entropy of adsorption of phenol$_{(g)}$ from previous work in ref [22,26] to the experimentally measured value here of phenol$_{(aq)}$.

For the gas-phase adsorption of phenol, we have previously used a correlation from Campbell and Sellers[21] to estimate the entropy of adsorbed phenol relative to gaseous phenol using **Eq. 4.4:**

$$\begin{aligned}\Delta S^{\circ}_{ad,phenol(g),no\ solvent} &= S^{\circ}_{phenol(ad)} - S^{\circ}_{phenol(g)} \\ &= \left(0.70 S^{\circ}_{phenol(g)} - 3.3R\right) - S^{\circ}_{phenol(g)}\end{aligned} \quad (4.4)$$

For the value of $S^{\circ}_{phenol(g)}$ of 315 J mol^{-1} K^{-1} = 37.9R from ref [41], $\Delta S^{\circ}_{ad,phenol(g),no\ solvent}$= $-14.7R$. The value of $-14.7R$ was calculated assuming a standard state coverage of θ° = 0.054, and so to convert to the standard state coverage of θ° used here (θ° = 1/2), $\Delta S^{\circ}_{ad,aq,phenol(g)}$ must be changed by 2.5R to $-17.2R$.[42] (Note that because of the small values of α in **Table 4.1**, the experimental adsorption free energy values are not significantly affected by coverage, and any error is within the reported uncertainty) To estimate the adsorption entropy in the aqueous phase in previous work,[22] the assumptions were: (1) the interfacial water has similar structure whether or not phenol is adsorbed and (2) the adsorbed phenol has the same structure whether or not water is there. That is:

$$\Delta S^{\circ}_{ad,aq,phenol(g)} \cong \Delta S^{\circ}_{ad,phenol(g),no\ solvent} \quad (4.5)$$

Note that the equation above is for the entropy of adsorption of gas-phase phenol (as opposed to the entropy of adsorption of solvated phenol). Essentially, the assumption (1) above is that the displaced interfacial water molecules do not actually gain entropy upon adsorption of phenol, but rather they merely shift from being an ordered structure on Pt to being an ordered structure on phenol, with an unchanged entropy. If, however, the entropy of displacement of water from the surface was significant (i.e., the interfacial water did not have similar structure whether or not the phenol adlayer was there), then:

$$\Delta S^{\circ}_{ad,aq,phenol(g)} = \Delta S^{\circ}_{ad,phenol(g),no\ solvent} - n\Delta S^{\circ}_{ad,aq,water(l)} \quad (4.6)$$

where *n* is the number of water molecules desorbed upon phenol adsorption, determined to be 6.5 for Pt(111)[22,23,43] and Pt (100).[26] $\Delta S^{\circ}_{ad,aq,water(l)}$ is water's entropy of adsorption (such that $-\Delta S^{\circ}_{ad,aq,water(l)}$ is the entropy of desorption). The difference between the gas-phase adsorption entropy of phenol with and without solvent can be estimated after determining the entropy of adsorption of liquid water.

Although a similar correlation performed for phenol can be used to approximate liquid water's adsorption entropy that correlation is mainly for low coverage gas phase adsorbates, and may not be as accurate for an ordered interfacial water structure. Instead, we will assume the entropy of the adsorbed water is similar to solid water based on the structure of interfacial adsorbed water being "ice-like".[44,45]

Using the entropy of solid water, $S^{\circ}_{water(s)} = 44.8$ J mol^{-1} K^{-1},[46] to approximate the entropy of adsorbed water, and with the tabulated value of the entropy of liquid water, $S^{\circ}_{water(l)} = 69.95$ J mol^{-1} K^{-1},[40] the entropy of adsorption of the water layer can be calculated using **Eq. 4.7**:

$$\Delta S^{\circ}_{ad,aq,water(l)} = S^{\circ}_{water(ad)} - S^{\circ}_{water(l)} = 44.8 \text{ J mo}l^{-1}\, K^{-1} - 69.95 \text{ J mo}l^{-1}\, K^{-1} \quad (4.7)$$

$$= -25.2 \text{ J mo}l^{-1}\, K^{-1}$$

This value of −25.2 J mol^{-1} K^{-1} for the entropy of adsorption of water, or $-3.03R$ will be used to approximate the entropy of adsorption (or desorption) of the interfacial water layer being displaced by phenol.

If all the water entropy is gained when desorbing 6.5 water molecules from the surface of Pt(111) upon phenol adsorption, then the entropy of adsorption of phenol in the aqueous phase would be (using **Eq. 4.6**):

$$\Delta S^{\circ}_{ad,aq,phenol(g)} = \Delta S^{\circ}_{ad,phenol(g),no\ solvent} - 6.5 \times \Delta S^{\circ}_{ad,water(l)} = -17.2R + 19.7R$$

Clearly, whether or not the displaced water gains entropy can have a large effect on the entropy of adsorption of $\text{phenol}_{(g)}$ in aqueous phase, ranging from $-17.2R$ (displaced water does not gain entropy, as assumed in our previous work) to $+2.5R$ (displaced water gains all the entropy of going from bulk solid water to bulk liquid water). This effect was discussed as a potential point of error in ref [23] and a positive entropy of adsorption has been attributed to the water layer in several earlier works.[24,25,27,47] DFT calculations show that on Rh(111) and Rh(100) surfaces, the same number of water molecules are desorbed upon phenol adsorption as on Pt(111),[26] hence a similar analysis with 6.5 displaced water molecules was used for the Rh surfaces.

We compare this range of entropy values ($-17.2R$ to $+2.5R$) to the experimental values of $\Delta S^{\circ}_{ad,aq,phenol(aq)}$ from **Figure 4.3** and **Figure 4.5** by converting between the aqueous and gaseous phenol adsorption entropy. For simplicity, $\Delta S_{ad,aq}$ is used to refer to our experimental value of the entropy of adsorption of aqueous-phase phenol from **Figure 4.3** and **Figure 4.5**. We use $\Delta S^{\circ,correlation,no\ water}_{ad,aq,phenol(aq)}$ and $\Delta S^{\circ,correlation,no\ water}_{ad,aq,phenol(g)}$ to refer to our values for the entropy of adsorption of aqueous-phase and gas-phase phenol, respectively. These values are estimated from the correlation from ref [21] assuming displaced water does not gain entropy. We use $\Delta S^{\circ,correlation,full\,water}_{ad,aq,phenol(aq)}$ and $\Delta S^{\circ,correlation,full\,water}_{ad,aq,phenol(g)}$ using the same correlation for the entropy of phenol, but now assuming displaced water does gain all the entropy associated with the change from solid water at the interface to bulk liquid water.

As discussed earlier, **Eq. 4.3**, was used to convert between gas and aqueous phase phenol.

$$\Delta S^{\circ}_{ad,aq,phenol(aq)} = \Delta S^{\circ}_{ad,aq,phenol(g)} + 12.5R$$

Thus, the entropy estimates of $\Delta S^{\circ,correlation,no\,water}_{ad,aq,phenol(aq)}$ = $-4.7R$ (displaced water does not gain entropy) and $\Delta S^{\circ,correlation,full\,water}_{ad,aq,phenol(aq)}$ = $+15.0R$ (displaced water gains all the entropy of bulk liquid water). These values and the corresponding structure are shown schematically in **Figure 4.6**.

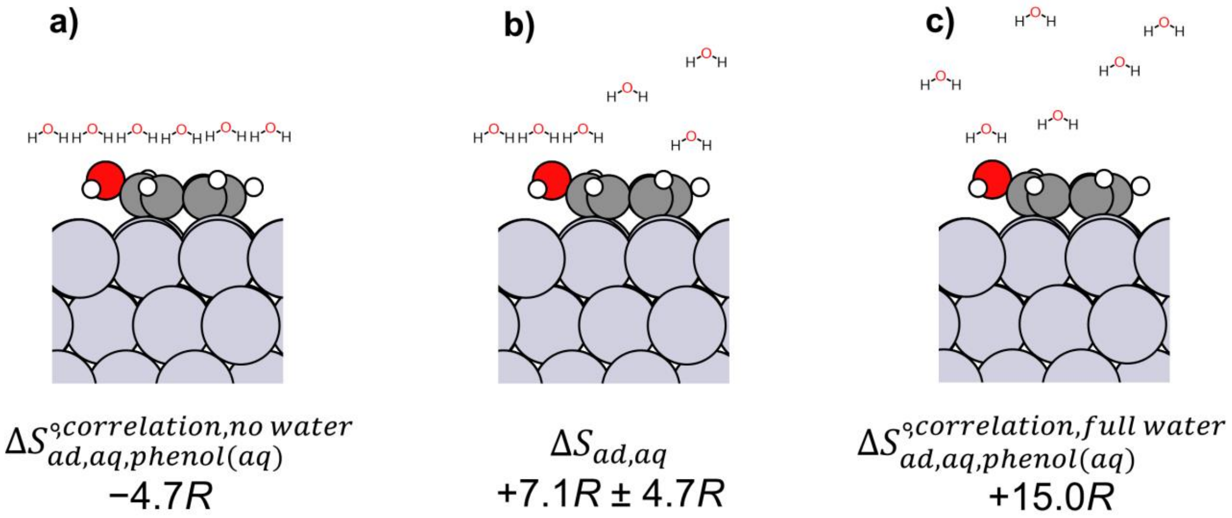

Figure 4.6 Structures of displaced interfacial water and corresponding phenol adsorption entropy for different situations. a) The water layer retains its ordered structure and entropy upon adsorption of phenol, so there is no gain of entropy from displacing the interfacial water layer, and the entropy of adsorption is solely due to the loss of $\text{phenol}_{(aq)}$ entropy. **b)** The entropy of adsorption experimentally determined in this work from the van't Hoff plot in Figure 4.3a. About half of the entropy of the displaced water layer is gained, assuming the adsorbed water has the same entropy as solid water (ice), and free water has the entropy of liquid water. **c)** Entropy of adsorption of phenol if the displaced water gains entropy corresponding to that of 6.5 water molecules displaced into the bulk liquid solution from a solid state (adsorbed as ice-like layer). All three entropy values could be converted to be relative to gas-phase phenol, instead of solvated phenol, by using the solvation entropy of phenol, ($-12.5R$).

Discrepancies in the entropy estimations we have made could also arise from inaccuracies of the entropy correlation used for phenol, the entropy of solvation of phenol, the entropy of adsorbed water, the experimental equilibrium constants obtained from isotherms, or in the van't Hoff analysis used. Assuming that the value approximating the effective entropy is consistent with the correlations applied, the entropy value of $+7.1R \pm 4.7R$ for the stronger binding site 1 of Pt compared to the estimated values of $-4.7R$ to $+15.0R$ in **Figure 4.6** would indicate that the water displaced by phenol does not completely gain the entropy of bulk liquid water, but approximately half of that entropy. This entropy gain is the cause of the different enthalpy of adsorption measured here compared to our extracted enthalpy assuming the entropy of adsorption of phenol is not different because of the water layer.[22,26] The positive entropy values for Pt site 2 and Rh sites also imply that the water displaced by phenol gains a portion of the entropy of bulk liquid water.

4.4.5 Differences in Entropies and Enthalpies of Adsorption in Gas and Aqueous Phase

The entropy of adsorption determined here implies that the water layer structure affects the organic adsorption entropy, or that our estimate of the entropy of the adsorbed phenol in aqueous phase does not exactly follow the correlation by Sellers and Campbell.[21] A portion of the difference is from the less negative entropy of the aqueous phenol as opposed to the gaseous phenol ($12.5R$), but there is also a contribution from the gain of entropy by displacement of water at the interface (e.g., ~$11.8R$ on the stronger binding Pt site). At 298 K, an entropy of displacement of water of $11.8R$ corresponds to an increase in the Gibbs free energy of adsorption of 29 kJ mol^{-1}. However, this entropy contribution to the free energy is significantly smaller than the impact on the enthalpy of adsorption previously discussed (of the order of 110–150 kJ mol^{-1})[22,23] in aqueous compared to gas phase. As discussed by Gileadi,[25] the water layer weakens the enthalpic driving force for adsorption, but increases the entropic driving force for adsorption. The slightly positive entropy of adsorption is the reason for the small temperature dependence of adsorption in aqueous phase compared to gas phase.

4.4.6 Implications for Aqueous-Phase Hydrogenation Kinetics

There are two consequences of the findings here on aqueous-phase reactions, one related to the molecular structure of the aqueous-phase electrode/phenol/water interface and one related to the coverage dependence on temperature. The first tells us about the structure of the water layer once it has been displaced by phenol adsorption. If the displaced water maintained the entropy of interfacial water, one would expect an ordered ("ice-like") layer of water to reside on top of the adsorbed phenol. Because instead the results shown here indicate that the displaced water gains some of the entropy it would have as free water, this water above the adsorbed phenol is not particularly ordered. When studying the conversion of phenol or other organic molecules, the structure of the nearby water will impact transport of reactant molecules from solution and reaction rates. This may have important consequences in interpreting molecular dynamics simulations of the conversion with water present.[48,49]

The second consequence of the findings here is related to the use of temperature to control the reaction rate. For gas-phase surface reactions, increasing the reaction temperature both increases the rate constant, but also typically decreases the adsorption coefficient of the species on the surface due to negative entropies of adsorption. This decreased adsorption coefficient will decrease the coverages. If the adsorption coefficient would cause too significant of a decrease in coverage, high partial pressures of the reactants are needed to maintain sufficient coverage for a reaction to occur. Our findings here indicate that in aqueous phase, due to the weaker dependence of the coverage on temperature, there is less concern in lowering reactant coverages with increasing temperature. This finding of the relatively constant coverages with temperature also aids the interpretation of rate data, particularly activation energy measurements, for aqueous-phase hydrogenations. In practice, the activation energy for many hydrogenation reactions is obtained by using the intrinsic turnover frequency (TOF) to represent the reaction rate constant in an Arrhenius plot.[2,5,29,50] However, strictly, changes in the TOF with temperature for a Langmuir-Hinshelwood surface limited reaction such as hydrogenation of phenol on Pt group metals would include both the change in the reaction rate constant and the change in coverages of the adsorbates. The results here show that because phenol coverage in aqueous phase is weakly dependent on temperature in the range of 10 °C to 40 °C, changes in the reaction rate with temperature are primarily due to the reaction rate constant.

4.5 Conclusions

We have extracted the effective entropy and enthalpy of adsorption of aqueous phenol onto Pt and Rh surfaces by employing an electrochemical technique to indirectly measure the adsorption of phenol as a function of phenol concentration and temperature. The aqueous phenol enthalpy of adsorption here is more positive (weaker) than previously estimated assuming the displaced interfacial water structure is unchanged upon phenol adsorption. Previous work has shown that the phenol enthalpy of adsorption in water solvent is reduced by about 100 to 150 kJ mol^{-1} compared to gas phase. This enthalpy decrease is because of the water adhesion energy and number of water molecules that must be displaced upon adsorption of phenol. In this work, we show that the entropy of adsorption of solvated phenol is more positive compared to phenol adsorption in gas phase not only because of the large loss of entropy by solvation of phenol but also because the ordered water layer, once displaced, gains approximately half of the entropy associated with bulk liquid water. These results are consistent with the understanding of electrosorption or solution-phase adsorption as a replacement reaction. The consequences of the positive phenol adsorption entropy are that increasing the temperature in electrocatalytic systems for phenol hydrogenation does not significantly decrease the equilibrium coverage of phenol. The results here shows that temperature may be an effective way to increase the rate for bio-oil conversion reactions, by increasing the rate constant without significantly lowering reactant coverages, so long as side reactions such as reactant decomposition do not occur at elevated temperatures.

4.6 References

(1) Jung, S.; Karaiskakis, A. N.; Biddinger, E. J. Enhanced Activity for Electrochemical Hydrogenation and Hydrogenolysis of Furfural to Biofuel using Electrodeposited Cu Catalysts. *Catal. Today* **2019**, *323*, 26–34.

(2) Song, Y.; Sanyal, U.; Pangotra, D.; Holladay, J. D.; Camaioni, D. M.; Gutiérrez, O. Y.; Lercher, J. A. Hydrogenation of Benzaldehyde via Electrocatalysis and Thermal Catalysis on Carbon-Supported Metals. *J. Catal.* **2018**, *359*, 68–75.

(3) Biddinger, E. J.; Modestino, M. A. Electro-Organic Syntheses for Green Chemical Manufacturing. *Electrochem. Soc. Interface* **2020**, *29*, 43–47.

(4) Chadderdon, X. H.; Chadderdon, D. J.; Matthiesen, J. E.; Qiu, Y.; Carraher, J. M.; Tessonnier, J. P.; Li, W. Mechanisms of Furfural Reduction on Metal Electrodes: Distinguishing Pathways for Selective Hydrogenation of Bioderived Oxygenates. *J. Am. Chem. Soc.* **2017**, *139*, 14120–14128.

(5) Sanyal, U.; Song, Y.; Singh, N.; Fulton, J. L.; Herranz, J.; Jentys, A.; Gutiérrez, O. Y.; Lercher, J. A. Structure Sensitivity in Hydrogenation Reactions on Pt/C in Aqueous-phase. *ChemCatChem* **2019**, *11*, 575–582.

(6) Carneiro, J.; Nikolla, E. Electrochemical Conversion of Biomass-Based Oxygenated Compounds. *Annu. Rev. Chem. Biomol. Eng.* **2019**, *10*, 85–104.

(7) Garedew, M.; Lin, F.; Song, B.; DeWinter, T. M.; Jackson, J. E.; Saffron, C. M.; Lam, C. H.; Anastas, P. T. Greener Routes to Biomass Waste Valorization: Lignin Transformation through Electrocatalysis for Renewable Chemicals and Fuels Production. *ChemSusChem* **2020**, *13*, 4214–4237.

(8) Xu, C.; Paone, E.; Rodríguez-Padrón, D.; Luque, R.; Mauriello, F. Recent Catalytic Routes for the Preparation and the Upgrading of Biomass Derived Furfural and 5-Hydroxymethylfurfural. *Chem. Soc. Rev.* **2020**, *49*, 4273–4306.

(9) Sanyal, U.; Yuk, S. F.; Koh, K.; Lee, M.-S.; Stoerzinger, K.; Zhang, D.; Meyer, L. C.; Lopez-Ruiz, J. A.; Karkamkar, A.; Holladay, J. D.; Camaioni, D. M.; Nguyen, M.; Glezakou, V.-A.; Rousseau, R.; Gutiérrez, O. Y.; Lercher, J. A. Hydrogen Bonding Enhances the Electrochemical Hydrogenation of Benzaldehyde in the Aqueous Phase. *Angew. Chemie* **2021**, *133*, 294–300.

(10) Akhade, S. A.; Singh, N.; Gutiérrez, O. Y.; Lopez-Ruiz, J.; Wang, H.; Holladay, J. D.; Liu, Y.; Karkamkar, A.; Weber, R. S.; Padmaperuma, A. B.; Lee, M.-S.; Whyatt, G. A.; Elliott, M.; Holladay, J. E.; Male, J. L.; Lercher, J. A.; Rousseau, R.; Glezakou, V.-A. Electrocatalytic Hydrogenation of Biomass-Derived Organics: A Review. *Chem. Rev.* **2020**, *120*, 11370–11419.

(11) Sanyal, U.; Koh, K.; Meyer, L. C.; Karkamkar, A.; Gutiérrez, O. Y. Simultaneous Electrocatalytic Hydrogenation of Aldehydes and Phenol over Carbon-Supported Metals. *J. Appl. Electrochem.* **2021**, *51*, 27–36.

(12) Weber, R. S.; Holladay, J. E. Modularized Production of Value-Added Products and Fuels from Distributed Waste Carbon-Rich Feedstocks. *Engineering* **2018**, *4*, 330–335.

(13) Chou, P.; Vannice, M. A. Benzene Hydrogenation over Supported and Unsupported Palladium II. Reaction Model. *J. Catal.* **1987**, *107*, 140–153.

(14) Singh, N.; Song, Y.; Gutiérrez, O. Y.; Camaioni, D. M.; Campbell, C. T.; Lercher, J. A. Electrocatalytic Hydrogenation of Phenol over Platinum and Rhodium: Unexpected Temperature Effects Resolved. *ACS Catal.* **2016**, *6*, 7466–7470.

(15) Singh, N.; Lee, M. S.; Akhade, S. A.; Cheng, G.; Camaioni, D. M.; Gutiérrez, O. Y.; Glezakou, V. A.; Rousseau, R.; Lercher, J. A.; Campbell, C. T. Impact of PH on Aqueous-Phase Phenol Hydrogenation Catalyzed by Carbon-Supported Pt and Rh. *ACS Catal.* **2019**, *9*, 1120–1128.

(16) Bondue, C. J.; Koper, M. T. M. Electrochemical Reduction of the Carbonyl Functional Group: The Importance of Adsorption Geometry, Molecular Structure, and Electrode Surface Structure. *J. Am. Chem. Soc.* **2019**, *141*, 12071–12078.

(17) Bondue, C. J.; Calle-Vallejo, F.; Figueiredo, M. C.; Koper, M. T. M. Structural Principles to Steer the Selectivity of the Electrocatalytic Reduction of Aliphatic Ketones on Platinum. *Nat. Catal.* **2019**, *2*, 243–250.

(18) Mortensen, P. M.; Grunwaldt, J. D.; Jensen, P. A.; Knudsen, K. G.; Jensen, A. D. A Review of Catalytic Upgrading of Bio-Oil to Engine Fuels. *Appl. Catal. A Gen.* **2011**, *407*, 1–19.

(19) Hansen, S.; Mirkouei, A.; Diaz, L. A. A Comprehensive State-of-Technology Review for Upgrading Bio-Oil to Renewable or Blended Hydrocarbon Fuels. *Renew. Sustain. Energy Rev.* **2020**, *118*, 109548.

(20) Patel, M.; Kumar, A. Production of Renewable Diesel through the Hydroprocessing of Lignocellulosic Biomass-Derived Bio-Oil: A Review. *Renew. Sustain. Energy Rev.* **2016**, *58*, 1293–1307.

(21) Campbell, C. T.; Sellers, J. R. V. The Entropies of Adsorbed Molecules. *J. Am. Chem. Soc.* **2012**, *134*, 18109–18115.

(22) Singh, N.; Sanyal, U.; Fulton, J. L.; Gutiérrez, O. Y.; Lercher, J. A.; Campbell, C. T. Quantifying Adsorption of Organic Molecules on Platinum in Aqueous Phase by Hydrogen Site Blocking and in Situ X-ray Absorption Spectroscopy. *ACS Catal.* **2019**, *9*, 6869–6881.

(23) Singh, N.; Campbell, C. T. A Simple Bond-Additivity Model Explains Large Decreases in Heats of Adsorption in Solvents versus Gas Phase: A Case Study with Phenol on Pt(111) in Water. *ACS Catal.* **2019**, *9*, 8116–8127.

(24) Bockris, J. O.; Jeng, K. T. In-Situ Studies of Adsorption of Organic Compounds on Platinum Electrodes. *J. Electroanal. Chem.* **1992**, *330*, 541–581.

(25) Gileadi, E. Electrosorption of Uncharged Molecules on Solid Electrodes. *J. Electroanal. Chem.* **1966**, *11*, 137–151.

(26) Akinola, J.; Barth, I.; Goldsmith, B. R.; Singh, N. Adsorption Energies of Oxygenated Aromatics and Organics on Rhodium and Platinum in Aqueous Phase. *ACS Catal.* **2020**, *10*, 4929–4941

(27) Goobes, R.; Goobes, G.; Campbell, C. T.; Stayton, P. S. Thermodynamics of Statherin Adsorption onto Hydroxyapatite. *Biochemistry* **2006**, *45*, 5576–5586.

(28) Soriaga, M. P.; White, J. H.; Hubbard, A. T. Orientation of Aromatic Compounds Adsorbed on Platinum Electrodes. The Effect of Temperature. *J. Phys. Chem.* **1983**, *87*, 3048–3054.

(29) Song, Y.; Gutiérrez, O. Y.; Herranz, J.; Lercher, J. A. Aqueous Phase Electrocatalysis and Thermal Catalysis for the Hydrogenation of Phenol at Mild Conditions. *Appl. Catal. B*

Environ. **2016**, *182*, 236–246..

(30) Sasaki, K.; Kunai, A.; Harada, J.; Nakabori, S. Electrolytic Hydrogenation of Phenols in Aqueous Acid Solutions. *Electrochim. Acta* **1983**, *28*, 671–674.

(31) Wieckowski, A.; Sobrowski, J.; Zelenay, P.; Franaszczuk, K. Adsorption of Acetic Acid on Platinum, Gold and Rhodium Electrodes. *Electrochim. Acta* **1981**, *26*, 1111–1119.

(32) Vassiliev, Y. B.; Bagotzky, V. S.; Khazova, O. A.; Cherny, V. V.; Meretsky, A. M. Mechanism of Adsorption, Electroreduction and Hydrogenation of Compounds with Ethylenic Bonds on Platinum and Rhodium: Part I. Kinetics of Adsorption and Electroreduction. *J. Electroanal. Chem. Interfacial Electrochem.* **1979**, *98* (2), 253–272.

(33) Garrone, E.; Bolis, V.; Fubini, B.; Morterra, C. Thermodynamic and Spectroscopic Characterization of Heterogeneity among Adsorption Sites: CO on Anatase at Ambient Temperature. *Langmuir* **1989**, *5*, 892–899.

(34) Singh, N.; Nguyen, M. T.; Cantu, D. C.; Mehdi, B. L.; Browning, N. D.; Fulton, J. L.; Zheng, J.; Balasubramanian, M.; Gutiérrez, O. Y.; Glezakou, V. A.; Rousseau, R.; Govind, N.; Camaioni, D. M.; Campbell, C. T.; Lercher, J. A. Carbon-Supported Pt during Aqueous Phenol Hydrogenation with and without Applied Electrical Potential: X-ray Absorption and Theoretical Studies of Structure and Adsorbates. *J. Catal.* **2018**, *368*, 8–19.

(35) Woods, R.; Bard, A. J. *Electroanalytical Chemistry: A Series of Advances*; Marcel Dekker and Basel: New York, **1976**; Vol. 9.

(36) Biegler, T.; Rand, D. A. J.; Woods, R. Limiting Oxygen Coverage on Platinized Platinum; Relevance to Determination of Real Platinum Area by Hydrogen Adsorption. *J. Electroanal. Chem. Interfacial Electrochem.* **1971**, *29*, 269–277.

(37) Gómez, R.; Orts, J. M.; Álvarez-Ruiz, B.; Feliu, J. M. Effect of Temperature on Hydrogen Adsorption on Pt(111), Pt(110), and Pt(100) Electrodes in 0.1 M $HClO_4$. *J. Phys. Chem. B* **2004**, *108*, 228–238.

(38) Zolfaghari, A.; Chayer, M.; Jerkiewicz, G. Energetics of the Underpotential Deposition of Hydrogen on Platinum Electrodes: I. Absence of Coadsorbed Species. *J. Electrochem. Soc.* **1997**, *144*, 3034–3041

(39) Cao, D. V.; Sircar, S. Temperature Dependence of the Isosteric Heat of Adsorption. *Adsorpt. Sci. Technol.* **2001**, *19*, 887–894.

(40) NIST. *WebBook*; "Standard reference database number 69" National Institute of Standards and Technology: Gaithersburg MD 20899, **2017**.

(41) Kudchadker, S. A.; Kudchadker, A. P.; Wilhoit, R. C.; Zwolinski, B. J. Ideal Gas Thermodynamic Properties of Phenol and Cresols. *J. Phys. Chem. Ref. Data* **1978**, *7*, 417–423.

(42) Campbell, C. T.; Sprowl, L. H.; Árnadóttir, L. Equilibrium Constants and Rate Constants for Adsorbates: Two-Dimensional (2D) Ideal Gas, 2D Ideal Lattice Gas, and Ideal Hindered Translator Models. *J. Phys. Chem. C* **2016**, *120*, 10283–10297.

(43) Carey, S. J.; Zhao, W.; Mao, Z.; Campbell, C. T. Energetics of Adsorbed Phenol on Ni(111) and Pt(111) by Calorimetry. *J. Phys. Chem. C* **2019**, *123*, 7627–7632.

(44) Björneholm, O.; Hansen, M. H.; Hodgson, A.; Liu, L. M.; Limmer, D. T.; Michaelides, A.; Pedevilla, P.; Rossmeisl, J.; Shen, H.; Tocci, G.; Tyrode, E.; Walz, M. M.; Werner, J.; Bluhm, H. Water at Interfaces. *Chem. Rev.* **2016**, *116*, 7698–7726.

(45) Rossmeisl, J.; Nørskov, J. K.; Taylor, C. D.; Janik, M. J.; Neurock, M. Calculated Phase Diagrams for the Electrochemical Oxidation and Reduction of Water over Pt(111). *J. Phys. Chem. B* **2006**, *110*, 21833–21839.

(46) Job, G.; Herrmann, F. Chemical Potential—a Quantity in Search of Recognition. *Eur. J. Phys.* **2006**, *27*, 353–371.

(47) Heiland, W.; Gileadi, E.; Bockris, J. O. M. Kinetic and Thermodynamic Aspects of the Electrosorption of Benzene on Platinum Electrodes. *J. Phys. Chem.* **1966**, *70*, 1207–1216.

(48) Yuk, S. F.; Lee, M.-S.; Akhade, S. A.; Nguyen, M.-T.; Glezakou, V.-A.; Rousseau, R. First-Principle Investigation on Catalytic Hydrogenation of Benzaldehyde over Pt-Group Metals. *Catal. Today* **2022**, *388–389*, 208–215.

(49) Calle-Vallejo, F.; Koper, M. T. M. First-Principles Computational Electrochemistry: Achievements and Challenges. *Electrochim. Acta* **2012**, *84*, 3–11.

(50) Sanyal, U.; Lopez-Ruiz, J.; Padmaperuma, A. B.; Holladay, J.; Gutiérrez, O. Y. Electrocatalytic Hydrogenation of Oxygenated Compounds in Aqueous Phase. *Org. Process Res. Dev.* **2018**, *22*, 1590–1598.

Chapter 5 Effects of Solvents on Adsorption: A General Bond Additivity Model

This chapter is adapted from **Akinola, J**.; Campbell, C. T.; Singh, N. Effects of Solvents on Adsorption Energies: A General Bond-Additivity Model. J. Phys. Chem. C **2021**, 125, 24371–24380. Copyright American Chemical Society.

5.1 Summary

While a vast body of knowledge exists about adsorption energies of catalytic reaction intermediates on solid surfaces in gas or vacuum conditions based on experimental studies and calculations using quantum mechanics, much less is known about adsorption energies in the presence of liquid solvents. We present here a method for estimating adsorption energies in liquid phase based on the gas-phase adsorption energy, the solvent's adhesion energy to the solid surface and the gas-phase adsorbate's solvation energy. A simple bond-additivity model was recently developed for approximating the change in adsorption energy (relative to gas phase) due to the additional presence of liquid solvents using the solvent's adhesion energy and the gaseous adsorbate's solvation energy, but that model was limited to adsorbates whose thickness is much smaller than its lateral dimension (parallel to the surface).

Here we present a simple extension of that model to adsorbates of finite thickness and general shape. We propose a model to convert the experimental solvation energy of a gaseous molecule into a molecule-solvent adhesion energy by assuming isotropic interaction of the molecule with the solvent. This adhesion energy allows us to estimate the fraction of this solvation energy that is retained when the molecule is adsorbed, based on the molecule's shape, size, and adsorption geometry. As in the earlier bond-additivity model, adsorption energies in solvent are lower in magnitude than in the gas phase by an amount approximately equal to the adhesion energy

of the solvent to the surface times the surface area of the solvent molecules displaced upon adsorption. We also report the predicted effects of different solvents for molecules on metal surfaces where solvation energies, gas-phase adsorption energies and solvent/surface adhesion energies are available in the literature.

5.2 Introduction

Understanding the adsorption energetics of molecules on solid surfaces in liquid solvents is important for improving catalytic and electrocatalytic reactions such as used in fuel production and combustion, fuel cells, biomass conversions, catalytic methane and CO_2 conversions, plastics upcycling, and environmental remediation. The increasing importance of these reactions on solid surfaces in liquid phase, for example in catalytic biomass conversions and in electrochemical storage of renewable energy, requires an improved understanding of the effect of solvents on adsorption. The solvent is well known to strongly influence catalytic activity and selectivity.[1–13] The reasons for this are still not well understood, but certainly derive from the effect of the solvent on the energies of adsorbed reaction intermediates and elementary-step transition states. Adsorption energies on solid surfaces in liquid phase also play a large role in controlling corrosion, whose annual costs are in the hundreds of billions of dollars.[14]

Learning how to transfer current knowledge of the energetics of reactions at gas/solid interfaces to liquid/solid interfaces would be extremely valuable due to the vast knowledge of reactions at gas/solid interfaces and methods for studying them compared to liquid/solid interfaces. Particularly important would be to develop methods for estimating the effect of liquid solvents on the energies of adsorbed reaction intermediates and transition states in catalytic and electrocatalytic reaction mechanisms, as this would facilitate the development of microkinetic models for estimating reaction kinetics that have been so fruitful in gas-phase catalysis research, but sorely lacking for reactions in liquid solutions. There have been numerous studies to compare heats of adsorption measured in liquid solvents with those in the gas phase[15–18] and to use simulations to clarify the role of the solvent.[1,2,12,16,18–20] There are several reviews and viewpoints that discuss the challenges involved in modeling solvent effects.[21,22] Generally, modeling efforts to speed up computational work incorporating solvent effects include implicit modeling of the solvent as a homogeneous constant dielectric continuum, bilayer adsorption (ice model), explicit modeling of the solvent by inclusion of solvent molecules in the simulation, and mixtures of implicit and explicit solvation.[21–25] Examples of implicit models are the conductor-like screening model (COSMO[26]) which uses an approximation of the solvent as a dielectric continuum with a cavity for the molecule.[27,28] Explicit models may make use of molecular dynamics and density functional theory (DFT).[29,30] Explicit hybrid quantum-mechanical/molecular mechanics (QM/MM) have been used to capture the effect for phenol on Pt(111) in water.[31]

We have recently shown how a simple bond-additivity model can be employed to estimate adsorption energies in the liquid phase for "flat" neutral molecules using measured gas phase adsorption energies and the adhesion energy of the solvent to the solid, explaining the difference in aqueous-phase and gas-phase adsorption energies for phenol and benzene on Pt(111).[32,33] This model built upon the concept from Gileadi[34] and Bockris and Jeng[15] to account for the displacement of solvent at the interface, but incorporated important additional solvent-solvent and solvent-adsorbate interactions. This model showed that solvent/solid adhesion energies are critical in understanding solvent effects on adsorption energies. We also reported experimental adhesion energies for a range of solvents on Pt(111) and Ni(111).[33] Using this bond-additivity method together with some experimental data mentioned above allowed predictions of aqueous adsorption energies for several adsorbates on Pt and Rh surfaces from simple gas-phase DFT calculations, with reasonable agreement with experimental results.[35]

In this work, we extend that simple bond-additivity model for flat molecules[32] to adsorbates of finite thickness and arbitrary shape. We derive an equation that allows one to estimate the adsorption energy in liquid solvents for a reactant molecule of arbitrary shape based on five values that are known or can be measured or estimated with reasonable accuracy: (1) the molecule's gas-phase adsorption energy, (2) the adhesion energy of the solvent to the solid surface, (3) the area on the surface where solvent molecules are blocked by the adsorbate, (4) the total "surface area" of the solvent cavity that must be created to solvate the free reactant molecule, and (5) the reactant's solvation energy (relative to the free gas-phase molecule), which can be derived from the temperature dependence of its Henry's law constant. This opens up many opportunities for predicting solvent effects on adsorption energies and, from that, solvent effects on catalytic reaction rates.

We show that the adsorption energy in solvent is smaller in magnitude than in gas phase by an amount approximately equal to the adhesion energy of the solvent to the solid times the area of the surface where solvent molecules are displaced upon reactant adsorption.

5.3 Results and Discussion

5.3.1 Bond-Additivity Model for Molecules of Finite Thickness

In **Figure 5.1**, we show a diagram of the individual steps involved in the adsorption of a reactant molecule, R, onto a solid surface, M, in the presence of solvent, S. This model is similar to the bond-additivity model proposed previously,[32,33] but here accounts for adsorbates of finite thickness. The original model was for uncharged adsorbates like benzene and phenol that lie flat on the surfaces of metals like Pt(111) and Rh(111), whose thickness is very small compared to the dimension parallel to the surface. The total outer surface area of such adsorbates (σ_{tot}) is approximately just the area of the top and bottom of the molecule. We extend that model here to the more general case for uncharged adsorbates of arbitrary thickness, to now include the sides of the molecule in estimating the energies of these steps. **Figure 5.1** applies only to low coverages of the adsorbate, so that these sides contact solvent molecules rather than other adsorbates, and any adsorbate-adsorbate interactions are neglected here.

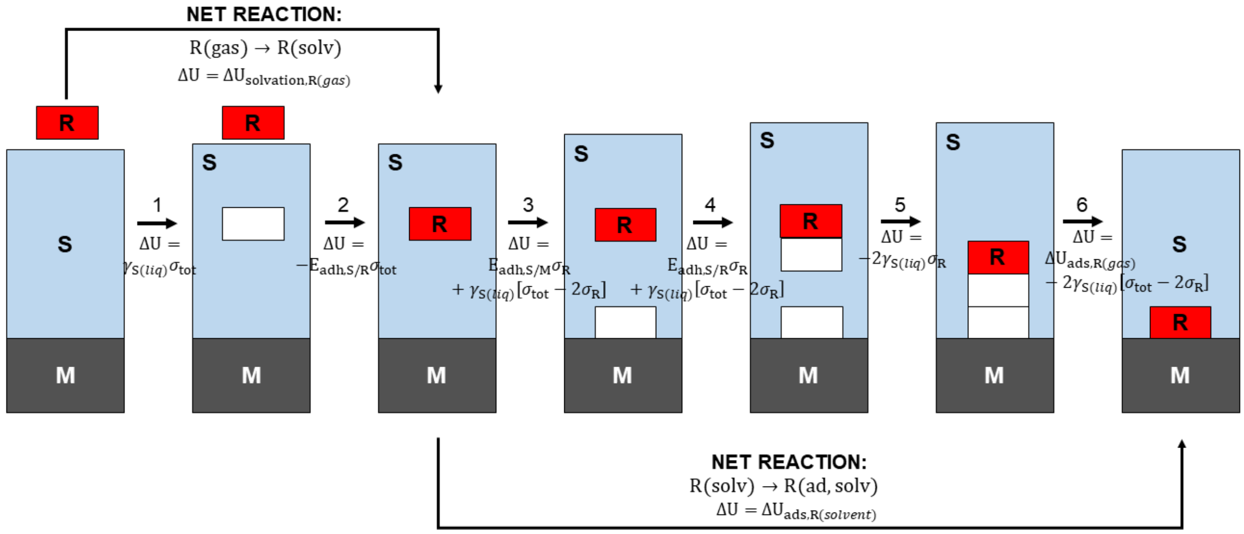

Figure 5.1 Thermodynamic cycle to determine the energy of adsorption of a reactant molecule (R) with finite thickness onto a solid surface (M) in a condensed-phase solvent (S) from its energy of adsorption in the gas-phase. Each numbered step's change in internal energy (ΔU) is indicated. The gas-phase adsorption energy is denoted $\Delta U_{\text{ads,R}(gas)}$. The solvent surface energy ($\gamma_{S(liq)}$) and adhesion energy of the solvent onto the surface ($E_{\text{adh,S/M}}$) and of the solvent onto the molecule ($E_{\text{adh,S/R}}$) are energies per unit area. They are multiplied by areas of either the footprint of the molecule on the surface (σ_{R}), in the particular adsorbed configuration of interest, or the total outer surface of the molecule (σ_{tot}).

5.3.2 Solvation Energy

The first two steps depicted in **Figure 5.1** consist of solvation of the gas-phase reactant (R). First a cavity or void volume is created in the solvent (S) with the volume and shape required for the reactant molecule (Step 1), giving an internal energy penalty equal to the surface energy of the solvent ($\gamma_{S(liq)}$) multiplied by the total outer surface area associated with the newly formed cavity (σ_{tot}). This is analogous to the use of a solvent cavity for computation of solvation energies as previously reported.[36,37] Then, as the gas-phase R is moved into this cavity (Step 2), there is a favorable energy equal to the interaction energy per unit surface area between the solvent and the reactant ($\mathrm{E_{adh,S/R}}$) multiplied by σ_{tot}. We use the term adhesion energy to refer to $\mathrm{E_{adh,S/R}}$ due to its conceptual similarity to the commonly-known "adhesion energy" between any two surfaces of condensed phases, which is generally accepted to mean the attractive interaction energy per unit area between the two surfaces, starting with them in vacuum and well separated (as used here also). The net energy of these two steps is equal to the solvation energy of the molecule, which is tabulated and readily available for many molecules:

$$\Delta \mathrm{U}_{\mathrm{solvation,R}(gas)} = \gamma_{\mathrm{S}(liq)}\sigma_{\mathrm{tot}} - \mathrm{E_{adh,S/R}}\sigma_{\mathrm{tot}} \tag{5.1}$$

This allows us to determine the adhesion energy per surface area between the solvent and the reactant, $\mathrm{E_{adh,S/R}}$, if the outer surface area of the reactant is known:

$$\mathrm{E_{adh,S/R}} = \frac{-\Delta \mathrm{U}_{\mathrm{solvation,R}(gas)}}{\sigma_{\mathrm{tot}}} + \gamma_{\mathrm{S}(liq)} \tag{5.2}$$

The outer area could be estimated, for example, from the molecular geometry (gas-phase structure) by smoothly connecting the outer van der Waals radii of the outer atoms. We show other methods for estimating σ_{tot} below. **Eq. 5.2** assumes that the interaction energy per unit area between the reactant molecule and solvent molecules is uniform around this outer surface area of the molecule, i.e., isotropic.

For flat adsorbates that are only one atom thick, like benzene and phenol[32,33], we previously assumed they are infinitely thin as a reasonable approximation. In that limit, the total surface area is just the surface area of the top and bottom of the molecule (both equal to the footprint area of the molecule, σ_{R}). In that limit, this interaction energy in **Eq. 5.2** reduces to:

$$\mathrm{E}_{\mathrm{adh,S/R}} = \frac{-\Delta \mathrm{U}_{\mathrm{solvation,R}(gas)}}{2\sigma_{\mathrm{R}}} + \gamma_{\mathrm{S}(liq)} \tag{5.3}$$

This matches the result we derived previously for such a shape.[33] To make this more clear, we rearrange this and use the definition of S-R from that previous work[33] to give:

$$\mathrm{E}_{\mathrm{adh,S/R}}\sigma_{\mathrm{R}} \equiv \text{S-R} = \frac{-\Delta \mathrm{U}_{\mathrm{solvation,R}(gas)}}{2} + \gamma_{\mathrm{S}(liq)}\sigma_{\mathrm{R}} \tag{5.4}$$

In an example case of a square molecule that is not flat, but instead has a thickness that is ¼ of its side length (such that $\sigma_{\mathrm{tot}} = 3\sigma_{\mathrm{R}}$), **Eq. 5.2** gives:

$$\mathrm{E}_{\mathrm{adh,S/R}} = \frac{-\Delta \mathrm{U}_{\mathrm{solvation,R}(gas)}}{3\sigma_{\mathrm{R}}} + \gamma_{\mathrm{S}(liq)} \tag{5.5}$$

5.3.3 Adsorption Energy of Solvated Reactant Molecule

We now analyze the energies of a set of elementary steps which combine to result in the adsorption of this solvated molecule onto the solid surface, and thus has a net energy equal to its adsorption energy with both the unbound and adsorbed reactant in liquid solution, $\Delta \mathrm{U}_{\mathrm{ads,R}(solvent)}$. Once the molecule is solvated, another cavity must be formed, but instead of in the bulk solution, this cavity is at the surface of the solid (M) (Step 3). The energy of this cavity formation includes the energies to remove solvent from some of the solid surface and to create gas/solvent surfaces around the edges of this cavity. The first contribution is reverse (negative) of the adhesion energy of the solvent to the solid surface ($\mathrm{E}_{\mathrm{adh,S/M}}$) multiplied by the area of the adsorbate footprint (σ_{R}). Note that this is a different adhesion energy than between the solvent and the adsorbate and instead of the total surface area, only the footprint area is used. The second contribution is the energy penalty of breaking solvent-solvent bonds to make solvent/gas surface (which costs γ per unit area created), but only for the area of the cavity touching the solvent that is not touching the solid surface, i.e., only the “sides” of the cavity, $\sigma_{\text{tot}} - 2\sigma_{\text{R}}$. (Creating the top surface of the cavity is included in the definition of $\text{E}_{\text{adh,S/M}}$ above, so is not included here.) The combined energy for Step 3 is thus $\Delta\text{U}_3 \ = \ \text{E}_{\text{adh,S/M}}\sigma_{\text{R}} + \gamma_{\text{S}(liq)}[\sigma_{\text{tot}} - 2\sigma_{\text{R}}]$.

In Step 4, another cavity is formed just below the solvated adsorbate, again of the same size and shape as the molecule. This energy penalty is similar to that of the cavity formed at the surface, with a solvent/molecule adhesion energy $\text{E}_{\text{adh,S/R}}$ (determined from the solvation energy as described above), multiplied by the footprint of the cavity plus the surface energy of the solvent multiplied by the area of the “sides” of the cavity: $\Delta\text{U}_4 \ = \ \text{E}_{\text{adh,S/R}}\sigma_{\text{R}} + \gamma_{\text{S}(liq)}[\sigma_{\text{tot}} - 2\sigma_{\text{R}}]$. In Step 5, these two cavities in the solvent are combined, with the favorable energy from decreasing the solvent/gas surface area (twice σ_{R} because two interfaces are removed: the top of the cavity on the solid surface and the bottom of the cavity under the adsorbate) times the surface energy of the solvent: $\Delta\text{U}_5 \ = -2\gamma_{\text{S}(liq)}\sigma_{\text{R}}$.

The final step (Step 6) is adsorption of the molecule, which is downhill in energy due to the bonding of the molecule to the solid surface and the removal of solvent/gas surface area. In this simple bond-additivity model, we assume that the bond energy of the molecule to the solid surface equals the energy of adsorption of that molecule in the gas-phase, $\Delta\text{U}_{\text{ads,R}(gas)}$, and is unaffected by the presence of the solvent on the other surfaces of the molecule. The removal of solvent/gas surface area along the cavity “sides” is downhill in energy by $2\gamma_{\text{S}(liq)}[\sigma_{\text{tot}} - 2\sigma_{\text{R}}]$. The combined energy for Step 6 thus equals $\Delta\text{U}_6 \ = \ \Delta\text{U}_{\text{ads,R}(gas)} \ - 2\gamma_{\text{S}(liq)}[\sigma_{\text{tot}} - 2\sigma_{\text{R}}]$.

Thus, the overall adsorption energy of the solvated molecule R (Steps 3-6) equals the sum of these steps’ energies:

$$\begin{gathered}\Delta\text{U}_{\text{ads,R}(solvent)} = \text{E}_{\text{adh,S/M}}\sigma_{\text{R}} + \gamma_{\text{S}(liq)}[\sigma_{\text{tot}} - 2\sigma_{\text{R}}] + \text{E}_{\text{adh,S/R}}\sigma_{\text{R}} \\ +\gamma_{\text{S}(liq)}[\sigma_{\text{tot}} - 2\sigma_{\text{R}}] - 2\gamma_{\text{S}(liq)}\sigma_{\text{R}} + \Delta\text{U}_{\text{ads,R}(gas)} - 2\gamma_{\text{S}(liq)}[\sigma_{\text{tot}} - 2\sigma_{\text{R}}]\end{gathered} \tag{5.6}$$

The contributions from the solvent surface energy associated with the sides of the molecules cancel here, so this simplifies to:

$$\begin{aligned}\Delta \mathrm{U}_{\mathrm{ads,R}(solvent)} &= \mathrm{E}_{\mathrm{adh,S/M}}\sigma_{\mathrm{R}} + \mathrm{E}_{\mathrm{adh,S/R}}\sigma_{\mathrm{R}} - 2\gamma_{\mathrm{S}(liq)}\sigma_{\mathrm{R}} + \Delta \mathrm{U}_{\mathrm{ads,R}(gas)} \\ &= \Delta \mathrm{U}_{\mathrm{ads,R}(gas)} + \left[\mathrm{E}_{\mathrm{adh,S/M}} + \mathrm{E}_{\mathrm{adh,S/R}} - 2\gamma_{\mathrm{S}(liq)}\right]\sigma_{\mathrm{R}}\end{aligned} \tag{5.7}$$

This is the same equation as we obtained for a flat molecule previously.[33] However, a difference arises when we substitute for $\mathrm{E}_{\mathrm{adh,S/R}}$ here our equation above for $\mathrm{E}_{\mathrm{adh,S/R}}$ in terms of the molecule's experimental solvation energy (**Eq. 5.2**). That gives:

$$\begin{aligned}\Delta \mathrm{U}_{\mathrm{ads,R}(solvent)} &= \Delta \mathrm{U}_{\mathrm{ads,R}(gas)} \\ &+ \left[\mathrm{E}_{\mathrm{adh,S/M}} + \left(\frac{-\Delta \mathrm{U}_{\mathrm{solvation,R}(gas)}}{\sigma_{\mathrm{tot}}} + \gamma_{\mathrm{S}(liq)}\right) - 2\gamma_{\mathrm{S}(liq)}\right]\sigma_{\mathrm{R}}\end{aligned} \tag{5.8}$$

This can be rearranged to obtain the adsorption energy in solvent as a function of the gas-phase adsorption energy, the adhesion energy of the solvent to the surface, the solvation energy of the adsorbate, the surface energy of the solvent, and the footprint and total area of the molecule:

$$\Delta \mathrm{U}_{\mathrm{ads,R}(solvent)} = \Delta \mathrm{U}_{\mathrm{ads,R}(gas)} + \left[\mathrm{E}_{\mathrm{adh,S/M}} - \frac{\Delta \mathrm{U}_{\mathrm{solvation,R}(gas)}}{\sigma_{\mathrm{tot}}} - \gamma_{\mathrm{S}(liq)}\right]\sigma_{\mathrm{R}} \tag{5.9}$$

For the simple case of a "flat adsorbate" as discussed above, $\sigma_{\mathrm{tot}} = 2\sigma_{\mathrm{R}}$, and **Eq. 5.9** simplifies to:

$$\Delta \mathrm{U}_{\mathrm{ads,R}(solvent)} = \Delta \mathrm{U}_{\mathrm{ads,R}(gas)} + \mathrm{E}_{\mathrm{adh,S/M}}\sigma_{\mathrm{R}} - \frac{\Delta \mathrm{U}_{\mathrm{solvation,R}(gas)}}{2} - \gamma_{\mathrm{S}(liq)}\sigma_{\mathrm{R}} \tag{5.10}$$

This is the same as we previously obtained.[33]

When the total area is instead three times that of the footprint:

$$\Delta \mathrm{U}_{\mathrm{ads,R}(solvent)} = \Delta \mathrm{U}_{\mathrm{ads,R}(gas)} + \mathrm{E}_{\mathrm{adh,S/M}}\sigma_{\mathrm{R}} - \frac{\Delta \mathrm{U}_{\mathrm{solvation,R}(gas)}}{3} - \gamma_{\mathrm{S}(liq)}\sigma_{\mathrm{R}} \tag{5.11}$$

5.3.4 Reactant Molecule of Non-Rectangular Shape

Here we show that the equations derived above (i.e., **Eq. 5.2** to determine $\mathrm{E_{adh,S/R}}$ and **Eq. 5.9** to determine $\Delta\mathrm{U}_{\mathrm{ads,R}(solvent)}$) also apply to molecules that do not have 'sides' that are perpendicular to the top and bottom. For example, in **Figure 2** we show a case where the 'top' of the molecule has a different area ($\sigma_{\mathrm{R,top}}$) than the 'footprint' of the molecule on the solid surface (σ_{R}). Here, the solvation of the molecule (Steps 1 plus 2) is the same as for **Figure 5.1**, so the solvation energy and **Eq. 5.2** are unchanged. Just as with **Figure 5.1**, **Figure 5.2** applies only to low coverages of the adsorbate, so that the sides of the adsorbate contact solvent molecules rather than other adsorbates, and any adsorbate-adsorbate interactions are neglected here.

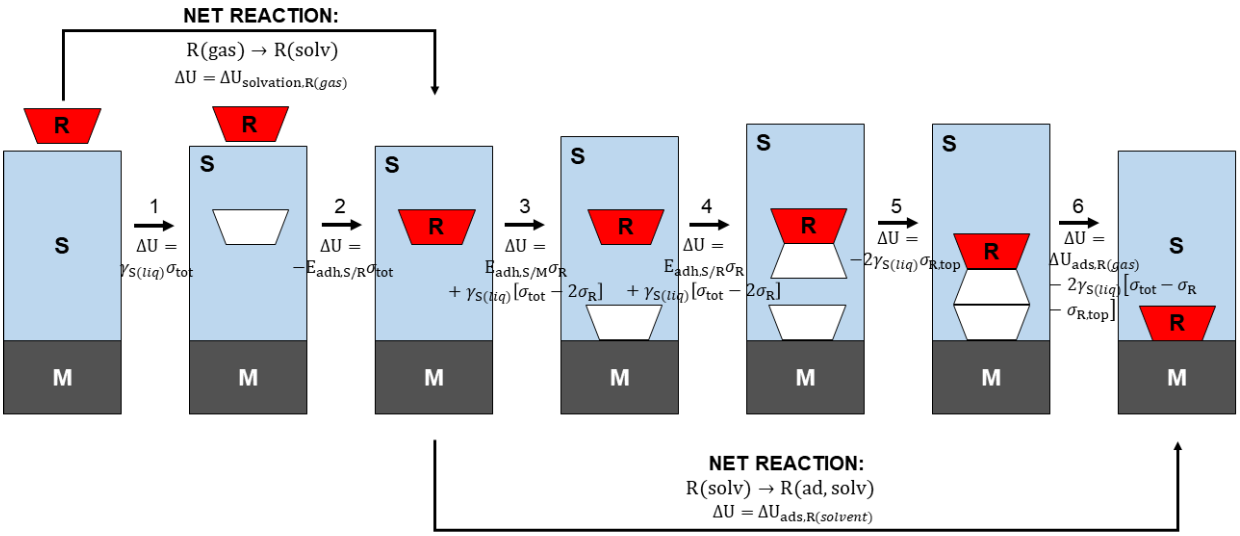

Figure 5.2 Thermodynamic cycle to determine the energy of adsorption of a reactant molecule (R) with finite thickness onto a solid surface (M) in a condensed-phase solvent (S) from its energy of adsorption in the gas-phase, where the reactant has a top area ($\sigma_{\mathrm{R,top}}$) that is different than its footprint area on the surface (σ_{R}).

In Step 3, the energy penalty to create the cavity is still the same as in **Figure 5.1**:

$$\Delta\mathrm{U}_3 = \mathrm{E_{adh,S/M}}\sigma_{\mathrm{R}} + \gamma_{\mathrm{S}(liq)}[\sigma_{\mathrm{tot}} - 2\sigma_{\mathrm{R}}].$$

It is the same because the area of the cavity touching the solvent that is not touching the solid surface is still $\sigma_{\mathrm{tot}} - 2\sigma_{\mathrm{R}}$. (Again, creating a part of the top surface area of the cavity equal to σ_{R} is included in the definition of $\mathrm{E_{adh,S/M}}$, so is not included here.)

Similarly, in Step 4 a cavity is formed but in this case the adhesion energy is that of the solvent and the molecule: $\Delta\mathrm{U}_4 = \mathrm{E}_{\mathrm{adh,S/R}}\sigma_{\mathrm{R}} + \gamma_{\mathrm{S}(liq)}[\sigma_{\mathrm{tot}} - 2\sigma_{\mathrm{R}}]$, the same as in **Figure 5.1**. The cavity 'formed' in Step 4 is inverted to include the areas of the new interfaces formed and was simply needed for the derivation, but is not meant to indicate that an actual physical inverted cavity formed during an adsorption process.

Step 5 combines the cavities, where now the interfacial area being removed is that of the "top" of the molecule, $\sigma_{\mathrm{R,top}}$: $\Delta\mathrm{U}_5 = -2\gamma_{\mathrm{S}(liq)}\sigma_{\mathrm{R,top}}$

In the final step, Step 6, the reactant molecule is adsorbed as before, and the interfacial area of the sides of the cavities are removed. The difference here compared to Step 6 in **Figure 5.1** is that the area of the sides of the molecule is not $\sigma_{\mathrm{tot}} - 2\sigma_{\mathrm{R}}$, but instead $\sigma_{\mathrm{tot}} - \sigma_{\mathrm{R}} - \sigma_{\mathrm{R,top}}$: $\Delta\mathrm{U}_6 = \mathit{\Delta}\mathrm{U}_{\mathrm{ads,R}(gas)} - 2\gamma_{\mathrm{S}(liq)}\left[\sigma_{\mathrm{tot}} - \sigma_{\mathrm{R}} - \sigma_{\mathrm{R,top}}\right]$

The adsorption energy of the solvated molecule is the sum of the energies of Steps 3, 4, 5, 6, giving:

$$\begin{gathered}\Delta\mathrm{U}_{\mathrm{ads,R}(solvent)} = \mathrm{E}_{\mathrm{adh,S/M}}\sigma_{\mathrm{R}} + \gamma_{\mathrm{S}(liq)}[\sigma_{\mathrm{tot}} - 2\sigma_{\mathrm{R}}] \\ +\mathrm{E}_{\mathrm{adh,S/M}}\sigma_{\mathrm{R}} + \gamma_{\mathrm{S}(liq)}[\sigma_{\mathrm{tot}} - 2\sigma_{\mathrm{R}}] - 2\gamma_{\mathrm{S}(liq)}\sigma_{\mathrm{R,top}} \\ +\Delta\mathrm{U}_{\mathrm{ads,R}(gas)} - 2\gamma_{\mathrm{S}(liq)}\left[\sigma_{\mathrm{tot}} - \sigma_{\mathrm{R}} - \sigma_{\mathrm{R,top}}\right]\end{gathered} \tag{5.12}$$

This is analogous to **Eq. 5.6** above and similar. Through cancellation of terms and rearranging, **Eq. 5.12** simplifies to again give **Eq. 5.7**:

$$\Delta\mathrm{U}_{\mathrm{ads,R}(solvent)} = \Delta\mathrm{U}_{\mathrm{ads,R}(gas)} + \left[\mathrm{E}_{\mathrm{adh,S/M}} + \mathrm{E}_{\mathrm{adh,S/R}} - 2\gamma_{\mathrm{S}(liq)}\right]\sigma_{\mathrm{R}} \tag{5.7}$$

This proves that **Eq. 5.7** and **Eq. 5.9** are completely independent of the shape of the reactant molecule, from a negligibly thin, flat molecule as when originally derived[32] to the more complex, realistic shapes in Figures 1 and 2. It requires knowing the area of contact between the solvent molecules and the solid surface that is blocked upon the reactant's adsorption (σ_{R}) and the adhesion energies ($\mathrm{E_{adh,S/M}}$ and $\mathrm{E_{adh,S/R}}$) to relate the reactant's adsorption energy in solvent to that in gas phase.

From **Eq. 5.7**, **Eq. 5.9** can be obtained in the same way as above (i.e., using **Eq. 5.2** to get $\mathrm{E_{adh,S/R}}$ from the solvation energy of R(gas), $\Delta\mathrm{U}_{\mathrm{solvation,R}(gas)}$), to give:

$$\Delta\mathrm{U}_{\mathrm{ads,R}(solvent)} = \Delta\mathrm{U}_{\mathrm{ads,R}(gas)} + \left[\mathrm{E_{adh,S/M}} - \frac{\Delta\mathrm{U}_{\mathrm{solvation,R}(gas)}}{\sigma_{\mathrm{tot}}} - \gamma_{\mathrm{S}(liq)}\right]\sigma_{\mathrm{R}} \tag{5.9}$$

This equation too is independent of the shape of the molecule except in that the shape determines the ratio $\sigma_{\mathrm{R}}/\sigma_{\mathrm{tot}}$. The value of σ_{tot} is not in **Eq. 5.7**, but it arises here because it was needed in **Eq. 5.2** to determine $\mathrm{E_{adh,S/R}}$ from the solvation energy.

Eq. 5.9, or **Eq. 5.7** and **Eq. 5.2** make a complete picture of the energy difference between adsorption in the gas phase versus adsorption in a liquid phase solvent which is independent of molecule shape (except via the ratio $\sigma_{\mathrm{R}}/\sigma_{\mathrm{tot}}$). It assumes pairwise bond-additivity within the special context we introduced in ref [32] which extends bond energies beyond the usual concept of atom-atom or molecule-molecule bond energies to instead consider the bond energy per unit contact area between substances, i.e., adhesion energies. It requires that the molecule's "surface" is isotropic in its interaction with solvent molecules, as this was assumed in deriving the relationship between $\mathrm{E_{adh,S/R}}$ and $\Delta\mathrm{U}_{\mathrm{solvation,R}(gas)}$ given in **Eq. 5.2**.

The ratio $\sigma_{\mathrm{R}}/\sigma_{\mathrm{tot}}$ is dependent on the adsorption configuration on the surface. The application of **Eq. 5.9**, or **Eq. 5.7** and **Eq. 5.2** should therefore be for the specific configuration and orientation of interest. This is particularly important for molecules which can adsorb in multiple different configurations or that have coverage-dependent adsorption configurations. The adsorption energy in the gas phase also changes with the adsorbate's configuration / orientation.

Eq. 5.9 shows that the reactant's adsorption energy in the solvent is smaller in magnitude than in the gas phase by an amount that is proportional to its footprint on the solid (i.e., the area where it blocks solvent molecules from binding to the solid). The proportionality constant $(\mathrm{E}_{\mathrm{adh,S/M}} - \frac{\Delta \mathrm{U}_{\mathrm{solvation,R}(gas)}}{\sigma_{\mathrm{tot}}} - \gamma_{\mathrm{S}(liq)})$ equals the adhesion energy of the solvent to the solid plus the magnitude of the reactant's solvation energy per unit of reactant total surface area minus the solvent's surface energy. It also can be written as $\mathrm{E}_{\mathrm{adh,S/M}} + \mathrm{E}_{\mathrm{adh,S/R}} - 2\gamma_{\mathrm{S}(liq)}$. This proportionality constant is dominated by the adhesion energy of the solvent to the solid since the other two terms are smaller and opposite in sign so they nearly cancel (see below). This near cancellation was found also from applications of the original bond-additivity model to relatively flat molecules on Pt and Rh surfaces.[32,35]

Table 5.1 lists the magnitude of this proportionality constant (in the last column) for various reactant molecules in various solvents adsorbing on the Pt(111) surface near room temperature. Also listed are the molecules' solvation energies, taken from tabulated enthalpies of solvation after converting to energies by adding RT. The value of σ_{tot}, the total surface area of the molecule in contact with the solvent in bulk solution (per mole), is also needed to estimate this proportionality constant. It is estimated here by assuming the molecule's shape, thickness and footprint area on the surface (σ_{R} per mole) estimated as follows. For benzene, phenol and n-hexane, their maximum coverages when adsorbed on Pt(111) terraces in their most stable structure are known from experimental measurements (equal to 1/9, 1/9 and 1/7 per Pt surface atom, respectively[38–40]). Dividing the area per mole of Pt atoms on Pt(111) (4.02×10^4 m^2/mol) by this maximum coverage gives the footprint area per mole of molecule, σ_{R}. We then use the known molar volume of the reactant molecule (V_{m}, calculated from its reported density as a pure bulk liquid) together with this footprint area to estimate the molecule's thickness, t, as $\mathrm{t} = \mathrm{V}_{\mathrm{m}} / \sigma_{\mathrm{R}}$ for these three reactant molecules. As expected, this gives a thickness which is within a few percent for benzene and phenol (0.247 and 0.251 nm). We then assume this same thickness as with phenol for all of the other aromatic molecules in **Table 5.1**: t = 0.251 nm. Similarly, we assume that all n-alkanes have the same thickness as estimated in this way for n-hexane: t = 0.465 nm. Given this estimated thickness, the footprint area for each of the other molecules (for which the maximum coverage is not already known from the literature) is then estimated from its molar volume by: $\sigma_{\mathrm{R}} = V_{\mathrm{m}} / t$. The value of σ_{tot} is estimated from σ_{R} and t by assuming a simplified molecular shape. We assume a thin cylindrical disk shape for: benzene, phenol, toluene, and benzaldehyde; and a shallow rectangular box shape for n-alkanes, naphthalene, acetophenone, and styrene. The box width for all aromatics is assumed to be the same as the width (diameter) of benzene's circular disk shape (0.874 nm). The box length for all n-alkanes is estimated as the distance between the farthest two terminal H atoms in the gas-phase structure (as reported in the NIST's CCBDB database) plus twice the van der Waals radius of H atoms in alkanes (0.11 nm [41]), giving 1.04 and 1.30 nm for n-hexane and n-octane, respectively.

Table 5.1 Solvation energy, footprint surface area (σ_R), total surface area exposed to solvent in bulk solution (σ_tot), solvation energy per unit area, solvent/reactant adhesion energy ($\text{E}_{\text{adh,S/R}}$), and predicted change in adsorption energy on Pt(111) due to the solvent for reactants in different solvents. Solvent surface energies and adhesion energies to Pt(111) (taken from the literature) are included for each solvent. The numbers in brackets after the values refer to literature citations.

Solvent = water, $\gamma_{\text{S}(liq)}$ = 0.073 J/m^2, $\text{E}_{\text{adh,S/M}}$ for Pt(111) = 0.32 J/m^2 [32,33,d]						
Reactant (R)	$\Delta\text{U}_{\text{solvation,R}(gas)}$ (kJ/mol)[a]	$\sigma_\text{R} \times 10^{-5}$ (m^2/mol)[b]	$\sigma_\text{tot} \times 10^{-5}$ (m^2/mol)[c]	$\Delta\text{U}_{\text{solvation,R}(gas)}/\sigma_\text{tot}$ (J/m^2)	$\text{E}_{\text{adh,S/R}}$ (J/m^2)	$\text{E}_{\text{adh,S/M}} + \text{E}_{\text{adh,S/R}} - 2\gamma_{\text{S}(liq)}$ (J/m^2)
Pyridine	−46.5	3.21	12.4	−0.0375	0.111	0.28
Phenol	−47.5	3.61	11.4	−0.0417	0.115	0.29
Benzene	−30.5	3.61	11.3	−0.0270	0.100	0.27
Toluene	−34.5	4.24	13.0	−0.0266	0.100	0.27
n-Hexane	−59.5	2.81	17.0	−0.0349	0.108	0.28
n-Octane	−62.5	3.49	21.2	−0.0294	0.102	0.28
Benzaldehyde	−39.5	4.01	12.4	−0.0318	0.105	0.28
Naphthalene	−27.5	4.48	14.2	−0.0194	0.092	0.27
Styrene	−32.5	4.57	14.4	−0.0226	0.096	0.27
Acetophenone	−47.5	4.66	14.6	−0.0325	0.106	0.28
Solvent = benzene, $\gamma_{\text{S}(liq)}$= 0.0288 J/m^2, $\text{E}_{\text{adh,S/M}}$ for Pt(111) = 0.447 J/m^2 [33]						
Reactant (R)	$\Delta\text{U}_{\text{solvation,R}(gas)}$ (kJ/mol)	$\sigma_\text{R} \times 10^{-5}$ (m^2/mol)	$\sigma_\text{tot} \times 10^{-5}$ (m^2/mol)	$\Delta\text{U}_{\text{solvation,R}(gas)}/\sigma_\text{tot}$ (J/m^2)	$\text{E}_{\text{adh,S/R}}$ (J/m^2)	$\text{E}_{\text{adh,S/M}} + \text{E}_{\text{adh,S/R}} - 2\gamma_{\text{S}(liq)}$ (J/m^2)
Phenol	−48.8 [42]	3.61	11.4	−0.0424	0.071	0.46
Solvent = n-hexane, $\gamma_{\text{S}(liq)}$= 0.0179 J/m^2, $\text{E}_{\text{adh,S/M}}$ for Pt(111) = 0.16 J/m^2 [43]						
Reactant (R)	$\Delta\text{U}_{\text{solvation,R}(gas)}$ (kJ/mol)	$\sigma_\text{R} \times 10^{-5}$ (m^2/mol)	$\sigma_\text{tot} \times 10^{-5}$ (m^2/mol)	$\Delta\text{U}_{\text{solvation,R}(gas)}/\sigma_\text{tot}$ (J/m^2)	$\text{E}_{\text{adh,S/R}}$ (J/m^2)	$\text{E}_{\text{adh,S/M}} + \text{E}_{\text{adh,S/R}} - 2\gamma_{\text{S}(liq)}$ (J/m^2)
Benzene	−28 [44]	3.61	11.3	−0.0249	0.043	0.17
Solvent = methanol, $\gamma_{\text{S}(liq)}$= 0.0225 J/m^2,[45] $\text{E}_{\text{adh,S/M}}$ for Pt(111) = 0.168 J/m^2 [33]						
Reactant (R)	$\Delta\text{U}_{\text{solvation,R}(gas)}$ (kJ/mol)	$\sigma_\text{R} \times 10^{-5}$ (m^2/mol)	$\sigma_\text{tot} \times 10^{-5}$ (m^2/mol)	$\Delta\text{U}_{\text{solvation,R}(gas)}/\sigma_\text{tot}$ (J/m^2)	$\text{E}_{\text{adh,S/R}}$ (J/m^2)	$\text{E}_{\text{adh,S/M}} + \text{E}_{\text{adh,S/R}} - 2\gamma_{\text{S}(liq)}$ (J/m^2)
Benzene	−29 [44]	3.61	11.3	−0.027	0.049	0.17
Toluene	−34 [44]	4.24	13.0	−0.026	0.049	0.17

a. Energies of solvation in water are from the temperature dependence of Henry’s law constant listed in the NIST WebBook.

b. The σ_R value is based on experimental measurements for benzene, phenol, and n-hexane, and estimated for other reactants by using its molar volume (from its density as a pure bulk liquid) and assuming its thickness as described in the text.

c. The σ_tot value is estimated by assuming the molecule’s shape and thickness as described in the text, and the σ_R value from the previous column.

d. The $\text{E}_{\text{adh,S/M}}$ value for water / Pt(111) is different from ref 33 versus ref 32 (0.32 vs. 0.251 J/m^2, where the difference arose from the use of the surface energy of solid water versus liquid water in its calculation from the heats of water adsorption[33]). We use here the value from ref 32 to be consistent with the calculations in our original paper[32] that introduced this bond additivity model.

Using **Eq. 5.9** and the values in **Table 5.1**, one is able to use reported adsorption energies in gas-phase to estimate their adsorption energies in liquid solvents. As examples, we show values estimated in this way for several molecules on Pt(111) and Ni(111) in several solvents in **Table 5.2**. An example calculation of this type for the specific case of phenol on Pt(111) is described in the following section.

Table 5.2 Predicted energies of adsorption in solvents estimated from experimental gas-phase heats of adsorption using Eq. 5.9 and listed values in Table 5.1. Experimental energies of adsorption in solvents are included where available in the literature.

Molecule (R)	Metal (M)	Solvent (S)	$E_{\mathrm{adh,S/M}}$ (J/m^2)[a]	$\Delta U_{\mathrm{ads,R}(g)}$ (kJ/mol)[b]	$\sigma_R \times 10^{-5}$ (m^2/mol)	$\Delta U_{\mathrm{ads,R}(solvent)}$ (kJ/mol) from bond-additivity	$\Delta U_{\mathrm{ads,R}(solvent)}$ (kJ/mol) from experiment
Phenol	Pt(111)	Water	0.32 [32,33,c]	−174 [39]	3.61	−70	−19 [46]
	Pt(111)	Benzene	0.447 [33]	−174 [39]	3.61	−7.7	
	Ni(111)	Water	0.417 [33,c]	−175 [39]	2.91	−62	
	Ni(111)	Benzene	0.60 [33]	−175 [39]	2.91	+5	
Benzene	Pt(111)	Water	0.32 [32,33,c]	−162 [38]	3.61	−63	
	Pt(111)	n-Hexane	0.16 [43]	−162 [38]	3.61	−102	
	Pt(111)	Methanol	0.168 [33]	−162 [38]	3.61	−100	
	Ni(111)	Water	0.417 [33,c]	−168 [38]	2.91	−59	
n-Hexane	Pt(111)	Water	0.32 [32,33,c]	−80 [40]	2.81	−1	

a. Adhesion energy of liquid solvent to this metal surface (apart from water, see footnote c).

b. Standard enthalpies of adsorption (averaged from zero up to the maximum coverage), converted to energies by adding *RT*. We assume that the value is the same at 300 K as the T used in the specified references. Calorimetry measurements were done at T = 90 K or 150 K.

c. The $E_{\mathrm{adh,S/M}}$ value for water / Pt(111) is different from ref 33 versus ref 32 (0.32 vs. 0.251 J/m^2). We use here the value from ref 32 to be consistent with the calculations in our original paper[32] that introduced this bond additivity model. Consequently, the $E_{\mathrm{adh,S/M}}$value for water / Ni(111) is also different from the value given in ref 33 (0.345 J/m^2), since we changed it to be consistent with the way it was calculated for Pt(111) in ref 32.

The only experiment available to compare to these predictions in **Table 5.2** at this stage is phenol on Pt(111) in water. Although the model predicts that the heat of adsorption in water will decrease by 104 kJ/mol compared to the gas phase, the observed decrease is 155 kJ/mol. Most but not all of the solvent effect is captured with this model. As we have noted before,[32] part of this disagreement is probably due to the fact that phenol may be at higher local coverage for this experimental result in water, whereas the gas-phase adsorption energy used here is the average for the first layer, which decreases by over 60 kJ/mol in the first layer.[39] As another source of error, this bond-additivity model assumes that the bond strength between the reactant (phenol) and the surface (Pt(111)) does not change when solvent (water) is added on top of the phenol. It seems this water weakens that bond to some extent. That is not unexpected since this same effect (the weakening of bonds as more neighbors are added) is the well-known weakness of the bond-additivity model for predicting atom-atom bonding energetics within molecules.

Because the effect of the solvent on heats of reactant adsorption is so large, and because most of it is captured with this new model, this model will be useful for predicting trends in how different solvents affect adsorption energies. It also provides an intuitive approach for understanding and explaining the various contributions to solvent effects. This method is intended for application to relatively small adsorbates where a substantial fraction of the total molecular area is in contact with the solid surface. It is not likely to be accurate for highly flexible, polyfunctional molecules. It is not intended for adsorbed transition states for elementary surface reaction steps, although if the solvent has a similar effect on the adsorption energies of both the adsorbed reactant and the adsorbed product for an elementary step, it seems reasonable to assume that the transition state might be similarly affected too, unless it has charge separation present in neither reactant nor product.

Although this method enables one to estimate energies, free energies can also be estimated from these by also estimating the entropies of adsorption. This can be done by referencing to a gas phase molecule, using established correlations between the gas phase entropy and the entropy of the adsorbed molecule,[47] as we have done for phenol adsorption on Pt(111) in water.[46]

5.3.5 Case study for Effect of Adsorbate Thickness

As an example of the use of **Eq. 5.9** to determine how much the adsorption energy changes (compared to the gas-phase value) due to a solvent within this modified bond-additivity model, we consider the specific case of phenol adsorbing onto a Pt(111) surface in water. We compare the case where phenol is assumed to have negligible thickness with the result using the more realistic thickness estimated in **Table 5.1**. The phenol molecule was approximated in **Table 5.1** to have the shape of a thin cylindrical disk for simplicity, as shown in **Figure 5.3**. The footprint area of phenol (σ_R) is 0.60 nm^2 per phenol or 3.61×10^5 m^2 per mole phenol based on the structure of highest-coverage of adsorbed phenol in its most stable structure on Pt(111), corresponding to a (3x3) overlayer with an absolute coverage of 1/9 per Pt(111) surface atom.[32,48] Note that this footprint corresponds to a radius of $r = 4.37 \times 10^{-10}$ m for a circular area. The molar volume of phenol is $V_m = 0.0000905$ m^3 per mole or 1.50×10^{-28} m^3 per phenol based on its reported density. The thickness of a cylinder that has this volume and footprint is $t = V_m / \sigma_\mathrm{R} = 2.51 \times 10^{-10}$ m (2.51 Å). The total outer surface area of that cylinder is $\sigma_\mathrm{tot} = 2\sigma_\mathrm{R} + 2\pi rt = 1.14 \times 10^6$ m^2 per mole, as listed in **Table 5.1**. Note that this gives that $\sigma_\mathrm{tot} = 3.16\ \sigma_\mathrm{R}$, which is approximately $\sigma_\mathrm{tot} = 3\ \sigma_\mathrm{R}$, such that the surface area of the sides is approximately equal to the surface area of the footprint. We instead used $\sigma_\mathrm{tot} = 2\ \sigma_\mathrm{R}$ when we assumed negligible thickness in our original bond-additivity model.[32]

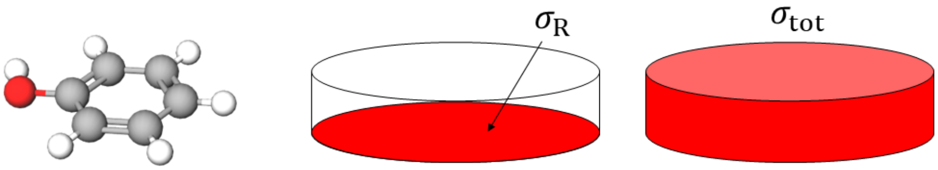

Figure 5.3 Phenol represented as a uniform molecule with footprint σ_R and total outer surface area σ_tot. If phenol is infinitely thin, $\sigma_\mathrm{tot} = 2\ \sigma_\mathrm{R}$. If the thickness (height) of the molecule is 2.51 Å and its footprint area is 0.60 nm^2, as estimated here (see **Table 5.1**), then $\sigma_\mathrm{tot} = 3.16\ \sigma_\mathrm{R}$.

Note that the shape of the molecule does not have to be a cylinder to apply such an approach as in **Figure 5.3**, so long as the footprint area and the total surface area can be estimated based on the shape and size. To solve **Eq. 5.7**, we need a few values. We will use the reported experimental solvation energy for phenol in water:[32,49] $\Delta \mathrm{U}_{\mathrm{solvation,R}(gas)} = -47.5\ \mathrm{kJ\ mol^{-1}}$. The surface energy of liquid water is 0.073 J m^{-2}.[50]

In the case where phenol is assumed to be infinitely thin, we can use **Eq. 5.3** (that special case of **Eq. 5.2**) to calculate $\mathrm{E}_{\mathrm{adh,S/R}}\sigma_\mathrm{R}$ in water:

$$\mathrm{E}_{\mathrm{adh,S/R}}\sigma_{\mathrm{R}} \equiv \text{S-R} = \frac{-(-47.5\ \mathrm{kJ\ mol^{-1}})}{2} + (0.073\ \mathrm{J\ m^{-2}})(3.61 \times 10^{5}\ \mathrm{m^{2}\ mol^{-1}}) \tag{5.13}$$

$$= 50.1\ \mathrm{kJ\ mol^{-1}}$$

This is the same as previously reported.[32,33] The value of $\mathrm{E}_{\mathrm{adh,S/R}}$ is thus (for the infinitely thin molecule):

$$\mathrm{E}_{\mathrm{adh,S/R}} = \frac{50.1\ \mathrm{kJ\ mol^{-1}}}{3.61 \times 10^{5}\ \mathrm{m^{2}\ mol^{-1}}} = 0.139\ \mathrm{J\ m^{-2}} \tag{5.14}$$

In the case where phenol is not infinitely thin, but instead $\sigma_{\mathrm{tot}} = 3.16\ \sigma_{\mathrm{R}}$, we can use **Eq. 5.5** (that special case of **Eq. 5.2**) to obtain:

$$\mathrm{E}_{\mathrm{adh,S/R}} = \frac{-(-47.5\ \mathrm{kJ\ mol^{-1}})}{3.16(3.61 \times 10^{5}\ \mathrm{m^{2}\ mol^{-1}})} + 0.073\ \mathrm{J\ m^{-2}} = 0.115\ \mathrm{J\ m^{-2}} \tag{5.15}$$

As expected, the interaction (adhesion) of the phenol to the water solvent on an area basis is lower than with the completely flat phenol, because of the higher surface area that we are considering for the phenol. Using the average calorimetric gas-phase adsorption energy of phenol on Pt(111) from zero to maximum coverage:[39]

$$\Delta\mathrm{U}_{\mathrm{ads,R}(gas)} = -174\ \mathrm{kJ\ mol^{-1}} \tag{5.16}$$

The adsorption energy in the limit of low coverage is stronger, but it increases (weakens) by at least 50 kJ/mol in the first layer. (We argued previously that hydrophobic effects may drive phenol to reach higher local coverage when in water, even when its average coverage is very low.[32]) Thus, here and in **Table 5.2** we use the average energy. The adhesion energy of water to Pt(111) is:[32,51,52]

$$\mathrm{E}_{\mathrm{adh,S/M}} = 0.32\ \mathrm{J\ m^{-2}} \tag{5.17}$$

The adsorption energy of phenol in water assuming an infinitely flat molecule can be calculated from **Eq. 5.9**, using the gas-phase adsorption energy of phenol and the other above values:

$$\Delta U_{ads,R(solvent)} = \Delta U_{ads,R(gas)} + \left[E_{adh,S/M} - \frac{\Delta U_{solvation,R(gas)}}{\sigma_{tot}} - \gamma_{S(liq)}\right]\sigma_R$$

$$= (-174\ \mathrm{kJ\ mol^{-1}})$$

$$+ \left[0.32\ \mathrm{J\ m^{-2}} - \frac{-47.5\ \mathrm{kJ\ mol^{-1}}}{7.22 \times 10^5\ \mathrm{m^2\ mol^{-1}}} - (0.073\ \mathrm{J\ m^{-2}})\right](3.61 \times 10^5\ \mathrm{m^2\ mol^{-1}}) \tag{5.18}$$

$$= -61\ \mathrm{kJ\ mol^{-1}}$$

For the case where phenol is not infinitely thin, but instead $\sigma_{tot} = 3.16\ \sigma_R$, the adsorption energy of phenol in water can again be calculated from **Eq. 5.9**.

$$\Delta U_{ads,R(solvent)} = \Delta U_{ads,R(gas)} + \left[E_{adh,S/M} - \frac{\Delta U_{solvation,R(gas)}}{\sigma_{tot}} - \gamma_{S(liq)}\right]\sigma_R \tag{5.19}$$

$$= (-174\ \mathrm{kJ\ mol^{-1}})$$

$$+ \left[0.32\ \mathrm{J\ m^{-2}} - \frac{-47.5\ \mathrm{kJ\ mol^{-1}}}{1.14 \times 10^6\ \mathrm{m^2\ mol^{-1}}} - (0.073\ \mathrm{J\ m^{-2}})\right](3.61 \times 10^5\ \mathrm{m^2\ mol^{-1}}) = -70\ \mathrm{kJ\ mol^{-1}}$$

Note that in both of these models for phenol's structure, the difference in adsorption energy in solvent versus gas phase is dominated by $E_{adh,S/M}\sigma_R$ (and approximately equal to this). Here when using $\sigma_{tot} = 3.16\ \sigma_R$, the adsorption energy is ~9 kJ/mol (~15%) more negative (stronger) than in the infinitely-thin approximation ($\sigma_{tot} = 2\ \sigma_R$) because the phenol is retaining more of its bonding to water when (properly) assuming that its sides are also exposed to the water after adsorption. Essentially, if $\sigma_{tot} = 2\ \sigma_R$, when the phenol is adsorbed, only half of it remains "solvated", the top surface. This means there is a larger penalty when adsorbing in the aqueous-phase. When we assume $\sigma_{tot} = 3.16\ \sigma_R$, ~2/3 of the phenol remains "solvated", the top surface and the sides (which we assume to be the same area as the surface and bottom of the phenol molecule).

We plot the predicted adsorption energy of phenol in water as a function of $\sigma_{\mathrm{R}}/\sigma_{\mathrm{tot}}$ in **Figure 4** using **Eq. 5.7**. As this ratio increases (i.e., more solvation is lost upon adsorption), the adsorption energy in solvent is weakened, but this change is minor compared to the difference between the gas-phase and aqueous-phase adsorption energy. Note that when changing the value of $\sigma_{\mathrm{R}}/\sigma_{\mathrm{tot}}$, σ_{R} is being held constant at its experimental value.

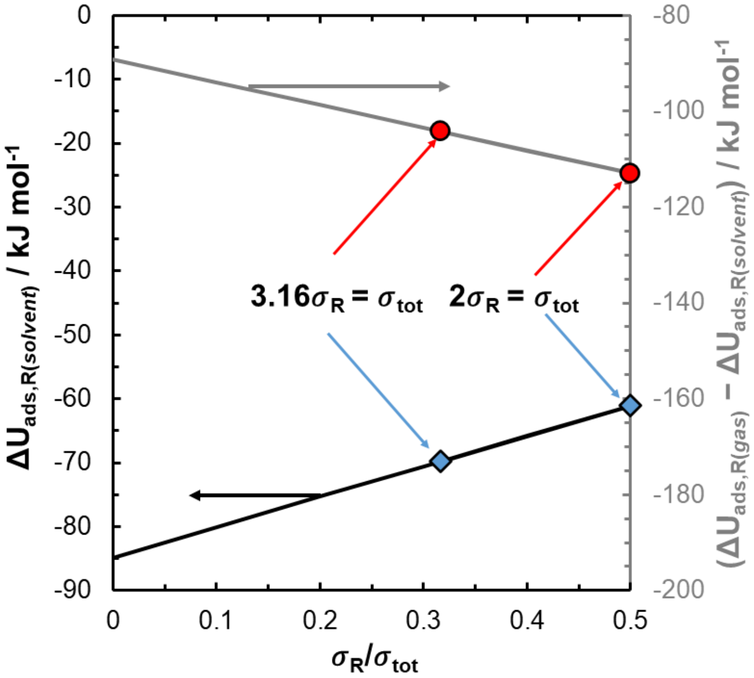

Figure 5.4 Energy of adsorption of phenol onto Pt(111) in water at 298 K as a function of the ratio of the footprint of phenol on the Pt surface to the total surface area of phenol, calculated using Eq. 5.7. The ratio of the footprint of phenol to the total surface area is essentially the fraction of solvation of the molecule that is lost due to adsorption. The right-hand axis shows the calculated difference in adsorption energy between gas phase and aqueous phase. For phenol on Pt(111) as described in the text: $\sigma_{\mathrm{R}} = 3.61 \times 10^5\ \mathrm{m^2\ mol^{-1}}$, $\mathrm{E_{adh,S/M}} = 0.32\ \mathrm{J\ m^{-2}}$, $\Delta \mathrm{U}_{\mathrm{solvation,R}(gas)} = -47.5\ \mathrm{kJ\ mol^{-1}}$, $\gamma_{\mathrm{S}(liq)} = 0.073\ \mathrm{J\ m^{-2}}$, and $\Delta \mathrm{U}_{\mathrm{ads,R}(gas)} = -174\ \mathrm{kJ\ mol^{-1}}$.

5.3.6 Solvation Energies per Unit Molecular Area, and Organic/Solvent Adhesion Energies

The negative of the solvation energy per unit molecular area ($-\Delta \mathrm{U}_{\mathrm{solvation,R}(gas)}/\sigma_{\mathrm{tot}}$) listed for organic molecules in **Table 5.1** equals the adhesion energy at the solvent/organic interface minus the surface energy of the solvent ($\mathrm{E}_{\mathrm{adh,S/R}} - \gamma_{\mathrm{S}(liq)}$). It is important to note that this value is quite similar for all the aromatic molecules in water (~0.02 to 0.03 J/m^2) except for the one that has an OH group (phenol), which is ~0.01 J/m^2 larger, presumably due to its ability to hydrogen bond with water. After adding to these values the surface energy of water (0.073 J/m^2), we see in **Table 5.1** that the water/organic adhesion energies ($\mathrm{E}_{\mathrm{adh,S/R}}$) are ~0.092 to 0.100 J/m^2 for all the aromatics unless they contain an oxygen, for which $\mathrm{E}_{\mathrm{adh,S/R}}$ is ~0.105 and 0.115 J/m^2 for =C=O and –OH groups, respectively. These values for oxygen-free aromatics are similar to but ~35% larger than those found from contact angle measurements for bulk liquid/liquid adhesion energies.[53] Larger adhesion energies than bulk values are expected for such small objects, at least based on measurements of metal nanoparticle adhesion to oxide surfaces.[54] The $\mathrm{E}_{\mathrm{adh,S/R}}$ values for the alkanes/water in **Table 5.1** are also quite similar. Adhesion energies in **Table 5.1** for aromatics to benzene are ~30% smaller than to water, and ~50% smaller for aromatics to n-hexane and methanol than to water. The physically reasonable values for $\mathrm{E}_{\mathrm{adh,S/R}}$ found in this way in **Table 5.1** lend credence to the assumptions used above in the derivation of **Eq. 5.9**. Since the values are so similar for similar classes of molecules, they also allow estimations to be made of solvent effects for other species not listed in **Table 5.1** and **Table 5.2**. One can imagine using such differences in $\mathrm{E}_{\mathrm{adh,S/R}}$ values for different classes of adsorbates to further refine the model by breaking down the total surface area of the adsorbate into different parts, for which different $\mathrm{E}_{\mathrm{adh,S/R}}$ values would be applied.

5.4 Conclusions

We recently developed a bond-additivity model one can use to estimate adsorption energies of “flat” molecules in liquid solvents using the experimental gas-phase adsorption energy of the molecule to the surface, the solvent’s adhesion energy to the surface, as well as the energy of solvation of the gas molecule, and showed that it provides moderate accuracy compared to experiments and enables predictions in important trends.[32] In this present work, we show that this model can be extended to molecules that are not infinitely flat but have larger thickness by assuming the interaction between the reactant molecule and solvent molecules is isotropic, and using the geometry of the molecule to estimate the fraction of its “solvation area” that is retained upon adsorption. This modified model allows application of the bond-additivity model to a wider variety of adsorbates of interest for catalysis and electrocatalysis. According to this model, the adsorption energy in solvent can be predicted from the adsorption energy in gas phase using **Eq. 5.13**:

$$\Delta \mathrm{U}_{\mathrm{ads,R}(solvent)} = \Delta \mathrm{U}_{\mathrm{ads,R}(gas)} + \left[\mathrm{E}_{\mathrm{adh},S/\mathrm{M}} - \frac{\Delta \mathrm{U}_{\mathrm{solvation,R}(gas)}}{\sigma_{\mathrm{tot}}} - \gamma_{\mathrm{S}(liq)}\right]\sigma_{\mathrm{R}} \tag{5.9}$$

As seen, the two adsorption energies differ by an amount proportional to the footprint area of the molecule on the surface, with a proportionality constant that is dominated by the adhesion energy of the solvent to the surface, with smaller and nearly cancelling contributions from the molecule’s solvation energy per unit molecular area and the solvents surface energy. This equation is independent of the shape of the molecule except in that the shape determines σ_{R} and the ratio $\sigma_{\mathrm{R}}/\sigma_{\mathrm{tot}}$. It reduces to the equation from our original bond-additivity model for molecules (like phenol and benzene) which were assumed to have negligible thickness (i.e., where $\sigma_{\mathrm{tot}} = 2\ \sigma_{\mathrm{R}}$, by simply replacing $\sigma_{\mathrm{R}}/\sigma_{\mathrm{tot}}$ with 1/2. This modified bond-additivity model offers a marked improvement for molecules that are relatively thicker and retain significantly more than half of their “solvation area” after adsorption.

5.5 References

(1) Walker, T. W.; Chew, A. K.; Li, H.; Demir, B.; Zhang, Z. C.; Huber, G. W.; Van Lehn, R. C.; Dumesic, J. A. Universal Kinetic Solvent Effects in Acid-Catalyzed Reactions of Biomass-Derived Oxygenates. *Energy Environ. Sci.* **2018**, *11*, 617–628.

(2) Mellmer, M. A.; Sanpitakseree, C.; Demir, B.; Bai, P.; Ma, K.; Neurock, M.; Dumesic, J. A. Solvent-Enabled Control of Reactivity for Liquid-Phase Reactions of Biomass-Derived Compounds. *Nat. Catal.* **2018**, *1*, 199–207.

(3) Segal, E.; Madon, R. J.; Boudart, M. Catalytic Hydrogenation of Cyclohexene. I. Vapor-Phase Reaction on Supported Platinum. *J. Catal.* **1978**, *52*, 45–49.

(4) Madon, R. J.; O’Connell, J. P.; Boudart, M. Catalytic Hydrogenation of Cyclohexene: Part II. Liquid Phase Reaction on Supported Platinum in a Gradientless Slurry Reactor. *AIChE J.* **1978**, *24*, 904–911.

(5) Gonzo, E. E.; Boudart, M. Catalytic Hydrogenation of Cyclohexene. 3. Gas-Phase and Liquid-Phase Reaction on Supported Palladium. *J. Catal.* **1978**, *52*, 462–471.

(6) Qi, L.; Alamillo, R.; Elliott, W. A.; Andersen, A.; Hoyt, D. W.; Walter, E. D.; Han, K. S.; Washton, N. M.; Rioux, R. M.; Dumesic, J. A.; et al. Operando Solid-State NMR Observation of Solvent-Mediated Adsorption-Reaction of Carbohydrates in Zeolites. *ACS Catal.* **2017**, *7*, 3489–3500.

(7) He, J.; Liu, M.; Huang, K.; Walker, T. W.; Maravelias, C. T.; Dumesic, J. A.; Huber, G. W. Production of Levoglucosenone and 5-Hydroxymethylfurfural from Cellulose in Polar Aprotic Solvent-Water Mixtures. *Green Chem.* **2017**, *19*, 3642–3653.

(8) Mellmer, M. A.; Sener, C.; Gallo, J. M. R.; Luterbacher, J. S.; Alonso, D. M.; Dumesic, J. A. Solvent Effects in Acid-Catalyzed Biomass Conversion Reactions. *Angew. Chemie - Int. Ed.* **2014**, *53*, 11872–11875.

(9) Iyemperumal, S. K.; Deskins, N. A. Evaluating Solvent Effects at the Aqueous/Pt(111) Interface. *ChemPhysChem* **2017**, *18*, 2171–2190.

(10) Singh, N.; Sanyal, U.; Ruehl, G.; Stoerzinger, K. A.; Gutiérrez, O. Y.; Camaioni, D. M.; Fulton, J. L.; Lercher, J. A.; Campbell, C. T. Aqueous Phase Catalytic and Electrocatalytic Hydrogenation of Phenol and Benzaldehyde over Platinum Group Metals. *J. Catal.* **2020**, *382*, 372–384.

(11) Chen, F.; Shetty, M.; Wang, M.; Shi, H.; Liu, Y.; Camaioni, D. M.; Gutiérrez, O. Y.; Lercher, J. A. Differences in Mechanism and Rate of Zeolite-Catalyzed Cyclohexanol Dehydration in Apolar and Aqueous Phase. *ACS Catal.* **2021**, *11*, 2879–2888.

(12) Xie, T.; Bodenschatz, C. J.; Getman, R. B. Insights into the Roles of Water on the Aqueous Phase Reforming of Glycerol. *React. Chem. Eng.* **2019**, *4*, 383–392.

(13) Sheng, W.; Zhuang, Z.; Gao, M.; Zheng, J.; Chen, J. G.; Yan, Y. Correlating Hydrogen Oxidation and Evolution Activity on Platinum at Different pH with Measured Hydrogen Binding Energy. *Nat. Commun.* **2015**, *6*, 5848.

(14) Koch, G. H.; Brongers, M. P. H.; Thompson, N. G.; Virmani, Y. P.; Payer, J. H. *Corrosion Cost and Preventive Strategies in the United States*; **2002**.

(15) Bockris, J. O.; Jeng, K. T. In-Situ Studies of Adsorption of Organic Compounds on Platinum Electrodes. *J. Electroanal. Chem.* **1992**, *330*, 541–581.

(16) Kristoffersen, H. H.; Shea, J.-E.; Metiu, H. Catechol and HCl Adsorption on TiO_2(110) in Vacuum and at the Water–TiO_2 Interface. *J. Phys. Chem. Lett.* **2015**, *6*, 2277–2281.

(17) Song, W.; Martsinovich, N.; Heckl, W. M.; Lackinger, M. Born-Haber Cycle for Monolayer Self-Assembly at the Liquid-Solid Interface: Assessing the Enthalpic Driving Force. *J. Am. Chem. Soc.* **2013**, *135*, 14854–14862.

(18) Yoon, Y.; Rousseau, R.; Weber, R. S.; Mei, D.; Lercher, J. A. First-Principles Study of Phenol Hydrogenation on Pt and Ni Catalysts in Aqueous Phase. *J. Am. Chem. Soc.* **2014**, *136*, 10287–10298.

(19) Singh, N.; Lee, M.-S.; Akhade, S. A.; Cheng, G.; Camaioni, D. M.; Gutiérrez, O. Y.; Glezakou, V.-A.; Rousseau, R.; Lercher, J. A.; Campbell, C. T. Impact of pH on Aqueous-Phase Phenol Hydrogenation Catalyzed by Carbon-Supported Pt and Rh. *ACS Catal.* **2019**, *9*, 1120–1128.

(20) Magnussen, O. M.; Groß, A. Toward an Atomic-Scale Understanding of Electrochemical Interface Structure and Dynamics. *J. Am. Chem. Soc.* **2019**, *141*, 4777–4790.

(21) Saleheen, M.; Heyden, A. Liquid-Phase Modeling in Heterogeneous Catalysis. *ACS Catal.* **2018**, *8*, 2188–2194.

(22) Zhang, X.; Sewell, T. E.; Glatz, B.; Sarupria, S.; Getman, R. B. On the Water Structure at Hydrophobic Interfaces and the Roles of Water on Transition-Metal Catalyzed Reactions: A Short Review. *Catal. Today* **2017**, *285*, 57–64.

(23) Zhang, X.; Defever, R. S.; Sarupria, S.; Getman, R. B. Free Energies of Catalytic Species Adsorbed to Pt(111) Surfaces under Liquid Solvent Calculated Using Classical and Quantum Approaches. *J. Chem. Inf. Model.* **2019**, *59*, 2190–2198.

(24) Granda-Marulanda, L. P.; Builes, S.; Koper, M. T. M.; Calle-Vallejo, F. Influence of Van Der Waals Interactions on the Solvation Energies of Adsorbates at Pt-Based Electrocatalysts. *ChemPhysChem* **2019**, *20*, 2968–2972.

(25) Schweitzer, B.; Steinmann, S. N.; Michel, C. Can Microsolvation Effects Be Estimated from Vacuum Computations? A Case-Study of Alcohol Decomposition at the H_2O/Pt(111) Interface. *Phys. Chem. Chem. Phys.* **2019**, *21*, 5368–5377.

(26) Klamt, A.; Schüürmann, G. COSMO: A New Approach to Dielectric Screening in Solvents with Explicit Expressions for the Screening Energy and Its Gradient. *J. Chem. Soc. Perkin Trans. 2* **1993**, *0*, 799–805.

(27) Zare, M.; Solomon, R. V.; Yang, W.; Yonge, A.; Heyden, A. Theoretical Investigation of Solvent Effects on the Hydrodeoxygenation of Propionic Acid over a Ni(111) Catalyst Model. *J. Phys. Chem. C* **2020**, *124*, 16488–16500.

(28) Gray, C. M.; Saravanan, K.; Wang, G.; Keith, J. A. Quantifying Solvation Energies at Solid/Liquid Interfaces Using Continuum Solvation Methods. *Mol. Simul.* **2017**, *43*, 420–427.

(29) Zhang, X.; Savara, A.; Getman, R. B. A Method for Obtaining Liquid-Solid Adsorption Rates from Molecular Dynamics Simulations: Applied to Methanol on Pt(111) in H_2O. *J. Chem. Theory Comput.* **2020**, *16*, 2680–2691.

(30) Yuk, S. F.; Lee, M.-S.; Akhade, S. A.; Nguyen, M.-T.; Glezakou, V.-A.; Rousseau, R. First-Principle Investigation on Catalytic Hydrogenation of Benzaldehyde over Pt-Group Metals. *Catal. Today* **2020**. https://doi.org/10.1016/j.cattod.2020.07.039.

(31) Clabaut, P.; Schweitzer, B.; Götz, A. W.; Michel, C.; Steinmann, S. N. Solvation Free

Energies and Adsorption Energies at the Metal/Water Interface from Hybrid Quantum-Mechanical/Molecular Mechanics Simulations. *J. Chem. Theory Comput.* **2020**, *16*, 6539–6549.

(32) Singh, N.; Campbell, C. T. A Simple Bond-Additivity Model Explains Large Decreases in Heats of Adsorption in Solvents Versus Gas Phase: A Case Study with Phenol on Pt(111) in Water. *ACS Catal.* **2019**, *9*, 8116–8127.

(33) Rumptz, J. R.; Campbell, C. T. Adhesion Energies of Solvent Films to Pt(111) and Ni(111) Surfaces by Adsorption. *ACS Catal.* **2019**, *9*, 11819–11825.

(34) Gileadi, E. Electrosorption of Uncharged Molecules on Solid Electrodes. *J. Electroanal. Chem.* **1966**, *11*, 137–151.

(35) Akinola, J.; Barth, I.; Goldsmith, B. R.; Singh, N. Adsorption Energies of Oxygenated Aromatics and Organics on Rhodium and Platinum in Aqueous Phase. *ACS Catal.* **2020**, *10*, 4929–4941.

(36) Barone, V.; Cossi, M.; Tomasi, J. A New Definition of Cavities for the Computation of Solvation Free Energies by the Polarizable Continuum Model. *J. Chem. Phys.* **1997**, *107*, 3210–3221.

(37) Skyner, R. E.; McDonagh, J. L.; Groom, C. R.; Van Mourik, T.; Mitchell, J. B. O. A Review of Methods for the Calculation of Solution Free Energies and the Modelling of Systems in Solution. *Phys. Chem. Chem. Phys.* **2015**, *17*, 6174–6191.

(38) Carey, S. J.; Zhao, W.; Campbell, C. T. Energetics of Adsorbed Benzene on Ni(111) and Pt(111) by Calorimetry. *Surf. Sci.* **2018**, *676*, 9–16.

(39) Carey, S.; Zhao, W.; Mao, Z.; Campbell, C. T. Energetics of Adsorbed Phenol on Ni(111) and Pt(111) by Calorimetry. *J. Phys. Chem. C* **2019**, *123*, 7627–7632.

(40) Silbaugh, T. L.; Campbell, C. T. Energies of Formation Reactions Measured for Adsorbates on Late Transition Metal Surfaces. *J. Phys. Chem. C* **2016**, *120*, 25161–25172.

(41) Mantina, M.; Chamberlin, A. C.; Valero, R.; Cramer, C. J.; Truhlar, D. G. Consistent van Der Waals Radii for the Whole Main Group. *J. Phys. Chem. A* **2009**, *113*, 5806–5812.

(42) Guedes, R. C.; Coutinho, K.; Costa Cabrai, B. J.; Canuto, S.; Correia, C. F.; Borges dos Santos, R. M.; Martinho Simões, J. A. Solvent Effects on the Energetics of the Phenol O-H Bond: Differential Solvation of Phenol and Phenoxy Radical in Benzene and Acetonitrile. *J. Phys. Chem. A* **2003**, *107*, 9197–9207.

(43) Rumptz, J. R.; Campbell, C. T. Adhesion Energies of Liquid Hydrocarbon Solvents onto Pt(111), MgO(100), Graphene and TiO_2(110) from Temperature Programmed Desorption Energies. *J. Phys. Chem. C* (submitted).

(44) Kiselev, V. D.; Shakirova, I. I.; Potapova, L. N.; Kashaeva, H. A.; Kornilov, D. A. Heats of Solution of Liquid Solutes in Various Solvents. *Dataset Pap. Chem.* **2013**, 1–3.

(45) Adamson, A. W.; Gast, A. P. *Physical Chemistry of Surfaces*, 6th ed.; 1997.

(46) Singh, N.; Sanyal, U.; Fulton, J. L.; Gutiérrez, O. Y.; Lercher, J. A.; Campbell, C. T. Quantifying Adsorption of Organic Molecules on Platinum in Aqueous Phase by Hydrogen Site Blocking and In Situ X-ray Absorption Spectroscopy. *ACS Catal.* **2019**, *9*, 6869–6881.

(47) Campbell, C. T.; Sellers, J. R. V. The Entropies of Adsorbed Molecules. *J. Am. Chem. Soc.* **2012**, *134*, 18109–18115.

(48) Lu, F.; Salaita, G. N.; Laguren-Davidson, L.; Stern, D. A.; Wellner, E.; Frank, D. G.; Batina, N.; Zapien, D. C.; Walton, N.; Hubbard, A. T. Characterization of Hydroquinone and Related Compounds Adsorbed at Pt(111) from Aqueous Solutions: Electron Energy-Loss Spectroscopy, Auger Spectroscopy, Low-Energy Electron Diffraction, and Cyclic

Voltammetry. *Langmuir* **1988**, *4*, 637–646.
(49) Sander, R. Henry's Law Constants. In *NIST Chemistry WebBook, NIST Standard Reference Database Number 69, Eds. P.J. Linstrom and W.G. Mallard, National Institute of Standards and Technology, Gaithersburg MD, 20899*; **2018**; pp 1–3.
(50) Israelachvili, J. N. *Intermolecular and Surface Forces*; Academic Press, 2011.
(51) Ketcham, W. M.; Hobbs, P. V. An Experimental Determination of the Surface Energies of Ice. *Philos. Mag.* **1969**, *19*, 1161–1173.
(52) Lew, W.; Crowe, M. C.; Karp, E.; Campbell, C. T. Energy of Molecularly Adsorbed Water on Clean Pt(111) and Pt(111) with Coadsorbed Oxygen by Calorimetry. *J. Phys. Chem. C* **2011**, *115*, 9164–9170.
(53) Pomerantz, P.; Clinton, W. C.; Zisman, W. A. Spreading Pressures and Coefficients, Interfacial Tensions, and Adhesion Energies of the Lower Alkanes, Alkenes, and Alkyl Benzenes on Water. *J. Colloid Interface Sci.* **1967**, *24*, 16–28.
(54) Campbell, C. T.; Mao, Z. Chemical Potential of Metal Atoms in Supported Nanoparticles: Dependence upon Particle Size and Support. *ACS Catal.* **2017**, *7*, 8460–8466.

Chapter 6 Electrocatalytic Hydrogenation of Phenol on Platinum-Cobalt Alloys

The computational work in this chapter was performed by Isaiah Barth.

6.1 Summary

Platinum-cobalt alloys enhance the hydrogen evolution reaction (HER) compared to Pt, although it is unclear if alloying also benefits electrocatalytic hydrogenation (ECH) of organics. We measure the HER exchange current density on Pt_xCo_y nanoparticles and find Pt_3Co to be the most active for HER due to it having the weakest hydrogen adsorption strength as predicted from density functional theory (DFT) modeling. We perform ECH of phenol on Pt_xCo_y and demonstrate that although under certain potentials Pt_xCo_y alloys are more active than Pt, the ECH activity does not correlate directly with the hydrogen adsorption energy (ΔG_H) despite adsorbed hydrogen being an intermediate in the rate-determining step. Combined electrochemical measurements, DFT calculations, and kinetic modeling reveal that ΔG_H is an insufficient descriptor for phenol ECH because the activation energies for hydrogenation scale more closely with reaction energies, which are more endothermic on Pt_xCo_y compared to Pt. By incorporating the computed activation enthalpies into a simple hydrogenation kinetic model, we describe the qualitative trends in the ECH of phenol on Pt_xCo_y alloys as a function of applied potential and Co composition.

6.2 Introduction

The search for sustainable energy and chemicals has led to a growing interest in hydrogen-related processes, such as the hydrogen evolution reaction (HER) and the electrocatalytic hydrogenation (ECH) of bio-oil. Electrocatalytic hydrogenation offers a sustainable pathway to stabilize lignin-derived bio-oil on the route to producing specialty chemicals and transportation fuels.[1–7] Understanding the mechanism and catalyst structure-activity relations for ECH of components of bio-oil may aid the transition to sustainable chemical and fuel production. In this study, we investigate phenol in aqueous acetate buffer as a representative lignin-derived phenolic compound in bio-oil,[8] and we study ECH on Pt alloyed with Co (Pt_xCo_y) to understand the mechanism and alloy nanoparticle catalyst design rules.

Electrocatalytic hydrogenation of phenol on Pt follows a Langmuir-Hinshelwood mechanism, such that the reaction rate is governed, in part, by the adsorption energies of hydrogen and phenol.[9,10] Surface-adsorbed hydrogen can either hydrogenate the phenol or combine via HER to form H_2 as a side reaction. There are multiple examples of controlling the adsorption energies of reactants through alloying for thermocatalytic hydrogenation (TCH).[11–18] Gas-phase TCH of cyclohexene on Pt alloyed with Fe, Co, Ni, or Cu reached a maximum activity at moderate cyclohexene and hydrogen adsorption energies.[19] The catalytic activity of Ni_xFe_y alloys for hydrogenation of C=C, C=O, and C-N bonds positively correlate with weakening hydrogen adsorption, and Ni_2Fe sites had the weakest hydrogen adsorption energy and highest hydrogenation activity.[20] Hydrogen adsorption energy (ΔG_H) is also an effective descriptor for the HER activity of metals and alloys.[21–27] There are much fewer studies using alloys for ECH of organics,[28–30] and the use of organic adsorption energy and ΔG_H as ECH descriptors is underexplored. Generally, there is limited understanding of how alloying affects adsorption energies and reaction barriers of organics in the aqueous phase and whether ΔG_H is a useful descriptor for ECH activity.

Whether a simple descriptor for ECH exists may depend highly on the structure of the alloy surface under reaction conditions. The activity of alloys is highly dependent on the composition of the surface and subsurface as well as nanostructure through strain,[31–33] ligand,[34,35] and ensemble[36,37] effects. The possibility of enrichment of certain elements in the catalyst surface is particularly important under reaction conditions where catalyst restructuring is possible and difficult to detect.[38] For example, Oezaslan *et al.* report that Pt_xCo_y forms a Pt skin in 0.1 M $HClO_4$,[39] whereas others report that the surface in 0.1 M $HClO_4$ or 1 M HNO_3 consists of a mixture of Pt and Co atoms rather than a pure Pt skin.[40–42] The activity of a surface consisting only of Pt atoms may differ considerably from a catalyst surface consisting of both Pt and Co atoms in close proximity, even if the subsurface composition is similar.

In this work, we synthesize and characterize Pt_xCo_y alloys of different Co compositions to understand how the catalyst structure and hydrogen adsorption energy are related to ECH activity and current efficiency. We select these Pt_xCo_y alloys because Pt is an active metal for ECH and subsurface alloying of Co is reported to weaken the hydrogen adsorption energy as a result of compressive strain and ligand effects.[31,33,34] We postulate that weakening the hydrogen adsorption energy will enhance HER activity, but ECH activity will depend more strongly on the nanostructure and presence of surface Co in the Pt_xCo_y. Our X-ray absorption spectroscopy (XAS) and scanning transmission electron microscopy (STEM) characterization of the Pt_xCo_y alloy nanoparticles show that although the surface is enriched in Pt rather than Co relative to the bulk, the surfaces are still a mixture of Pt and Co atoms (as opposed to a pure Pt skin over a Pt_xCo_y core). On our Pt_xCo_y alloys, the ECH activity does not simply trend with the hydrogen adsorption energy. Our density functional theory (DFT) calculations indicate that the ECH activities of these alloys cannot be described by the ΔG_H alone because hydrogenation barriers tend to follow a Brønsted-Evans-Polanyi relationship with respect to the reaction energies of phenol hydrogenation, and surfaces with weaker hydrogen adsorption energies do not necessarily have lower hydrogenation barriers. We demonstrate how kinetic modeling is able to qualitatively describe the experimental activity of these alloys by incorporating not only the ΔG_H but also computed transition state energies on the mixed Pt and Co surfaces.

6.3 Experimental & Computational Methods

6.3.1 Chemicals and Materials

All chemicals purchased were used as received. Chloroplatinic acid hexahydrate, $H_2PtCl_6 \cdot 6H_2O$ (38–40% Pt, Sigma Aldrich) and cobalt hydroxide, $Co(OH)_2$ (95%, Sigma Aldrich) were used as metal precursors for catalyst synthesis. 37% HCl (Sigma Aldrich) was used to neutralize alkaline $Co(OH)_2$. Sodium borohydride, $NaBH_4$ (≥96%, Sigma Aldrich) was used as the chemical reductant. Carbon felt (6.35 mm thick, 99.0%, Alfa Aesar) was used as the conductive porous support for ECH measurements. A graphite rod (3.05 mm diameter, 99.9995%, Alfa Aesar) connected to carbon felt was used as the working electrode. Sodium acetate buffer solution (Sigma Aldrich, 3 M, pH 5.2) was used as supporting electrolyte for ECH and HER. Metal catalysts on Vulcan carbon, that is, 30 wt% Pt/C, 40 wt% Pt_3Co/C, and 40 wt% PtCo/C were purchased from the Fuel Cell store. A 5% Nafion 117 solution (Sigma Aldrich) was used as the binder for preparing catalyst inks for HER measurements. Boron nitride (99.5%, Alfa Aesar) was used to pelletize the metal catalysts for ex-situ X-ray absorption spectroscopy (XAS) measurements.

6.3.2 Catalyst Preparation

Two sets of Pt_xCo_y alloys were prepared. Pt_xCo_y/C refers to purchased nanoparticles of Pt_xCo_y supported on Vulcan carbon. Pt_xCo_y/C were used to measure HER activity on a rotating disk electrode (RDE). Pt_xCo_y/felt denotes Pt_xCo_y nanoparticles synthesized on a conductive porous carbon felt. Pt_xCo_y/felt were used for ECH activity measurements because higher surface area catalysts were needed for product quantification and because of difficulties in loading the Pt_xCo_y/C onto a porous support without mechanical loss of catalyst at the negative potentials explored in this work. Both sets of samples were exposed to acid and electrochemically cycled prior to testing for activity to avoid any leaching during activity measurements. This pretreatment process is described below.

6.3.2.1 Preparation of Platinum-Cobalt Alloy Nanoparticles on Vulcan Carbon for Rotating Disk Electrode

To perform HER measurements using a RDE, catalysts inks were prepared by adding 3 mg of the supported catalyst (i.e., 30 wt% Pt/C, 40 wt% Pt_3Co/C, or 40 wt% PtCo/C) into a mixture of 2.5 mL Millipore water and 2.5 mL isopropyl alcohol and 17.5 µL of 5 wt% Nafion solution as the binding agent. The mixture was sonicated for 2 hrs to disperse the catalyst in the solution. A glassy carbon disk substrate for the inks was thoroughly polished using a 0.05 µm alumina suspension and rinsed three times with Millipore water and then sonicated in water for 30 min. 8 µL of the freshly sonicated catalyst ink was deposited on the clean glassy carbon disk substrate assembled in a Teflon rotating disk holder in two separate depositions (16 µL total) performed 30 min apart to achieve a catalyst loading of 9.6 µg. The deposited catalysts were air dried in a closed compartment for at least 1 hr to form a catalyst film before experiments.

6.3.2.2 Synthesis of Platinum-Cobalt Alloy Nanoparticles on Porous Carbon Felt Support

Pieces of carbon felt (1.5 cm × 1.5 cm × 6.35 mm thick) were first thermally pretreated in air at 400 °C for 16 hrs to increase their surface area. Pt_xCo_y was directly synthesized on carbon felts by chemical reduction using a sodium borohydride method.[43] The target compositions of Pt and Co were adjusted to synthesize Pt/felt, Pt_3Co/felt, PtCo/felt, and $PtCo_3$/felt. An amount of $Co(OH)_2$ to achieve the desired Co metal loading and metal atomic ratio was dissolved in 20 mL mixture of 1:1 volume ratio of methanol to Millipore water. After 37% HCl was added dropwise with a precision pipette to bring the solution to pH 2. Similarly, the desired amount of $H_2PtCl_6 \cdot 6H_2O$ was used to prepare a separate 20 mL aqueous solution of chloroplatinic acid. The two solutions were mixed, and the wetted carbon felt was sonicated in the solution for 2 hrs. $NaBH_4$ was added to 5 mL of water in a separate vial to achieve $NaBH_4$:metal molar ratio of 12:1. Sodium borohydride solution was added dropwise to the precursor solution containing the felt in a water bath and sonicated for 3 hrs. The felt was afterwards removed from the solution, rinsed three times with Millipore water, and left to dry in a vacuum oven set at 80 °C for 15 hrs. Before use for ECH measurements, the felt was thoroughly rinsed with Millipore water.

6.3.3 Catalyst Characterization and Surface Area Measurements

6.3.3.1 Pretreatment of Platinum-Cobalt Alloys Before Use

To minimize dissolution of Co during activity testing, the Pt_xCo_y catalysts were first subjected to cyclic voltammetry by applying 1500 potential sweeps between 0.05 and 1.5 V vs. RHE at 500 mV/s in acetate buffer. The same procedure was used for the Pt_xCo_y/C and Pt_xCo_y/felt samples and is based on a protocol that is known to both remove any residual unalloyed Co in the catalyst and leach Co from the Pt_xCo_y/C surface. This process is reported to result in either a Pt shell with a Pt_xCo_y core or to form an enriched Pt surface although with surface Co present (i.e., a mixed alloy surface).[40–42] Our results here indicate that we form a mixed alloy surface that contains both Pt and Co as described in the Results and Discussion. The pretreated catalysts following cyclic voltammetry were used for all HER and ECH activity measurements and all characterization except where specified otherwise.

6.3.3.2 Bulk Elemental Analysis

The Pt and Co loadings of the as prepared Pt_xCo_y and pretreated Pt_xCo_y catalysts (i.e., following cyclic voltammetry) were measured using a PerkinElmer NexION 2000 ICP-MS. 1 mg of the catalyst was digested in 2 mL aqua regia solution (3:1 molar HCl:HNO3). This solution was further diluted with Millipore water by a factor of 10000 to about 10–20 ppb. 20 ppb bismuth and 20 ppb scandium were co-fed as internal standard in the instrument to normalize Pt and Co intensities, respectively. The concentrations of Pt and Co were extracted by comparing to calibration standards of Pt and Co. The composition based on inductively coupled plasma-mass spectrometry (ICP-MS) is used for the catalyst naming convention.

6.3.3.3 X-ray Absorption Spectroscopy

The pretreated Pt_xCo_y/C and Pt_xCo_y/felt catalysts were crushed to powder and mixed with calculated amounts of boron nitride as a pelletizer to obtain desired edge steps and X-ray transmission through the samples. The catalysts and boron nitride were made into pellets (13 mm diameter and 1–2 mm thick) and probed at the Pt L_3-edge (11564 eV) and Co K-edge (7709 eV). These samples were also analyzed in our custom made in-situ XAS cell[44] under negative cathodic potential with and without phenol in the supporting electrolyte to understand the catalyst structure during ECH. Samples were analyzed in transmission mode or fluorescence mode depending on the quality of the data. In-situ XAS measurements were performed only in fluorescence mode because of hydrogen bubble formation that interfered with transmission signal. A minimum of three scans were taken for each sample at either edge. Pre- processing and linear combination fitting of the XANES region was performed using Athena while EXAFS fitting was performed using Artemis.[45] Pt and Co foils were used as standards for either edge and used as reference in data alignment and fitting.

6.3.3.4 X-ray Diffraction (XRD)

X-ray diffraction was performed on the Pt_xCo_y/C and Pt_xCo_y/felt catalysts using a Rigaku Miniflex X-ray diffractometer with Cu Kα radiation and a Ni filter that has an X-ray wavelength of 1.5406 Å. For the Pt_xCo_y/felt samples, 10 mg of the catalyst on felt was crushed to powder and put into a transparent sample holder before setting the voltage and current to 40 kV and 15 mA, respectively. For the Pt_xCo_y/C samples, the powder was directly used. Scanning was carried out at 3°/min with a 0.02° step in the range of $10° < 2\theta < 90°$. The Scherrer equation was used to estimate the average crystallite size.

6.3.3.4 Transmission Electron Microscopy (TEM) and Scanning Transmission Electron Microscopy (STEM) Measurements

A Thermo Fisher Scientific Talos F200X G2 electron microscope equipped with a Super-X EDX detector and operating at an accelerating voltage of 200 keV was used for the STEM and TEM imaging and analysis. A portion of the catalyst on carbon felt was washed, dried, and grounded before dissolving 1 mg of the ground catalyst in 1 mL of isopropanol. A drop of the suspension was deposited on a clean Cu grid. The Cu grid was left to dry overnight before imaging was performed. The average size and distribution of particles were acquired with the ImageJ software.

6.3.3.5 Hydrogen Underpotential Deposition (H_{upd})

The electrochemically active surface area (ECSA) of exposed Pt surface metal atoms on the Pt_xCo_y/felt and Pt_xCo_y/C catalysts was measured using H_{upd}. The catalysts were electrochemically cleaned using cyclic voltammetry (CV) at 100 mV/s for 50 cycles at potentials –0.2 to 1.5 V vs. RHE. After electrochemical cleaning, CV was done at a 20 mV s^{-1} scan rate in the potential window of 0.05 V to 1.2 V and the H_{upd} charge from the oxidative region after subtracting the baseline capacitive charge was used to estimate the ECSA of the Pt sites using a charge density of 210 μC cm^{-2}.

6.3.4 Hydrogen Evolution Reaction (HER)

Hydrogen evolution was performed in a 3 M acetate buffer solution in a three-electrode single compartment batch electrolysis cell at room temperature. The working electrode was the glassy carbon disk with the deposited catalysts assembly used in an RDE setup (Pine Instruments). A Ag/AgCl double junction electrode was used as the reference electrode and a Pt wire loop was used as the counter electrode. The catalysts were first pretreated as discussed above, and the ECSA was measured by H_{upd} before performing linear scan voltammetry at 10 mV s^{-1} between −0.2 V and 1.1 V vs. RHE at rotation rates of 400, 900, 1600, and 2500 rpm. The applied potential was corrected for potential loss due to series resistance as measured by the real part of the impedance measured at high frequency. The measured current was normalized to ECSA to obtain the current density. Based on the measurements, 1600 rpm was sufficiently high that mass transport artifacts were not observed (**Figure 6.1a–c**), thus the current densities at 1600 rpm were used to evaluate intrinsic kinetics (kinetic current density). Tafel plots were constructed by plotting the log of the current density at 1600 rpm against the overvoltage for the HER rates (**Figure 6.1d**). The Tafel slope and exchange current density were determined by fitting the log of current density vs.

overvoltage to a linear line (log $i = \eta/b + \log i_0$), where i is the kinetic current density, b is the Tafel slope, η is the overvoltage, and i_0 is the exchange current density. Only overvoltage values ≥100 mV were used in the fit to the Tafel equation to extract the exchange current density.

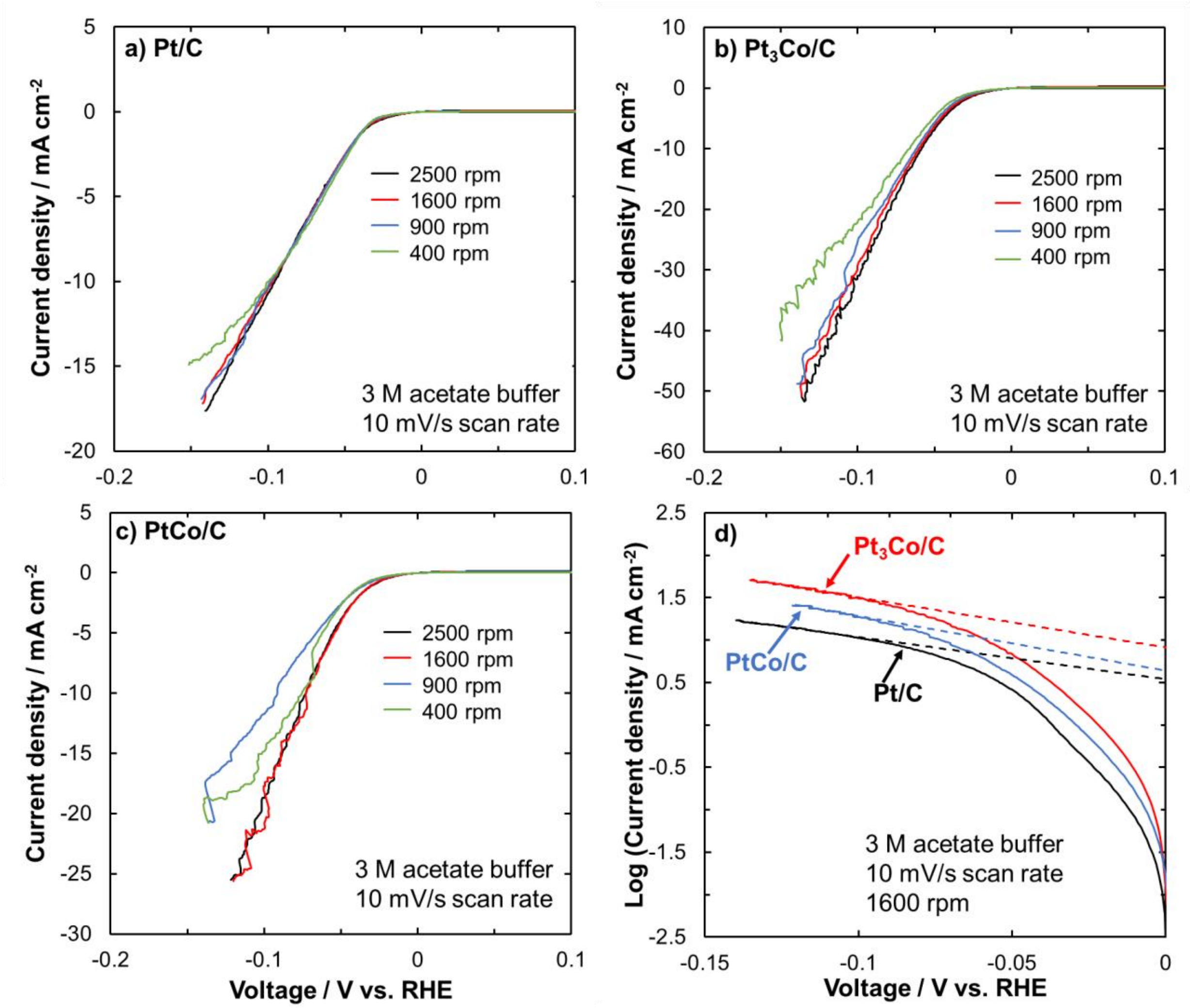

Figure 6.1 Linear scan voltammograms and Tafel plots for Pt/C and Pt_xCo_y/C. LSVs were performed at 23.3°C in 3 M acetate buffer (pH 5.2) and a scan rate of 10 mV/s at rotation speeds of 400, 900, 1600, and 2500 rpm for **a)** Pt/C, **b)** Pt_3Co/C, and **c)** PtCo/C. **d)** Log(current density) vs. the HER overpotential for Pt/C, Pt_3Co/C, and PtCo/C for measurements at 1600 rpm. The Tafel lines (dashed lines) were obtained by fitting the data at potentials ≤ –0.1 V vs. RHE to the Tafel equation as described in the methods. The Tafel slopes for Pt/C, Pt_3Co/C and PtCo/C are 142 mV dec^{-1}, 170 mV dec^{-1} and 154 mV dec^{-1}, respectively.

6.3.5 Electrocatalytic Hydrogenation of Phenol

6.3.5.1 ECH Measurement

ECH was performed on the Pt_xCo_y/felt catalysts using a two-compartment batch electrolysis cell where the cathodic and anodic compartments were separated with a Nafion 117 membrane. The Pt_xCo_y/felt catalysts were attached to a 3 mm diameter graphite rod (Sigma Aldrich, 99.99%) and used as the working electrode in the 140 mL cathodic compartment. Acetate buffer (3M, pH 5.2) sparged with N_2 was used as the supporting electrolyte in both cathodic and anodic compartments. A Ag/AgCl double junction electrode was used as the reference electrode and the counter electrode was a 3 mm diameter graphite rod (Sigma Aldrich, 99.99%). To perform ECH, the desired potential was first applied for 1 hr to the working electrode to polarize the catalyst surface and saturate the solution with in-situ generated H_2. Phenol sparged with N_2 was added to the cathodic compartment to achieve 20 mM phenol concentration before performing ECH at a fixed potential of either −0.1, −0.15 and −0.2 V vs. RHE using a Bio-Logic VSP-300. The series resistance was automatically compensated at 85% using impedance spectroscopy at a frequency of 200 kHz and the remaining 15% was manually corrected to give ±10 mV of the reported iR-free applied potentials. No change in the pH of acetate buffer plus phenol solution before and after performing ECH for 2 hrs was observed, indicating sufficient buffering capacity.

6.3.5.2 Product Quantification During ECH of Phenol

A 1 mL aliquot was taken from the cathodic compartment every 30 mins to monitor ECH reaction progress. ECH products (i.e., cyclohexanone and cyclohexanol) and the phenol reactant were extracted from the aqueous supporting electrolyte into an organic phase using through three sequential liquid-liquid extractions with ethyl acetate as the solvent. For every extraction step, about 5 mg of sodium chloride was added to the aliquot before mixing with 1 mL of pure ethyl acetate to aid separation of the organic and aqueous phase. Any water present in the organic phase was removed using anhydrous Na_2SO_4 (Sigma Aldrich 99%). Dimethoxybenzene (DMB) was used as an external standard, where 10 µL DMB was mixed with 1 mL of the dried organic phase before injecting 1 µL of the mixture to an Agilent Varian 450 gas chromatograph equipped with a flame ionization detector. ECH was performed at less than 10% conversion and carbon balances were greater than 90%. The turnover frequency (TOF) for each Pt_xCo_y/felt catalyst was calculated from the rate of cyclohexanol and cyclohexanone formed per surface Pt atom estimated from the hydrogen underpotential deposition.

6.3.6 Density Functional Theory Modeling

The Vienna Ab initio Simulation Package (VASP) was used for Kohn-Sham DFT calculations.[46–49] The exchange-correlation energy was calculated using the Perdew-Burke-Ernzerhof functional[50] and the semi-empirical D3 dispersion correction.[51] The projector augmented wave method and a plane wave kinetic energy cutoff of 400 eV were used for all calculations.[52,53] The first-order Methfessel-Paxton smearing scheme with a 0.2 eV smearing width was used.[54] All calculations performed on slabs containing Co were spin-polarized. Spin polarization had a negligible effect on the pure Pt surface.

We modeled Pt and Pt_xCo_y intermetallics (i.e., Pt, Pt_3Co, PtCo, and $PtCo_3$) and Pt/Pt_xCo_y core-shell (i.e., a monolayer of pure Pt over a Pt_xCo_y subsurface) systems to investigate how Pt enrichment in the alloy surface affects adsorption of phenol and hydrogen and the catalytic performance for HER and ECH. Four-atom bulk face-centered cubic (FCC) unit cells of Pt, Pt_3Co, PtCo, and $PtCo_3$ were optimized in VASP with a $21 \times 21 \times 21$ Monkhorst-Pack *k*-point grid.[55] We modeled only the FCC crystal structure because it is the crystal structure observed experimentally in our purchased and synthesized catalysts from XRD. The expected change in lattice constant with Co fraction (i.e., from Vegard's law) from the FCC lattice constants matches the change in lattice constant from our powder XRD data for Pt_xCo_y/C for their expected Co fraction (**Figure 6.2**), indicating alloys are formed. Previous work found that the (111) facet of Pt and other metals like Rh are the active facet for hydrogenation of aromatics.[56,57] Therefore, we constructed the (111) facets of Pt, Pt_3Co, PtCo, and $PtCo_3$ from the bulk unit cells. The Pt/Pt_xCo_y slabs were modeled by replacing all Co atoms in the top layer of the slabs with Pt to achieve a pure Pt surface layer. The Pt_xCo_y and Pt/Pt_xCo_y systems were modeled using 4 × 4 × 4 slabs, where the bottom two layers were fixed in their bulk lattice coordinates and the top two layers were relaxed during geometry optimization. A 3 × 3 × 1 Mokhorst-Pack *k*-point grid was used for all slab calculations. The climbing-image nudged elastic band method was used to find the transition states for the hydrogenation reactions.[58] The enthalpies and free energies of adsorbed phenol, hydrogen, and reaction intermediates were evaluated in the harmonic limit without solvation corrections, and the free energies of non-adsorbed species were evaluated using ideal gas thermodynamic corrections at 300 K. Implicit solvation was not used to model adsorption or hydrogenation because it was found to improperly describe solvent effects for phenol adsorption and had little effect on the adsorption energies of hydrogen or the hydrogenation barriers using default parameters.[56,59]

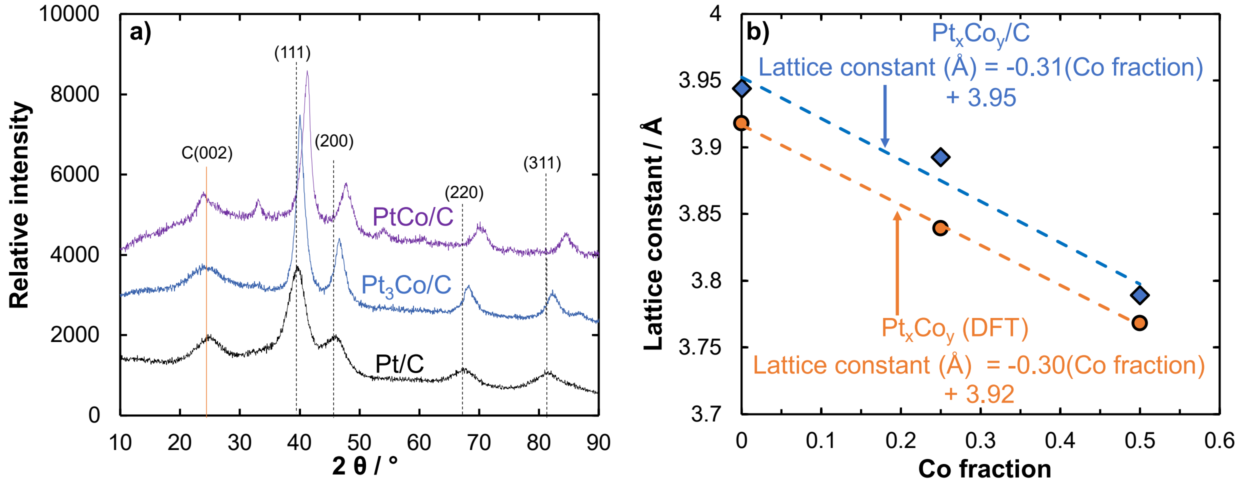

Figure 6.2 XRD spectra and lattice constant as a function of Co fraction for Pt, Pt_3Co and PtCo face-centered cubic structures. a) XRD spectra for Pt_xCo_y/C. The vertical lines in a) correspond to the 2θ peak locations for the Pt/C to observe the shift in peak location for Pt_xCo_y/C. **b)** Lattice constants from our DFT-modelled Pt_xCo_y slabs and lattice constants from Pt_xCo_y/C obtained using Bragg's law.

6.4 Results and Discussion

6.4.1 Comparing Hydrogen Evolution Activity to Hydrogen Adsorption Energy on Pt_xCo_y/C

In **Figure 6.3a** we show the HER exchange current densities on Pt_xCo_y/C catalysts is a function of Co fraction where Pt_3Co/C is the most active for HER, followed by PtCo/C and Pt/C. The exchange current density of Pt/C in acetate buffer (pH 5.2) obtained here (4.1 mA cm^{-2}) matches that reported by Zheng and coworkers (4.0 mA cm^{-2}) in the same electrolyte and pH.[22] The HER activity trend between Pt/C and Pt_3Co/C is consistent with past studies that reported Pt_3Co to be superior to Pt,[42,60] although the structure of the Pt_3Co surface impacts the HER performance. Specifically, a Pt_3Co catalyst with both Pt and Co present on the surface and a Pt_3Co catalyst with a pure Pt surface layer (core-shell) were reported to increase the current density by two and five times compared to pure Pt, respectively.[42] Exposing Pt_xCo_y catalysts to acidic conditions can form a Pt-enriched surface (i.e., a surface with both Pt and Co) or a Pt-skin structure on a Pt_xCo_y core. However, the structure of Pt_xCo_y alloys in our supporting electrolyte (3 M acetate buffer, pH 5) has never been reported. The enhancement we observe in **Figure 6.3a** for Pt_3Co/C

compared to Pt/C (a factor of 2.25) is close to the reported enhancement for a Pt_3Co catalyst with both Pt and Co present on the surface. Although there are reports of sub-nanometer PtCo clusters with enhanced HER activity relative to pure Pt,[61] our PtCo/C, with a diameter of approximately 5 nm (characterization provided below), is less active than Pt_3Co/C and more similar to Pt/C. To better understand the trends in HER exchange current densities on the Pt_xCo_y/C catalysts, we use DFT to model hydrogen adsorption on Pt_xCo_y for two possible types of structures: 1) both Pt and Co present in the surface and 2) a pure Pt surface covering a Pt_xCo_y core (Pt/Pt_xCo_y).

In **Figure 6.3b** we show that an increasing Co fraction in Pt/Pt_xCo_y core-shell alloys causes the surface Pt to adsorb H weaker, but high fractions of Co in the surface of Pt_xCo_y alloys cause the surface to behave more like Co and bind H more strongly (ΔG_H on Co(0001) is computed to be -42 kJ mol^{-1}). For Pt/Pt_xCo_y the presence of Co in the alloy subsurface interacts with the Pt overlayer through a combination of strain and ligand effects[62–64] to cause a monotonic weakening of the computed hydrogen adsorption energy as Co increases. For the mixed Pt_xCo_y surfaces, the hydrogen adsorption energy weakens initially in the Pt_3Co case but then strengthens with increasing Co in the PtCo and $PtCo_3$ cases because of the strong Co-H interactions that are possible when high fractions of Co are on the surface. In fact, the three-fold Co sites on $PtCo_3$ are predicted to adsorb hydrogen less than 1 kJ mol^{-1} weaker than a pure Co(0001) surface.

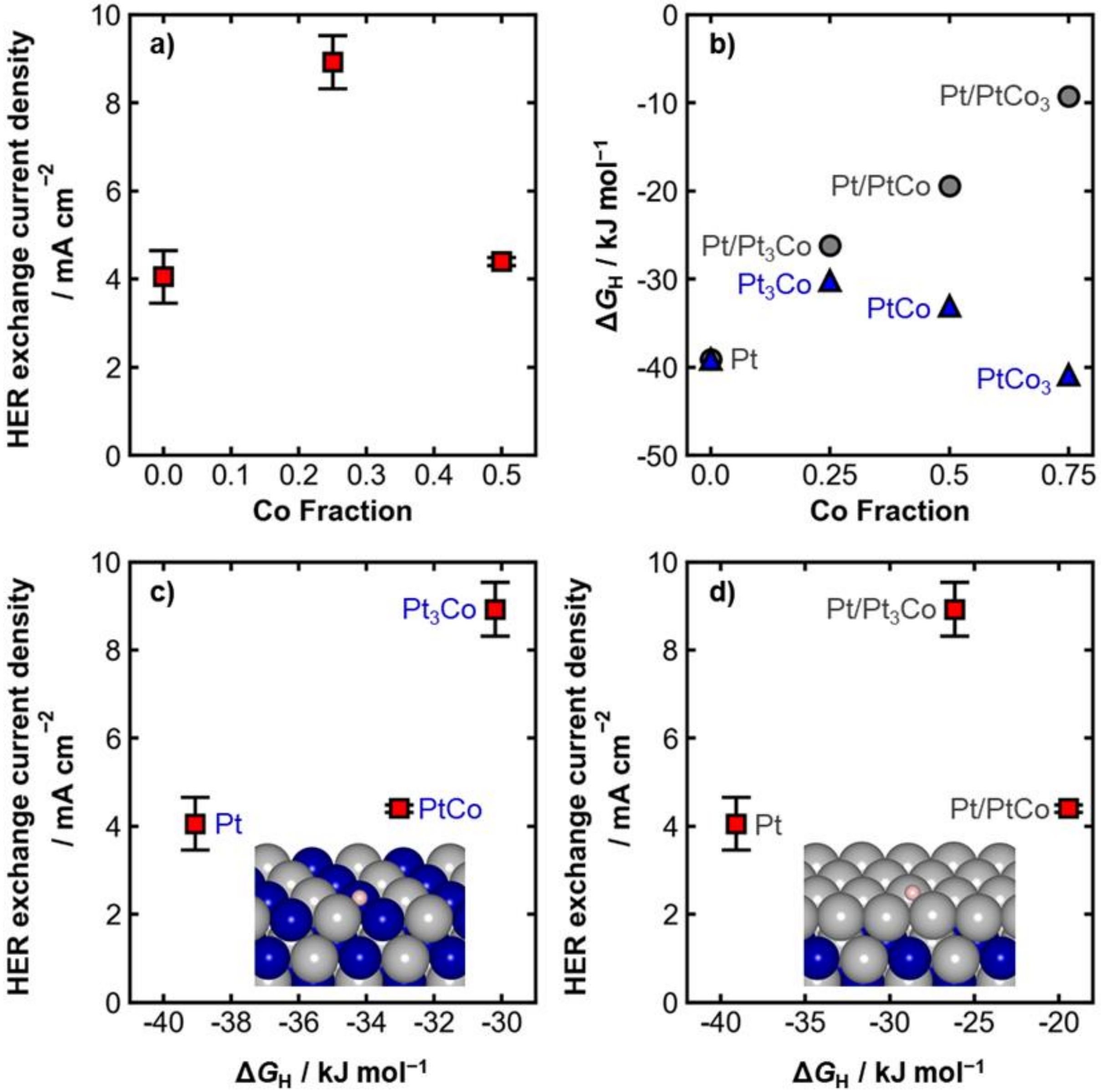

Figure 6.3 Hydrogen evolution activity related to the hydrogen adsorption energy on different Pt_xCo_y structures. a) HER measured exchange current densities at 23.3°C as a function of Co fraction for the Pt_xCo_y/C catalysts. Exchange current densities were extracted from Tafel plots shown in the supplemental information for the Pt_xCo_y/C catalysts deposited on glassy carbon in 3 M acetate buffer supporting electrolyte (pH 5.2) sparged with H_2. **b)** DFT-calculated hydrogen adsorption free energies on Pt_xCo_y and Pt/Pt_xCo_y alloys as a function of Co content at 300 K. **c)** Measured HER exchange current densities as a function of the calculated hydrogen adsorption free energies on Pt_xCo_y alloys. **d)** HER measured exchange current densities as a function of the calculated hydrogen adsorption free energies on Pt/Pt_xCo_y surfaces. Images of hydrogen adsorbed on PtCo and Pt/PtCo are inset in c) and d), respectively. Hydrogen is colored peach, Pt is colored grey, and Co is colored blue. Error bars for a), c) and d) denote the standard deviation from the average of two separate experiments.

By comparing the experimental HER exchange current density to the computed hydrogen adsorption energies, we hypothesize that our experimental catalysts form a mixed Pt and Co surface, rather than a Pt skin on a Pt_xCo_y core. We show the experimental HER exchange current density for the Pt_xCo_y/C catalysts against the computed ΔG_H assuming a mixture of Pt and Co on the surface in **Figure 6.3c**. We do the same assuming a Pt/Pt_xCo_y structure in **Figure 6.3d**. For the mixed Co and Pt surface, the HER exchange current density increases with weakening hydrogen adsorption (**Figure 6.3c**). The HER exchange current density does not increase with weakening of the predicted hydrogen adsorption on the Pt/Pt_xCo_y models (**Figure 6.3d**). Because generally HER activity for Pt group metals is expected to increase with weakening hydrogen adsorption,[22,27] the results in **Figure 6.3c** compared to **Figure 6.3d** indicate that the Pt_xCo_y/C catalysts pretreated in 3 M acetate buffer (pH 5.2) do not form a Pt skin, but instead have both Pt and Co present on the catalyst surface. Using DFT, we calculate the energy to substitute subsurface Co with surface Pt in a Pt/Pt_xCo_y slab with and without adsorbed hydrogen to determine the preferred structure of the slabs. Our calculations suggest that the presence of H*, which interacts more strongly with Co than with Pt, has the potential to stabilize Co in catalyst. This modeling prediction corroborates our observation of the enhancement of Pt_3Co/C compared to Pt/C matching what is expected for a surface with both Pt and Co present. The dependence of ΔG_H on the Pt_xCo_y structure highlights the importance of identifying the surface composition for electrocatalysis, because a Pt/Pt_xCo_y catalyst may have considerably different activity than a Pt_xCo_y catalyst.

6.4.2 Synthesis and Characterization of Pt_xCo_y Alloys Supported on Conductive Carbon Felt

To measure ECH activity for Pt_xCo_y alloys, we synthesize Pt_xCo_y nanoparticles with varying compositions of Co directly on a conductive carbon felt support (Pt_xCo_y/felt) to achieve sufficiently high catalyst loading to detect the products of ECH of phenol (cyclohexanol and cyclohexanone). We cycle these catalysts from 0.05−1.5 V vs. RHE prior to use for ECH and do not detect any remaining unalloyed Co (see **Appendix**), implying alloys are formed rather than mixtures of bulk Co and Pt.[41] Although these catalysts are supported on carbon felt as opposed to the catalysts shown in **Figure 6.3** (Pt_xCo_y/C, supported on Vulcan carbon), we show they form similar structures as discussed below.

We show the Pt L_3-edge EXAFS of the Pt_xCo_y/felt samples in **Figure 6.4a** that confirms local coordination of Co with Pt. The Pt-Pt bond length of the Pt_{100}/felt matches that of a Pt foil, and this Pt-Pt bond length decreases with increasing bulk Co content as measured by ICP-MS. The peak between 2.4‒2.6Å indicates scattering between two nearest neighbor Pt atoms in the first shell. With increasing Co content, Pt atoms are replaced by smaller Co atoms, which lead to smaller interatomic distances. The fits of the EXAFS data of the Pt foil and the Pt_xCo_y/felt are shown in the **Appendix** and the Pt-Pt and Pt-Co coordination number and bond lengths extracted from the fits to a first and second shell are shown in **Table 6.1**. With increasing Co content, we also see an increase in the Pt-Co coordination numbers, further indicating the formation of alloys.

Table 6.1 Tabulated fitting results for EXAFS of the Pt foil and pretreated Pt_xCo_y/felt catalysts at the Pt L_3-edge. When fitting the Pt foil, the Pt coordination numbers for the 1st and 2nd shell was set to 12 and 6 (bolded), respectively to obtain the amplitude factor $S_0^2 = 0.852 \pm 0.035$ that is used to fit the Pt_xCo_y/felt spectra. The results of the fittings and errors for *R*, CN, σ^2, and ΔE_0 are given in the table.

	Material	**Pt foil**	**Pt_{100}/felt**	**$Pt_{86}Co_{14}$/felt**	**$Pt_{80}Co_{20}$/felt**	**$Pt_{62}Co_{38}$/felt**
Pt-Pt	*R* (Å)	2.765 ± 0.002	2.758 ± 0.003	2.744 ± 0.004	2.744 ± 0.0029	2.743 ± 0.004
	CN	**12**	10.70 ± 0.64	9.77 ± 1.13	9.63 ± 0.86	9.59 ± 1.04
	σ^2 (Å^2)	0.005 ± 0.0002	0.006 ± 0.0003	0.006 ± 0.0005	0.006 ± 0.0004	0.007 ± 0.0005
	ΔE_0 (eV)	8.35 ± 0.36	7.54 ± 0.52	7.26 ± 0.47	6.67 ± 0.68	6.71 ± 0.54
Pt-Co	*R* (Å)	N/A	N/A	2.663 ± 0.041	2.663 ± 0.023	2.663 ± 0.023
	CN	N/A	N/A	1.06 ± 1.17	1.09 ± 0.72	1.15 ± 0.79
	σ^2 (Å^2)	N/A	N/A	0.013± 0.0106	0.010± 0.0055	0.009± 0.0054
	ΔE_0 (eV)	8.35 ± 0.36	7.54 ± 0.52	7.26 ± 0.47	6.67 ± 0.68	6.71 ± 0.54
Pt-Pt (2nd shell)	*R* (Å)	3.909 ± 0.008	3.901 ± 0.014	3.879 ± 0.019	3.879 ± 0.017	3.885 ± 0.019
	CN	**6**	3.83 ± 2.03	2.54 ± 1.86	2.87 ± 1.65	2.53 ± 1.74
	σ^2 (Å^2)	0.006 ± 0.0008	0.007 ± 0.0028	0.006± 0.0036	0.007± 0.0032	0.006± 0.0035
	ΔE_0 (eV)	8.35 ± 0.36	7.54 ± 0.52	7.26 ± 0.47	6.67 ± 0.68	6.71 ± 0.54

Our measured lattice constant of the alloys from XRD also corroborates the formation of Pt_xCo_y alloys. We show the XRD patterns for the Pt_xCo_y/felt catalysts in **Figure 6.4b** with the Pt FCC lattice peak highlighted. There is no evidence of pure Co phases in the XRD. The Pt FCC peak shifts to higher 2θ values compared to Pt, shown in the inset image in **Figure 6.4b**. We calculate the Co fraction from the shift of the 2θ values of the (111) plane using Vegard's law (**Figure 6.2**) and plot this Co fraction from XRD in **Figure 6.4c** along with the fraction of Co in the lattice based on the fitted EXAFS data using the Pt-Pt and Pt-Co coordination numbers. The Co fraction from EXAFS and XRD are similar to one another, but they differ quantitatively from the Co fraction measured using ICP-MS, although they follow the same qualitative trend. Although the higher Co content measured from ICP-MS following complete dissolution of the catalyst may indicate some unalloyed Co in the catalyst, we do not see any indication of pure Co or Co oxide redox reactions based on the cyclic voltammetry following our pretreatment (see **Appendix**). One possibility is that excess cobalt may arise from unalloyed Co in the catalyst core that is not in contact with the electrolyte. Thus, this excess bulk Co should not influence the surface reaction.

The Pt_xCo_y/felt catalysts are only slightly oxidized ex-situ and mostly metallic under applied cathodic potential. We show in **Figure 6.4d** and **Figure 6.4e** the ex-situ XANES of the catalysts on felt at the Pt L_3-edge and Co K-edge. The shape and intensity of the white line for the metallic Pt foil is similar to that of the Pt_xCo_y/felt samples, indicating Pt is mainly in the metallic phase. Using linear combination analysis of the XANES data in **Figure 6.4d** compared to Pt foil and PtO_2 we show that less than 2% of Pt forms PtO_2 (see **Appendix**). We expect 20% of all bulk Pt to be on the surface based on an average particle size of 5 nm, thus only a small fraction of the surface Pt seems to be oxidized. Under applied cathodic potential (−0.05 V vs. RHE), the XANES of Pt_{100}/felt show a white line similar to that of the metallic Pt foil except for the broad shoulder indicating the formation of adsorbed H on Pt at negative potentials (see **Appendix)**.[44] Thus, we do not expect significant differences in the electronic structure of Pt during operating conditions. Contrary to the Pt L_3-edge, the white line at the Co K-edge in **Figure 6.4e** increases with Co content which could indicate the formation of oxidized Co species. These oxidized Co species are likely from surface Co since subsurface Co would not be exposed to air.

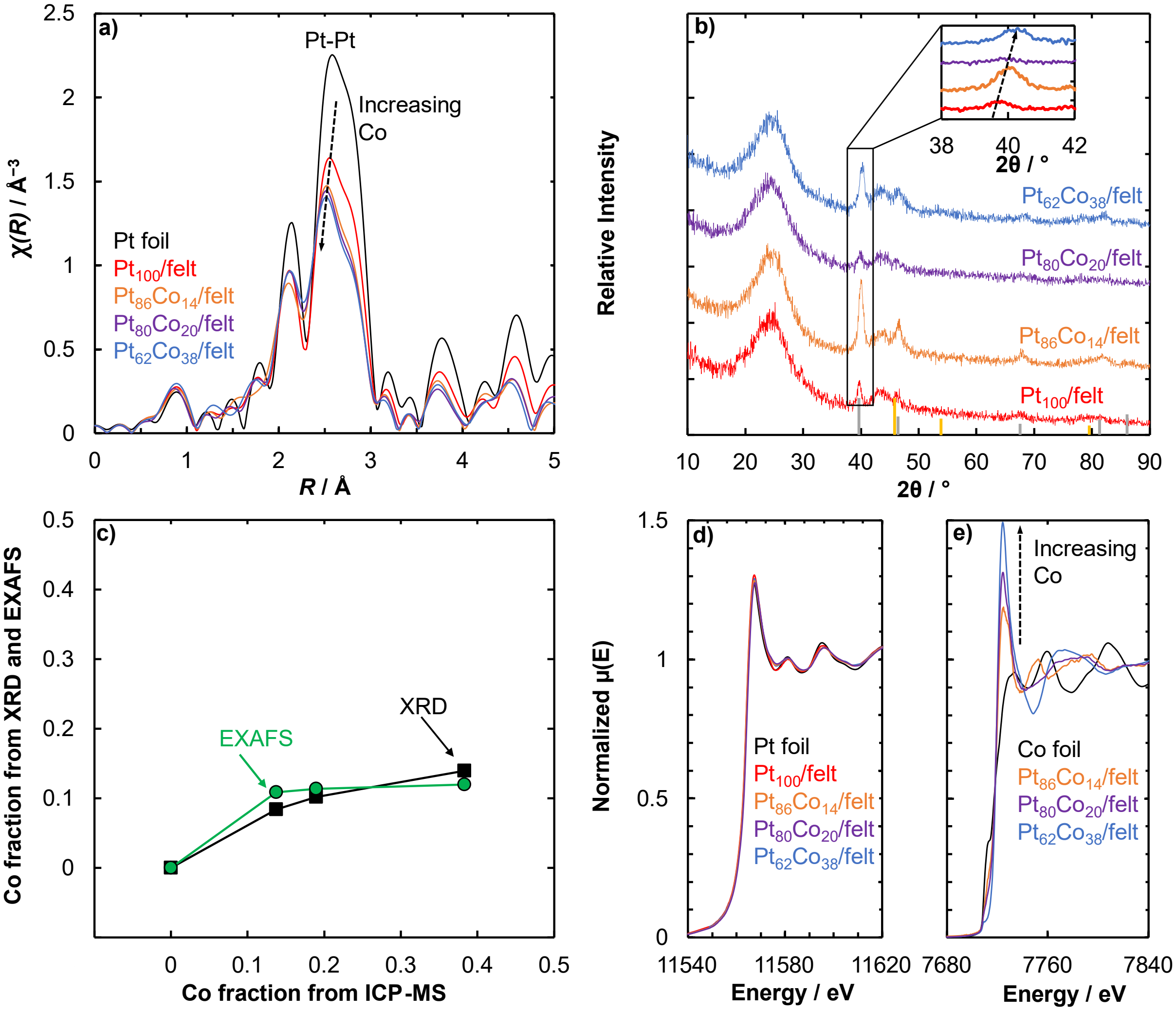

Figure 6.4 Ex-situ XAS and XRD for Pt_xCo_y/felt catalysts. a) Unadjusted k-weighted EXAFS spectra of Pt foil and Pt_xCo_y/felt in real space collected at the Pt L_3-edge. **b)** XRD spectra of Pt_xCo_y/felt with Pt #04–0802 and Co #15–0806 standards indicated by ash and gold vertical lines, respectively. Inset corresponds to region attributed to (111). **c)** Co fraction from XRD and EXAFS as a function of the Co fraction measured from ICP-Ms. The x and y in Pt_xCo_y are the bulk atomic ratio of Pt and Co measured from ICP-MS after leaching protocol was performed. Normalized XANES spectra of metal foils and Pt_xCo_y/felt at the **d)** Pt L_3-edge and **e)** Co K-edge.

This observation of surface oxidized Co is similar to reports of surface oxidized Ni in PtNi alloys, which was interpreted as being due to Ni being present in the surface.[65,66] The presence of oxidized surface Co indicates that Pt_xCo_y does not form a Pt skin, but rather there is Co present on the surface. We were unable to evaluate the Co K-edge under operating conditions because of the noise in the XANES signal from H_2 bubble formation, but we hypothesize Co may reduce under the potentials relevant for ECH.

The Pt_xCo_y/felt nanoparticles have similar particle sizes despite the variation in bulk Co fraction, so that differences in their ECH performance can be attributed to varying the Co content, rather than structure sensitivity effects.[56,57] We have previously shown that phenol ECH on Pt and Rh is a structure sensitive reaction,[56] with larger particles with a higher fraction of terrace sites showing higher turnover frequencies. The TEM images and distribution in **Figure 6.5a**, **6.5b**, and **6.5d** show that Pt_{100}/felt, $Pt_{86}Co_{14}$/felt and $Pt_{80}Co_{20}$/felt have similar average nanoparticle sizes (5.8 ± 1.3 nm, 5.8 ± 1.8 nm and 5.5 ± 1.2 nm, respectively) and are well dispersed on the treated carbon felt. Although, the average particle size and distribution is larger for the $Pt_{62}Co_{38}$/felt catalyst in **Figure 6.5e** (13.6 ± 3.2 nm), the expected increase in activity because of a higher fraction of the active terraces was not observed as we will discuss in the subsequent section. We give the average nanoparticle sizes from TEM, XRD crystallite sizes calculated from the Scherrer equation, and the EXAFS first shell total coordination number in **Table 6.2**. The trend in particle sizes from these different methods in **Table 6.2** are qualitatively in agreement.

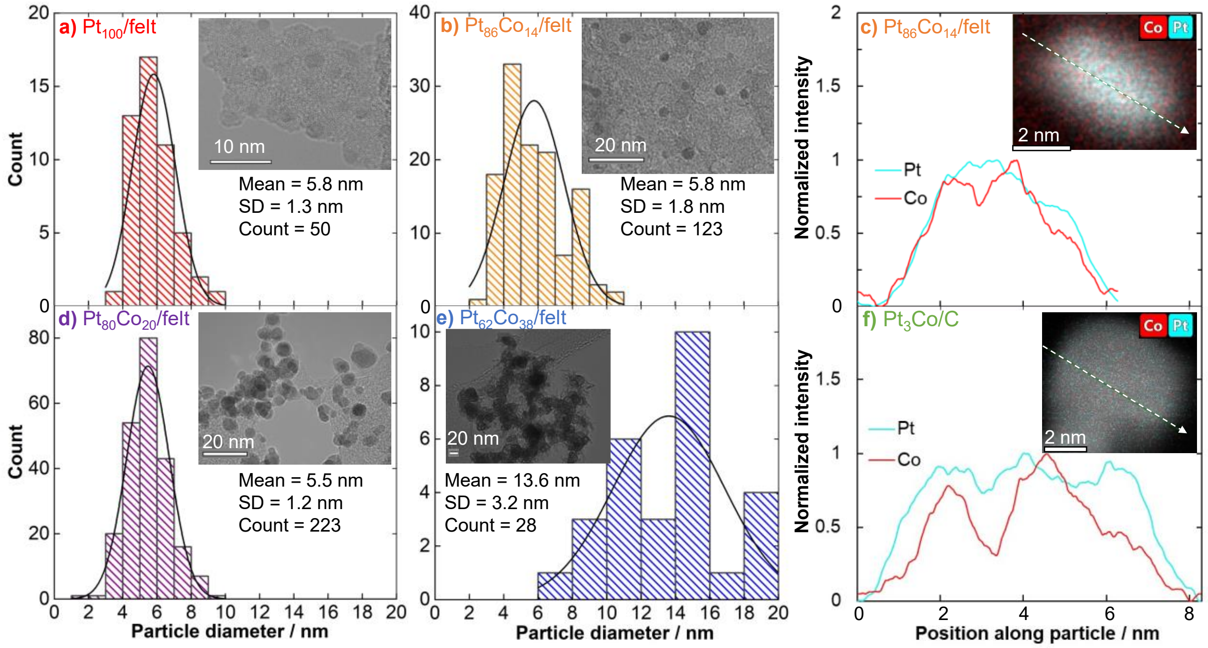

Figure 6.5 TEM histogram distribution of particle diameters and representative micrograph (inset image) of the Pt_xCo_y catalysts. a) Pt_{100}/felt, **b)** $Pt_{86}Co_{14}$/felt, **d)** $Pt_{80}Co_{20}$/felt, and **e)** $Pt_{62}Co_{38}$. A STEM-EDS line profile analysis across a single nanoparticle of the lcatalysts for **c)** $Pt_{86}Co_{14}$/felt, and **f)** Pt_3Co/C commercial catalyst. Inset image in **b)** and **c)** shows a 2D elemental mapping of Pt (teal) and Co (red) across the nanoparticle for which the line scan was performed.

We show by STEM line scans for $Pt_{86}Co_{14}$/felt in **Figure 6.5c** and Pt_3Co/C in **Figure 6.5e** that both the carbon felt and Vulcan carbon supported catalysts do not form a Pt skin but instead form a surface with both Pt and Co present. The Co and Pt line scan across a single nanoparticle shows a similar ratio of the Pt and Co intensity at the edges of the particles as in the core of the particle, indicating no visible Pt shell is formed. This further corroborates our evidence that both the Pt_xCo_y supported on carbon felt (Pt_xCo_y/felt) and Pt_xCo_y supported on Vulcan carbon (Pt_xCo_y/C) have a surface containing both Pt and Co atoms.

Table 6.2 Particle sizes from TEM and XRD using the Scherrer equation for the pretreated Pt_xCo_y on felts and on Vulcan carbon. The first shell Pt-metal coordination number from EXAFS and particle size from the correlation in ref 8 is shown.

Catalyst	**TEM particle size / nm**	**XRD crystallite size / nm**	**EXAFS total 1st shell coordination number**	**Particle size range based on EXAFS coordination / nm**
Pt_{100}/felt	5.8 ± 1.3	9.7	10.7 ± 0.6	2.3−4.3
$Pt_{86}Co_{14}$/felt	5.8 ± 1.8	8.0	10.8 ± 1.2	2.0–8.5
$Pt_{80}Co_{20}$/felt	5.5 ± 1.2	8.0	10.7 ± 0.9	2.1–5.5
$Pt_{62}Co_{38}$/felt	13.6 ± 3.3	7.9	10.7 ± 1.0	2.0–6.0
Pt/C	4.2 ± 0.7	2.5	7.2 ± 1.2	0.9−1.4
Pt_3Co/C	5.3 ± 1.2	4.6	9.4 ± 0.9	1.4–2.5
PtCo/C	5.1 ± 1.1	4.4	8.5 ± 1.0	1.2–1.9

6.4.3 Electrocatalytic Hydrogenation of Phenol on Pt_xCo_y Alloys

Unlike our observation that the hydrogen adsorption energy shows a clear trend with the HER activity (**Figure 6.3**) the more complex ECH performance in **Figure 6.6** prevents us from using a simple descriptor to understand the Pt_xCo_y/felt catalysts. For example, the catalyst with the highest TOF at −0.1 V vs. RHE ($Pt_{86}Co_{14}$/felt) is not the most active at more negative potentials. The more negative potentials may result in lower ECH TOFs on the Pt_{100}/felt and $Pt_{86}Co_{14}$/felt due to increased hydrogen coverage that blocks adsorption of phenol.[10] The more negative potential and hydrogen site-blocking also results in a lower current efficiency to ECH for those catalysts (**Figure 6.6b)**.

Additionally, even though $Pt_{86}Co_{14}$/felt has the highest TOF of the catalysts and conditions tested, it has a low current efficiency (**Figure 6.6b**), due to it high HER activity. For $Pt_{62}Co_{38}$/felt, the ECH TOF instead increases with more negative potential along with a corresponding increase in current efficiency. This opposite behavior on $Pt_{62}Co_{38}$/felt may be because the hydrogen coverage is much lower than on Pt_{100}/felt and $Pt_{86}Co_{14}$/felt, such that more negative potential enhances ECH. The complicated trend in activity and current efficiency on the alloys suggests a more complicated model than a single adsorption energy descriptor is needed to understand phenol

ECH on platinum cobalt alloys. To understand the multiple effects of adsorption energies and coverage, applied potential, and activation barriers, we use a microkinetic model based on a Langmuir-Hinshelwood mechanism to capture the experimental trends. To perform this, we investigate the effects of Co fraction on phenol adsorption and the barrier for hydrogenation in the next section.

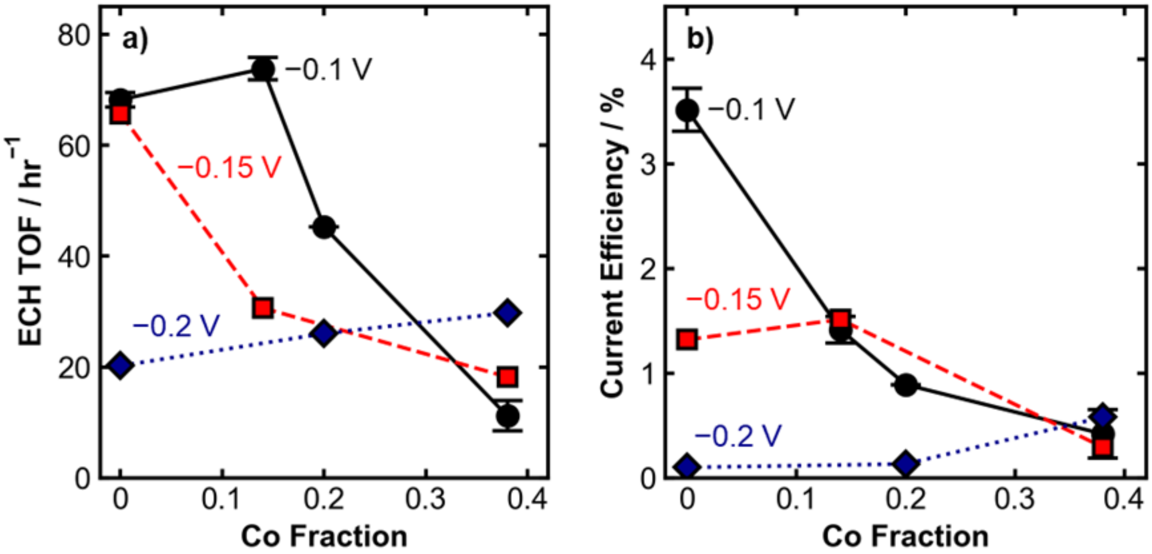

Figure 6.6 Experimental ECH turnover frequency and current efficiency on Pt_xCo_y/felt catalysts as a function of Co fraction for different applied potentials. a) ECH TOF in 20 mM phenol in 3 M acetate buffer supporting electrolyte (pH 5.2) at 23.3 °C and −0.1, −0.15 or −0.2 V vs. RHE. The applied potential was directly corrected for 85% of the series resistances using the potentiostat ZIR technique and the remaining 15% series resistance was further corrected manually to give ±0.01 V of target potential. The number of surface atoms of the catalysts used to calculate the TOF was estimated from the Pt H_{upd} surface area. **b)** current efficiency to ECH calculated from the moles of ECH products with respect to the amount of charge passed.

6.4.4 Effect of Co Alloying on Phenol Adsorption and Hydrogenation Barriers

In aqueous phase, we do not find a significant change in the experimental adsorption free energy of phenol with increasing Co fraction (**Figure 6.7**) despite the varying ECH TOF with Co fraction. We find the adsorption free energy of phenol to be −22.5 kJ mol^{-1}, −19.0 kJ mol^{-1}, and −20.5 kJ mol^{-1} kJ mol^{-1} on Pt/C, Pt_3Co/C, and PtCo/C, respectively. We find the adsorption energies are independent of phenol coverage. This constant aqueous phenol adsorption energy with

Co fraction highlights that the phenol adsorption energy is also not a descriptor for ECH. To extract the free energy for phenol adsorption at low coverage, we fit the coverage vs. concentration data to a Temkin isotherm shown in **Eq. 6.1**.

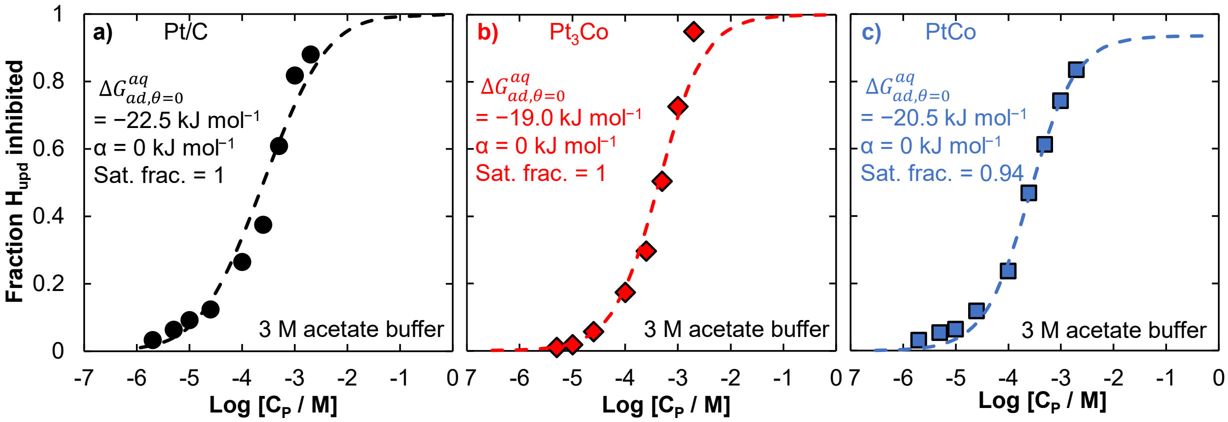

Figure 6.7 Phenol adsorption energies from adsorption experiments on Pt$_x$Co$_y$/C catalysts. Phenol adsorption isotherm on **a)** Pt/C **b)** Pt$_3$Co/C **c)** PtCo/C from inhibition of hydrogen underpotential deposition with different bulk phenol concentrations in 3 M acetate buffer and 23°C. The dashed lines in **a)**, **b)** and **c)** is a fit of the data to a Temkin adsorption model to extract the aqueous adsorption energy and its coverage dependence α.

$$\frac{\theta_P}{\theta_{sat}} = \frac{\exp\left(\frac{-(\Delta G^{aq}_{ad,\theta=0}+\alpha\theta_P)}{RT}\right)C_P}{\left(1+\exp\left(\frac{-(\Delta G^{aq}_{ad,\theta=0}+\alpha\theta_P)}{RT}\right)C_P\right)} \tag{6.1}$$

Here θ_P is the phenol coverage, θ_{sat} is the saturation coverage, $\Delta G^{aq}_{ad,\theta=0}$ is the aqueous adsorption free energy in kJ mol^{-1} at a phenol coverage of zero, α is how adsorbate-adsorbate interactions influence the adsorption energy as a function of coverage in kJ mol^{-1}, C_P is the concentration of phenol, R is the ideal gas constant, and T is temperature in Kelvin. A caveat of these adsorption isotherms is that they probe the coverage of phenol as a function of bulk phenol concentration solely on the surface Pt atoms because the coverage of phenol on Co atoms cannot be probed using H_{upd}. We have previously shown that metals such as Pt and Rh which adsorb organic molecules (e.g., phenol) with very different energies in the gas phase have similar aqueous-phase adsorption energies.[59] We attributed this similar phenol adsorption between Pt and Rh to the energy penalty of displacing water molecules from the liquid/metal interface which offsets the energy difference observed in the gas phase, i.e., although Rh adsorbs phenol in the gas phase more strongly than Pt, it also adsorbs water more strongly, and so the penalty for displacing water is larger on Rh than on Pt.[67,68]

Through DFT modeling, we show that the structure and composition of the alloy surface has a significant impact on the activation enthalpy of the first hydrogenation step. The DFT-predicted geometries for the first hydrogenation step of phenol on PtCo and Pt/PtCo are shown in **Figure 6.8a**. In **Figure 6.8** we show the computed activation enthalpy ($\Delta H_f^\ddagger$) as a function of Co fraction (y_{Co}) for $\mathrm{Pt_xCo_y}$ and $\mathrm{Pt/Pt_xCo_y}$. We calculate $\Delta H_f^\ddagger$ as the enthalpy of the transition state for the first hydrogenation step relative to the enthalpy of surface-adsorbed hydrogen and phenol. The activation enthalpy increases almost linearly with Co fraction on the $\mathrm{Pt_xCo_y}$ surfaces but decreases linearly with Co fraction for the $\mathrm{Pt/Pt_xCo_y}$ surfaces. The significantly different trend in activation enthalpy with Co fraction on the two types of surfaces highlights the impact of having Co and Pt on the surface ($\mathrm{Pt_xCo_y}$) compared to only Pt on the surface ($\mathrm{Pt/Pt_xCo_y}$).

By comparing the activation enthalpy to the hydrogenation reaction enthalpy, we observe why the $\mathrm{Pt_xCo_y}$ and $\mathrm{Pt/Pt_xCo_y}$ surfaces are predicted to have such different trends in hydrogenation rates with Co fraction. We show $\Delta H_f^\ddagger$ as a function of the computed hydrogen adsorption enthalpy (ΔH_{H}) on each respective surface in **Figure 6.8c**. On the $\mathrm{Pt/Pt_xCo_y}$ surface, $\Delta H_f^\ddagger$ decreases with a weakening of the hydrogen adsorption energy. We have previously hypothesized that weakening the hydrogen adsorption energy on a pure Pt catalyst through controlling the pH can influence the hydrogenation barrier through Brønsted-Evans-Polanyi (BEP) relations.[69] Briefly, with all else being held constant, a weaker adsorbed hydrogen would result in a more favorable hydrogenation reaction energy and consequently a lowered hydrogenation barrier. Although ΔH_{H} seems to be a descriptor for the Pt/Pt_xCo_y surfaces, $\Delta H_f^{\ddagger}$ is not simply a function of ΔH_{H} for the Pt_xCo_y surfaces.

By examining $\Delta H_f^{\ddagger}$ on Pt_xCo_y as a function of the hydrogenation reaction enthalpy (ΔH_{rxn}) in **Figure 6.8d**, we demonstrate that hydrogenation on Pt_xCo_y follows a BEP relationship, with a higher reaction enthalpy correlating with a higher activation enthalpy. The Pearson correlation of $R^2 = 0.89$ implies a late transition state. For the Pt_xCo_y surfaces, however, the surface with the weakest hydrogen adsorption is not the surface with the least endothermic reaction enthalpy. Therefore, hydrogen adsorption enthalpy is not an effective descriptor for $\Delta H_f^{\ddagger}$ on Pt_xCo_y. We elucidate why the Pt_xCo_y and Pt/Pt_xCo_y surfaces have different trends in $\Delta H_f^{\ddagger}$ with Co fraction by understanding how the surfaces impact the reaction enthalpy. The more endothermic ΔH_{rxn} on the Pt_xCo_y surfaces compared Pt/Pt_xCo_y surfaces indicate that the hydrogenated intermediate species (PH*) is less stable than the reactants (P* + H*) when there is Co in the surface catalyst layer. This more endothermic ΔH_{rxn} on the Pt_xCo_y surfaces results in higher hydrogenation activation enthalpies (**Figure 6.8d**). Ultimately, despite adsorbed hydrogen being an important reactant, the hydrogen adsorption energy alone is not a suitable descriptor for phenol hydrogenation like it is for HER. Instead, the activation enthalpy more closely follows a BEP relationship, and the higher $\Delta H_f^{\ddagger}$ on Pt_xCo_y surfaces than on Pt or Pt/Pt_xCo_y surfaces is caused by the weaker interaction between the hydrogenated phenol intermediate and the Pt_xCo_y surface.

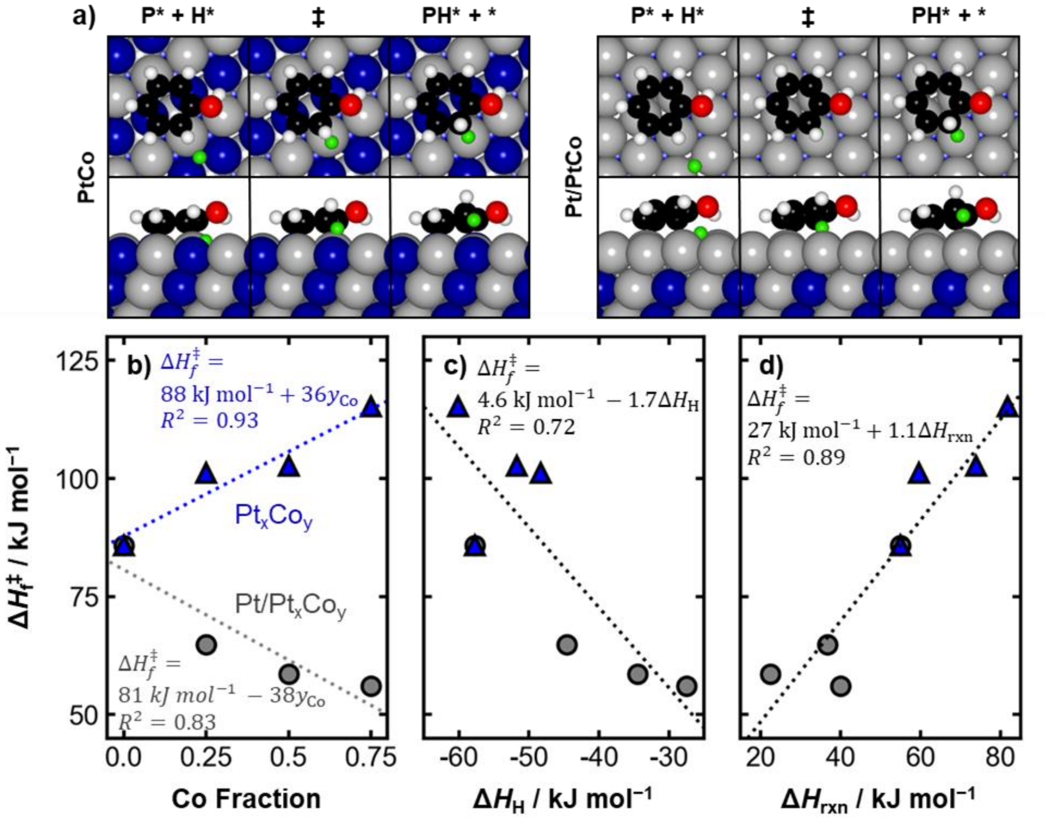

Figure 6.8 Activation enthalpy for the first hydrogenation step of phenol. a) Top and side views of DFT-predicted geometries corresponding to the initial, transition, and final states for the first hydrogenation of phenol on the (111) facet of both PtCo and Pt/PtCo. Color legend: Pt = gray, Co = blue, O = red, C = black, and H = white. The H* atom participating in the hydrogenation reaction is colored green. Activation enthalpy for the first hydrogenation of phenol on Pt$_x$Co$_y$ and Pt/Pt$_x$Co$_y$ as a function of **b)** Co fraction, **c)** the adsorption enthalpy of hydrogen (ΔH_H), and **d)** the reaction enthalpy for the first hydrogenation step of phenol at 300 K (ΔH_{rxn}). Blue triangles correspond to activation enthalpies calculated on Pt$_x$Co$_y$ and gray circles correspond to barriers calculated on Pt/Pt$_x$Co$_y$. Linear fits to the data are shown along with corresponding equations.

6.4.5 Explaining ECH Activity on Pt$_x$Co$_y$ Alloys Using a Langmuir-Hinshelwood Model

We are able to describe the trend in experimental TOF with Co fractions and applied potentials shown in **Figure 6.6** using a Langmuir-Hinshelwood model to capture the effects of Co alloying on hydrogen adsorption energy, phenol adsorption energy, and hydrogenation activation enthalpy. Assuming that the first hydrogenation step is rate-determining, we estimate the TOF as a function of potential and Co fraction using a simple microkinetic model. In **Eq. 6.2**, we show that the equilibrium adsorption coefficient for hydrogen (K_H) is a function of the applied electrochemical potential (E) and the hydrogen adsorption free energy on a given surface. F is

Faraday's constant. We note that we assume the ΔG_{H} at 0 V vs. RHE here is the same as that computed for **Figure 6.3**, referenced to 1 bar H_2.

$$K_{\mathrm{H}}(E) = \exp\left(\frac{-\Delta G_{\mathrm{H}}(E = 0\ \mathrm{V\ vs.\ RHE})}{RT}\right) \exp\left(\frac{-FE}{RT}\right) \tag{6.2}$$

In **Eq. 6.3**, we assume that the phenol equilibrium adsorption coefficient (K_{P}) is independent of potential, although in reality there may be variations due to the impact of potential on the interfacial water layer.[70] The adsorption coefficient is dependent on the free energy of adsorption of phenol, $\Delta G_{\mathrm{ads,P}}$.

$$K_{\mathrm{P}} = \exp\left(\frac{-\Delta G_{\mathrm{ads,P}}}{RT}\right) \tag{6.3}$$

For the first hydrogenation step as the rate-determining step, the TOF will be described by **Eq. 6.4**, and includes contributions from the rate constant, k_{ECH}, and the product of the hydrogen and phenol coverage, θ_{H} and θ_{P}, respectively.[10] The coverages are given by the equilibrium adsorption coefficients when adsorption is quasi-equilibrated. As we have discussed in previous work,[59] here C_{P} is the concentration of phenol and C_{H} is an 'equivalent' chemical potential of hydrogen.

$$TOF = k_{ECH}\theta_{\mathrm{H}}\theta_{\mathrm{P}} = k_{ECH}\frac{K_{\mathrm{H}}C_{\mathrm{H}}K_{\mathrm{P}}C_{\mathrm{P}}}{(1 + K_{\mathrm{H}}C_{\mathrm{H}} + K_{\mathrm{P}}C_{\mathrm{P}})^2} \tag{6.4}$$

The rate constant depends on the enthalpy of the first hydrogenation step's transition state relative to the reactant energy ($\Delta H_f^{\ddagger}$) as we show in **Eq. 6.5**. *A* is a preexponential factor, which we assume to be independent of the Co content of the catalyst surface, and we do not include any influence of the applied potential on the rate constant.

$$k_{ECH} = A\exp\left(\frac{-\Delta H_f^{\ddagger}}{RT}\right) \tag{6.5}$$

We predict the rate constant is a function of the Co fraction due to a dependence of the activation barrier on the Co fraction, as shown by our results in **Figure 6.8**. The linear trend in **Figure 6.8** indicate that the rate constant would exponentially decrease with Co fraction on the mixed Co and Pt surface and exponentially increase with Co fraction on the Pt skin surface. As the hydrogen adsorption free energy is also a function of the Co fraction as shown in **Figure 6.3b**, we can describe the TOF as a function of Co content and potential if the first hydrogenation step is rate-determining. Here we assume K_P is constant with Co content, and we use a $\Delta G_{ads,P}$ value of -9 kJ mol^{-1} based on our previously obtained value for the adsorption energy of phenol on the active site of Pt for ECH.[10] Additional details of the kinetic model are shown in the **Appendix**.

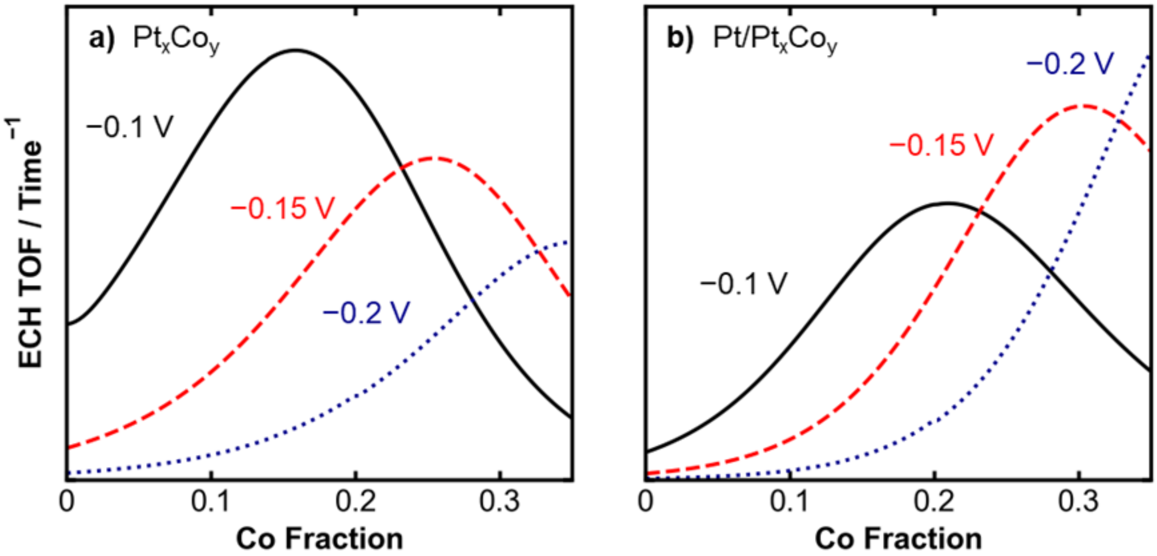

Figure 6.9 ECH turnover frequency on Pt_xCo_y/felt, as a function of Co fraction and potential using a Langmuir-Hinshelwood model. a) Calculated ECH TOF assuming the first hydrogenation step is rate-determining, and the transition state barrier increases as a function of Co fraction, as found for the for the mixed surface Pt_xCo_y structure (Pt_xCo_y) in **Figure 6.8**. **b)** Calculated ECH TOF assuming the first hydrogenation step is rate-determining, and the transition state barrier is decreases as a function of Co fraction, as found for the Pt skin structure (Pt/Pt_xCo_y) in **Figure 6.8**.

Combining **Eqs. 6.2−6.5** we show the prediction of the TOF as a function of potential and Co fraction in **Figure 6.9** for the two types of catalyst surfaces, where the results on the mixed Co and Pt surface qualitatively match our experimental results in **Figure 6.6a**. In **Figure 6.9a**, at more negative potentials the hydrogen coverage will increase, which for catalysts that adsorb hydrogen relatively strongly, will cause the phenol coverage to decrease and the TOF to go down. For higher Co fractions, where the hydrogen adsorption energy is weaker, the effect of more negative potential is less detrimental, as the phenol coverage remains high. In this way, the kinetic model captures why the maximum in ECH TOF with Co fraction varies as a function of applied potential. At comparable coverages of hydrogen and phenol for a pure Pt catalyst compared to a Pt_xCo_y alloy, the TOF is lower for the alloy due to the higher activation enthalpy (**Figure 6.8**). The increase in TOF with Co fraction observed experimentally at −0.1 V vs. RHE in **Figure 6.6a** is explained by our model as weakening the hydrogen adsorption energy, which allows a higher coverage of phenol on the surface, thus increasing the rate. Although this higher coverage of phenol results in an increase in the ECH rate, the current efficiency for ECH at −0.1 V vs. RHE may be lower with Co fraction (**Figure 6.6b**) because of an increase in the HER activity.

The model for the TOF on a Pt skin with a Pt_xCo_y core does not match our experimental values, further corroborating the mixed Pt_xCo_y surface indicated from our HER measurements, characterization, and DFT calculations of the energetically preferred surface. The decrease in activity at sufficiently high Co fractions is due to a decrease in the hydrogen coverage, conceptually similar to that described for **Figure 6.9a**. In **Figure 6.9b**, due to the prediction that an increasing Co fraction will decrease the hydrogenation barrier for a Pt/Pt_xCo_y structure, the ECH TOF is predicted to increase under almost all conditions up to high Co fractions, which is not what we observe experimentally. We predict a catalyst with a stable Pt skin and a Pt_xCo_y core structure (i.e., Pt/Pt_xCo_y) under ECH conditions would be a more active catalyst based on DFT-calculated activation energies and our kinetic modeling. Further study of Pt/Pt_xCo_y core-shell alloys is needed to test the stability of Pt/Pt_xCo_y catalysts under ECH conditions and to experimentally verify the enhanced activity for phenol ECH.

6.5 Conclusions

We find that Pt_xCo_y alloys at low Co fractions are more active toward ECH of phenol than pure Pt at low overpotentials (−0.1 V vs. RHE), but due to their high activity for the competing hydrogen evolution reaction, the ECH current efficiency is lower than pure Pt. Pt_xCo_y preferentially forms structures with Co and Pt on the surface under our ECH and HER conditions, as opposed to a Pt skin. Although the HER activity correlates with computed hydrogen adsorption energies on Pt_xCo_y surfaces, with surfaces that adsorb hydrogen more weakly having higher HER activity, the hydrogen adsorption energy is an insufficient descriptor for ECH activity. Rather, the hydrogenation activation enthalpies follow a Brønsted-Evans-Polanyi relationship with respect to the reaction enthalpies, and the Pt_xCo_y surfaces have more endothermic reaction enthalpies and larger activation enthalpies than Pt despite adsorbing hydrogen more weakly. By incorporating the applied potential dependence and the activation enthalpies into a kinetic model we qualitatively explain the experimental ECH TOF trends on the Pt_xCo_y surfaces. Our DFT and kinetic modeling predict that Pt/Pt_xCo_y alloys, i.e., a pure Pt surface layer with Pt_xCo_y core, would have enhanced ECH activity, although further work to synthesize and stabilize these structures is needed. Our findings demonstrate the importance of understanding how the surface composition and structure of a catalyst can influence intrinsic reaction kinetics especially when considering competitively adsorbing reactants (e.g., phenol and hydrogen) and competing reactions such as ECH and HER on a single surface.

6.6 References

(1) Aguilar, F. X.; Saunders, A. Policy Instruments Promoting Wood-to-Energy Uses in the Continental United States. *J. For.* **2010**, *108*, 132–140.

(2) Biddinger, E. J.; Gutierrez, O. Y.; Holladay, J. Electrochemical Routes for Biomass Conversion. *J. Appl. Electrochem.* **2021**, *51*, 1–3.

(3) Garedew, M.; Lam, C. H.; Petitjean, L.; Huang, S.; Song, B.; Lin, F.; Jackson, J. E.; Saffron,

C. M.; Anastas, P. T. Electrochemical Upgrading of Depolymerized Lignin: A Review of Model Compound Studies. *Green Chem.* **2021**, *23*, 2868–2899.

(4) Akhade, S. A.; Singh, N.; Gutiérrez, O. Y.; Lopez-Ruiz, J.; Wang, H.; Holladay, J. D.; Liu, Y.; Karkamkar, A.; Weber, R. S.; Padmaperuma, A. B.; et al. Electrocatalytic Hydrogenation of Biomass-Derived Organics: A Review. *Chem. Rev.* **2020**, *120*, 11370–11419.

(5) Cyr, A.; Chiltz, F.; Jeanson, P.; Martel, A.; Brossard, L.; Lessard, J.; Ménard, H. Electrocatalytic Hydrogenation of Lignin Models at Raney Nickel and Palladium-Based Electrodes. *Can. J. Chem.* **2000**, *78*, 307–315.

(6) Li, Z.; Garedew, M.; Lam, C. H.; Jackson, J. E.; Miller, D. J.; Saffron, C. M. Mild Electrocatalytic Hydrogenation and Hydrodeoxygenation of Bio-Oil Derived Phenolic Compounds Using Ruthenium Supported on Activated Carbon Cloth. *Green Chem.* **2012**, *14*, 2540.

(7) Lam, C. H.; Lowe, C. B.; Li, Z.; Longe, K. N.; Rayburn, J. T.; Caldwell, M. A.; Houdek, C. E.; Maguire, J. B.; Saffron, C. M.; Miller, D. J.; et al. Electrocatalytic Upgrading of Model Lignin Monomers with Earth Abundant Metal Electrodes. *Green Chem.* **2015**, *17*, 601–609.

(8) Kleinert, M.; Barth, T. Phenols from Lignin. *Chem. Eng. Technol.* **2008**, *31*, 736–745

(9) Song, Y.; Gutiérrez, O. Y.; Herranz, J.; Lercher, J. A. Aqueous Phase Electrocatalysis and Thermal Catalysis for the Hydrogenation of Phenol at Mild Conditions. *Appl. Catal. B Environ.* **2016**, *182*, 236–246.

(10) Singh, N.; Sanyal, U.; Ruehl, G.; Stoerzinger, K. A.; Gutiérrez, O. Y.; Camaioni, D. M.; Fulton, J. L.; Lercher, J. A.; Campbell, C. T. Aqueous Phase Catalytic and Electrocatalytic Hydrogenation of Phenol and Benzaldehyde over Platinum Group Metals. *J. Catal.* **2020**, *382*, 372–384.

(11) Lu, S.; Menning, C. A.; Zhu, Y.; Chen, J. G. Correlating Benzene Hydrogenation Activity with Binding Energies of Hydrogen and Benzene on Co-Based Bimetallic Catalysts. *ChemPhysChem* **2009**, *10*, 1763–1765.

(12) Do, P. T. M.; Foster, A. J.; Chen, J.; Lobo, R. F. Bimetallic Effects in the Hydrodeoxygenation of Meta-Cresol on γ-Al_2O_3 Supported Pt–Ni and Pt–Co Catalysts. *Green Chem.* **2012**, *14*, 1388.

(13) Lonergan, W. W.; Vlachos, D. G.; Chen, J. G. Correlating Extent of Pt-Ni Bond Formation with Low-Temperature Hydrogenation of Benzene and 1,3-Butadiene over Supported Pt/Ni Bimetallic Catalysts. *J. Catal.* **2010**, *271*, 239–250.

(14) Cheney, B. A.; Lauterbach, J. A.; Chen, J. G. Reverse Micelle Synthesis and Characterization of Supported Pt/Ni Bimetallic Catalysts on γ-Al2O3. *Appl. Catal. A Gen.* **2011**, *394*, 41–47..

(15) Resende, K. A.; Hori, C. E.; Noronha, F. B.; Shi, H.; Gutierrez, O. Y.; Camaioni, D. M.; Lercher, J. A. Aqueous Phase Hydrogenation of Phenol Catalyzed by Pd and PdAg on ZrO_2. *Appl. Catal. A Gen.* **2017**, *548*, 128–135.

(16) Santori, G. F.; Casella, M. L.; Siri, G. J.; Adúriz, H. R.; Ferretti, O. A. Effect of Particle Size in the Hydrogenation of Crotonaldehyde on Supported Pt and Pt-Sn Catalysts. *React. Kinet. Mech. Catal.* **2002**, *75*, 225–230.

(17) Meyer, R. J.; Zhang, Q.; Kryczka, A.; Gomez, C.; Todorovic, R. Perturbation of Reactivity with Geometry: How Far Can We Go? *ACS Catal.* **2018**, *8*, 566–570.

(18) Yu, W.; Porosoff, M. D.; Chen, J. G. Review of Pt-Based Bimetallic Catalysis: From Model

Surfaces to Supported Catalysts. *Chem. Rev.* **2012**, *112*, 5780–5817.

(19) Humbert, M. P.; Chen, J. G. Correlating Hydrogenation Activity with Binding Energies of Hydrogen and Cyclohexene on M/Pt(111) (M = Fe, Co, Ni, Cu) Bimetallic Surfaces. *J. Catal.* **2008**, *257*, 297–306.

(20) Liu, B.; Xiao, D.; Wang, Y.; Jia, P.; Huang, N.; Lan, X.; Wang, T. Correlating C═C, C═O, and C═N Hydrogenation Activity with Hydrogen Binding Energies on Ni–Fe Bimetallic Catalysts. *J. Phys. Chem. C* **2020**, *124* , 18595–18603.

(21) Greeley, J.; Jaramillo, T. F.; Bonde, J.; Chorkendorff, I.; Nørskov, J. K. Computational High-Throughput Screening of Electrocatalytic Materials for Hydrogen Evolution. *Nat. Mater.* **2006**, *5*, 909–913.

(22) Zheng, J.; Sheng, W.; Zhuang, Z.; Xu, B.; Yan, Y. Universal Dependence of Hydrogen Oxidation and Evolution Reaction Activity of Platinum-Group Metals on pH and Hydrogen Binding Energy. *Sci. Adv.* **2016**, *2*, 1–9.

(23) Nørskov, J. K.; Bligaard, T.; Logadottir, A.; Kitchin, J. R.; Chen, J. G.; Pandelov, S.; Stimming, U. Trends in the Exchange Current for Hydrogen Evolution. *J. Electrochem. Soc.* **2005**, *152*, J23.

(24) Trasatti, S. Work Function, Electronegativity, and Electrochemical Behaviour of Metals. III. Electrolytic Hydrogen Evolution in Acid Solutions. *J. Electroanal. Chem.* **1972**, *39*, 163–184.

(25) Savadogo, O.; Piron, D. L. New Hydrogen Cathodes in Acid Medium: Case of Nickel Electrodeposited with Heteropolyacids (HPAs). *Int. J. Hydrogen Energy* **1990**, *15*, 715–721.

(26) Skúlason, E.; Tripkovic, V.; Björketun, M. E.; Gudmundsdóttir, S.; Karlberg, G.; Rossmeisl, J.; Bligaard, T.; Jónsson, H.; Nørskov, J. K. Modeling the Electrochemical Hydrogen Oxidation and Evolution Reactions on the Basis of Density Functional Theory Calculations. *J. Phys. Chem. C* **2010**, *114*, 18182–18197.

(27) Greeley, J.; Nørskov, J. K. Large-Scale, Density Functional Theory-Based Screening of Alloys for Hydrogen Evolution. *Surf. Sci.* **2007**, *601*, 1590–1598.

(28) Pintauro, P. N.; Gil, M. P.; Warner, K.; List, G.; Neff, W. Electrochemical Hydrogenation of Soybean Oil with Hydrogen Gas. *Ind. Eng. Chem. Res.* **2005**, *44*, 6188–6195.

(29) Ma, J.; Wang, Z.; Majima, T.; Zhao, G. Role of Ni in PtNi Alloy for Modulating the Proton–Electron Transfer of Electrocatalytic Hydrogenation Revealed by the In Situ Raman–Rotating Disk Electrode Method. *ACS Catal.* **2022**, *12*, 14062–14071

(30) Du, Y.; Chen, X.; Liang, C. Selective Electrocatalytic Hydrogenation of Phenols over Ternary Pt_3RuSn Alloy. *Mol. Catal.* **2023**, *535*, 112831.

(31) Mavrikakis, M.; Hammer, B.; Nørskov, J. K. Effect of Strain on the Reactivity of Metal Surfaces. *Phys. Rev. Lett.* **1998**, *81*, 2819–2822.

(32) Wang, X.; Zhu, Y.; Vasileff, A.; Jiao, Y.; Chen, S.; Song, L.; Zheng, B.; Zheng, Y.; Qiao, S. Z. Strain Effect in Bimetallic Electrocatalysts in the Hydrogen Evolution Reaction. *ACS Energy Lett.* **2018**, *3*, 1198–1204.

(33) Pan, Y.; Li, D.; Sharma, S.; Wang, C.; Zachman, M. J.; Wegener, E. C.; Kropf, A. J.; Kim, Y. S.; Myers, D. J.; Peterson, A. A.; Cullen, D. A.; Spendelow, J. S. Ordered CoPt Oxygen Reduction Catalyst with High Performance and Durability. *Chem Catal.* **2022**, *2* (12), 3559–3572.

(34) Kitchin, J. R.; Nørskov, J. K.; Barteau, M. A.; Chen, J. G. Role of Strain and Ligand Effects in the Modification of the Electronic and Chemical Properties of Bimetallic Surfaces. *Phys.*

Rev. Lett. **2004**, *93*, 4–7.

(35) Wei, C.; Sun, Y.; Scherer, G. G.; Fisher, A. C.; Sherburne, M.; Ager, J. W.; Xu, Z. J. Surface Composition Dependent Ligand Effect in Tuning the Activity of Nickel-Copper Bimetallic Electrocatalysts toward Hydrogen Evolution in Alkaline. *J. Am. Chem. Soc.* **2020**, *142*, 7765–7775.

(36) Wang, Y.; Cao, L.; Libretto, N. J.; Li, X.; Li, C.; Wan, Y.; He, C.; Lee, J.; Gregg, J.; Zong, H.; et al. Ensemble Effect in Bimetallic Electrocatalysts for CO2 Reduction. *J. Am. Chem. Soc.* **2019**, *141*, 16635–16642.

(37) Sachtler, W. M. H.; Van Santen, R. A. Surface Composition and Selectivity of Alloy Catalysts. *Adv. Catal.* **1977**, *26*, 69–119.

(38) Long, N. V.; Yang, Y.; Minh Thi, C.; Minh, N. Van; Cao, Y.; Nogami, M. The Development of Mixture, Alloy, and Core-Shell Nanocatalysts with Nanomaterial Supports for Energy Conversion in Low-Temperature Fuel Cells. *Nano Energy* **2013**, *2*, 636–676.

(39) Oezaslan, M.; Hasché, F.; Strasser, P. Pt-Based Core-Shell Catalyst Architectures for Oxygen Fuel Cell Electrodes. *J. Phys. Chem. Lett.* **2013**, *4*, 3273–3291.

(40) Oezaslan, M.; Hasché, F.; Strasser, P. Oxygen Electroreduction on $PtCo_3$, PtCo and Pt_3Co Alloy Nanoparticles for Alkaline and Acidic PEM Fuel Cells. *J. Electrochem. Soc.* **2012**, *159*, B394–B405.

(41) Oezaslan, M.; Strasser, P. Activity of Dealloyed $PtCo_3$ and $PtCu_3$ Nanoparticle Electrocatalyst for Oxygen Reduction Reaction in Polymer Electrolyte Membrane Fuel Cell. *J. Power Sources* **2011**, *196*, 5240–5249.

(42) Saquib, M.; Halder, A. Dealloyed Pt_3Co Nanoparticles with Higher Geometric Strain for Superior Hydrogen Evolution Reaction. *J. Solid State Chem.* **2018**, *262*, 229–236.

(43) Leontyev, I. N.; Chernyshov, D. Y.; Guterman, V. E.; Pakhomova, E. V.; Guterman, A. V. Particle Size Effect in Carbon Supported Pt-Co Alloy Electrocatalysts Prepared by the Borohydride Method: XRD Characterization. *Appl. Catal. A Gen.* **2009**, *357*, 1–4.

(44) Singh, N.; Nguyen, M.-T.; Cantu, D. C.; Mehdi, B. L.; Browning, N. D.; Fulton, J. L.; Zheng, J.; Balasubramanian, M.; Gutiérrez, O. Y.; Glezakou, V.-A.; et al. Carbon-Supported Pt during Aqueous Phenol Hydrogenation with and without Applied Electrical Potential: X-ray Absorption and Theoretical Studies of Structure and Adsorbates. *J. Catal.* **2018**, *368*, 8–19.

(45) Ravel, B.; Newville, M. ATHENA , ARTEMIS , HEPHAESTUS : Data Analysis for X-ray Absorption Spectroscopy Using IFEFFIT. *J. Synchrotron Radiat.* **2005**, *12*, 537–541.

(46) Kresse, G.; Furthmüller, J. Efficiency of Ab-Initio Total Energy Calculations for Metals and Semiconductors Using a Plane-Wave Basis Set. *Comput. Mater. Sci.* **1996**, *6*, 15–50.

(47) Kresse, G.; Furthmüller, J. Efficient Iterative Schemes for Ab Initio Total-Energy Calculations Using a Plane-Wave Basis Set. *Phys. Rev. B* **1996**, *54*, 11169–11186.

(48) Kresse, G.; Hafner, J. Ab Initio Molecular Dynamics for Liquid Metals. *Phys. Rev. B* **1993**, *47*, 558–561.

(49) Kresse, G.; Hafner, J. Ab Initio Molecular-Dynamics Simulation of the Liquid-Metalamorphous- Semiconductor Transition in Germanium. *Phys. Rev. B* **1994**, *49*, 14251–14269.

(50) Perdew, J. P.; Burke, K.; Ernzerhof, M. Generalized Gradient Approximation Made Simple. *Phys. Rev. Lett.* **1996**, *77* (18), 3865–3868.

(51) Grimme, S.; Antony, J.; Ehrlich, S.; Krieg, H. A Consistent and Accurate Ab Initio Parametrization of Density Functional Dispersion Correction (DFT-D) for the 94 Elements

H-Pu. *J. Chem. Phys.* **2010**, *132*, 154104.
(52) Blöchl, P. E. Projector Augmented-Wave Method. *Phys. Rev. B* **1994**, *50*, 17953–17979.
(53) Kresse, G.; Joubert, D. From Ultrasoft Pseudopotentials to the Projector Augmented-Wave Method. *Phys. Rev. B* **1999**, *59*, 1758–1775.
(54) Methfessel, M.; Paxton, A. T. High-Precision Sampling for Brillouin-Zone Integration in Metals. *Phys. Rev. B* **1989**, *40*, 3616–3621.
(55) Monkhorst, H. J.; Pack, J. D. Special Points for Brillouin-Zone Integrations. *Phys. Rev. B* **1976**, *13*, 5188–5192.
(56) Barth, I.; Akinola, J.; Lee, J.; Gutiérrez, O. Y.; Sanyal, U.; Singh, N.; Goldsmith, B. R. Explaining the Structure Sensitivity of Pt and Rh for Aqueous-Phase Hydrogenation of Phenol. *J. Chem. Phys.* **2022**, *156*, 104703.
(57) Sanyal, U.; Song, Y.; Singh, N.; Fulton, J. L.; Herranz, J.; Jentys, A.; Gutiérrez, O. Y.; Lercher, J. A. Structure Sensitivity in Hydrogenation Reactions on Pt/C in Aqueous-phase. *ChemCatChem* **2019**, *11*, 575–582.
(58) Henkelman, G.; Uberuaga, B. P.; Jónsson, H. A Climbing Image Nudged Elastic Band Method for Finding Saddle Points and Minimum Energy Paths. *J. Chem. Phys.* **2000**, *113*, 9901–9904.
(59) Akinola, J.; Barth, I.; Goldsmith, B. R.; Singh, N. Adsorption Energies of Oxygenated Aromatics and Organics on Rhodium and Platinum in Aqueous Phase. *ACS Catal.* **2020**, *10*, 4929–4941.
(60) Kobayashi, S.; Tryk, D. A.; Uchida, H. Enhancement of Hydrogen Evolution Activity on Pt-Skin/Pt_3Co [(111), (100), and (110)] Single Crystal Electrodes. *Electrochem. commun.* **2020**, *110*, 106615.
(61) Guo, F.; Zou, Z.; Zhang, Z.; Zeng, T.; Tan, Y.; Chen, R.; Wu, W.; Cheng, N.; Sun, X. Confined Sub-Nanometer PtCo Clusters as a Highly Efficient and Robust Electrocatalyst for the Hydrogen Evolution Reaction. *J. Mater. Chem. A* **2021**, *9*, 5468–5474.
(62) Anniyev, T.; Kaya, S.; Rajasekaran, S.; Ogasawara, H.; Nordlund, D.; Nilsson, A. Tuning the Metal-Adsorbate Chemical Bond through the Ligand Effect on Platinum Subsurface Alloys. *Angew. Chemie Int. Ed.* **2012**, *51*, 7724–7728.
(63) Zhang, X.; Wang, H.; Key, J.; Linkov, V.; Ji, S.; Wang, X.; Lei, Z.; Wang, R. Strain Effect of Core-Shell Co@Pt/C Nanoparticle Catalyst with Enhanced Electrocatalytic Activity for Methanol Oxidation. *J. Electrochem. Soc.* **2012**, *159*, B270–B276.
(64) Hyman, M. P.; Medlin, J. W. Effects of Electronic Structure Modifications on the Adsorption of Oxygen Reduction Reaction Intermediates on Model Pt(111)-Alloy Surfaces. *J. Phys. Chem. C* **2007**, *111*, 17052–17060.
(65) Luo, H.; Yukuhiro, V. Y.; Fernández, P. S.; Feng, J.; Thompson, P.; Rao, R. R.; Cai, R.; Favero, S.; Haigh, S. J.; Durrant, J. R.; et al. Role of Ni in PtNi Bimetallic Electrocatalysts for Hydrogen and Value-Added Chemicals Coproduction via Glycerol Electrooxidation. *ACS Catal.* **2022**, *12*, 14492–14506.
(66) Jia, Q.; Zhao, Z.; Cao, L.; Li, J.; Ghoshal, S.; Davies, V.; Stavitski, E.; Attenkofer, K.; Liu, Z.; Li, M.; et al. Roles of Mo Surface Dopants in Enhancing the ORR Performance of Octahedral PtNi Nanoparticles. *Nano Lett.* **2018**, *18*, 798–804.
(67) Singh, N.; Campbell, C. T. A Simple Bond-Additivity Model Explains Large Decreases in Heats of Adsorption in Solvents Versus Gas Phase: A Case Study with Phenol on Pt(111) in Water. *ACS Catal.* **2019**, *9*, 8116–8127.
(68) Akinola, J.; Campbell, C. T.; Singh, N. Effects of Solvents on Adsorption Energies: A

General Bond-Additivity Model. *J. Phys. Chem. C* **2021**, *125*, 24371–24380.

(69) B Singh, N.; Lee, M.; Akhade, S. A.; Cheng, G.; Camaioni, D. M.; Gutiérrez, O. Y.; Glezakou, V.; Rousseau, R.; Lercher, J. A.; Campbell, C. T. Impact of pH on Aqueous-Phase Phenol Hydrogenation Catalyzed by Carbon-Supported Pt and Rh. *ACS Catal.* **2019**, *9*, 1120–1128.

(70) Bockris, J. O. M.; Jeng, K. T. In-Situ Studies of Adsorption of Organic Compounds on Platinum Electrodes. *J. Electroanal. Chem.* **1992**, *330* (1–2), 541–581.

Chapter 7 Conclusions and Future Projections

7.1 Summary and Conclusions

The state-of-the-art process of upgrading bio-oil using thermocatalytic hydrogenation (TCH) is unsustainable and expensive. In this dissertation, we present electrocatalytic hydrogenation (ECH) as a sustainable and cost-effective approach to upgrade bio-oil. This method will capitalize on the increasingly abundant and cheap renewable electricity[1] to drive the production of hydrogen from splitting water already present in bio-oil. This hydrogen will then be used in-situ to hydrogenate bio-oil in an electrochemical reactor. Techno-economic analysis has revealed that significant improvement in ECH current efficiencies and turnover frequencies reaching up to 1 s^{-1} are required for bio-oil to become a commercially viable option to traditional petroleum.[2] The presence of water in bio-oil plays a crucial role in determining the interaction strength between the electrode and the adsorbed bio-oil organic and hydrogen which will ultimately influence the ECH activity by dictating the surface coverages of adsorbates and tuning the intrinsic kinetics.[3–5] However, a knowledge gap exists in linking adsorption thermodynamics with the kinetics of aqueous and liquid-phase catalytic reactions as is obtainable for many gas-phase reactions like the famous Haber-Bosch process. This knowledge gap prevents the advancement of aqueous and liquid-phase heterogeneous catalytic processes such as ECH of bio-oil. In this dissertation, we completed several projects with the goal of addressing this knowledge gap, focusing on understanding aqueous-phase adsorption thermodynamics to rationalize ECH kinetics of model bio-oil molecules. The insights from these completed projects have contributed significantly to improving our understanding of aqueous-phase adsorption and catalyst design for

ECH. In addition, the projects in this dissertation have elicited exciting new questions to pursue for which I propose thoughts and preliminary results later in this chapter.

In **Chapter 3**, we investigated the differences between gas and aqueous-phase adsorption energies for five bio-oil-relevant molecules (phenol, benzaldehyde, furfural, benzyl alcohol and cyclohexanol) on Pt and Rh wires. A major goal of this chapter was to use aqueous-phase adsorption energies to explain two bewildering questions about aqueous-phase ECH kinetics. (1) Why are the gas-phase adsorption energies of phenol on Pt and Rh catalysts unable to explain the similar aqueous-phase ECH activity of phenol[6] on these catalysts? (2) Why do phenol, benzaldehyde, furfural and many other bio-oil molecules undergo aqueous-phase ECH with appreciable rates at room temperature, whereas their gas-phase adsorption energies suggest much higher temperatures are required? In this work, we found that the aqueous adsorption energies and enthalpies measured for these molecules are ~50−250 kJ mol^{-1} lower than their gas-phase values calculated from density functional theory (DFT). This difference in gas and aqueous-phase adsorption energies arises from organic solvation and solvent displacement which penalizes adsorption in aqueous phase but not in gas phase. The lower aqueous adsorption we measured better explain why room-temperature ECH was feasible for these molecules. We also found that Pt and Rh absorb phenol similarly in the aqueous phase which enabled us to explain their similar aqueous ECH activity, in contrast to their gas-phase values which are ~50 kJ mol^{-1} different.

In **Chapter 4**, we extended the work from **Chapter 3** basically to understand the structure of the displaced interfacial water. To calculate adsorption enthalpies from adsorption energies in **Chapter 3**, the adsorption entropy was estimated assuming the displaced water layer was only moved from an ordered structure on the metal surface to an ordered structure just above the adsorbed organic (**Figure 7.1**). This assumption of an unchanged water displacement entropy allowed us to use well established correlations to calculate the adsorption entropy upon the organic adsorption.[7] To probe this assumption, we used phenol in water as a model molecule and examined the temperature dependence of the aqueous-phase adsorption energies to establish the contributions of adsorption entropy and enthalpy. We show a positive adsorption entropy for aqueous-phase phenol because the ordered water layer, once displaced, gains approximately half of the entropy associated with bulk liquid water. This positive entropy is in stark contrast to the negative adsorption entropy of phenol in the gas phase, suggesting that temperature will have a less negative impact on organic coverages in aqueous phase compared to gas phase catalytic reactions.

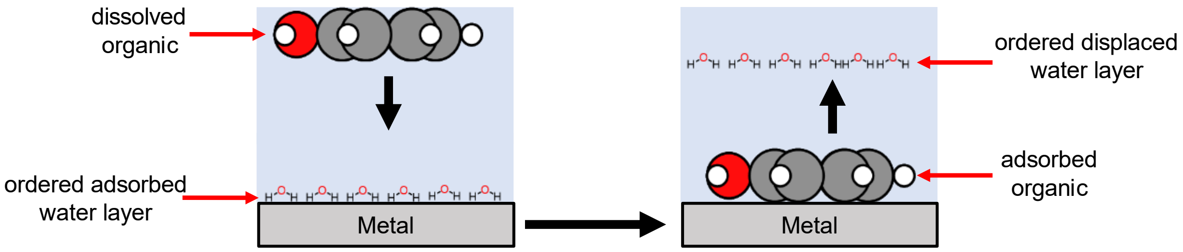

Figure 7.1 Schematic showing organic adsorption and displacement of water molecules in aqueous phase. Here the displaced interfacial water is assumed to retain the same ordered structure when adsorbed on the metal. Thus, phenol loses entropy upon adsorption but the interfacial water neither gains nor loses entropy upon displacement by phenol.

The work in **Chapter 5** was motivated by the need to predict accurate adsorption energies in liquid phase with inexpensive computations. Computational modelling like DFT calculations are typically used to model reaction pathways or predict active and selective catalysts for liquid-phase reactions. In most cases, the solvation penalty and in particular solvent displacement penalty on adsorption energies are not accounted for.[3] Considering that the enthalpic penalty for water displacement that we found in **Chapter 3** can be as high as 250 kJ mol^{-1} for aromatics with large footprints, computational predictions ignoring these penalties may not fully reflect the liquid environment. We developed a mathematical model to semi-quantitatively predict aqueous adsorption energies matching experiments by using gas-phase values from DFT or ultrahigh vacuum experiments along with readily accessible variables from thermochemistry tables. This model[8] improves greatly on a previous mathematical model[9] developed for molecules that adsorb flat because it accounts for the organic-solvent interaction on the sides of molecules with any shape or size or adsorption configuration. Molecules can adopt different adsorption configurations[10] that are not flat depending on the functional group and adsorption thermodynamics, thus a wider variety of adsorbates of interest to catalysis and electrocatalysis can be captured by the model developed in this dissertation. The use of solvent adhesion energies on metals in this model opens new ways of controlling molecule adsorption by choosing solvents with the appropriate adhesion energy.

In **Chapter 6**, we synthesized Pt_xCo_y alloys to modify the hydrogen and phenol adsorption energies in the aqueous phase and elucidate the activity of these alloys for phenol ECH and competing hydrogen evolution reaction (HER). We show that the hydrogen adsorption energies weaken with Co but the aqueous phenol adsorption energies are independent of the Co fraction. These alloys are more active for hydrogen evolution reaction than Pt, where the HER activity correlates to a weakened hydrogen adsorption energy. However, their activity for ECH depends on the Co fraction and applied potential, where at high hydrogen coverages a more negative applied potential enhances HER but limits ECH and vice versa. We find from DFT that the activation barrier towards ECH increases with Co fraction, which we find to follow a Brønsted Evans Polanyi (BEP) relationship with the reaction energy. By accounting for the weakened H adsorption energy and increasing barrier for ECH with Co content, we captured the trend in the measured ECH activity with Co and applied potential using microkinetic modelling based on Langmuir-Hinshelwood mechanism. The BEP relationship uncovered in this work suggests that higher ECH activity can be achieved for a different catalyst structure with a Pt monolayer on a Pt_xCo_y core.

7.2 Extension of Current Research

This dissertation has made significant contributions to understanding molecule adsorption in aqueous and liquid phase as well as linking aqueous-phase adsorption energies on metal and alloy surfaces to ECH kinetics. The new insights gained in this work are relevant to the development of ECH processes for upgrading bio-oil. New questions have also emerged that all together would improve our understanding of ECH that can serve as of possible extension of this dissertation. I provide thoughts on these in the following sections.

7.2.1 Measuring Adsorption Energies on Non-Pt Group Metals and Alloys

The work in **Chapter 3** highlighted that adsorption energies in aqueous phase more clearly explains ECH of bio-oil compounds than gas-phase values. We measured adsorption energies on Pt and Rh metals because these metals are active for ECH[6] but they are also able to adsorb hydrogen at sub-monolayer coverages in the underpotential region.[11,12] This property of Pt and Rh enabled the use of hydrogen underpotential deposition (H_{upd}) as a technique to extract phenol coverages and construct adsorption isotherms from which the aqueous adsorption energies were obtained. Non Pt group metals (PGMs) as well as Pt alloys containing these metals, e.g., Ni,[13] and Cu,[14] have been studied for ECH because they are inexpensive and relatively more abundant than PGMs. Measuring aqueous adsorption energies on non PGMs and their alloys to link aqueous adsorption thermodynamics to kinetics would help elucidate their ECH activity.

Potentiostatic electrochemical AC impedance spectroscopy (EIS) to measure the double layer capacitance and charge transfer resistance can be used as a technique to understand adsorption of model bio-oil compounds on these metals sites incapable of H_{upd}.[15] The capacitance technique where a decrease in double layer capacitance is proportional to adsorbate coverage (**Figure 7.2**),[16–18] can be benchmarked against the H_{upd} technique where decrease in the H_{upd} charge is proportional to adsorbate coverage. By benchmarking, one can ensure the measured coverages match using either technique under the same applied potential and reaction conditions. The double layer capacitance technique has an added benefit because it can be done at varying applied potentials, which will allow one to detect if the adsorption energy of the oxygenated aromatics changes as a function of potential.[18]

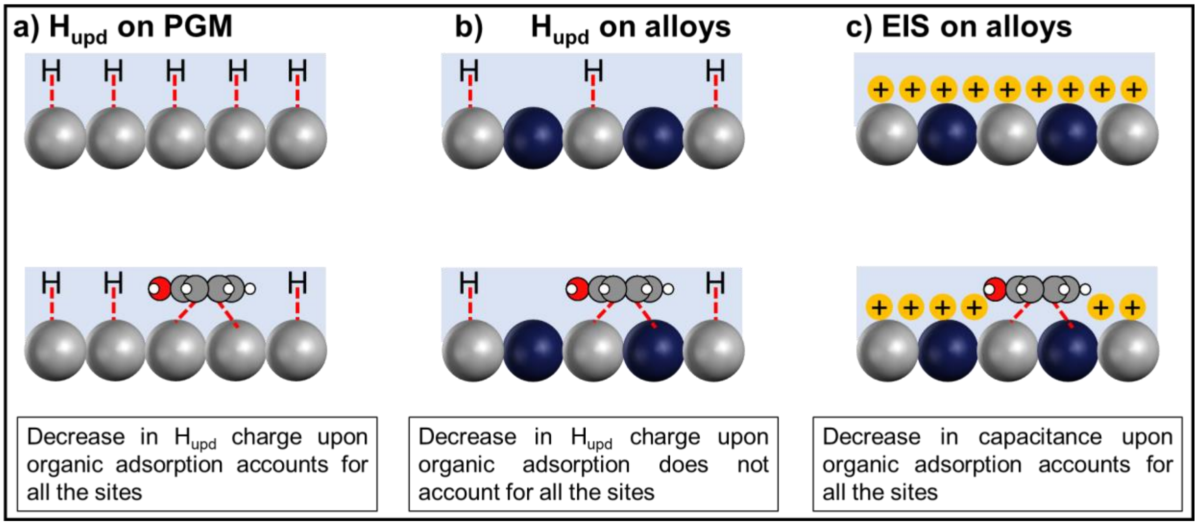

Figure 7.2 Schematic showing a catalyst surface for platinum group metals (PGMs) and alloys containing non PGMs during adsorption measurements using different methods. a) Hydrogen underpotential technique (H_{upd}) on PGMs showing hydrogen fully adsorbed on all the metal sites (top) and organic blocking a fraction of metal sites (bottom). **b)** H_{upd} technique on alloys showing hydrogen adsorbed only on the PGM metal sites (top) leading to inaccurate site counting and organic blocking on both PGM and non-PGM sites (bottom). **c)** Electrochemical impedance method showing the electrode surface (assuming electrode is negatively charged) and cations from the electrolyte forming a double layer (top) and organic adsorbed decreasing the double layer area and thus the double layer capacitance.

By analyzing the impedance spectrum at high and low frequencies and fitting to an equivalent circuit such as the Randle's circuit or a modified version of it, the double layer capacitance associated with the interface between the electrode and the electrolyte solution can be obtained when organic molecules adsorb onto the electrode surface.[19] The organic coverage at a given organic concentration can be indirectly obtained using **Eq. 7.1**. At different concentrations of organic in water, adsorption isotherms can be constructed and fitted to an adsorption model to obtain more accurate adsorption energies for these alloy surfaces containing non PGMs.

$$Organic\ coverage = \frac{Capacitance\ without\ organic - Capacitance\ with\ organic}{Capacitance\ without\ organic} \tag{7.1}$$

7.2.2 Probing Intrinsic and Apparent Adsorption Energies in Different Solvents

In **Chapter 5**, we developed a mathematical model (**Eq. 7.2**) to predict the apparent aqueous adsorption energies that accounts for solvation and solvent displacement. This model uses gas-phase adsorption energy along with values from thermochemistry tables to calculate the aqueous adsorption energy.

$$\Delta \mathrm{U}_{\mathrm{ads,R}(solvent)} = \Delta \mathrm{U}_{\mathrm{ads,R}(gas)} + \left[\mathrm{E}_{\mathrm{adh,S/M}} - \frac{\Delta \mathrm{U}_{\mathrm{solvation,R}(gas)}}{\sigma_{\mathrm{tot}}} - \gamma_{\mathrm{S}(liq)}\right]\sigma_{\mathrm{R}} \tag{7.2}$$

Where $\Delta \mathrm{U}_{\mathrm{ads,R}(solvent)}$ is the calculated aqueous adsorption energy, $\Delta \mathrm{U}_{\mathrm{ads,R}(gas)}$ is the adsorption energy in gas phase, $\mathrm{E}_{\mathrm{adh,S/M}}$ is the adhesion energy of the solvent to the metal, $\Delta \mathrm{U}_{\mathrm{solvation,R}(gas)}$, is the solvation energy of the gas-phase molecule, σ_{tot} is the total surface area, $\gamma_{\mathrm{S}(liq)}$ surface tension of the solvent, σ_{R} foot print of the molecule. We made an assumption in this model that the intrinsic bond energy of a molecule to the solid surface ($\Delta U_{ads,R}^{int}$) equals the adsorption energy of that molecule in the gas phase, $\Delta \mathrm{U}_{\mathrm{ads,R}(gas)}$, and is unaffected by the presence of the solvent environment around the molecule. Simply put as shown in **Figure 7.3**, $\Delta U_{ads,R}^{int}$ in solvent 1 (with strong adhesion to the metal) is the same as in solvent 2 (with a weaker adhesion to the metal) which is also the same as the adsorption energy in vacuum/gas phase $\Delta \mathrm{U}_{\mathrm{ads,R}(gas)}$.

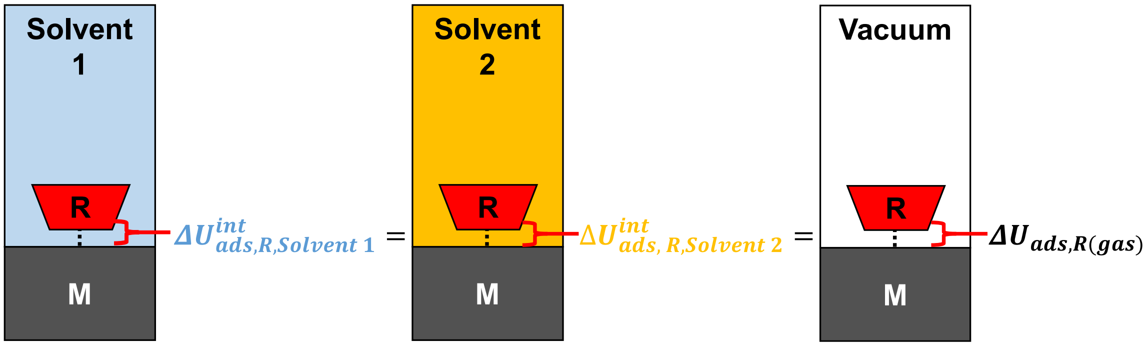

Figure 7.3 Final step in the bond additivity model showing the assumption that intrinsic bond energy between a molecule and the metal is unaffected by the solvent environment. Here solvent 1 is assumed to have a different adhesion energy to the metal compared to solvent 2, yet the intrinsic molecule bond strength is assumed to be the same in either solvent and is also equal to the adsorption energy in vacuum or gas phase.

For this model to be generally applicable to predict apparent adsorption energies in different solvents, it will be beneficial to test whether the intrinsic molecule bond strength is truly unaffected by the liquid environment. The H_{upd} method we used to obtain apparent adsorption energies is incapable of directly probing the intrinsic bond interaction with the metal. For this test, surface enhance Raman spectroscopy (SERS) can be used to directly probe the molecular vibrational frequency of hindered bonds upon adsorption in different solvents.[20,21] Certain bond vibrations, such as the aromatic "ring breathing" mode are affected by the intrinsic adsorption strength to an electrode surface, where a Raman red-shift compared to the bulk molecule is observed upon adsorption.[20,22] For toluene in water on Au[22] and Pd[20], a red shift in the ring breathing mode compared to bulk toluene was observed, which indicates how strongly toluene is interacting with the electrode surface. A smaller red shift on Au compared Pd was attributed to a weaker intrinsic adsorption strength of the toluene molecule to the metal surface. Differences in red shift in different solvents can be used to probe whether the intrinsic bond strength of a molecule is affected by the solvent environment or not.

In **Chapter 2**, I demonstrated ways to make roughened Au nanostructures and deposit relevant transition metals without Au pinholes while still obtaining high SERS sensitivity. Given the intricate nature of SERS data, it is important to implement certain measures and checks before, during, and after SERS experiments. I believe adopting a highly critical evaluation of SERS data is the best way to obtain the accurate interpretation of the data as I will show in some of my preliminary results. The following two experiment checks will be important:

1. The normal Raman spectra of the molecule (not adsorbed) in the solvent of interest should first be obtained. The vibrational frequency of a molecule in vacuum or in air may be influenced by solvation,[23] hence the correct reference for comparing any observed Raman red shift on a metal surface in a solvent should be the molecule in the solvated state
2. For thin metal films deposited on the SERS active substrate, performing pinhole check before and after SERS adsorption experiments will be very important especially if the adsorbate binds strongly to the underlaying SERS active material.

Preliminary results in **Figure 7.4a** for thionine adsorbing on Au compared to few monolayers of Pt deposited on roughened Au through electrodeposition or atomic layer deposition (ALD) showed possible exposure of Au pinholes during SERS experiments. I showed in **Chapter 2** that before SERS experiments, the Pt thin films do not show detectable Au pinholes by probing with CO.[24,25] Thionine is known to bind very strongly to Au,[26] particularly through the thiol group to form a Au-S bond, thus I expect to see a red shift between thionine adsorbed on Au compared to Pt. **Figure 7.4a** shows that all the thionine SERS feature on Au appears at the same Raman shift with Pt which can mean two things: (1) Pt and Au adsorbs thionine with the same strength which is very unlikely since one is a transition metal and the other is a noble metal and (2) a more likely explanation is that thionine is probably still bonded to Au despite the fact that Pt was clearly deposited on the Au substrate.

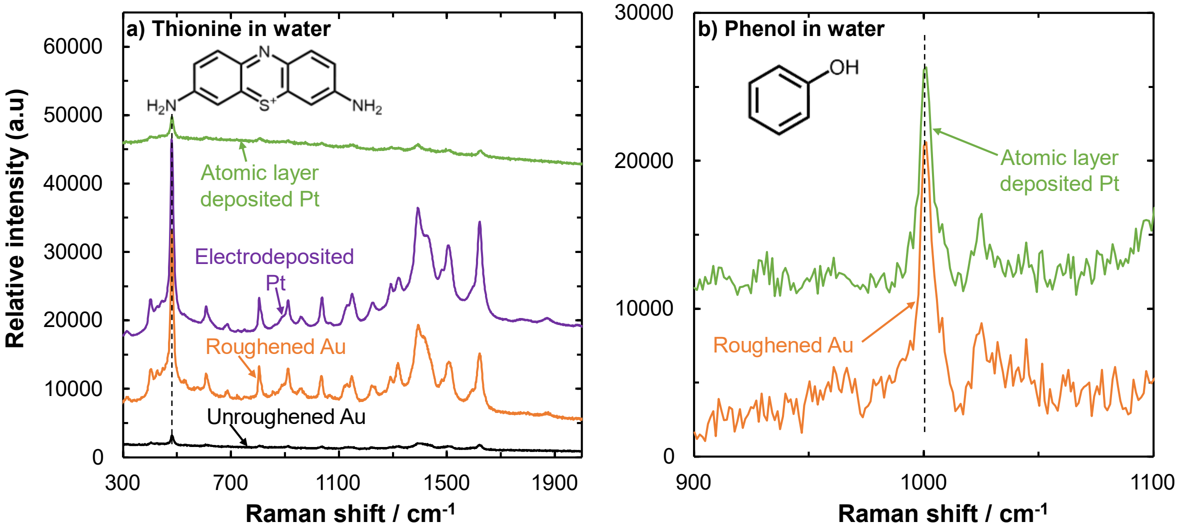

Figure 7.4 Surface enhanced Raman spectra on Au compared to Pt for thionine and phenol dissolved in water. a) Thionine acetate (8.7 µM) dissolved in water on unroughened Au, roughened Au, electrodeposited Pt on roughened Au, and atomic layer deposited Pt on roughened Au. **b)** Phenol (200 mM) in water on roughened Au, and atomic layer deposited Pt on roughened Au. SERS spectra were collected using a 633 nm laser at 23.75 mW power, with 8 accumulations, 10 seconds exposure time using 20x objective lens. SERS spectra for thionine were collected in extended mode while phenol spectra were collected in static mode. The vertical lines are drawn to show the dominant SERS features do not display any red shift on Pt compared to Au.

In the same manner, SERS of phenol dissolved in water on Au and Pt performed in static mode (**Figure 7.4b**) shows no red shift for the ring breathing mode (1003 cm^{-1}) on Pt compared to Au. Upon adsorption a larger red shift on Pt than Au is expected because of a stronger gas-phase chemisorption of phenol on Pt compared to weaker physisorption on Au.[27] Toluene adsorbs with the aromatic ring flat just like phenol and a larger red shift for toluene in water adsorbing on Pd (28 cm^{-1}) has been observed in comparison to Au (12 cm^{-1}). The fact that the ring breathing mode of phenol on Pt and Au both appear at 1001 cm^{-1} would indicate one of the following: (1) phenol is physisorbed on Au and also on Au pinholes on Pt, but is not chemisorbed on Pt, (2) the fact that the Raman red shift on both Pt and Au is just 2 cm^{-1} (1003–1001 cm^{-1}) compared to unadsorbed phenol could mean that we are perhaps probing the bulk phenol near the Au substrate that is receiving plasmon enhancement rather than a physisorbed or chemisorbed phenol. Unfortunately, attempts to probe the normal Raman spectra of the solvated phenol by focusing the Raman laser slightly away from the surface into the bulk phenol solution were dominated by Rayleigh scattering. Thus, it is currently a challenge to know whether the SERS feature is truly from an adsorbed molecule or for a molecule just near the Au SERS substrate without adsorbing but still receiving SERS enhancement. Addressing this challenge would be important to understand intrinsic adsorption strengths using SERS.

Preliminary results in **Figure 7.5** for thionine and phenol shows that their intrinsic adsorption strength on roughened Au and in different solvents may be unchanged potentially allowing the bond additivity model to be applicable to other solvents beyond water. Au substrate alone was studied here because the exposure of Au pinholes on Pt during SERS is a potential problem as discussed above. Adhesion energies of water, methanol, and formic acid have been measured on Pt(111) and Ni (111), increasing in the trend methanol< formic acid <water,[28] for both metals and might extend to Au as well. Choosing solvents with varying adhesion energies ($\mathrm{E_{adh,S/M}}$) would change the apparent adsorption energies ($\Delta \mathrm{U}_{\mathrm{ads,R}(solvent)}$) according to **Eq. 7.2**, making these solvents excellent candidates to test whether the intrinsic adsorption strength will change too. The Raman shift for the SERS features of thionine and phenol do not change in these solvents indicating that the intrinsic adsorption strength is independent of the solvent environment, establishing a potential application of the bond additivity model (**Eq. 7.2**) across different solvents. The immediate caveat here is to first certify that the molecule truly physisorbs or chemisorbs on the Au surface and not just sitting near the Au surface. This model's generalizability across various solvents would be very valuable, for example, if the aim is to enhance reaction rate for a liquid-phase reaction by increasing adsorbate coverage, employing solvents with weaker adhesion energies, such as methanol, could be advantageous.

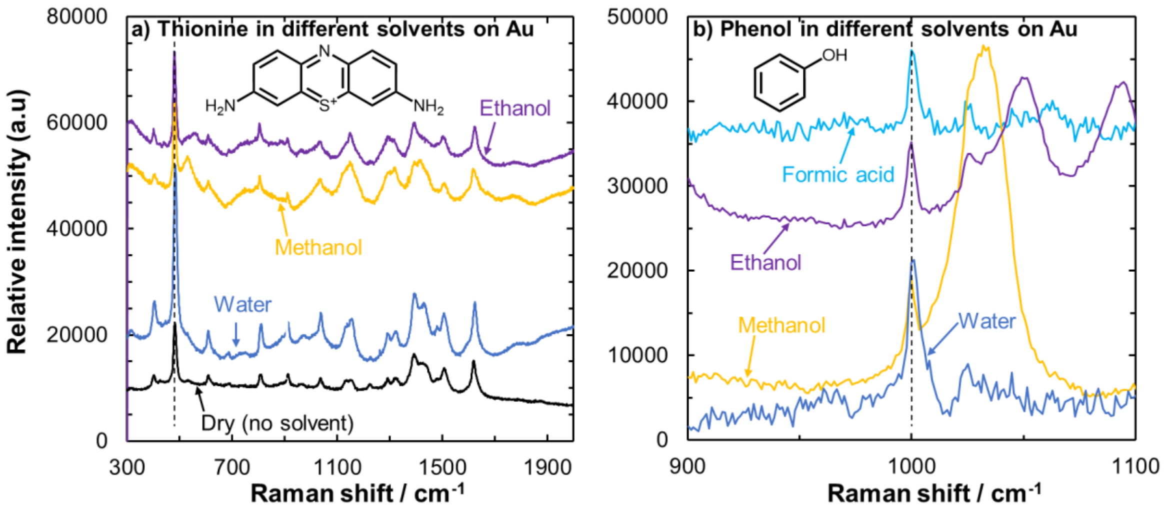

Figure 7.5 Surface enhanced Raman spectra of thionine and phenol dissolved in different solvents on roughened Au. a) Thionine acetate (8.7 µM), dry (i.e., dissolved in water and dried off on the substrate), dissolved in water, methanol, ethanol. **b)** Phenol (200 mM) dissolved in water, methanol, ethanol, and formic acid. SERS spectra were collected using 633 nm laser at 23.75 Mw power, with 8 accumulations, 10 seconds exposure time using 20x objective lens. SERS spectra for thionine were collected in extended mode while phenol spectra were collected in static mode.

7.2.3 Synthesis and Stabilization of Pt/Pt_xCo_y Catalyst Structure

In **Chapter 6** we uncovered that despite weakening the hydrogen adsoption energies on Pt_xCo_y alloys, the presence of surface Co increases the barrier towards ECH (**Figure 6.8** of **Chapter 6**). This increased barrier negatively impacted the measured ECH turnover frequency particularly for catalysts with high Co fractions. However, the DFT calculations in this work also suggested that alloy structures with a monolayer of Pt on a Pt_xCo_y core (i.e., Pt/Pt_xCo_y) would lower the ECH barriers with increasing Co fraction which would increase the turnover frequency. In the pursuit of developing a catalyst with high activity, synthesizing Pt/Pt_xCo_y catalysts would be a potential next step from this work. Although we have shown that even if these catalysts (a monolayer of Pt on Pt_xCo_y) are synthesized, the presence of adsorbed hydrogen under typical ECH conditions may cause Co segregation to the surface to become favorable. A higher thickness of surface Pt would help improve its stability; hence my first recommendation would be to revisit the DFT calculations for the Pt/Pt_xCo_y surfaces, but this time, incrementally increasing the number of

Pt monolayers over the Pt_xCo_y slab until the calculated barriers start approaching that of pure Pt. This will help establish the maximum Pt shell thickness to aim for during experimental synthesis.

Several synthesis techniques (**Figure 7.6**) have been employed to make nanoparticles with Pt shell on a Co or Pt_xCo_y core, typically for oxygen reduction reaction resulting in mass activities up to a factor of seven.[29–33] Amongst these studies, only a few use imaging techniques like scanning transmission electron microscopy (STEM) to verify the formation of a Pt shell rather than a Pt-rich surface with Co still present on the surface. The different synthesis procedure can be found in this review article,[34] and in ref [29–33]. Even though the Pt/Pt_xCo_y catalyst structure looks promising, because of its likely instability, I would recommend STEM characterization after catalyst synthesis and after ECH experiments, as this will ensure any measured catalytic performance will be accurately ascribed to the correct catalyst nanostructure.

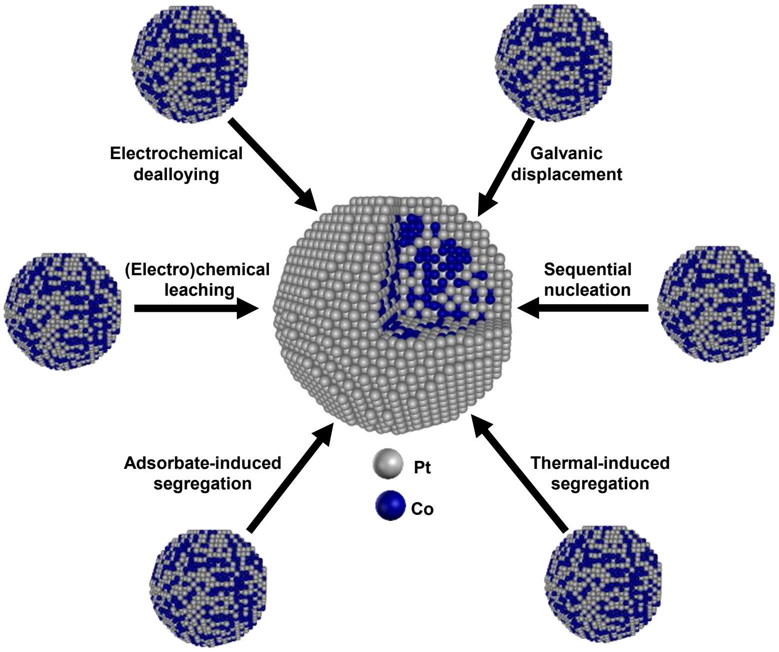

Figure 7.6 Synthesis methods employed to prepare Pt shell on a Pt_xCo_y core nanoparticle structure. They include electrochemical dealloying, electrochemical and chemical leaching, reaction routes such as strong binding of adsorbates like CO to segregate Pt to the surface and thermal annealing, deposition routes including nucleation and galvanic displacement and electrodeposition. This figure was modified from ref [34].

7.3 Outlooks

This dissertation has provided a fundamental understanding of adsorption and ECH kinetics in the aqueous phase and the results here will enable the design of the reaction environment, reaction conditions and catalyst materials to improve electrocatalytic hydrogenation. While we have focused on single model compounds to gain mechanistic understanding, a good next step will be to start increasing the complexity of the bio-oil mixtures by performing ECH in a mixture of two or three relevant model bio-oil organics. For example, in **Chapter 3** we found that phenol, furfural and benzaldehyde show comparable aqueous adsorption energies on Pt and Rh. A promising next step will be to simultaneously hydrogenate a mixture containing these molecules in similar concentrations to draw insights on the contribution of their individual rate constant to the overall turnover frequency, since their equilibrium coverages should essentially be similar.

The work we have done for ECH is only a subset of the entire bio-oil production process, hence great thoughts and research investments should also be allocated to other complementary areas to help translate the fundamental science we have done for ECH into practical production of marketable end use bio-oil. Obtaining enough feedstock is perhaps the first thing to consider. A 2016 DOE study showed that about 1 billion tons of non-food grade biomass is available annually in the US which can offset about 80% of petroleum energy use.[35] Even though petroleum will still be a major source of energy for the time being, they will eventually run out. Research dollars need to start going into ensuring consistent supply of lignin biomass, through identifying suitable land areas for sustainable tree growth as well as genetically engineering fast growing trees to increase their bio-oil yield.[36]

Pyrolysis and hydrothermal liquefaction (HTL) processes, used to break down solid biomass or plastic waste into liquid bio-oil, involve high energy consumption, occurring at elevated temperatures reaching up to 400°C. Integrating renewable electricity to heat up the HTL and pyrolysis reactors would help reduce the net CO_2 emissions in the overall bio-oil production process. This of course will require research investments for innovative reactor design with unique heat transfer and control systems to electrify HTL and pyrolysis reactors.

Government can also play a crucial part in developing policies that encourage the adoption of bio-oil by industries who currently use petroleum for fuels and chemical production. If the government provides incentives like tax exemptions or renewable energy credits, companies might be willing to change their feedstock to bio-oil. For example, Honeywell UOP company now makes aviation fuel containing 50% blend of sustainable feedstock.

To conclude, more work needs to be done to increase public awareness and support for sustainable energy and products. In times of environmental crises, such as the recent wildfires in Hawaii, enthusiasts for bio-derived fuels and chemicals can use opportunities like this to convey the environmental benefits of reducing carbon footprints. The goal can be to rally public support to press their constituency representatives to formulate policies that promote sustainable practices.

7.4 References

(1) EIA U.S. Energy Information Administration. *Annual Energy Outlook 2019 with Projections to 2050*; US Energy Information Administration, Office of Energy Analysis, U.S. Department of Energy: Washington, DC 20585, **2019**.
(2) Weber, R. S.; Holladay, J. E. Modularized Production of Value-Added Products and Fuels from Distributed Waste Carbon-Rich Feedstocks. *Engineering* **2018**, *4*, 330–335.
(3) Lopez-Ruiz, J. A.; Andrews, E.; Akhade, S. A.; Lee, M.; Koh, K.; Sanyal, U.; Yuk, S. F.; Karkamkar, A. J.; Derewinski, M. A.; Holladay, J.; Glezakou, V.; Rousseau, R.; Gutiérrez, O. Y.; Holladay, J. D. Understanding the Role of Metal and Molecular Structure on the Electrocatalytic Hydrogenation of Oxygenated Organic Compounds. *ACS Catal* **2019**, *9*, 9964–9972.
(4) Bondue, C. J.; Koper, M. T. M. Electrochemical Reduction of the Carbonyl Functional

Group: The Importance of Adsorption Geometry, Molecular Structure, and Electrode Surface Structure. *J. Am. Chem. Soc.* **2019**, *141*, 12071–12078.

(5) Matthiesen, J. E.; Carraher, J. M.; Vasiliu, M.; Dixon, D. A.; Tessonnier, J.-P. Electrochemical Conversion of Muconic Acid to Biobased Diacid Monomers. *ACS Sustain. Chem. Eng.* **2016**, *4*, 3575–3585.

(6) Singh, N.; Song, Y.; Gutiérrez, O. Y.; Camaioni, D. M.; Campbell, C. T.; Lercher, J. A. Electrocatalytic Hydrogenation of Phenol over Platinum and Rhodium: Unexpected Temperature Effects Resolved. *ACS Catal.* **2016**, *6*, 7466–7470.

(7) Campbell, C. T.; Sellers, J. R. V. The Entropies of Adsorbed Molecules. *J. Am. Chem. Soc.* **2012**, *134*, 18109–18115.

(8) Akinola, J.; Campbell, C. T.; Singh, N. Effects of Solvents on Adsorption Energies: A General Bond-Additivity Model. *J. Phys. Chem. C* **2021**, *125*, 24371–24380.

(9) Singh, N.; Campbell, C. T. A Simple Bond-Additivity Model Explains Large Decreases in Heats of Adsorption in Solvents versus Gas Phase: A Case Study with Phenol on Pt(111) in Water. *ACS Catal.* **2019**, *9*, 8116–8127.

(10) Bockris, J. O.; Jeng, K. T. In-Situ Studies of Adsorption of Organic Compounds on Platinum Electrodes. *J. Electroanal. Chem.* **1992**, *330*, 541–581.

(11) Łukaszewski, M.; Soszko, M.; Czerwiński, A. Electrochemical Methods of Real Surface Area Determination of Noble Metal Electrodes – an Overview. *Int. J. Electrochem. Sci* **2016**, *11*, 4442–4469.

(12) Jerkiewicz, G. Electrochemical Hydrogen Adsorption and Absorption. Part 1: Under-Potential Deposition of Hydrogen. *Electrocatalysis* **2010**, *1*, 179–199.

(13) Ma, J.; Wang, Z.; Majima, T.; Zhao, G. Role of Ni in PtNi Alloy for Modulating the Proton–Electron Transfer of Electrocatalytic Hydrogenation Revealed by the In Situ Raman–Rotating Disk Electrode Method. *ACS Catal.* **2022**, *12*, 14062–14071.

(14) Jin, M.; Liu, Y.; Zhang, X.; Wang, J.; Zhang, S.; Wang, G.; Zhang, Y.; Yin, H.; Zhang, H.; Zhao, H. Selective Electrocatalytic Hydrogenation of Nitrobenzene over Copper-Platinum Alloying Catalysts: Experimental and Theoretical Studies. *Appl. Catal. B Environ.* **2021**, *298* , 120545.

(15) Schouten, K. J. P.; Van Der Niet, M. J. T. C.; Koper, M. T. M. Impedance Spectroscopy of H and OH Adsorption on Stepped Single-Crystal Platinum Electrodes in Alkaline and Acidic Media. *Phys. Chem. Chem. Phys.* **2010**, *12*, 15217–15224.

(16) Hillson, P. . Adsorption and the Hydrogen Overpotential. *Trans. Faraday Soc.* **1952**, *48*, 462–473.

(17) Breiter, M. W. Comparative Voltammetric Study of Methanol Oxidation and Adsorption on Noble Metal Electrodes in Perchloric Acid Solutions. *Electrochim. Acta* **1963**, *8*, 973-983.

(18) McCafferty, E.; Hackerman, N. Double Layer Capacitance of Iron and Corrosion Inhibition with Polymethylene Diamines. *J. Electrochem. Soc.* **1972**, *119*, 146.

(19) Bierwagen, G.; Tallman, D.; Li, J.; He, L.; Jeffcoate, C. EIS Studies of Coated Metals in Accelerated Exposure. *Prog. Org. Coatings* **2003**, *46*, 149–158.

(20) Zou, S.; Williams, C. T.; Chen, E. K.-Y.; Weaver, M. J. Surface-Enhanced Raman Scattering as a Ubiquitous Vibrational Probe of Transition-Metal Interfaces: Benzene and Related Chemisorbates on Palladium and Rhodium in Aqueous Solution. *J. Phys. Chem. B* **1998**, *102*, 9039–9049.

(21) Wang, J.; Dong, J. C.; Yang, J.; Wang, Y.; Zhang, C. J.; Xu, M. M.; Mao, B. W.; Yao, J. L.; Li, J. F.; Tian, Z. Q. In Situ SERS and SHINERS Study of Electrochemical

Hydrogenation of P-Ethynylaniline in Nonaqueous Solvents. *Electrochem. commun.* **2017**, *78*, 16–20.

(22) Gao, P.; Weaver, M. J. Surface-Enhanced Raman Spectroscopy as a Probe of Adsorbate-Surface Bonding: Benzene and Monosubstituted Benzenes Adsorbed at Gold Electrodes. *J. Phys. Chem.* **1985**, *89*, 5040–5046.

(23) Volný, M.; Sengupta, A.; Wilson, C. B.; Swanson, B. D.; Davis, E. J.; Tureček, F. Surface-Enhanced Raman Spectroscopy of Soft-Landed Polyatomic Ions and Molecules. *Anal. Chem.* **2007**, *79*, 4543–4551.

(24) Zou, S.; Weaver, M. J. Surface-Enhanced Raman Scattering on Uniform Transition-Metal Films: Toward a Versatile Adsorbate Vibrational Strategy for Solid-Nonvacuum Interfaces? *Anal. Chem.* **1998**, *70*, 2387–2395.

(25) Zou, S.; Williams, C. T.; Chen, E. K.-Y.; Weaver, M. J. Probing Molecular Vibrations at Catalytically Significant Interfaces: A New Ubiquity of Surface-Enhanced Raman Scattering. *J. Am. Chem. Soc.* **1998**, *120*, 3811–3812.

(26) Yuanhua Ding, *; Xumin Zhang; Xiaoxia Liu, and; Rong Guo. Adsorption Characteristics of Thionine on Gold Nanoparticles. *Langmuir* **2007**, *23*, 11342–11342.

(27) Peköz, R.; Donadio, D. Effect of van Der Waals Interactions on the Chemisorption and Physisorption of Phenol and Phenoxy on Metal Surfaces. *J. Chem. Phys.* **2016**, *145*, 104701.

(28) Rumptz, J. R.; Campbell, C. T. Adhesion Energies of Solvent Films to Pt(111) and Ni(111) Surfaces by Adsorption Calorimetry. *ACS Catal.* **2019**, *9*, 11819–11825.

(29) Oezaslan, M.; Strasser, P. Activity of Dealloyed $PtCo_3$ and $PtCu_3$ Nanoparticle Electrocatalyst for Oxygen Reduction Reaction in Polymer Electrolyte Membrane Fuel Cell. *J. Power Sources* **2011**, *196*, 5240–5249.

(30) Oezaslan, M.; Heggen, M.; Strasser, P. Size-Dependent Morphology of Dealloyed Bimetallic Catalysts: Linking the Nano to the Macro Scale. *J. Am. Chem. Soc.* **2012**, *134*, 514–524.

(31) Oezaslan, M.; Hasché, F.; Strasser, P. Oxygen Electroreduction on $PtCo_3$, PtCo and Pt_3Co Alloy Nanoparticles for Alkaline and Acidic PEM Fuel Cells. *J. Electrochem. Soc.* **2012**, *159*, B394–B405.

(32) Wang, C.; Wang, G.; van der Vliet, D.; Chang, K. C.; Markovic, N. M.; Stamenkovic, V. R. Monodisperse Pt_3Co Nanoparticles as Electrocatalyst: The Effects of Particle Size and Pretreatment on Electrocatalytic Reduction of Oxygen. *Phys. Chem. Chem. Phys.* **2010**, *12*, 6933–6939.

(33) Mayrhofer, K. J. J.; Juhart, V.; Hartl, K.; Hanzlik, M.; Arenz, M. Adsorbate-Induced Surface Segregation for Core-Shell Nanocatalysts. *Angew. Chemie - Int. Ed.* **2009**, *48*, 3529–3531.

(34) Oezaslan, M.; Hasché, F.; Strasser, P. Pt-Based Core-Shell Catalyst Architectures for Oxygen Fuel Cell Electrodes. *J. Phys. Chem. Lett.* **2013**, *4*, 3273–3291.

(35) Langholtz, M.; Stokes, B.; Eaton, L. 2016 Billion-Ton Report: Advancing Domestic Resources for a Thriving Bioeconomy (Executive Summary). *Ind. Biotechnol.* **2016**, *12*, 282–289.

(36) Toraman, H. E.; Vanholme, R.; Borén, E.; Vanwonterghem, Y.; Djokic, M. R.; Yildiz, G.; Ronsse, F.; Prins, W.; Boerjan, W.; Van Geem, K. M.; Marin, G. B. Potential of Genetically Engineered Hybrid Poplar for Pyrolytic Production of Bio-Based Phenolic Compounds. *Bioresour. Technol.* **2016**, *207*, 229–236.

Appendix

Adsorption Measurements, Catalyst Characterization and Kinetic Modelling

A.1 Reversibility of Hydrogen Underpotential Deposition in the Presence of Furfural

The H_{upd} adsorption/desorption region on Pt and Rh in acetate buffer with increasing furfural concentration was not reversible (**Figure 3.4**) as opposed to the other organics tested here. The data in **Figure A.1** shows the adsorption (Q_{ads}) and desorption (Q_{des}) charges at different furfural concentrations. At low furfural concentrations, Q_{ads} is close to that of Q_{des} indicating H* is completely desorbed in the oxidative scan in the underpotential region (0.05 V to 0.35 V). However, at high furfural concentrations Q_{des} is lower than Q_{ads}, indicating that some H* is not desorbed in the oxidative scan. One possibility is that the H* reacts with a co-adsorbed species (such as furfural, or an adsorbed furfural fragment). If this reaction of H* with the adsorbed organic species is a catalytic reaction (i.e., one where multiple turnovers occur), the amount of H* that is reacted which would not be counted during desorption would increase proportionally with increasing time. That is, normalizing the amount of unrecovered charge to the time should result in a constant value (equivalent to a turnover frequency).

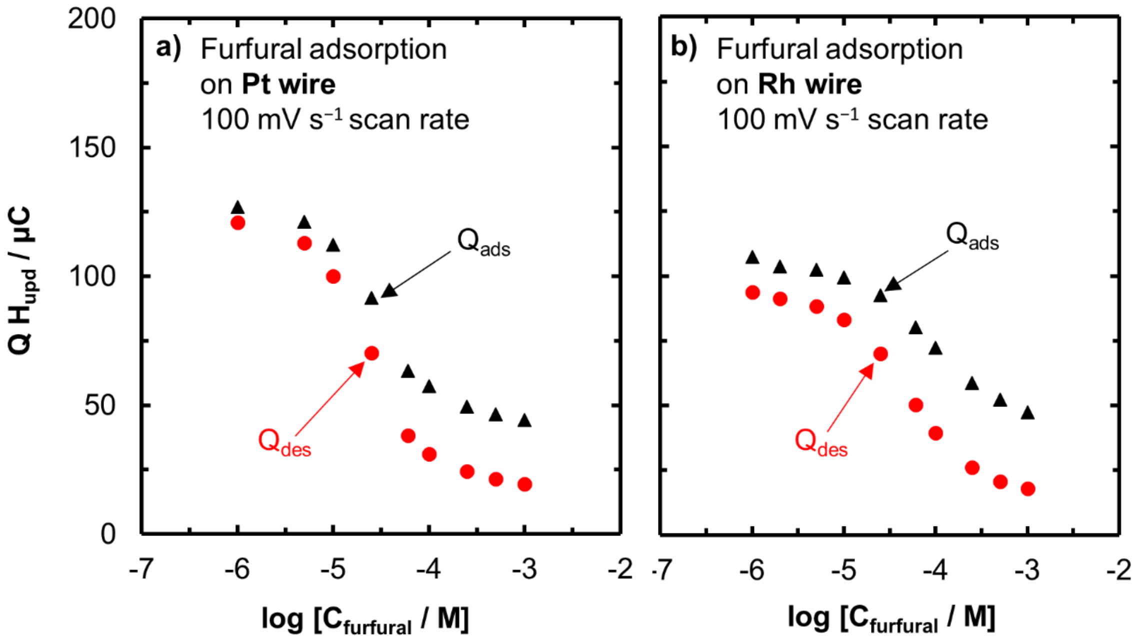

Figure A.1 The H_{upd} adsorption charge (Q_{ads}) and desorption charge (Q_{des}) as a function of furfural concentration. a) Pt and **b)** Rh. Charges are calculated from **Figure 3.4b.** The initial higher adsorption charge Q_{ads} for Rh is because of the Rh oxide reduction peak being convoluted into the H_{upd} reduction peak. The lack of reversibility of the H_{upd} charge is seen for furfural on both metals.

We show that the irreversibility of H_{upd} in the presence of furfural is not due to a catalytic reaction with H* because at lower scan rates (i.e., at longer times spent in the H_{upd} potential) there is no proportional increase in the loss of H*. The data in **Figure A.2a-b** shows the fraction of total H_{upd} on Pt and Rh that is not recovered at different scan rates. For all the scan rates, the unrecovered charge increases with furfural concentration. In **Figure A.2c-d**, we normalize this fraction to the average time that a hydrogen adatom spends on the metal surface during the scan, estimated as half of the total time during the H_{upd} region (t_{ave} = $V_{H_{upd}}$ / scan rate), where $V_{H_{upd}}$ is the H_{upd} potential window (0.3 V, from the 0.05 V–0.35 V window in the CVs). If the unrecovered reduction charge was due to a catalytic reaction of furfural with adsorbed hydrogen, it would be proportional to the amount of time spent in the region where hydrogen and furfural are coadsorbed, i.e., at slower scan rates (longer times) the amount of unrecovered charge would be larger. If this were the case, normalizing to the reaction time would result in equal values at different scan rates.

Because the results in **Figure A.2c-d** show that there is a large scan rate dependence on this term, it implies there is no turnover reaction occurring, but rather a set amount of charge is not recovered, essentially independent of the scan rate. Possible reasons for this irreversibility are that (i) furfural is partially being hydrogenated in the short scan time within the H adsorption region (0.05 V–0.35 V), but not turning over (i.e., furfural is partially hydrogenated, but remains adsorbed on the surface and does not go onto further products and desorb), (ii) the reaction time is insufficient for a turnover to occur, or (iii) furfural when adsorbed is decarbonylated,[1] to form a furyl intermediate and CO*, and then one of these species is irreversibly reduced/hydrogenated during the cathodic scan.

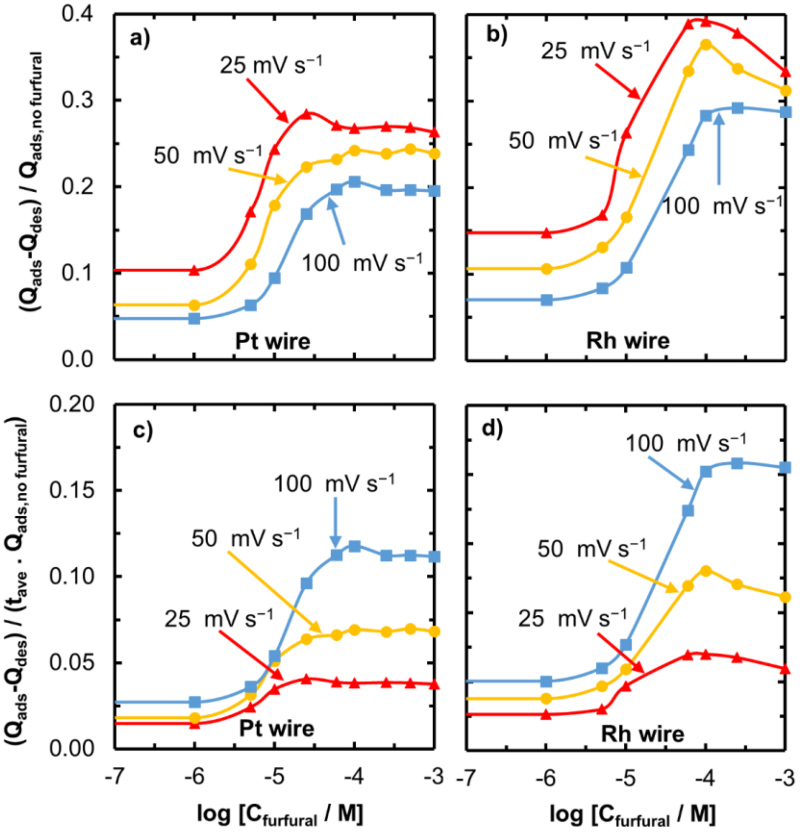

Figure A.2 Fraction of unrecovered H* (or electrons) in the desorption region ($Q_{ads} - Q_{des}$)/$Q_{ads,no\ furfural}$ as a function of furfural concentration at 25, 50 and 100 mV s^{-1} scan rates. a) a Pt wire and **b)** Rh wire. The data in **Figure A.1** is used for the 100 mV s^{-1} plots. The fraction of unrecovered H* from a) and b) normalized to the average scan time as a function of furfural concentration for 25, 50, and 100 mV s^{-1} on **c)** Pt wire and **d)** Rh wire. Here t_{ave} = $V_{H_{upd}}$/scan rate.

The adsorption information for furfural on Pt is shown in **Figure A.3**. As a note, although we report this as adsorption energies for furfural, recent reports indicate that furfural may not be adsorbed molecularly on Pt.[1] Although those studies were in more acidic conditions (pH = 1 rather than pH = 5 here) and higher furfural concentrations (100 mM vs. maximum of 1 mM here), there is evidence of low temperature furfural decarbonylation on Pt[2–4] that indicates the adsorbed species we are probing here may be a furfural fragment, rather than furfural itself.

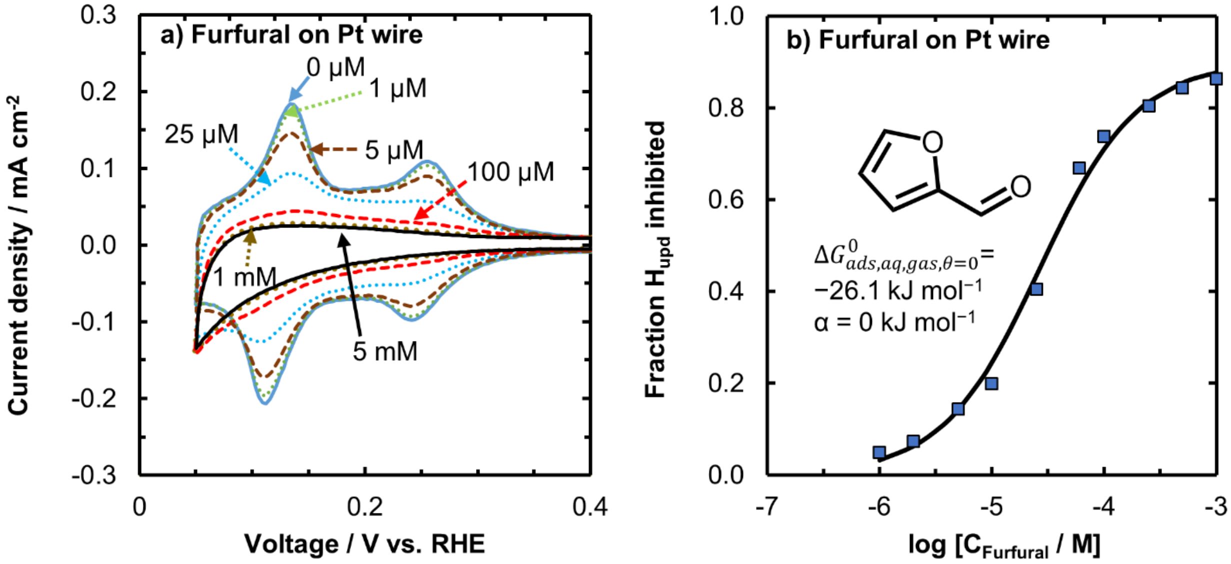

Figure A.3 Cyclic Voltammogram and adsorption isotherms of furfural on Pt wire. a) Cyclic voltammograms showing the H_{upd} region at different bulk furfural concentrations. **b)** Fraction of H_{upd} inhibited by furfural from the cyclic voltammograms in **a)** as a function of furfural concentration to construct an adsorption isotherm of furfural on Pt wire. The isotherm fit using a Temkin adsorption model is indicated by the black line.

A.2 Cyclic Voltammetry, X-ray Absorption, and Microscopy

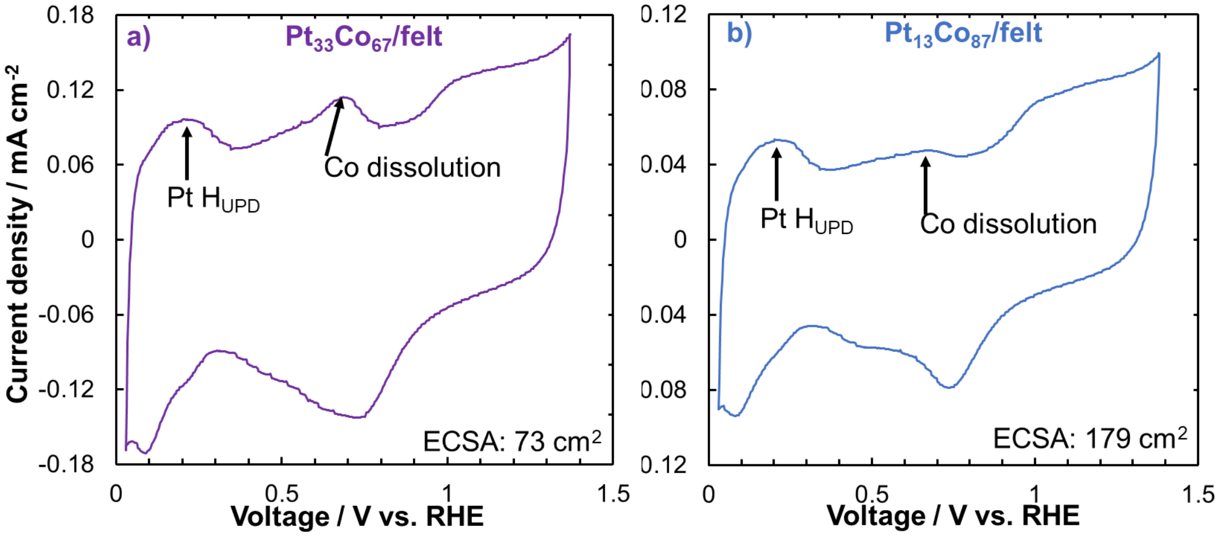

Figure A.4 Cyclic voltammograms of as prepared Pt_xCo_y/felt catalysts. a) Cycle #2 of the as prepared $Pt_{33}Co_{67}$/felt sample that became $Pt_{80}Co_{20}$/felt after pretreatment. **b)** Cycle #2 of the as prepared $Pt_{13}Co_{87}$/felt that became $Pt_{62}Co_{38}$/felt after pretreatment. CVs were performed in 3 M acetate buffer supporting electrolyte at 23.3°C and a scan rate of 20 mV/s.

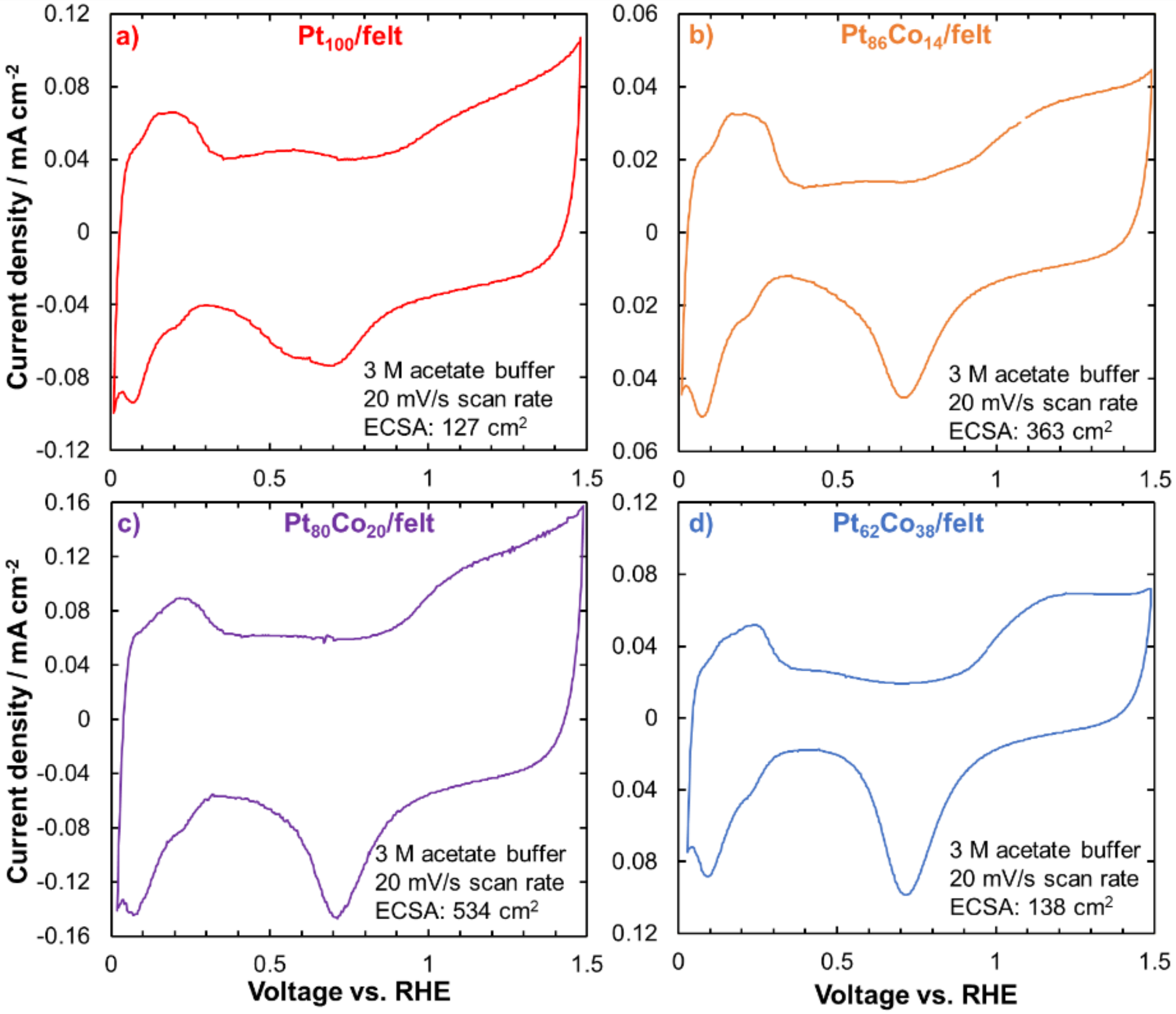

Figure A.5 Cyclic voltammograms of the pretreated catalysts synthesized on carbon felt support. a) Pt_{100}/felt, **b)** $Pt_{80}Co_{20}$/felt, **c)** $Pt_{86}Co_{14}$/felt, and **d)** $Pt_{62}Co_{38}$/felt. The CVs were performed in 3 M acetate buffer supporting electrolyte at 23.3 °C and at a scan rate of 20 mV/s.

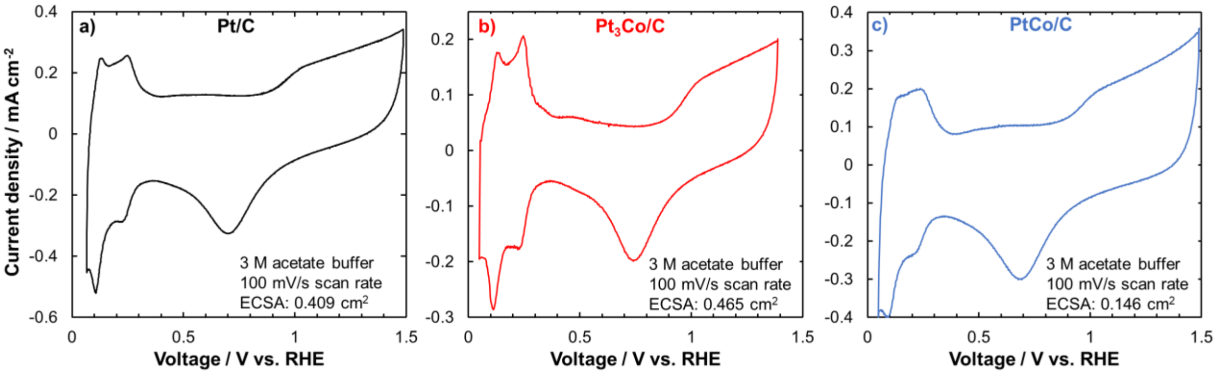

Figure A.6 Cyclic voltammograms of the pretreated catalysts supported on Vulcan carbon. a) Pt/C, **b)** Pt_3Co/C, and **c)** PtCo/C. The CVs were performed at 23.3°C in 3 M acetate buffer supporting electrolyte and at a scan rate of 100 mV/s. Cyclic voltammetry for the Vulcan carbon supported catalysts were performed in a rotating disk electrode set up. The much lower loading is the reason for the smaller ECSA compared to the catalysts supported on carbon felt in **Figure A.5**.

Cyclic voltammograms of the as-prepared catalyst, prior to cyclic voltammetry pretreatment, indicate dissolution of Co, as we show in **Figure A.4**. Following the pretreatment protocol, the oxidation peak corresponding to Co dissolution at −0.7 V vs. RHE no longer appears (**Figure A.5, Figure A.6**). The reduction peak at approximately −0.7 V vs. RHE corresponds to reduction of platinum oxide.

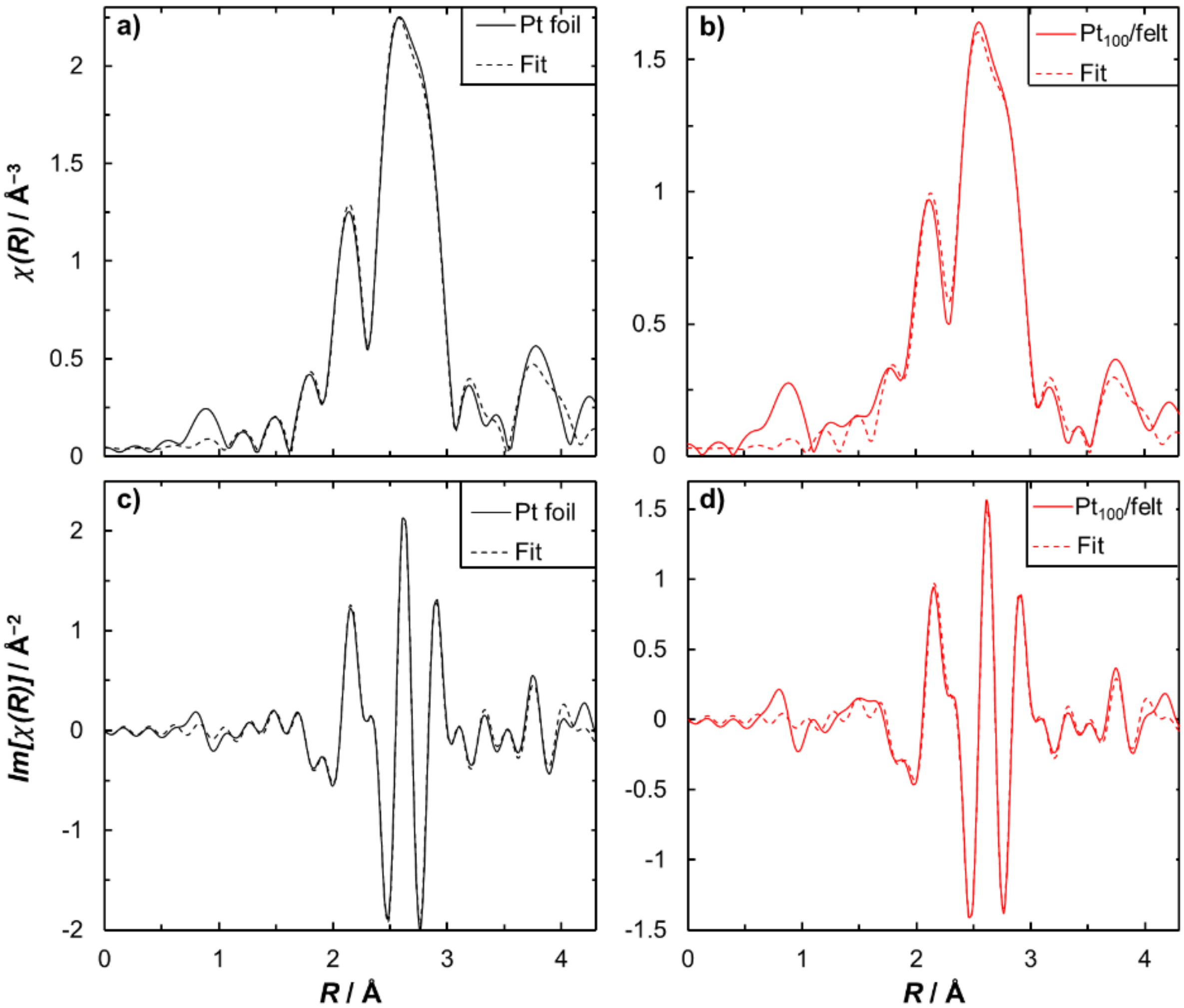

Figure A.7 EXAFS spectra of Pt foil and Pt_{100}/felt catalysts performed at the Pt L_3-edge and their fit. The magnitude of the *R*-space spectra (solid lines) and their fits (dashed lines) using a Pt-Pt first and second shell for **a)** Pt foil and **b)** Pt_{100}/felt. The imaginary *R*-space spectra (solid lines) and their Artemis fits (dashed lines) for **c)** Pt foil and **d)** Pt_{100}/felt.

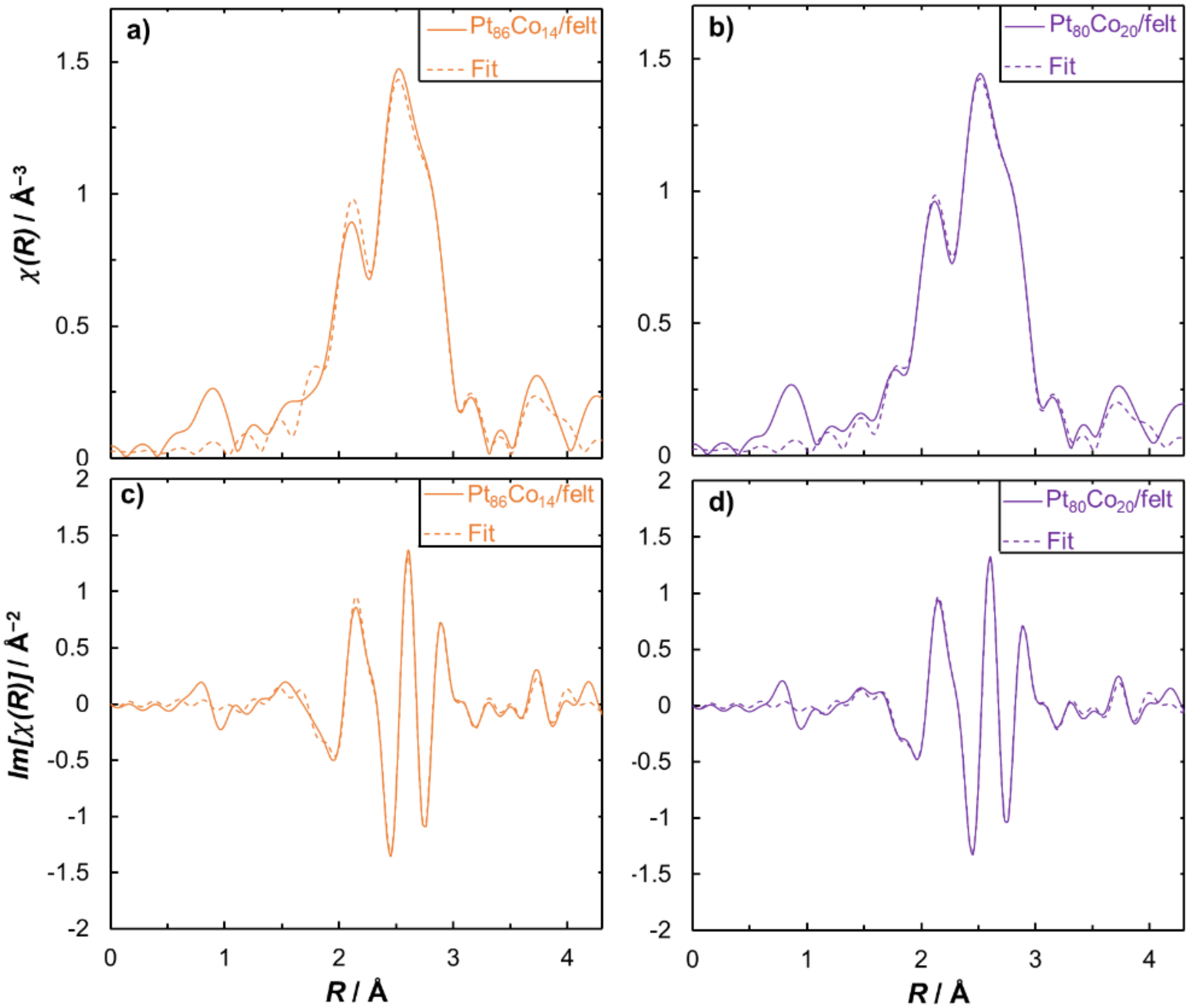

Figure A.8 EXAFS spectra of $Pt_{86}Co_{14}$/felt and $Pt_{80}Co_{20}$/felt catalysts performed at the Pt L_3-edge and their fit. The magnitude of the *R*-space spectra (solid lines) and their fits (dashed lines) to a Pt-Pt first and second shell and a Pt-Co first shell for **a)** $Pt_{86}Co_{14}$/felt and **b)** $Pt_{80}Co_{20}$/felt. The imaginary *R*-space spectra (solid lines) and their fits (dashed lines) for **c)** $Pt_{86}Co_{14}$/felt and **d)** $Pt_{80}Co_{20}$/felt.

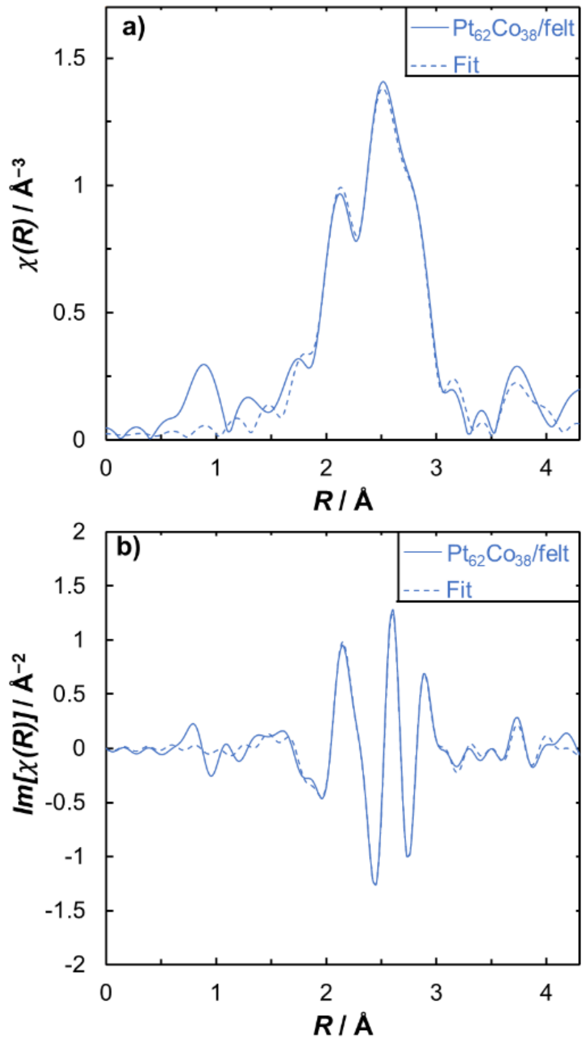

Figure A.9 EXAFS spectra of $Pt_{62}Co_{38}$/felt at the Pt L_3-edge and fit. a) The magnitude of the *R*-space spectrum (solid line) and its fit (dashed line) to a Pt-Pt first and second shell and a Pt-Co first shell. **b)** The imaginary *R*-space spectra (solid line) and its fit (dashed line).

Table A.1 Tabulated linear combination fitting results of XANES for Pt_xCo_y/felt catalysts at the Pt L_3-edge using Pt foil and PtO_2 as standards. Fitting was performed at −20 eV below the edge and 30 eV post edge.

Material	% Pt	% PtO_2
Pt_{100}/felt	97.7	2.3
$Pt_{86}Co_{14}$/felt	99.7	0.3
$Pt_{80}Co_{20}$/felt	99.4	0.6
$Pt_{62}Co_{38}$/felt	98.6	1.4

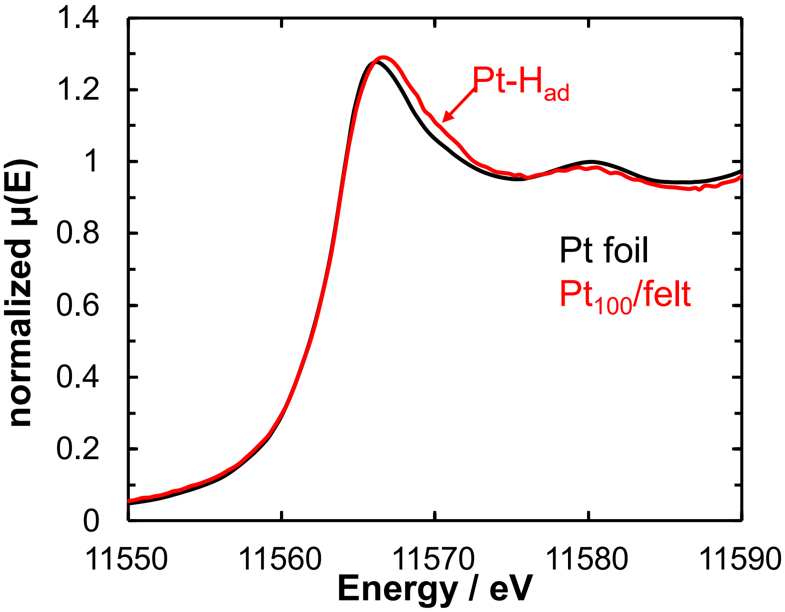

Figure A.10 XANES of Pt_{100}/felt at the Pt L_3-edge at −0.05 V vs. RHE and Pt foil. Supporting electrolyte is 3 M acetate buffer with graphite rod as counter and a leak-free Ag/AgCl as reference electrode. Reference electrode was calibrated to RHE before using it for experiments.

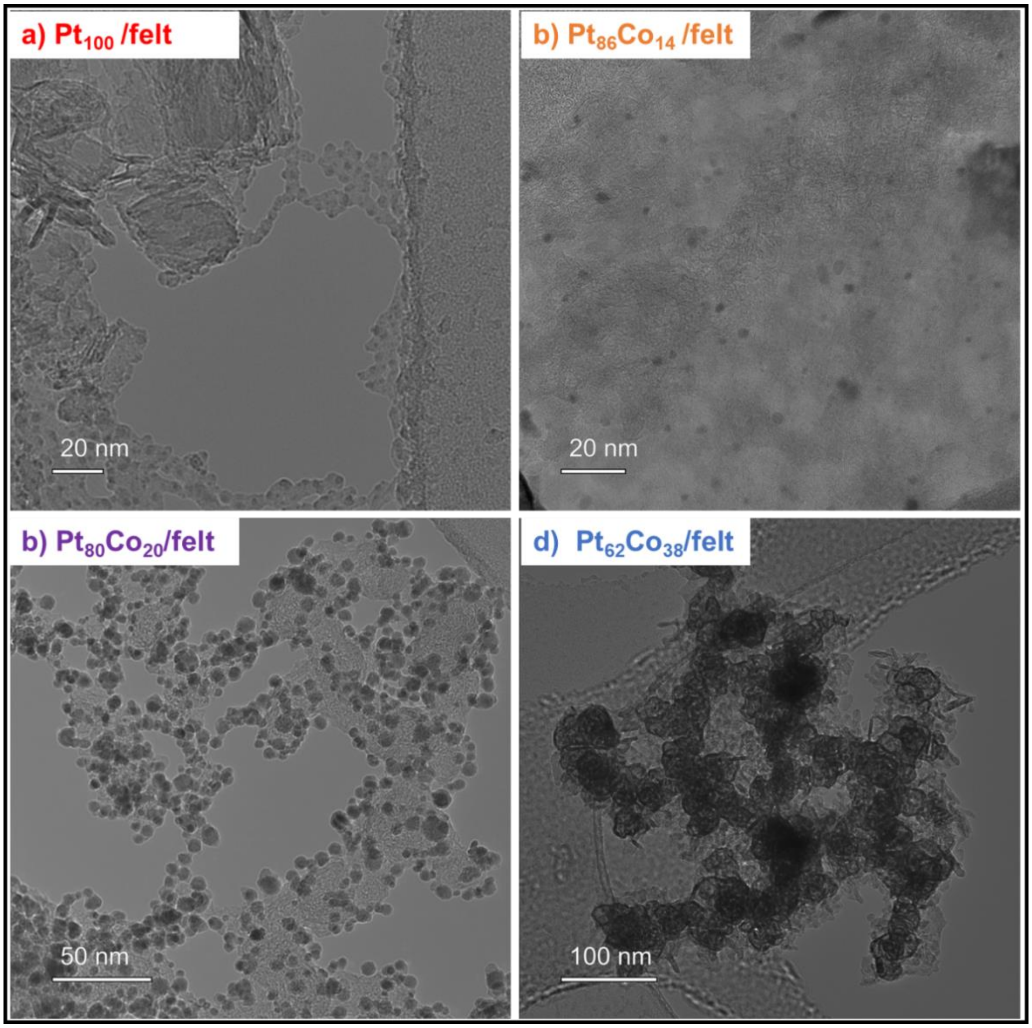

Figure A.11 Representative TEM micrographs of the catalysts. a) Pt_{100}/felt, **b)** $Pt_{86}Co_{14}$/felt, **c)** $Pt_{80}Co_{20}$/felt, **d)** $Pt_{62}Co_{38}$/felt. All images are taken after pretreatment to remove unalloyed Co, but before use for ECH.

A.3 Kinetic Model

We use a Langmuir-Hinshelwood kinetic model to understand the ECH TOF behavior on the Pt_xCo_y/felt catalysts as described in **Chapter 6** (**Eqs. A.2**–A.**5**). In addition to the assumptions described in **Chapter 6** (i.e., phenol adsorption is independent of applied electrochemical potential, hydrogen adsorption is a function of applied electrochemical potential, surface reaction is the rate-determining step, the rate constant is independent of potential), to describe the TOF as a function of Co fraction we make the following assumptions:

1. The H adsorption energy weakens with Co fraction for both the Pt_xCo_y and Pt/Pt_xCo_y structures provided the Co fraction is less than 0.5. Although at Co fraction = 0.5 the Pt_xCo_y structures shows stronger H adsorption, we model Co fractions < 0.5 for simplicity. Evidence for this assumption is shown in **Figure 6.3b** of **Chapter 6**.
2. The phenol adsorption energy is unaffected by Co fraction. Evidence for this is shown by the experimental values in **Figure 6.7** of **Chapter 6**.
3. The first hydrogenation barrier increases linearly with Co fraction for the Pt_xCo_y structure and reduces with Co fraction for the Pt/Pt_xCo_y structure. Evidence for this assumption is shown in **Figure 6.8** of **Chapter 6**.

In **Eq. A.1** we show our model for the TOF of phenol ECH as a function of both Co fraction in the catalyst (y_{Co}) and applied electrochemical potential (E). This equation and the variables are the same as combining **Eq. A.4** and **Eq. A.5** in **Chapter 6**, except here we indicate the dependence of certain terms on y_{Co} and E. For example, $K_{\mathrm{H}}(y_{\mathrm{Co}}, E)$ is the equilibrium adsorption coefficient of H as a function of Co content in the catalyst and applied potential.

$$TOF(y_{\mathrm{Co}}, E) = A \exp^{\left(\frac{-\Delta H_f^{\ddagger}(y_{\mathrm{Co}})}{RT}\right)} \frac{K_{\mathrm{H}}(y_{\mathrm{Co}}, E) C_{\mathrm{H}} K_{\mathrm{P}} C_{\mathrm{P}}}{(1 + K_{\mathrm{H}}(y_{\mathrm{Co}}, E) C_{\mathrm{H}} + K_{\mathrm{P}} C_{\mathrm{P}})^2} \tag{A.1}$$

We use a value of 10^8 sec^{-1} for the pre-exponential factor (A). The activation enthalpy for the first hydrogenation step ($\Delta H_f^{\ddagger}$) as a function of Co fraction is given by **Eq. A.2**:

$$\Delta H_f^{\ddagger}(y_{\mathrm{Co}}) = \Delta H_f^{\ddagger}(y_{\mathrm{Co}} = 0) + \beta_1 y_{\mathrm{Co}} \tag{A.2}$$

where $\Delta H_f^{\ddagger}(y_{\mathrm{Co}} = 0)$ is the activation enthalpy for pure Pt, R is the ideal gas constant = 8.314 kJ mol^{-1} and T is the temperature = 300 K. As we show in **Figure 6.8b**, the computed first hydrogenation activation enthalpy linearly scales with Co fraction, where it increases for the

Pt_xCo_y structure and decreases for the Pt/Pt_xCo_y structure. To capture this qualitatively in our kinetic model we use a value of β_1 = 8 kJ mol^{-1} for the Pt_xCo_y structures and β_1 = −8 kJ mol^{-1} for the Pt/Pt_xCo_y structures. We note that directly including the computed activation enthalpies into the model does not give quantitative agreement with our experimental rates, and so we look instead for qualitative trends here.

We assume the phenol adsorption equilibrium constant K_P is independent of the Co fraction and potential as discussed in **Chapter 6**. In reality, the potential may affect $\Delta G_{\mathrm{ads,P}}$ by strengthening the water-metal bond at potentials far away from the potential of zero charge of the metal in the system.[5] The adsorption energies from the isotherms fits on the Pt_xCo_y alloy in **Figure 6.7** are also almost independent of the Co fraction. The fitted value is an average value of both the active (111) facet and inactive (100) and (110) steps. We use the $\Delta G_{\mathrm{ads,P}}$ = −9 kJ mol^{-1} for the (111) facet of Pt which we have previously shown is the active facet for phenol ECH on Pt.[6] The concentration of phenol used in our experiments was 20 mM so we set C_{P} = 0.02 M in the model.

We show the dependence of the energy of adsorption of hydrogen onto the catalyst by **Eq. A.3**. We use a value of $\Delta G_{\mathrm{H}}(y_{\mathrm{Co}} = 0, E = 0 \text{ V vs. RHE})$ = −1 kJ mol^{-1} calculated in the aqueous-phase for Pt.[7] We use a value of β_2 = 40.4 kJ mol^{-1} in the model which represents how ΔG_{H} is weakened with increasing Co fraction from the trend in **Figure 6.3b** in **Chapter 6**.

$$\Delta G_{\mathrm{H}}(y_{\mathrm{Co}}, E = 0 \text{ V vs. RHE}) = \Delta G_{\mathrm{H}}(y_{\mathrm{Co}} = 0, E = 0 \text{ V vs. RHE}) + \beta_2 y_{\mathrm{Co}} \tag{A.3}$$

Combining **Eq. A.3** with **Eq. 6.2** in **Chapter 6** we describe the hydrogen adsorption coefficient as a function of Co fraction and potential in **Eq. A.4**.

$$K_{\mathrm{H}}(y_{\mathrm{Co}}, E) = \exp\left(\frac{-[\Delta G_{\mathrm{H}}(y_{\mathrm{Co}} = 0, E = 0 \text{ V vs. RHE}) + \beta_2 y_{\mathrm{Co}}]}{RT}\right)\exp\left(\frac{-FE}{RT}\right) \tag{A.4}$$

Coupling **Eqs. A.1**, **A.2**, and **A.4** and specified constants, we obtain an equation which we use to predict the ECH TOF shown in **Figure 6.9** in **Chapter 6**.

References

(1) Román, A. M.; Hasse, J. C.; Medlin, J. W.; Holewinski, A. Elucidating Acidic Electro-Oxidation Pathways of Furfural on Platinum. *ACS Catal.* **2019**, *9*, 10305–10316.

(2) Mark, L. O.; Jenkins, A. H.; Heinz, H.; Medlin, J. W. Furfuryl Alcohol Deoxygenation, Decarbonylation, and Ring-Opening on Pt(111). *Surf. Sci.* **2018**, *677*, 333–340.

(3) Shi, D.; Vohs, J. M. Deoxygenation of Biomass-Derived Oxygenates: Reaction of Furfural on Zn-Modified Pt(111). *ACS Catal.* **2015**, *5*, 2177–2183.

(4) Taylor, M. J.; Jiang, L.; Reichert, J.; Papageorgiou, A. C.; Beaumont, S. K.; Wilson, K.; Lee, A. F.; Barth, J. V.; Kyriakou, G. Catalytic Hydrogenation and Hydrodeoxygenation of Furfural over Pt(111): A Model System for the Rational Design and Operation of Practical Biomass Conversion Catalysts. *J. Phys. Chem. C* **2017**, *121*, 8490–8497.

(5) Bockris, J. O.; Jeng, K. T. In-Situ Studies of Adsorption of Organic Compounds on Platinum Electrodes. *J. Electroanal. Chem.* **1992**, *330*, 541–581.

(6) Singh, N.; Sanyal, U.; Ruehl, G.; Stoerzinger, K. A.; Gutiérrez, O. Y.; Camaioni, D. M.; Fulton, J. L.; Lercher, J. A.; Campbell, C. T. Aqueous Phase Catalytic and Electrocatalytic Hydrogenation of Phenol and Benzaldehyde over Platinum Group Metals. *J. Catal.* **2020**, *382*, 372–384.

(7) Yang, G.; Akhade, S. A.; Chen, X.; Liu, Y.; Lee, M.; Glezakou, V.; Rousseau, R.; Lercher, J. A. The Nature of Hydrogen Adsorption on Platinum in the Aqueous Phase. *Angew. Chemie Int. Ed.* **2019**, *58*, 3527–3532.